NASA

Technical Memorandum 83866

Winter and Summer Simulations with the GLAS Climate Model

J. Shukla, D. Straus, D. Randall, Y. Sud, L. Marx

December 1981

Laboratory for Atmospheric Sciences
Modeling and Simulation Facility

National Aeronautics and
Space Administration

Goddard Space Flight Center
Greenbelt, Maryland 20771

Winter and Summer Simulations with the GLAS Climate Model

J. Shukla, D. Straus, D. Randall and Y. Sud

Laboratory for Atmospheric Sciences

L. Marx

Sigma Data Services Corp.

December, 1981

National Aeronautics and Space Administration
Goddard Space Flight Center
Greenbelt, MD 20771

ABSTRACT

The GLAS climate model is a general circulation model based on the primitive equations in sigma coordinates on a global domain in the presence of orography. The model incorporates parameterizations of the effects of radiation, convection, large scale latent heat release, turbulent and boundary layer fluxes and ground hydrology.

Winter and summer simulations have been carried out with this model, and the resulting data compared to observations. These comparisons indicate that: (i) The simulated mean dynamical fields of the upper troposphere in winter and the lower troposphere in summer are more realistic than those of the lower troposphere in winter and the upper troposphere in summer. A serious problem is the unrealistically cold polar upper troposphere in both simulations. (ii) The latitude-height structure of the components of the simulated fields with various spatial (planetary wave, synoptic scale wave) scales and temporal (time mean, low frequency, medium frequency) scales shows overall agreement with the observations. However, the variance of low frequency planetary waves is somewhat too small. (iii) Maps of local variability indicate that the model's band-pass variances are well simulated except for the upper level heat and momentum fluxes. The local, low-pass variances are not realistic. (iv) The simulation of physical processes is generally realistic. The distribution of simulated evaporation, precipitation and surface stress show good agreement with observations. The surface sensible heat flux is somewhat too high, and the model shows a serious excess of supersaturation clouds in the lowest layer. (v) The Hadley cells in both seasons are somewhat too weak, but their location and depth are realistic. The model Walker circulation in the winter subtropics indicates rising over an oceanic precipitation maximum and sinking over land.

FOREWORD

This technical memorandum has been prepared as a documentation of the design and performance of the GLAS Climate Model. Although this global general circulation model is continually evolving, the results presented here should be useful both as an indication of modeling skill and as a basis for comparison with future model results.

ACKNOWLEDGMENTS

The authors gratefully acknowledge the helpful comments and suggestions of Dr. M. Halem and Dr. Y. Mintz. We also wish to acknowledge Mr. J. Abeles, Mr. E. Sabatino and Mr. K. Ha for their able technical assistance. Finally, special thanks are due to Miss D. Boyer for typing the manuscript and to Ms. L. Rumburg for drafting the figures.

CONTENTS

1. Introduction

General circulation models are mathematical tools for conducting sensitivity, predictability and observing system simulation studies. The simple quasi-geostrophic, channel model with prescribed heating and hydrologic cycle developed by Phillips (1956) led the way for development of more complex models (Smagorinsky, 1963; Mintz, 1964; Manabe et al. 1965, Leith, 1964, Arakawa et al. 1969), which were based on the primitive equations of motion on a global domain, and parameterized the physical processes of radiation, large scale and convective condensation, boundary layer and turbulent fluxes, and ground hydrology. The primary objective of these efforts was to simulate the space-time structure of the stationary and transient components of the circulation. Although further model developments are being carried out to determine and correct the deficiencies of the general circulation models (GCMs), their degree of success in simulating the observed circulation justifies their use for conducting appropriate sensitivity, predictability and observing system simulation studies.

In this paper we present the analysis of winter and summer circulations simulated by the GLAS (Goddard Laboratory for Atmospheric Sciences) general circulation climate model. The present version of the model has undergone substantial modifications since the publication of its earlier version seven years ago by Somerville et al. (1974). Results of simulations by an intermediate version of the model were presented by Halem et al. (1979) at the GARP/JOC (Joint Organizing Committee) conference on climate models.

The kind of controlled numerical experiments that can be carried out with a GCM depends upon the model's ability to simulate specific features of the circulation. As one of our main objectives is to conduct sensitivity studies to determine the role of the slowly varying boundary conditions of sea surface

temperature, soil moisture, sea ice and snow in determining the predictability of monthly and seasonal anomalies and their geographical distribution, we present a detailed spatial and temporal analysis of the physical state parameters and processes of the model atmosphere.

The model shows a serious deficiency in simulating the mean circulation near the poles. The upper tropospheric temperatures near the winter poles are too low compared to the observations and the corresponding upper level zonal winds are too strong. Another deficiency is that the tropical troposphere warms up by 2-3°C during the course of the simulation. We have not yet determined the precise cause of this deficiency. But the simulated tropospheric circulation in the middle latitudes and the tropics is realistic enough to warrant detailed analysis of its space-time variability.

Some of the primary objectives of NASA's climate modeling program are: 1) to conduct simulation studies which will help optimize space-observing systems; and 2) to determine how the global boundary conditions of sea surface temperature, soil moisture, sea ice and snow affect the variability and predictability of monthly and seasonal atmospheric anomalies. These studies are being carried out by NASA's own scientific staff, and also, in collaboration with scientists in other institutions. We hope this description and evaluation of the model's performance will enable the individual researchers to judge its utility as a GCM-experimentation tool. A bibliography of works dealing with the present and the earlier versions of the GLAS climate model is enclosed as an Appendix.

2. Model description

The GLAS climate model has evolved from the GISS GCM, described by Somerville et al. (1974) and Stone et al. (1977), which in turn, was based on the 9-level 1970 version of the GCM developed by A. Arakawa (1972) and Y. Mintz at UCLA. The model uses a form of the σ coordinate system (Phillips, 1957), with nine layers, all of the same σ thickness, and a 4 x 5 degree latitude-longitude grid, which is modified in the polar regions as discussed below. The variables are staggered in the horizontal according to the B-grid scheme of Arakawa and Lamb (1977), and in the vertical according to the scheme of Lorenz (1960). The upper boundary of the model is at 10 mb. The prognostic atmospheric variables are the surface pressure, the zonal and meridional components of the horizontal wind, the temperature, and the water vapor mixing ratio. The prognostic boundary variables are the bulk ground temperature and ground wetness, and the snow depth.

Although the current model is similar to the GISS GCM presented by Somerville et al. (1974) and Stone et al. (1977), significant changes have been made in both the finite-difference schemes and the physical parameterizations. As described by Halem and Russell (1973), Halem et al. (1979), and Herman and Johnson (1978), the model incorporates a "split grid," in which the number of grid points on a latitude circle is systematically reduced near the poles. This allows the use of a ten-minute time step, with only weak longitudinal smoothing at high latitudes. The idea is similar in principle to that proposed by Kurihara (1965), but is applied at only a few interfaces separating latitudinal bands within which the horizontal resolution is uniform. The resolution in each latitudinal band is twice that of its poleward adjacent neighbor. The differencing scheme maintains the quasi-conservative properties of kinetic energy and mean-square vorticity, as in the Arakawa scheme. Although written to handle an arbitrary number of bands, the geometry used in the present model has five

latitudinal bands, consisting of a central region extending from -66° to +66°, bounded by one set of bands from 70° to 78°, and a second set from 82° to 86°. The latitudinal resolution is 4° in all bands. The longitudinal resolutions are 5°, 10°, and 20°, respectively.

Once every simulated half hour, a sixteenth-order Shapiro filter (Shapiro, 1970) is applied, in the longitudinal direction, to the sea level pressure, and to the potential temperature and the wind components on the σ surfaces. The filter was introduced as an ad hoc device to suppress the "checkerboard" noise in the prognostic fields, which arises from the inability of the B-grid to simulate the geostrophic adjustment process at the two grid interval level (Arakawa and Lamb, 1977). However, a substantial price has been paid for this noise suppression. Filtering the potential temperature on the σ surfaces leads to a systematic cooling of the air over mountains and a systematic warming in the neighboring valleys. Filtering of the winds dissipates kinetic energy. Filtering of the sea-level pressure interferes with every conservation property of the model (except mass conservation). The magnitudes of some of these false, filter-induced sources and sinks have been determined. The filtering of potential temperature generates 2.5 W m^{-2} of potential energy, and filtering of the winds dissipates 1.5 W m^{-2} of kinetic energy.

The Matsuno forward-backward time differencing scheme is used. This scheme tends to damp high frequencies, and so it helps to control computational noise in the model, but at the cost of almost doubling the computing time required for the dynamics.

We use the cumulus parameterization developed by Arakawa (1969; see also Haltiner, 1971) for the three-level UCLA GCM; but as modified for use in a nine-level GCM by Sommerville et al. (1974; see also Helfand, 1979). Although this Arakawa cumulus parameterization predates the cumulus parameterization theory of Arakawa and Schubert (1974) and Lord and Arakawa (1981), many key

concepts employed by Arakawa and Schubert were already present in the 1969 paper, including the cumulus mass flux, a spectrum of clouds distinguished by their fractional entrainment rates, and closure formulated in terms of the stabilization of the environment by the clouds. Helfand (1979) modified the parameterization to include very deep clouds and cumulus friction, but these modifications are not incorporated into the present model.

The model also includes latent heat release due to large-scale saturation, which occurs when the relative humidity exceeds 100%.

The short-wave radiation parameterization is that presented by Lacis and Hansen (1974). It includes absorption by ozone, water vapor, and clouds.

The long-wave radiation parameterization of the current model is based on the method of Wu (1976), Wu et al. (1978), and Wu (1980). The parameterization includes a water vapor transmittance that uses a statistical band model with the strong line version of the Curtis-Godson (Godson, 1955) approximation; the water vapor dimer effect in the 8-13 window region; line-by-line precalculation of CO_2 transmittance including fundamental bands, hot bands, and isotopes; tables of ozone transmittance calculated by Dr. N. Scott (private communication); a special treatment of the nearby layer quadrature for increased accuracy in the numerical integration; and the effects of clouds. In order to calculate the incoming long wave flux at the 10 mb level, the top of the model, zonally-averaged climatological temperatures at 1 mb and 5 mb are prescribed. In order to save computing time, the time step for the long-wave radiation is 5 hours for the simulations presented in this paper.

Clouds are assumed to occur if and only if the model predicts cumulus convection (restricted to the lowest six layers) or large-scale saturation (in any layer). No parameterization of subgrid-scale fractional cloudiness is attempted; both supersaturation and convective clouds are assumed to completely fill a grid box. Moeng and Randall (1982) have recently studied the sensitivity of the

model to this extreme parameterization of convective cloudiness. The optical properties of the clouds are prescribed as shown in Table 2.1. In the terrestrial radiation parameterization, all clouds are assumed to be black bodies.

The planetary boundary layer (PBL) parameterization was formulated by Katayama, (as reported by Arakawa, 1972) and modified by Sommerville, et al. (1974). We have revised the parameterization in order to correct a defect noted by Charney et al. (1977): earlier versions of the model produced too little evaporation over land and too much over the oceans. We found a high-frequency (in time) computational mode in the surface evaporation and sensible heat flux fields. A simple revision of the numerical algorithm for computing these fluxes eliminated the computational mode, and the revised model produces more realistic surface flux distributions (Sud and Abeles, 1981).

The model incorporates a prognostic soil moisture, following the UCLA model (Arakawa, 1972), but with different formulations for the runoff, snow melt, and potential evapotranspiration, as developed by Lin et al. (1978).

A comprehensive, detailed, and up-to-date documentation of the model and its post-processing routines is in preparation as a NASA Technical Memorandum (Sud et al., 1982).

Table 2.1 Prescribed cloud properties in GLAS solar radiation calculations.

Cloud Form	Cloud Level	Cloud Type	Albedo (%)	Optical Thickness
Convective	mid-level	Ac	50	8
	low-level	Cu	70	16
	penetrating	Cb	80	32
Super-Saturation	0-400 mb	Ci	20	2
	400-700 mb	As	50	8
	700-1000 mb	St	70	16

3. Boundary and initial conditions

The present GLAS climate model uses the externally imposed boundary conditions listed in Table 3.1. The observed climatological values of these boundary conditions are available only in the form of monthly means. A continuously changing set of prescribed boundary conditions was obtained by assigning the observed values to the midpoint (in time) of the appropriate month, and computing the values on all other days by linear interpolation. Table 3.1 gives the source of the data for the winter and summer simulations, and the name of the GLAS data set containing the data. Fig. 3.1a shows the topography used for both runs, while Figs. 3.2 and 3.3 show the sea surface temperature, land-sea and snow-ice distributions, and surface albedo for the months of February and July.

As revealed by a comparison of Figs. 3.1a and b, the topography has been greatly smoothed, and the land-surface heights for Greenland substantially reduced. This was necessary in order to reduce the level of computational noise in the earlier versions of the model.

Observed values of the surface albedo are prescribed for the land, ocean and desert regions are shown in Figs. 3.3a and 3.3b. This data was prepared from that described by Posey and Clapp (1964). Although the snow depth is predicted by the model, prescribed albedoes were used exclusively in the present runs. The snow and ice distributions used to determine the surface albedo are those listed in Table 3.1 and plotted in Fig. 3.2.

The winter simulation described in this paper started with the observed state of the atmosphere for 00Z on January 1, 1975. The summer simulation is started with the observed state of the atmosphere for 00Z on June 15, 1979. In both runs, the initial ground temperatures for land and sea ice points were assumed to be equal to the suface air temperature. The initial soil moistures

were obtained from climatological surface air relative humidities, as explained by Stone et al. (1977). The initial snow boundaries were obtained from the climatological data of Matson (1978), and the initial snow depths were specified as functions of the surface albedo.

Table 3.1

Prescribed Boundary Condition	Data Source	GLAS Data Set Name
Topography	NASA/Goddard Institute for Space Studies	C1APF79T
Sea Surface Temperatures	NOAA/Geophysical Fluid Dynamics Laboratory	C1APF79T
Surface Albedoes	Posey and Clapp (1964)	C1APF79A
Snow/Ice Distributions	British Met. Office (1977) Matson (1978)	C1APF79S

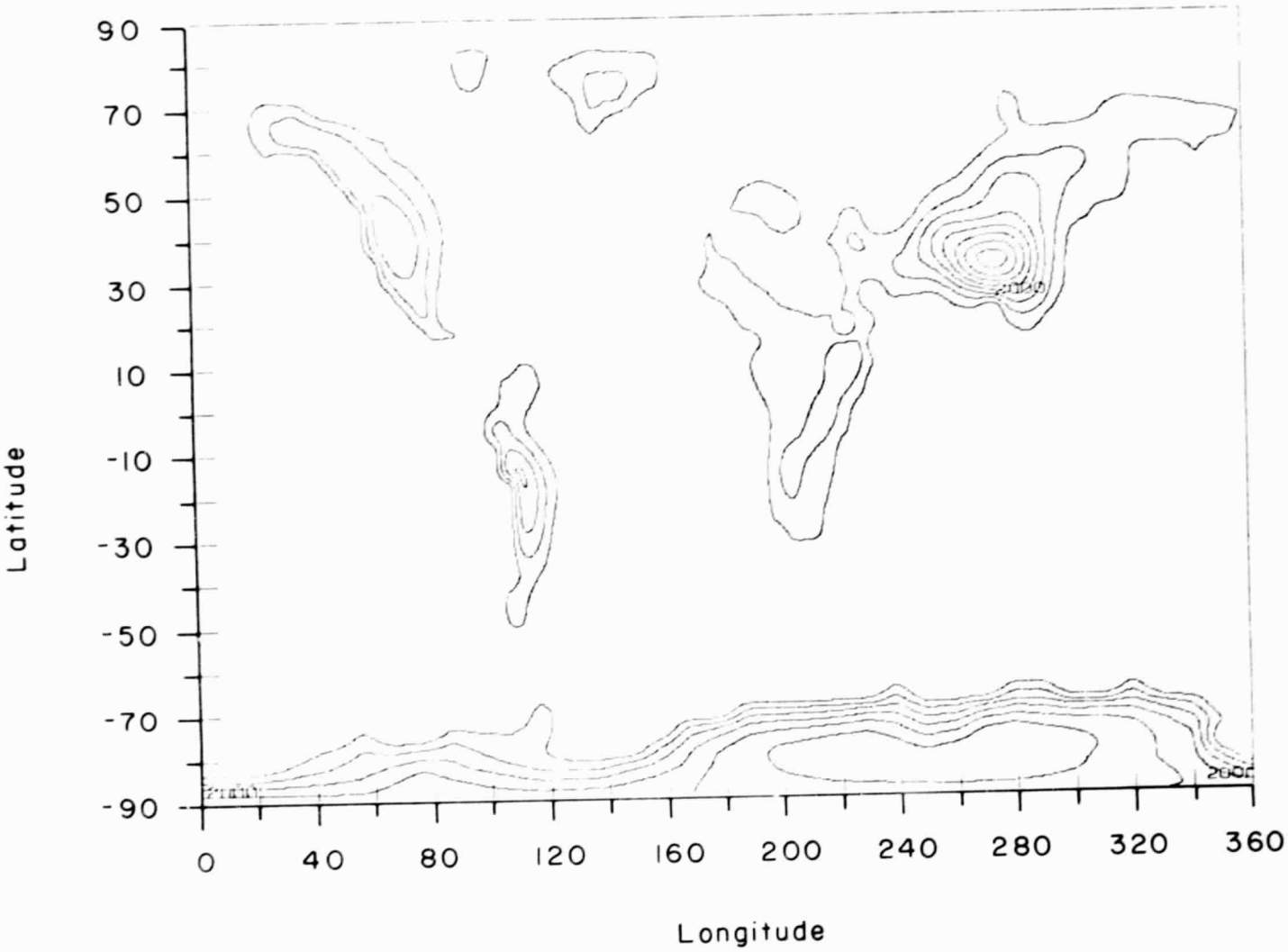

Figure 3.1a Topography used in the winter and summer simulations. The contour interval is 500 m.

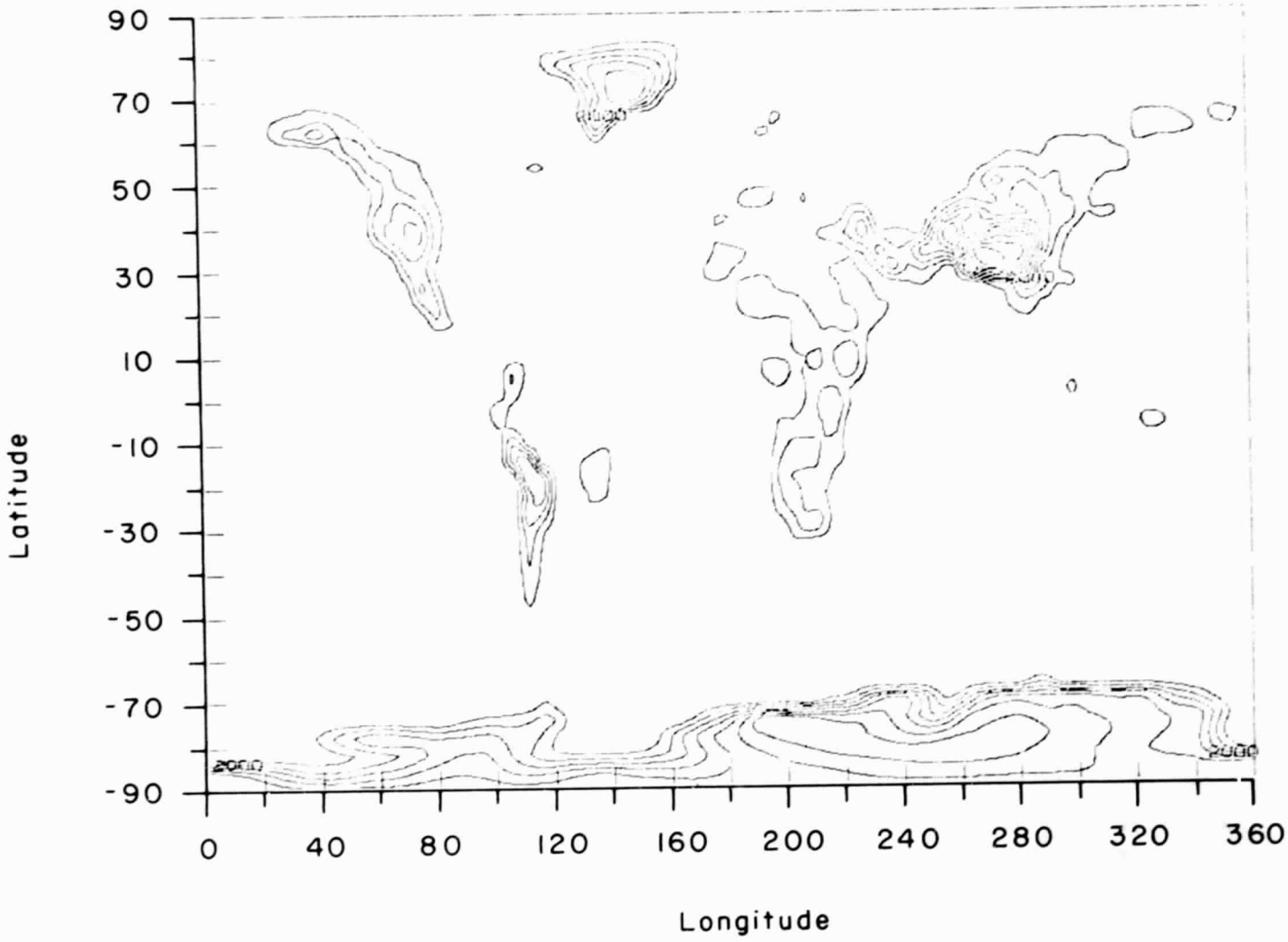

Figure 3.1b Topography obtained by simple area averaging on to a 4 x 5 degree latitude-longitude grid. The contour interval is 500 m.

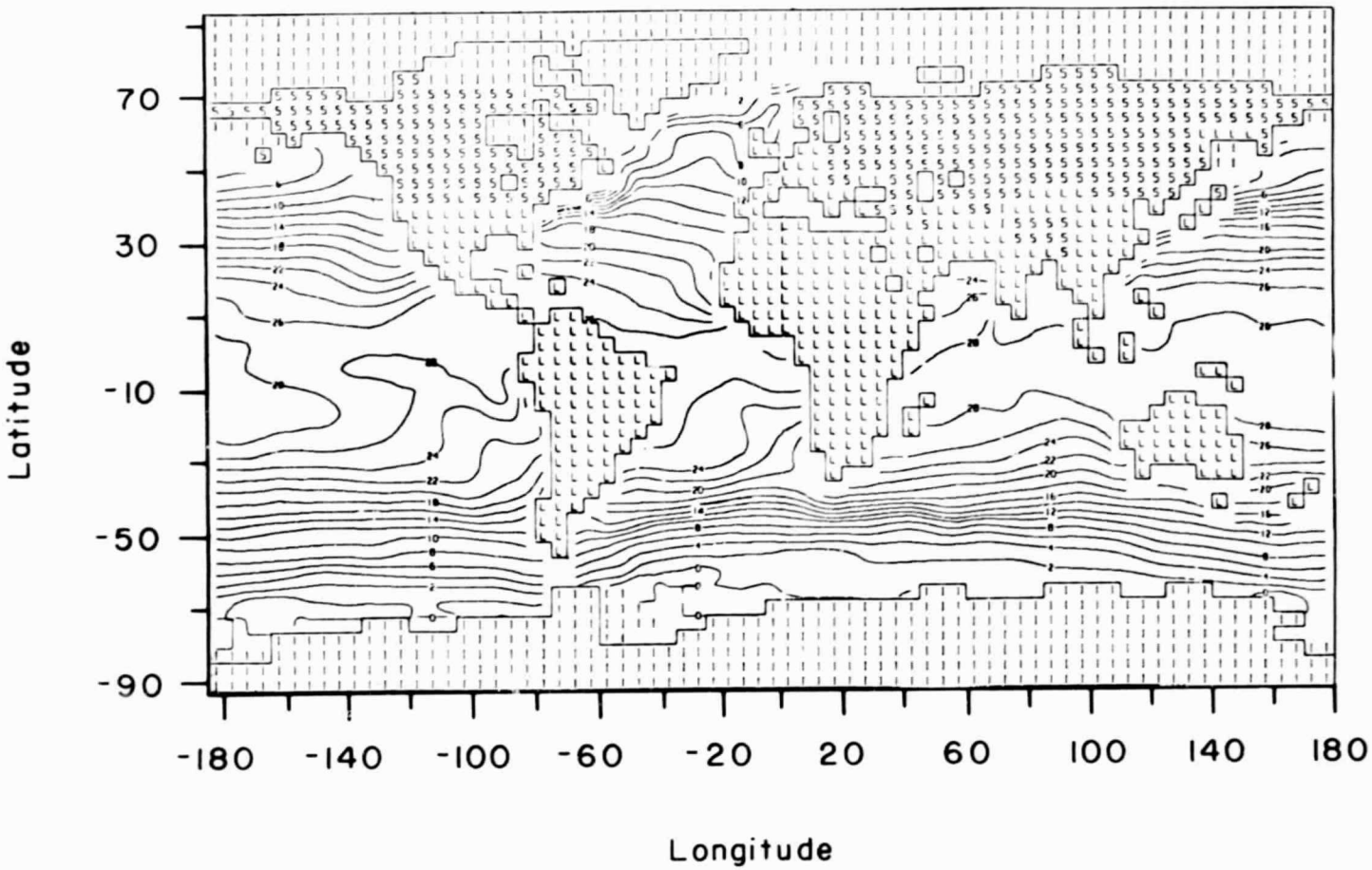

Figure 3.2a February sea surface temperatures, land-sea distribution, and snow/ ice distributions. The symbol meanings are: L = bare land, S = snow-covered land, I = ice.

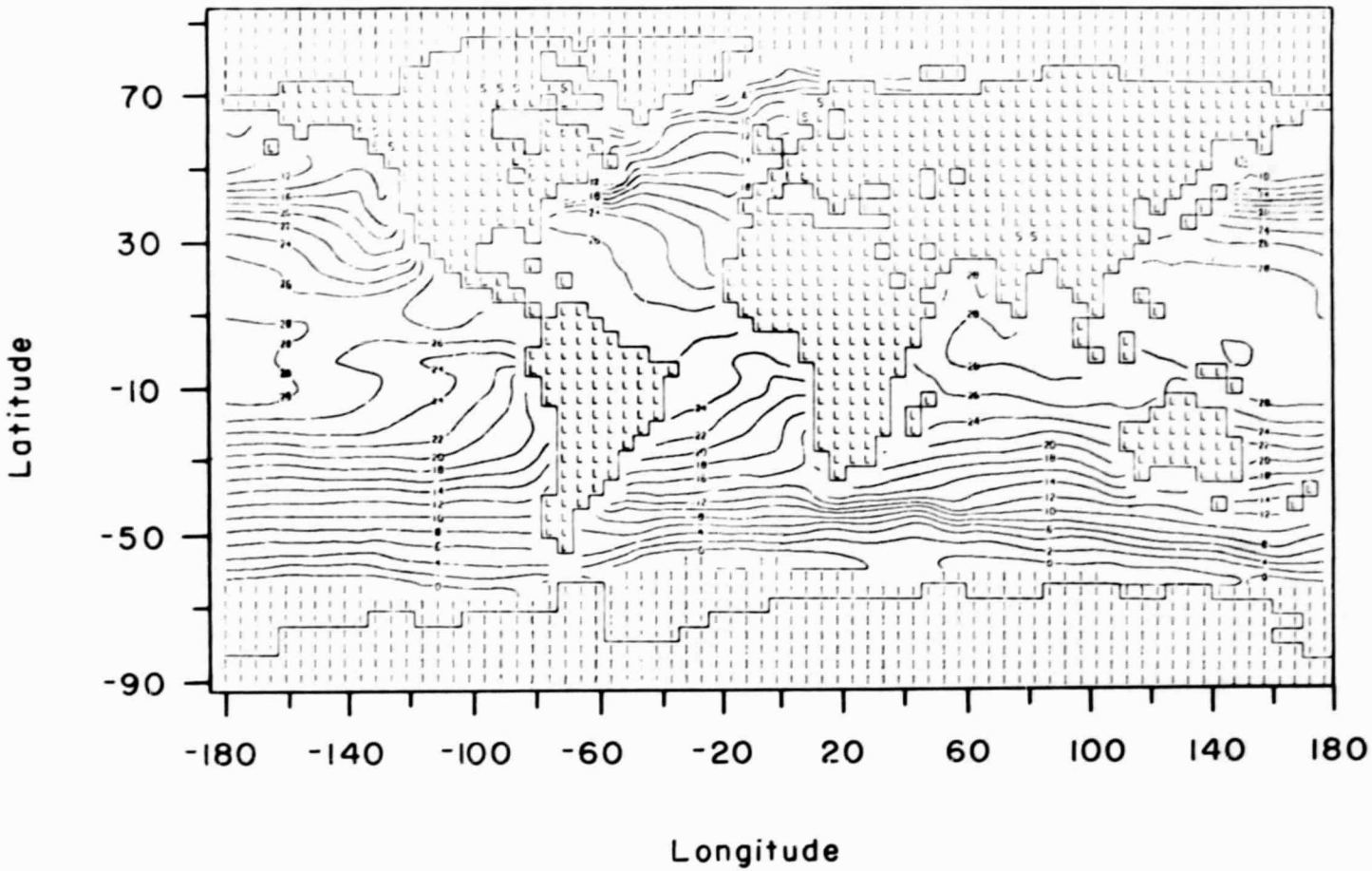

Figure 3.2b July sea surface temperatures, land-sea distribution, and snow/ice distributions. The symbol meanings are: L = bare land, S = snow-covered land, I = ice.

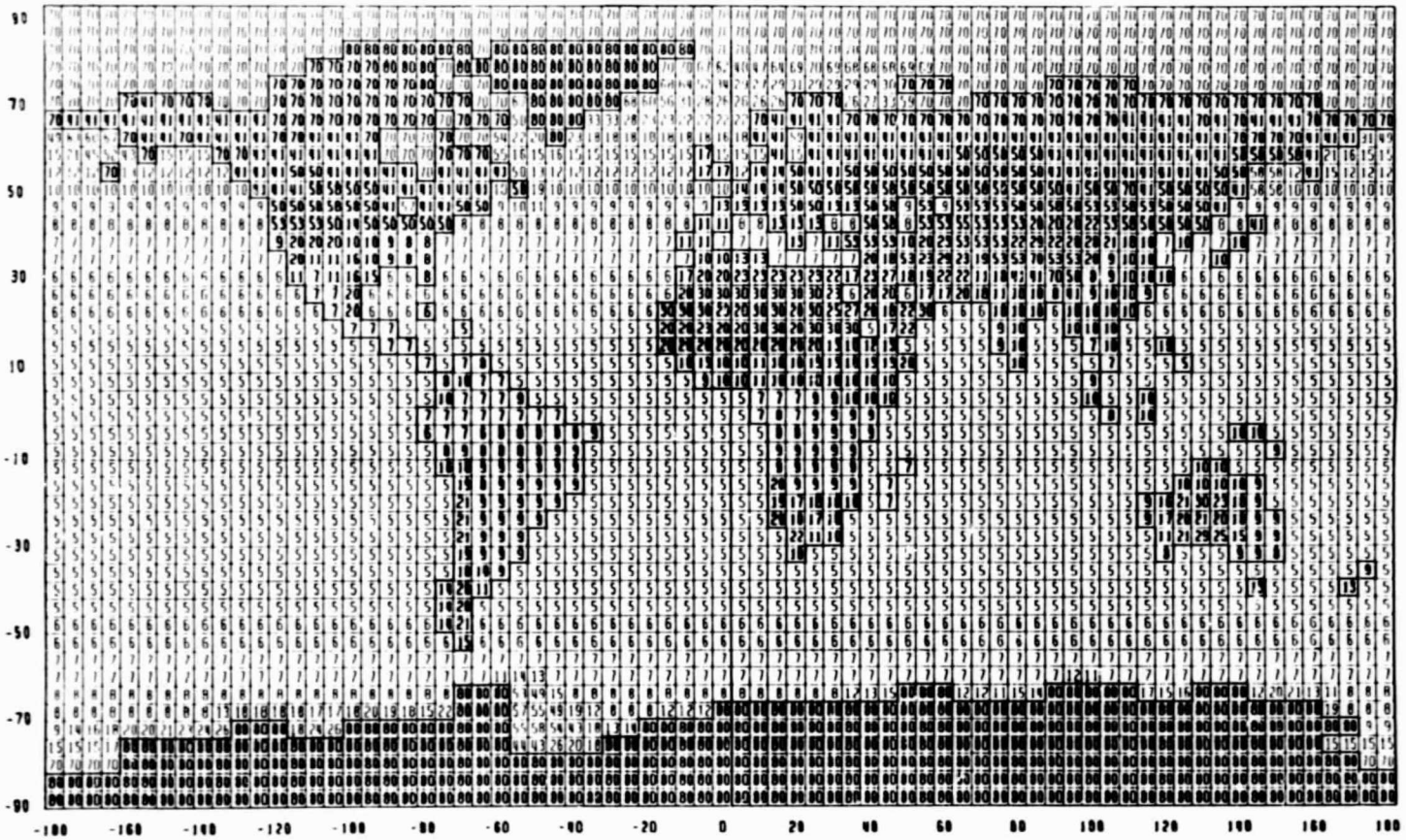

Figure 3.3a February prescribed surface albedoes, percent, based on the data of Posey and Clapp (1964).

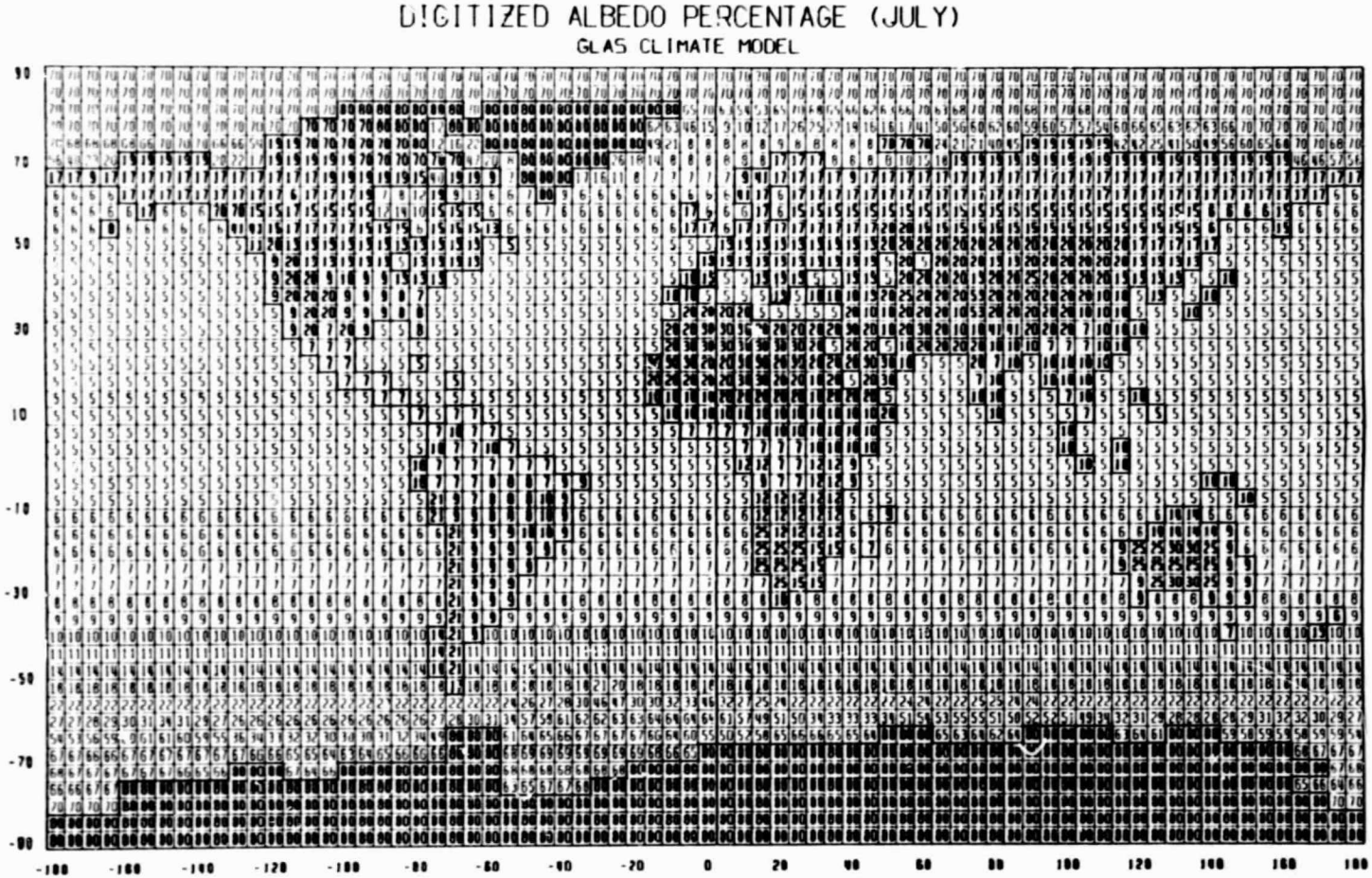

Figure 3.3b July prescribed surface albedoes, percent, based on the data of Posey and Clapp (1964).

4. Mean prognostic fields

a. Sea level pressure. Figures 4.1a and 4.2a show the 16 year mean sea level pressure for January and July reproduced from Godbole and Shukla (1981), and Figures 4.1b and 4.2b show the model simulated mean sea level pressure for the single February and July, respectively.

For February, the simulation of the prominent Northern Hemispheric circulation features, such as the Aleutian low, the Icelandic low and the Siberian high are fairly realistic. When comparing a single month model simulation with the mean climatology, one must keep in mind that there is considerable interannual variability in the observed monthly means. For example, the structure and intensity of the Aleutian and the Icelandic lows show considerable variability over the 16 years analyzed by Godbole and Shukla (1981) and the model simulation that is shown here falls well within the range of this variability. However, the discrepancy in the structure and intensity of the Siberian high (Compare Figs. 4.1a and 4.1b) is too large to be accounted for by the interannual variability or by differences between January and February. It has been conjectured by Halem et al. (1979) that the lack of a well organized Siberian high is due to excessive stratus formation over the region. The most serious deficiency of the simulated sea level pressure field in February is in the Southern Hemisphere. The observed sea level pressure is zonally uniform between about 40°S-60°S, while the simulated pressure field shows a large eddy structure in this zone. It has been our general experience that the simulation of the Southern Hemisphere pressure field is very sensitive to the model physics and numerics.

For July, the simulated sea level pressure field is also in fairly good agreement with the observations. The high pressure cell over the North Atlantic is very well simulated both with regard to intensity and to structure. Over the north Pacific the simulated high pressure cell is too small in the east-west

direction, and its major axis is oriented NNW-SSE instead of WSW-ENE. The Asiatic monsoon low is well simulated. The subtropical high pressure cells in the Southern Hemisphere are well simulated over the Indian Ocean, Atlantic Ocean and the eastern Pacific but not over Australia. The westerly zonal geostrophic flow that is shown by the isobars between 40°S and 60°S is fairly well simulated over the south Atlantic and south Indian Ocean; but in the south Pacific Ocean the simulated geostrophic flow is easterly between 40°S-60°S. For summer and winter, the model shows a common deficiency of distinct non-zonal isobar configurations in the southern hemispheric mid-latitudes.

b. Geopotential heights. Figures 4.3a and 4.4a show the observed (Crutcher and Davis, 1969) 200 mb geopotential height field for winter (December, January, February) and summer (June, July, August), and Figures 4.3b and 4.4b show the corresponding model simulation results for February and July respectively.

For February, the model simulation of the trough over the northeast USA and eastern Canada, the ridge over the eastern Atlantic and the jet stream over Japan are quite realistic. The ridge over the west coast of the USA is displaced to the east. The simulation of the upper level anticyclonic circulation over the tropics is reasonable. The actual values of the geopotential, however, are higher than the mean climatology. The southern hemispheric flow is also well simulated. Model simulations show more distinct eddy structure in the southern hemispheric circumpolar flow along 40°-60°S. It will be shown in section 5 that the model simulated stationary variance is in excellent agreement with the observed stationary variance.

For July, the model simulated 200 mb flow shows large amplitude short waves over North America and the adjacent Pacific Ocean. The ridge over central U.S.A. is well simulated but the trough off the west coast of U.S.A. is not present in the observed climatology. Although the local maximum associated with the

Tibetan high is not well simulated, the large scale anticyclone over the Asiatic monsoon is reasonable. The geopotential height in the tropical belt is higher by about 200 gpm than climatology. This is due to a gradual warming of the tropical atmosphere in the model simulation. We do not yet know the reason for this problem. The location of the simulated mid-Atlantic trough does not agree with the observations. The observed and simulated upper-level flows are both predominantly zonal in the Southern Hemisphere.

The surface circulation during July and the upper level circulation during January are, in general, better simulated than the surface circulation during winter and the upper level circulation during summer.

c. Flow at 200 mb. Figures 4.5a and 4.6a show the observed 200 mb flow pattern for February and July, and Figures 4.5b and 4.6b show the corresponding model simulations for February and July, respectively. The observed 200 mb flow for February was obtained from the NMC analysis of February, 1979 and for July it is reproduced from Sadler (1975).

For February, the locations and the intensities of the jet streams in both hemispheres are well simulated. The model simulated jet stream speeds in both hemispheres, are, in general, stronger than the observations of February, 1979, especially in the Southern Hemisphere. Away from the equator, the flow patterns are quite consistent with the geopotential height fields shown earlier.

The simulated July 200 mb geopotential height field does not compare well with the observations. One deficiency is the weakness of the summer monsoon easterly jet stream along 10°N. The subtropical jet stream near Japan is reasonable in terms of location and intensity, but the flow pattern over the subtropics of the Western Hemisphere is not realistic.

d. Zonal wind. Figures 4.7a and 4.8a (solid lines) show the observed zonal wind for February and July 1979, and Figures 4.7b and 4.8b (solid lines) show

the corresponding model simulations for February and July, respectively.

For February, the most conspicuous deficiency of the simulation is the absence of the closed maximum near 200 mb which is seen in the observations. The model simulated zonal wind increases with height and tilts towards the north so that the model simulated zonal wind near the upper boundary is stronger than is observed. This model deficiency is related to very low model temperatures in the the upper tropospheric polar regions. The locations of the strongest zonal wind maxima in both hemispheres is fairly well simulated. The zonally averaged equatorial easterlies are a little too weak. The configuration of the zero wind line is not unreasonable except that it is too low south of the equator.

The dashed lines in Figures 4.7a and 4.7b show the zonally averaged temperature. The largest discrepancy is found near the upper boundary over the polar regions. Dynamical heat fluxes are not sufficient to compensate for the excessive radiative cooling associated with high level supersaturation clouds which are treated as black bodies. The middle troposphere over the polar regions is warmer than the observations. The model simulated tropical atmosphere is considerably warmer than the observations. In a separate study Shukla and Wallace have found that most of the warming of the tropics occurs in first 30 days.

For July, the observed and simulated zonal wind fields are in very good agreement, except that the jet in the Southern Hemisphere increases monotonically with height so that the maximum value occurs near the upper boundary. Zonally averaged temperatures (dashed line) near the northern pole are lower in the model simulations than in the observations. The model simulated tropical atmosphere is again warmer than observations and this may be one of the reasons for a stronger westerly jet in the Southern Hemisphere.

e. Zonally averaged specific humidity. Figures 4.9a and 4.10a show the observed zonally averaged specific humidity for February and July, 1979, and

Figures 4.9b and 4.10b show the corresponding model simulations for February and July, respectively. For both seasons, the general latitudinal and vertical structure of the humidity field is quite reasonable. However, the simulated specific humidity at the lower levels is larger than observed. As will be shown later, the simulated rates of evaporation and precipitation are comparable to the observations. Therefore, the high values of specific humidity may be related to the boundary layer parameterization and the values of surface transfer coefficients used in the simulations.

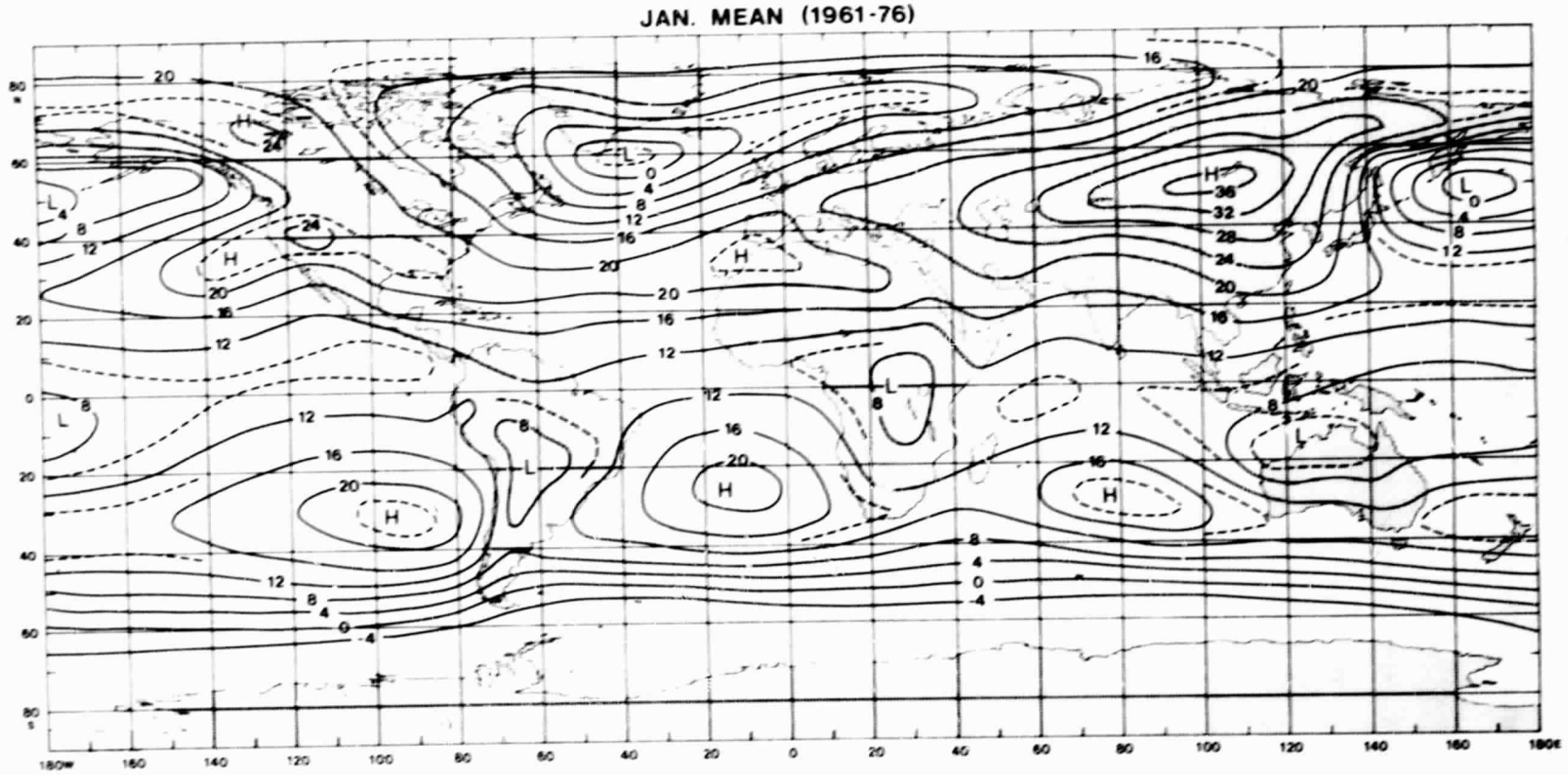

Figure 4.1a Observed mean sea level pressure (-1000 mb) for January (Godbole and Shukla, 1980).

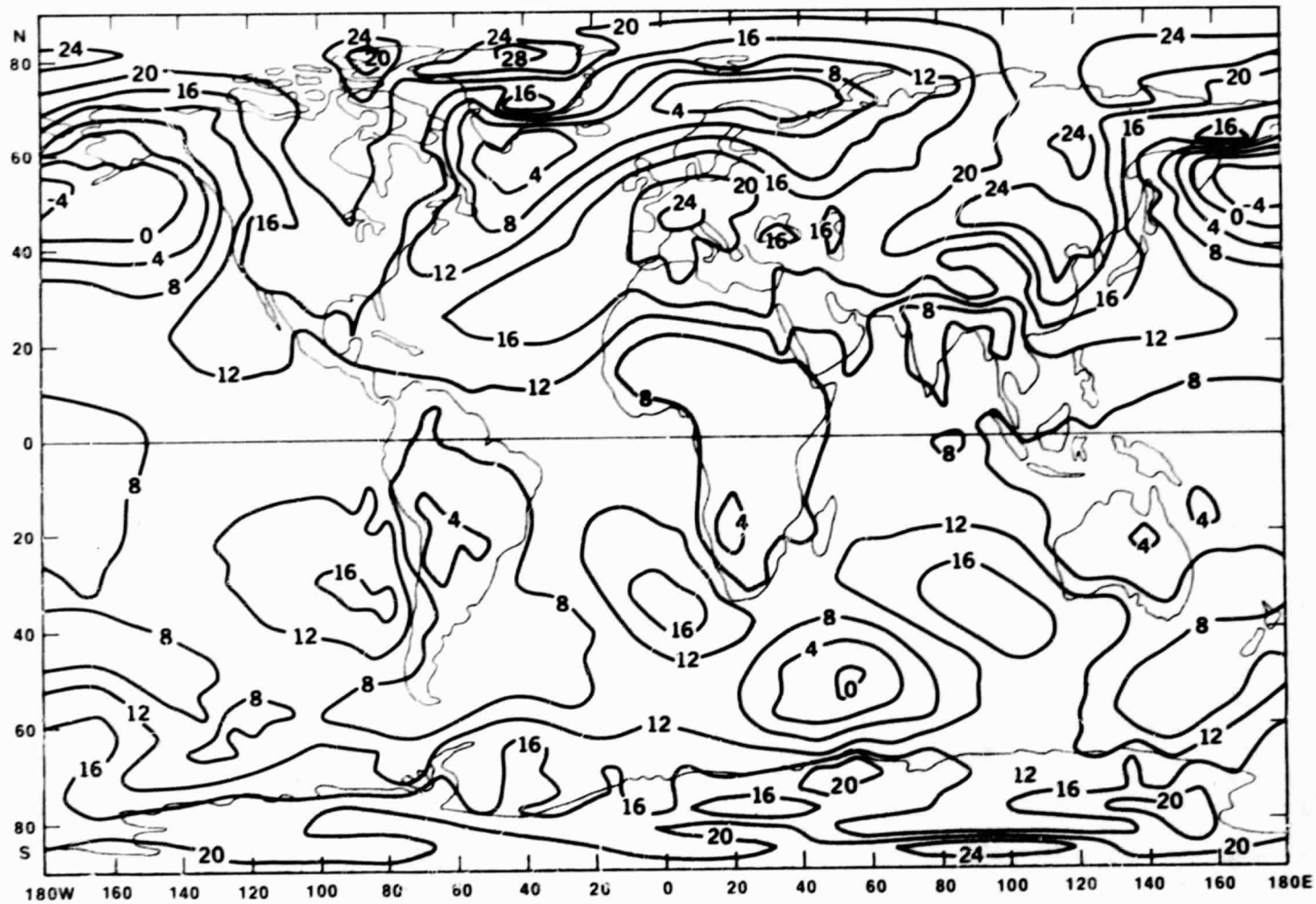

Figure 4.1b Model simulated sea level pressure (-1000 mb) for February.

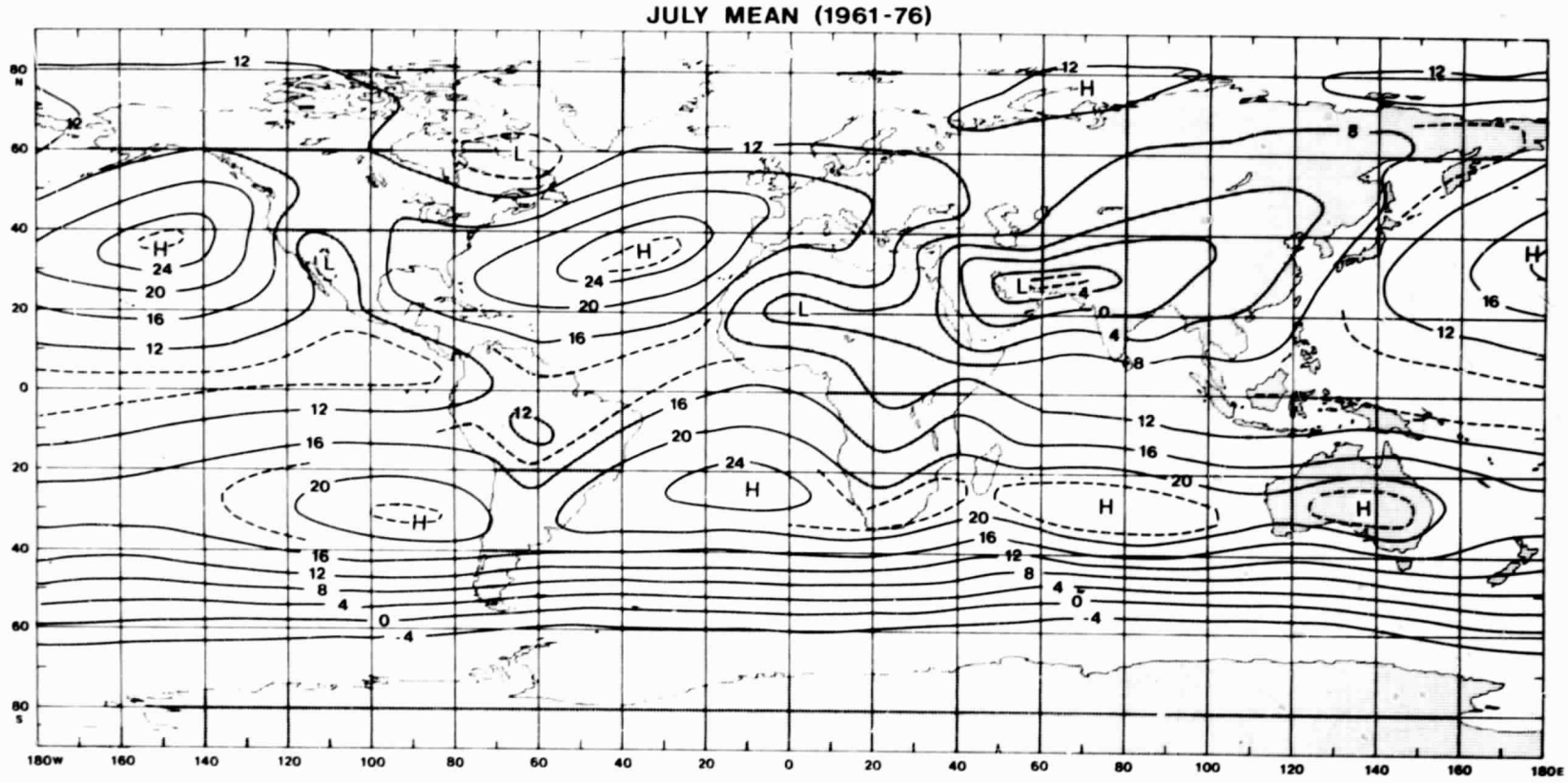

Figure 4.2a Observed mean sea level pressure (-1000 mb) for July (Godbole and Shukla, 1980).

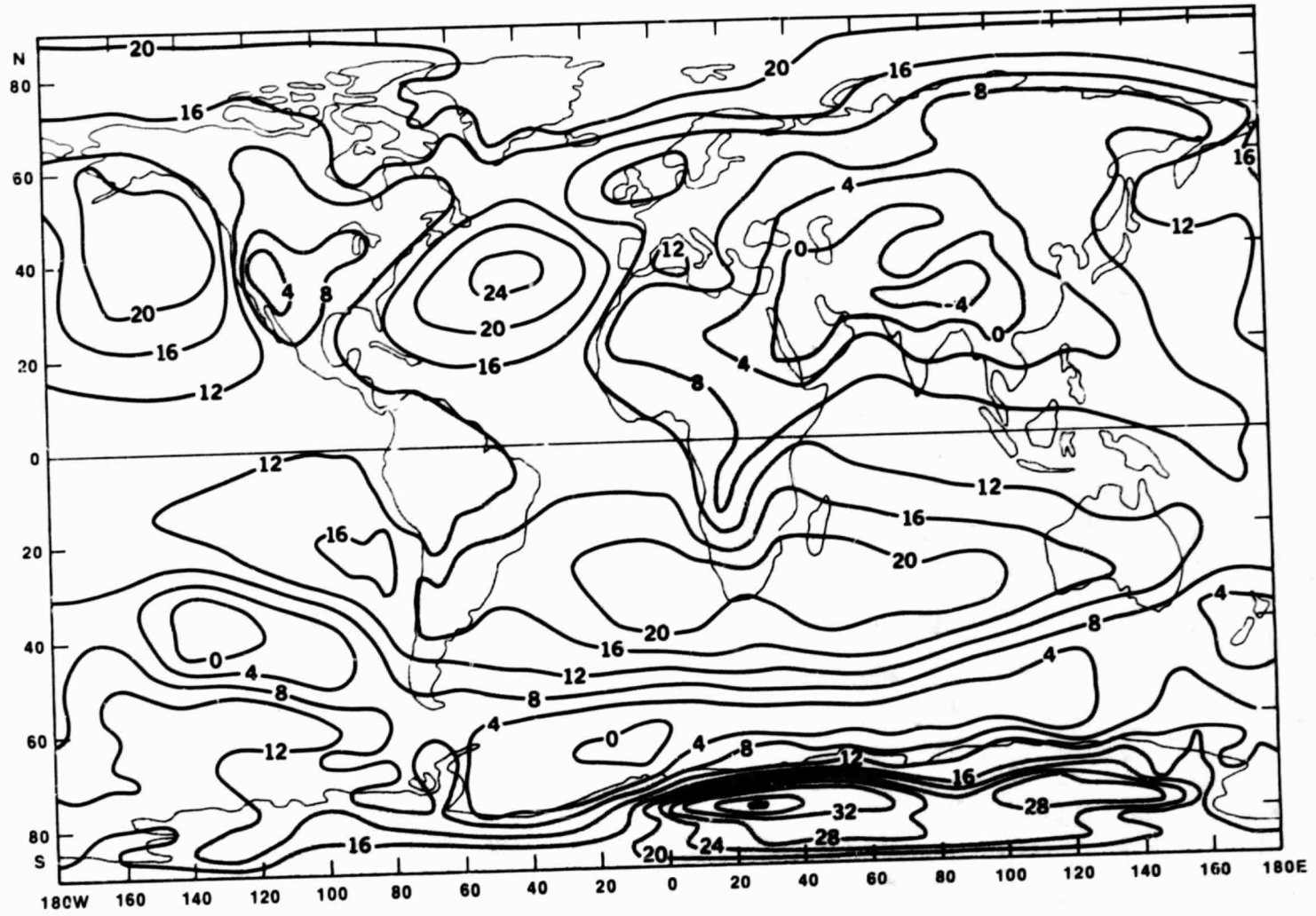

Figure 4.2b Model simulated sea level pressure (-1000 mb) for July.

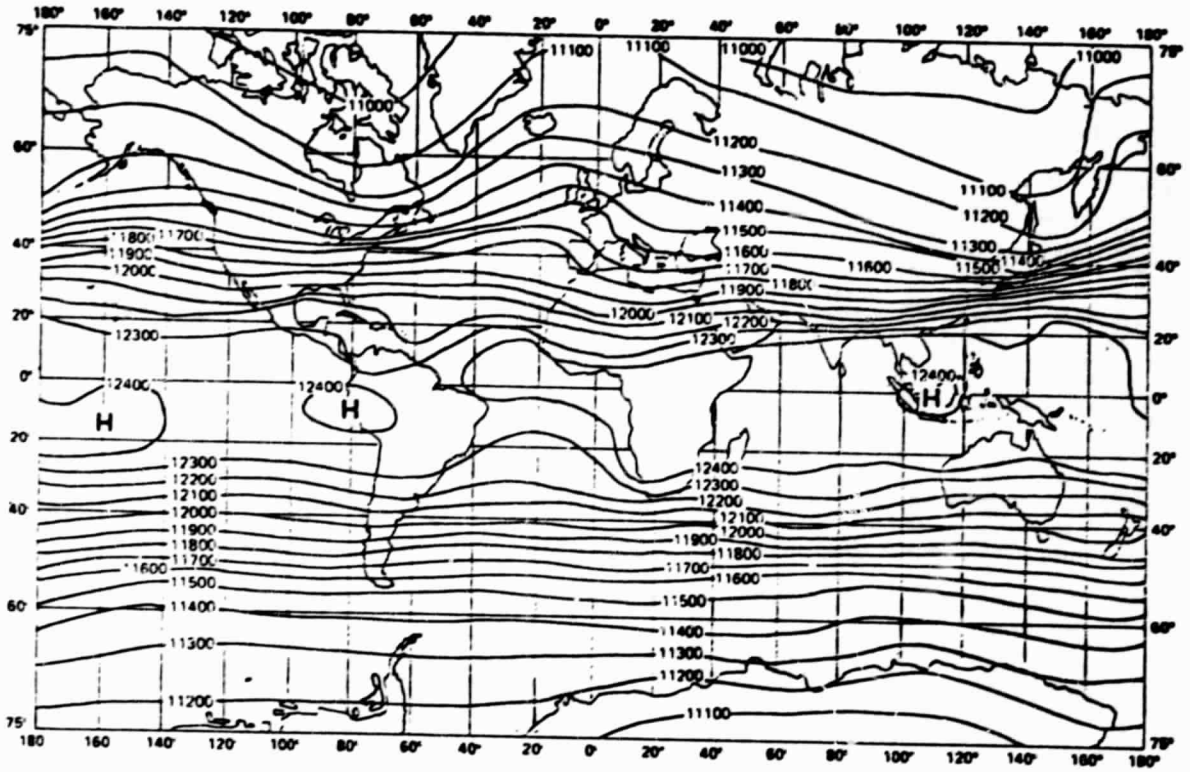

Figure 4.3a Observed mean geopotential height (gpm) at 200 mb for December, January and February (Crutcher and Davis, 1969).

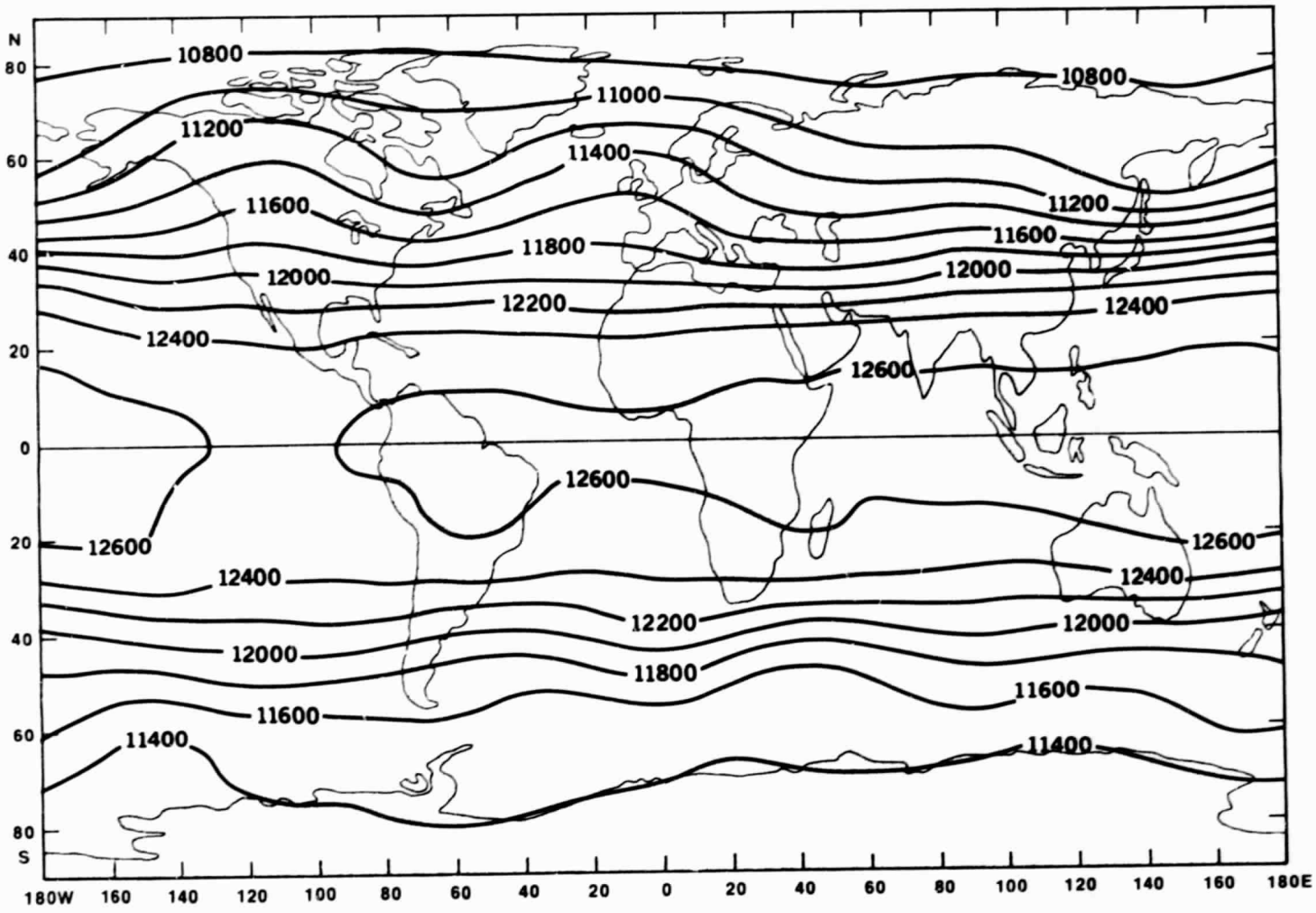

Figure 4.3b Model simulated geopotential height (gpm) at 200 mb for February.

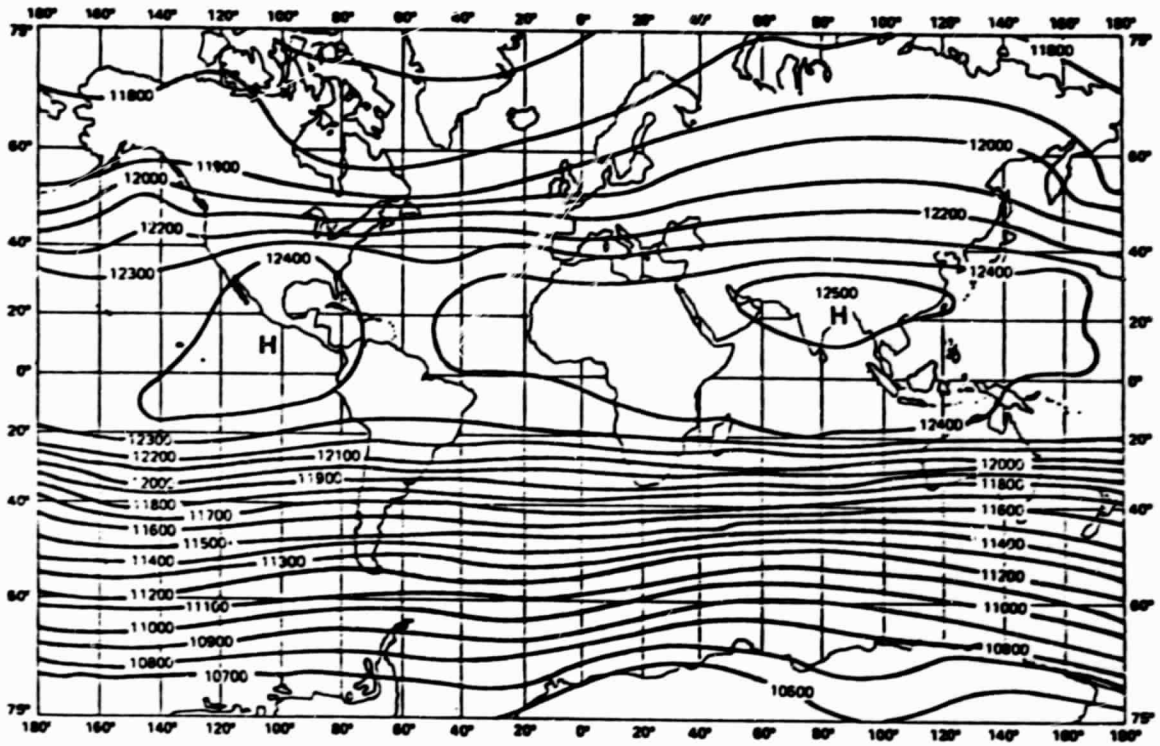

Figure 4.4a Observed mean geopotential height (gpm) at 200 mb for June, July and August (Crutcher and Davis, 1969).

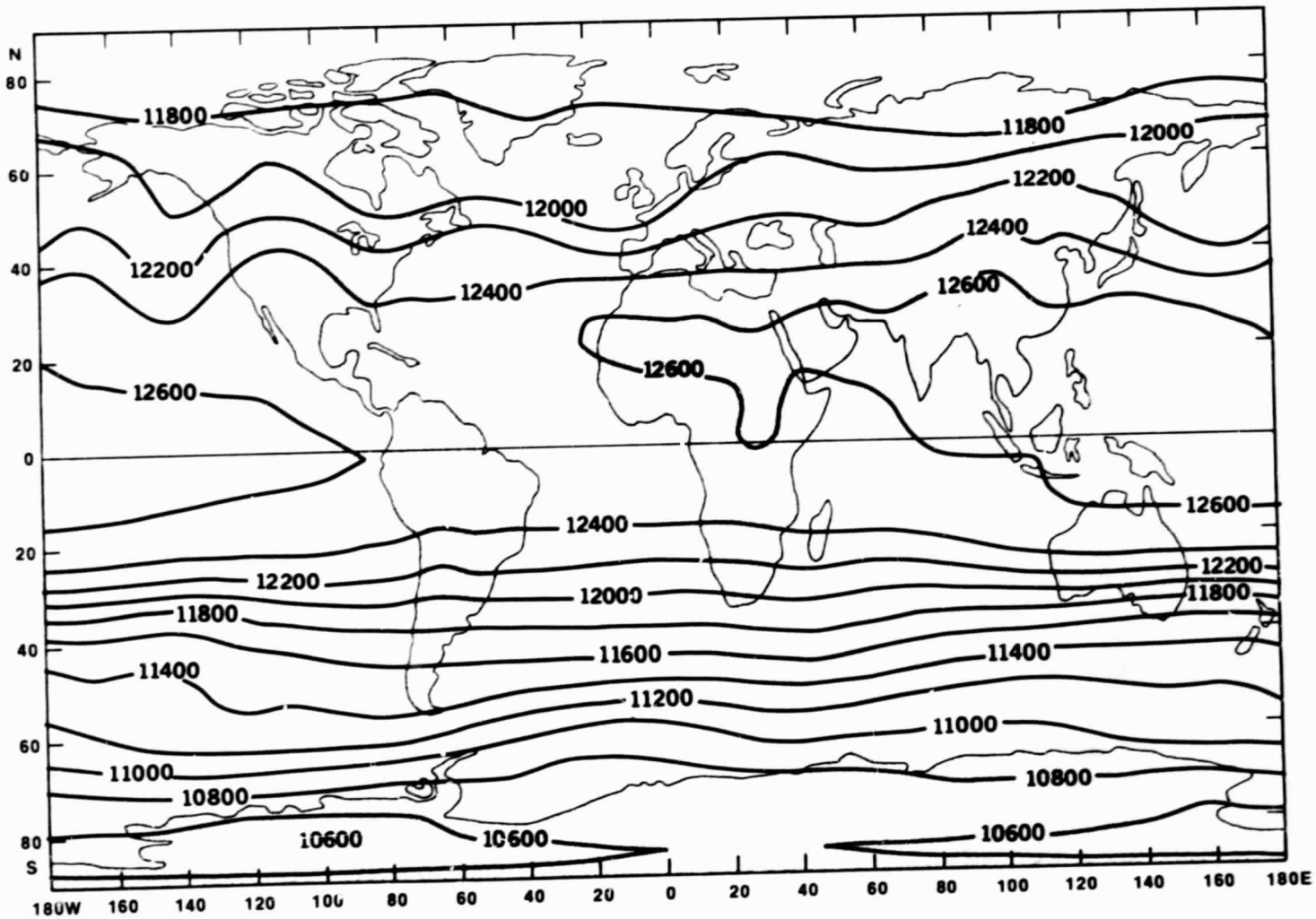

Figure 4.4b Model simulated geopotential height (gpm) at 200 mb for July.

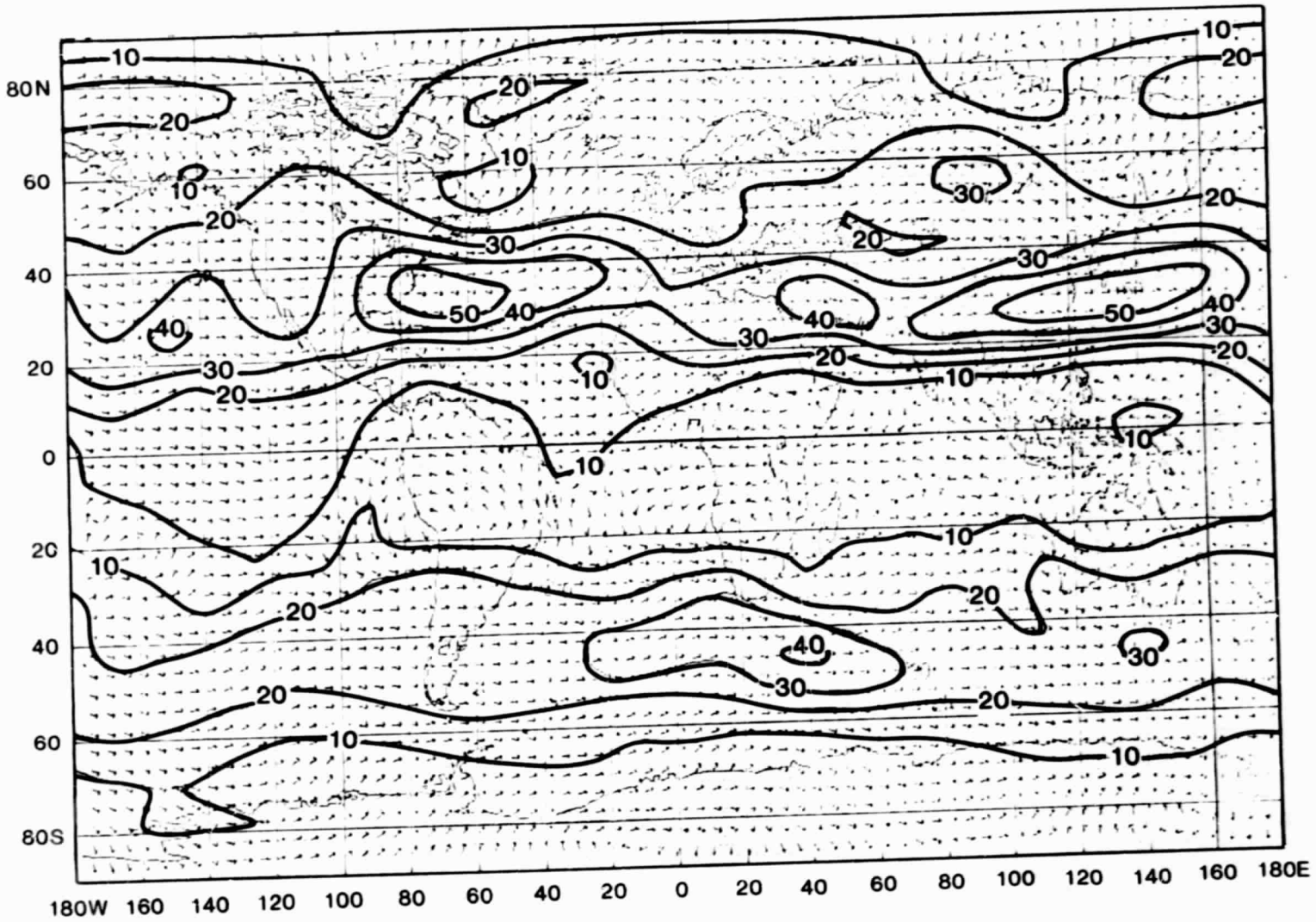

Figure 4.5a Observed wind direction and speed (ms^{-1}) at 200 mb for February, 1979.

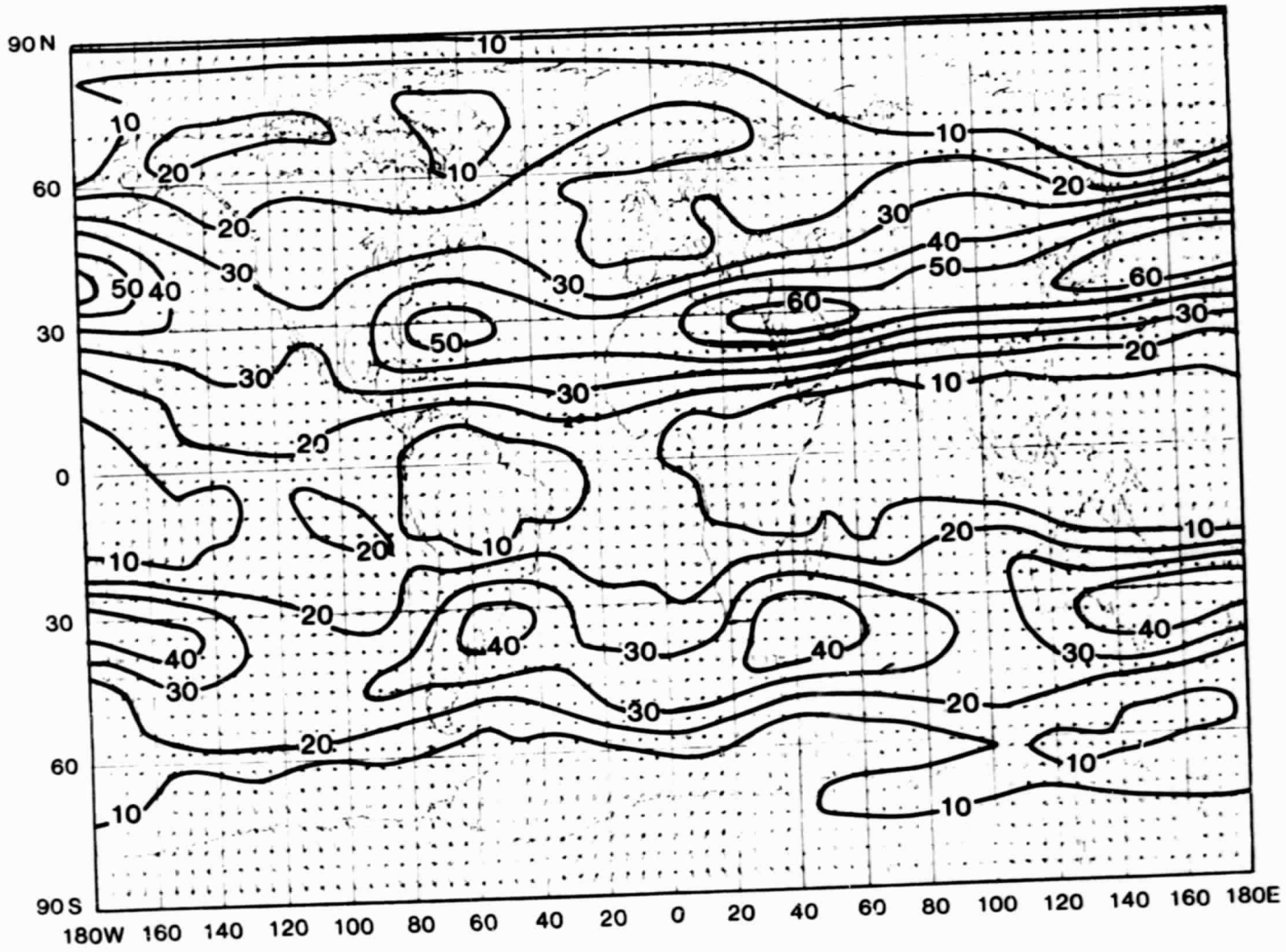

Figure 4.5b Model simulated wind direction and speed (ms^{-1}) at 200 mb for February.

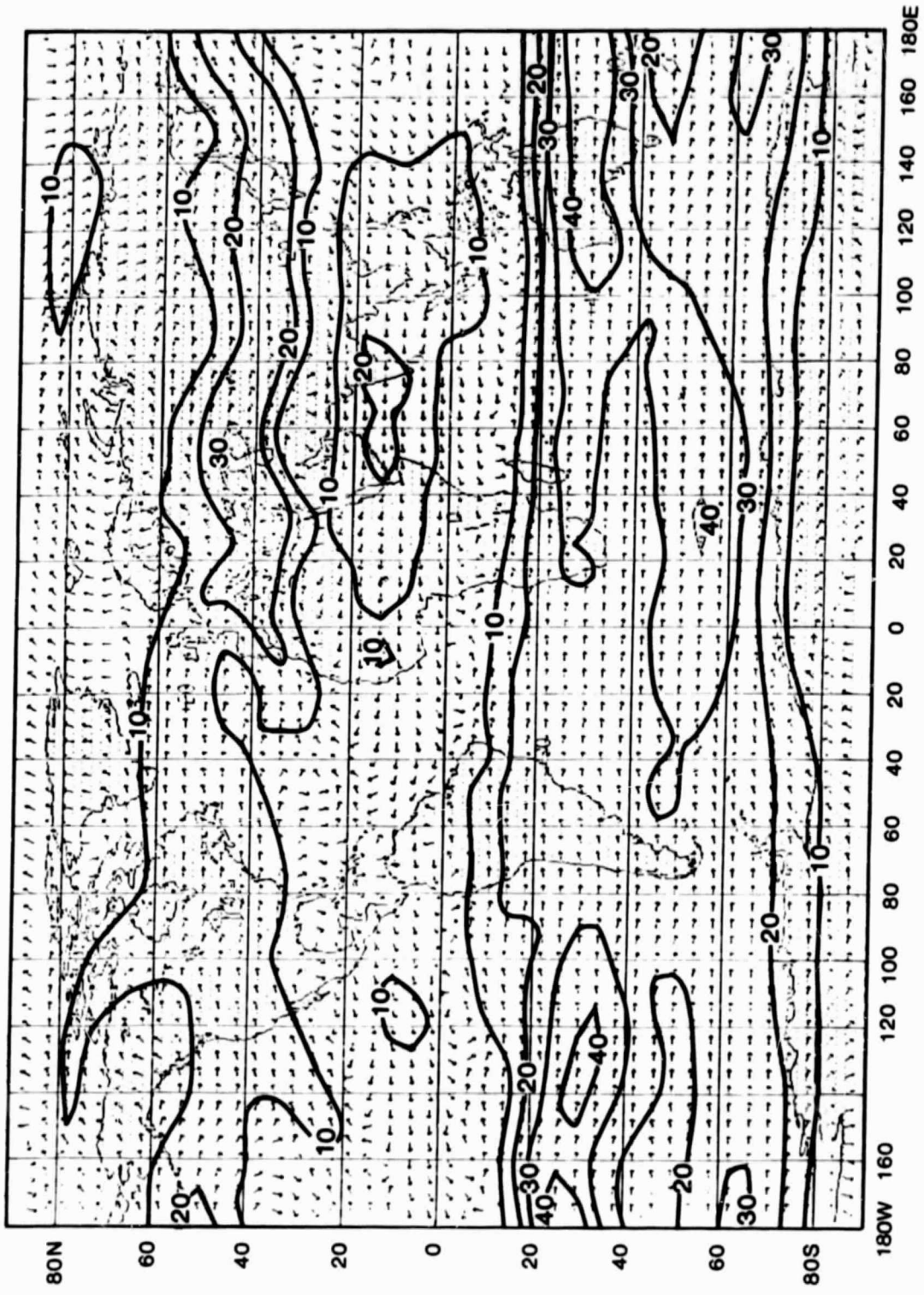

Figure 4.6a Observed wind direction and speed (ms^{-1}) at 200 mb for July, 1979.

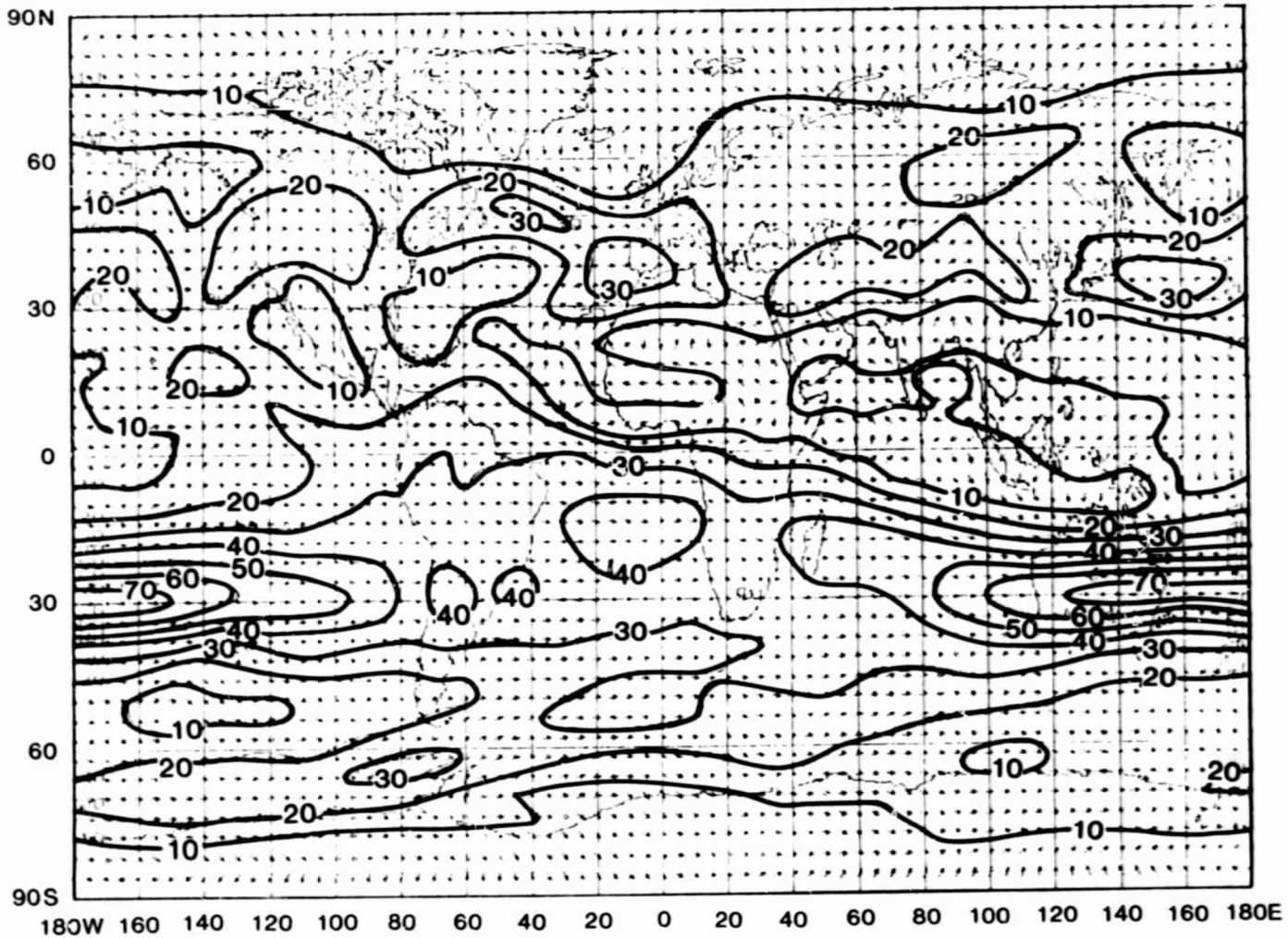

Figure 4.6b Model simulated wind direction and speed (ms^{-1}) for July.

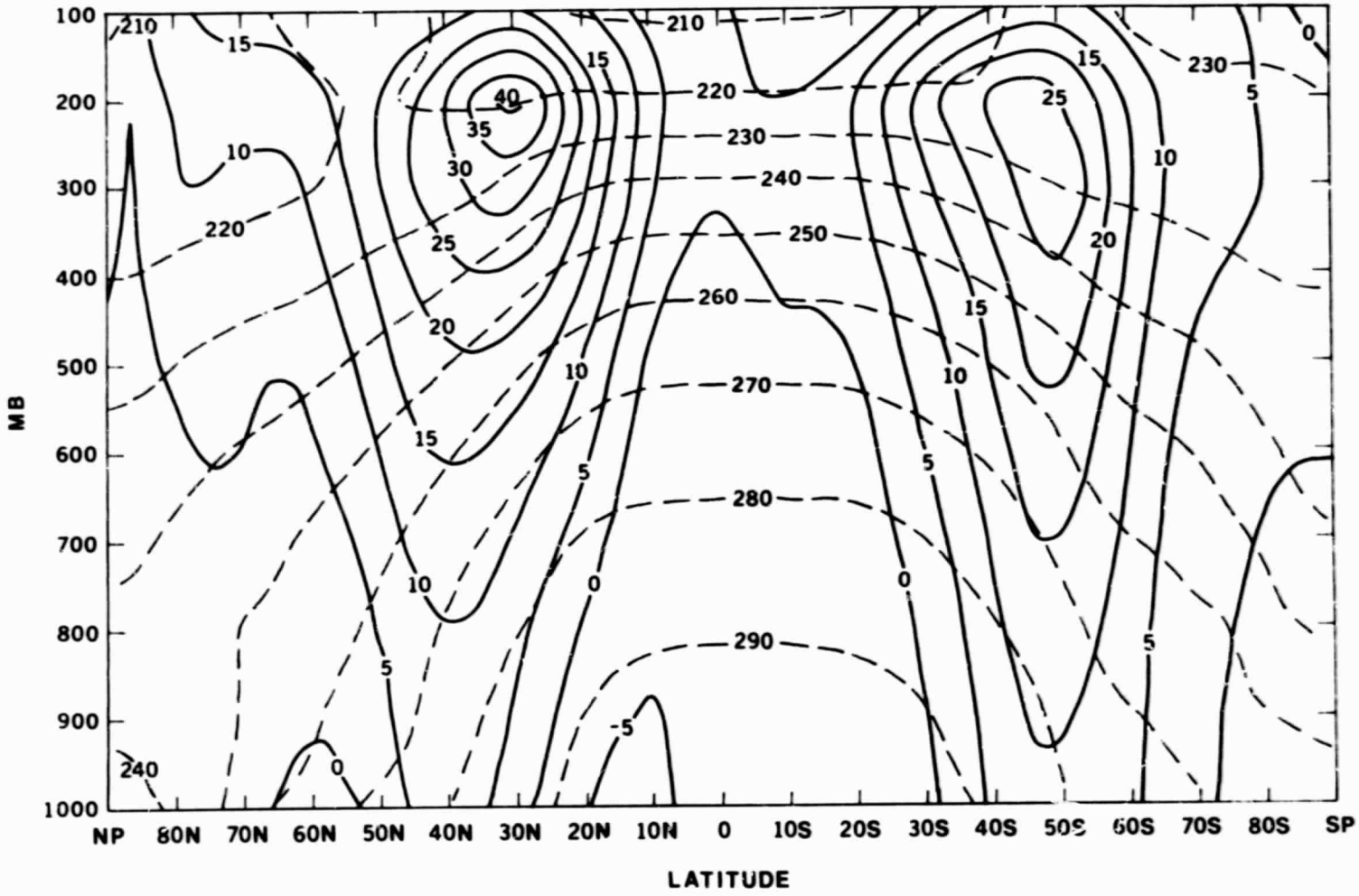

Figure 4.7a Observed zonally averaged zonal wind (ms^{-1}, solid lines) and temperature (°K, dashed lines) for February, 1979.

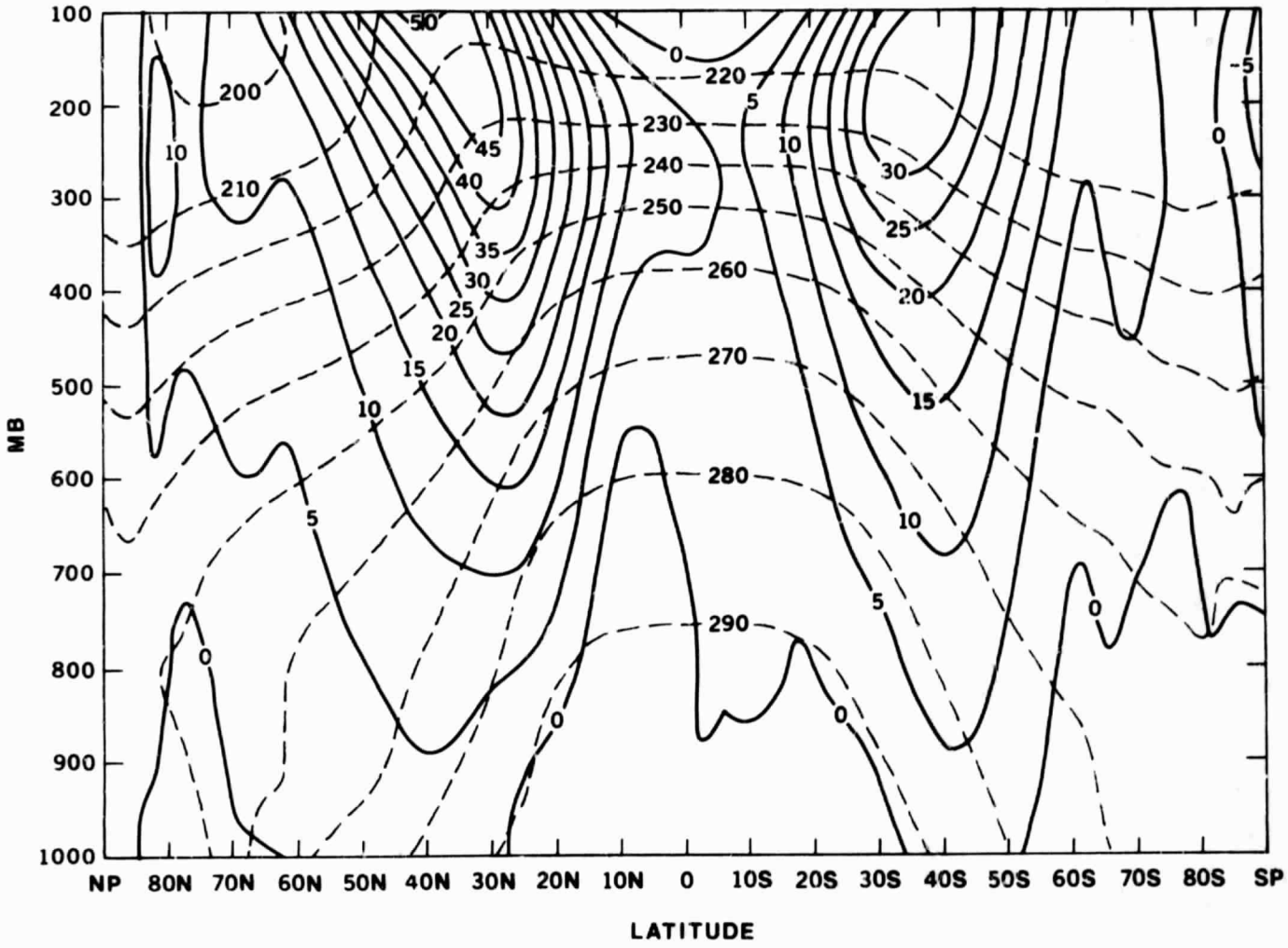

Figure 4.7b Model simulated zonally averaged zonal wind (ms^{-1}, solid lines) and temperature (°K, dashed lines) for February.

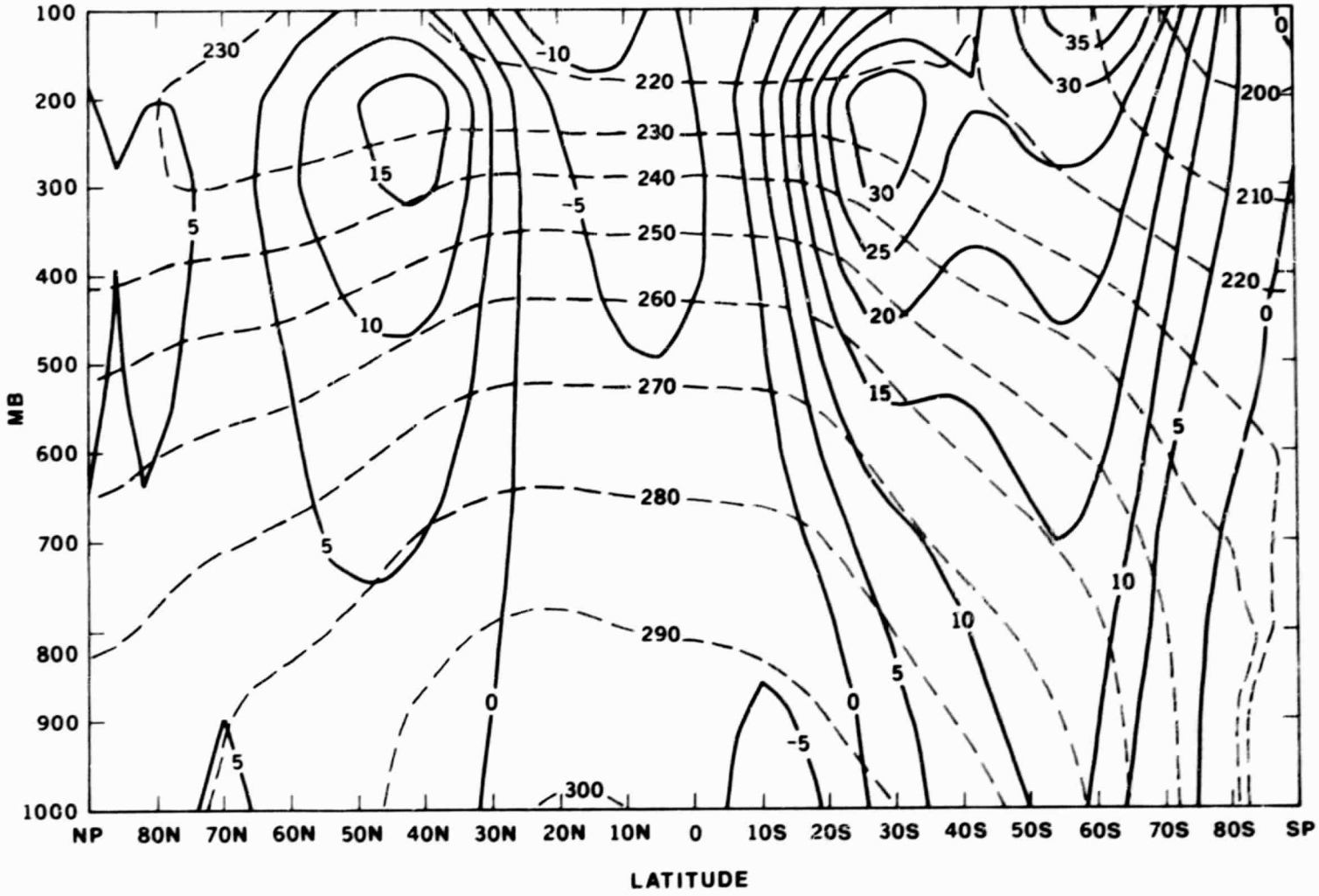

Figure 4.8a Observed zonally averaged mean zonal wind (ms^{-1}, solid lines) and temperature (°C, dashed lines) for July, 1979.

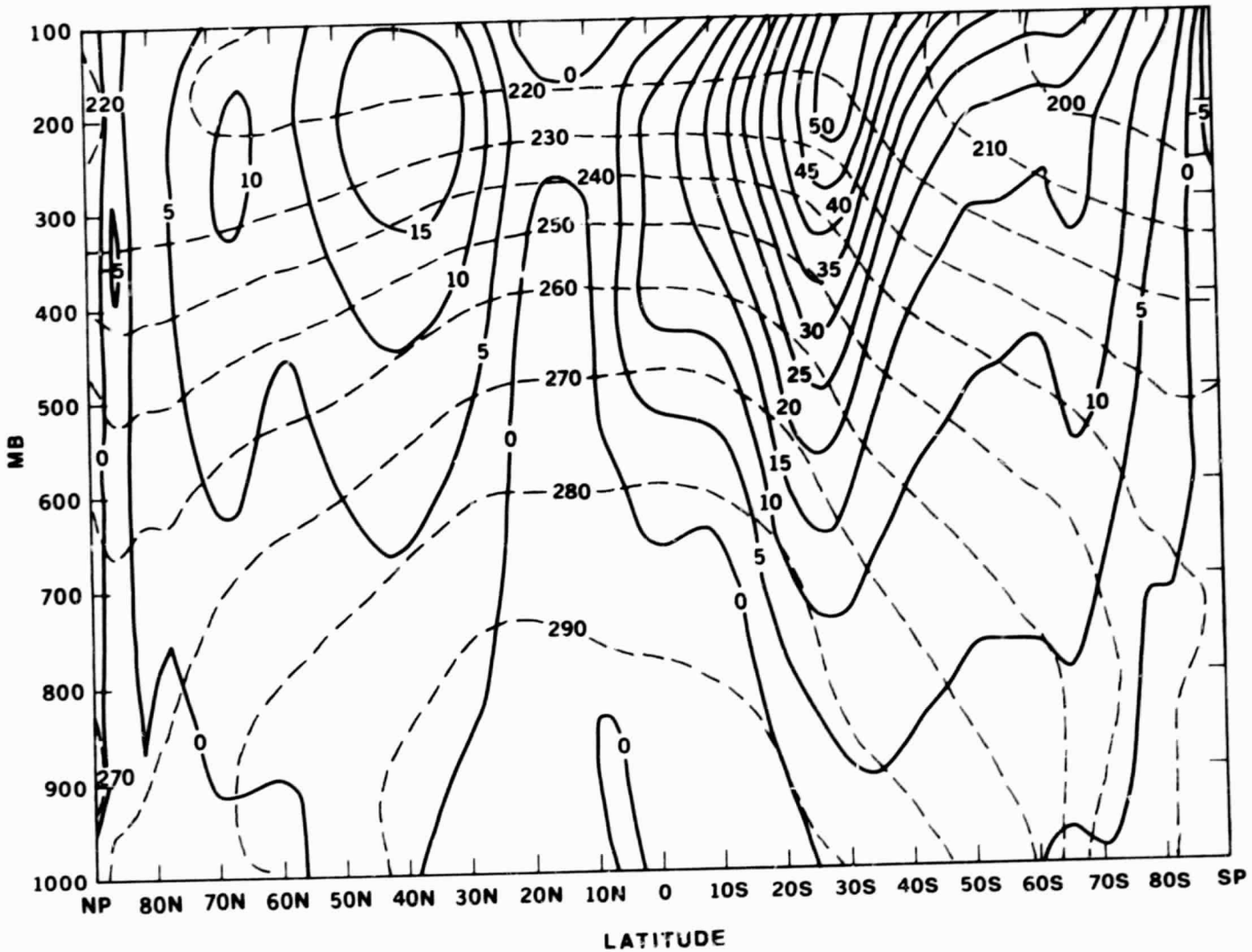

Figure 4.8b Model simulated zonally averaged zonal wind (ms^{-1}, solid lines) and temperature (°K, dashed lines) for July.

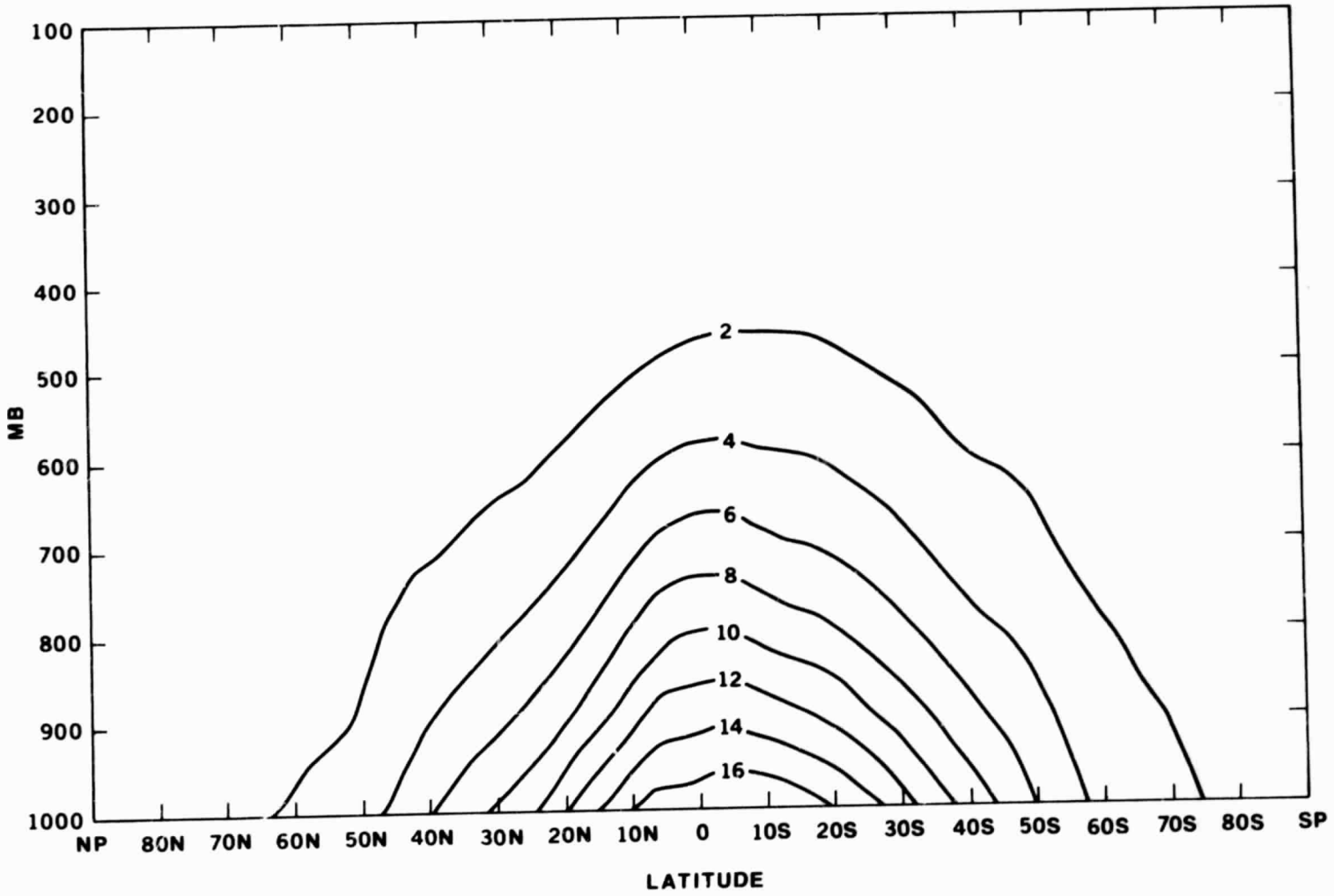

Figure 4.9a Observed zonally averaged specific humidity (g kg^{-1}) for February, 1979.

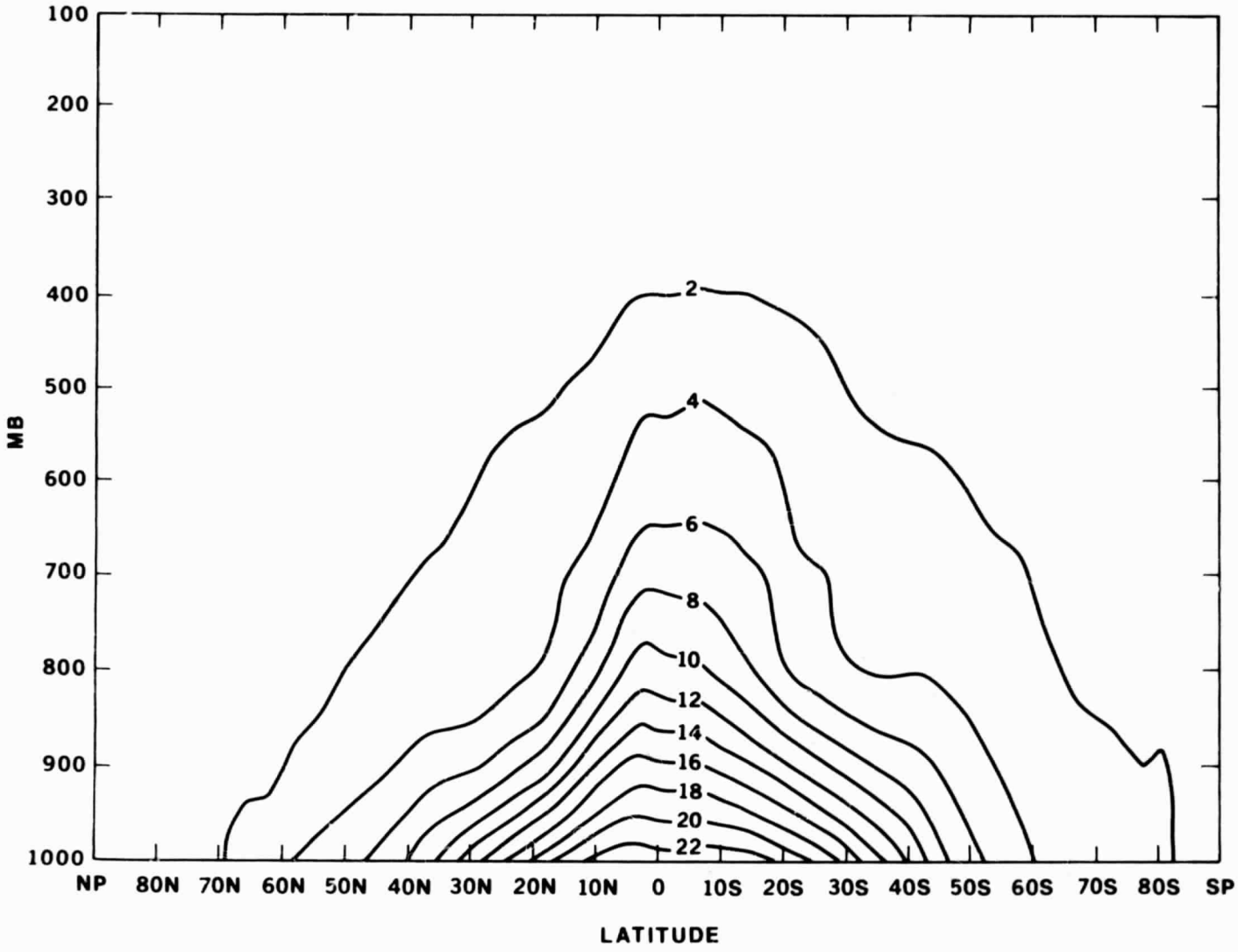

Figure 4.9b Model simulated zonally averaged specific humidity (g kg^{-1}) for February.

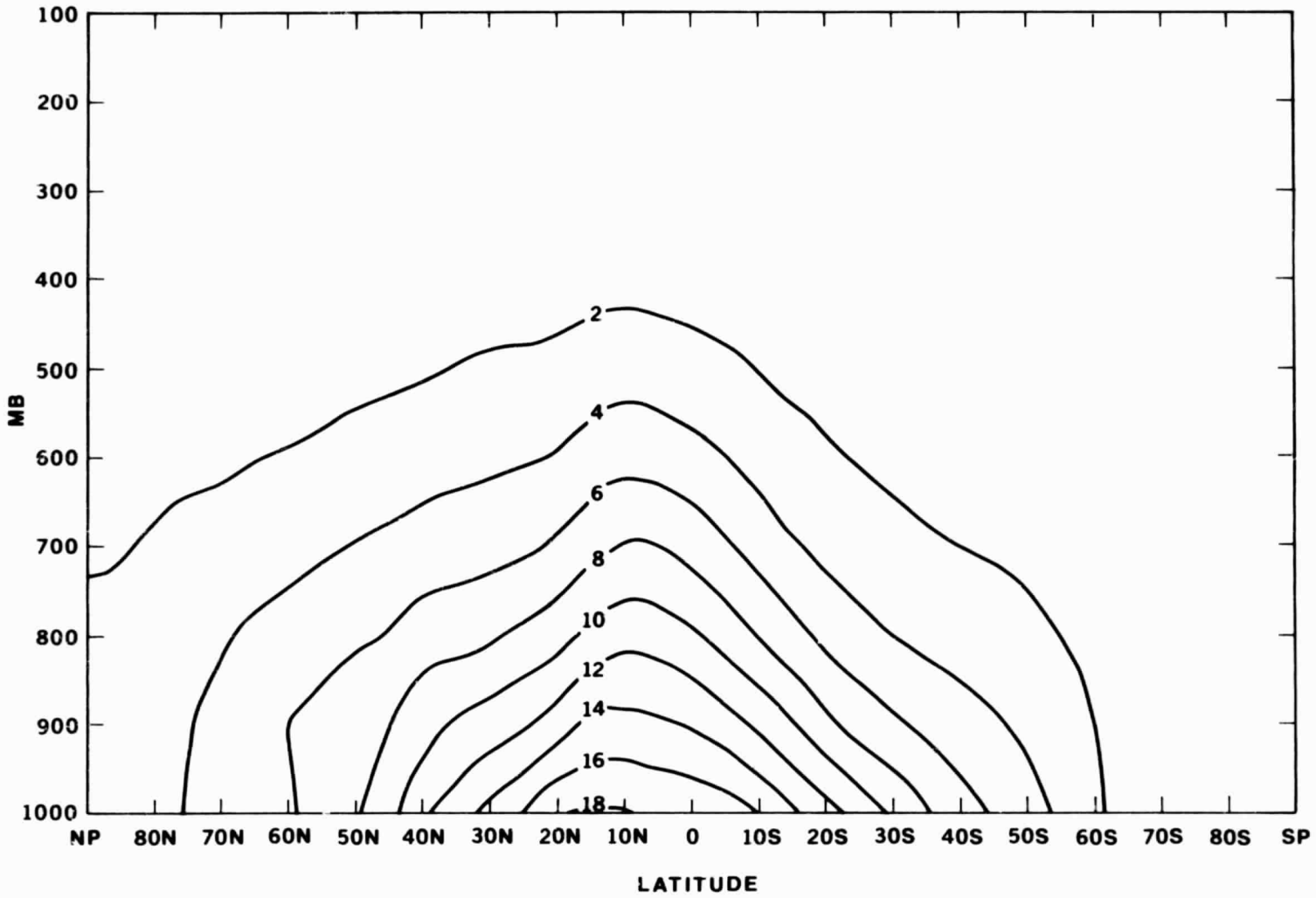

Figure 4.10a Observed zonally averaged specific humidity (g kg^{-1}) for July, 1979.

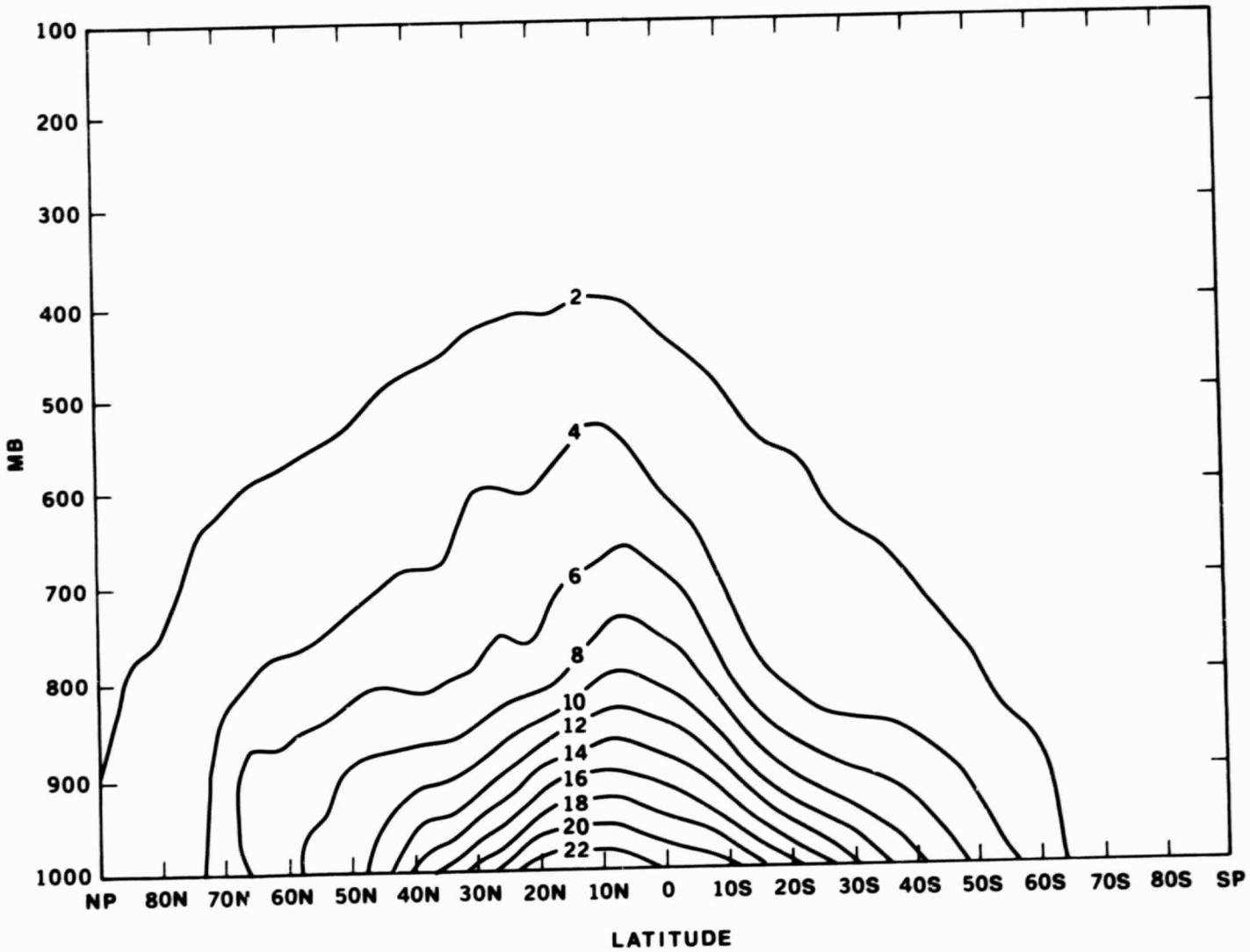

Figure 4.10b Model simulated zonally averaged specific humidity (g kg^{-1}) for July.

5. Fluctuations in space and time

a. Energetics-hemispheric energy cycles. The energy cycle is an entity which summarizes the energy content of the atmosphere, its resolution into various components, and the transformations between these components (Lorenz, 1955; Oort, 1964). Figures 5.1 and 5.2 present the energy cycles of the simulated winter and summer seasons, and those estimated for the real atmosphere (Oort and Peixoto, 1974). Each energy cycle is computed in the space-time domain (Oort, 1964) and on a hemispheric basis[1].

The observed energetics for January in the Northern Hemisphere (Figure 5.1a) indicate a strong (baroclinic) flow of energy from zonal available potential (P_M) to eddy available potential (P_E) to eddy kinetic (K_E) energy, and a weaker (barotropic) flow from eddy kinetic to zonal kinetic (K_M) energy. Also indicated is a conversion from K_M to P_M, although this estimate has a large degree of uncertainty associated with it (Oort and Peixoto, 1974). These energy transfers are reproduced remarkably well in the model Northern Hemisphere energy cycle for February (Figure 5.1b). The sizable conversion of K_M to P_M in the model suggests that the energy conversion of the thermally indirect Ferrel cell overcompensates that of the thermally direct Hadley cell. This is not inconsistent with the much larger mass flux associated with the Hadley cell, since the Ferrel cell exhibits a much larger temperature difference between the ascending and descending branches. The energy amounts in the model simulation agree well with the observations except for K_M; the fact that the model K_M is almost twice that of the observations is consistent with the model's unrealistically strong subtropical jet. Given the large uncertainties in estimating the

[1] The model conversions from potential to kinetic energy were computed using the "$\omega\alpha$" formulation, while the estimates given by Oort and Peixoto (1974) used the "$V \cdot \nabla Z$" formulation. Hence it was necessary to transform the observed estimates to the "$\omega\alpha$" formulation by making use of the observed fluxes of energy across the equator (Oort and Peixoto, 1974; Peixoto and Oort, 1974).

generation and dissipation of energy in the real atmosphere (Oort and Peixoto, 1974), it is difficult to assess the model's performance with regard to these quantities. The dissipation of kinetic energy in the model's Northern Hemisphere (in winter) is within a factor of two of the observed estimate, with the model showing less dissipation of eddy kinetic energy than the observations. The model's winter generation of P_M (due to both dry and moist processes) is much stronger than the observed estimate. This may be due to excessive cooling near the winter pole and warming of the tropical atmosphere. The model also predicts a small net diabatic loss of P_E, in contrast with the estimate for the atmosphere.

The Southern Hemisphere energy cycle for the winter (July) simulation is indicated in Figure 5.1c, and it is seen to be quite similar to the simulated Northern Hemisphere winter cycle (Figure 5.1b). The only energy conversion which is substantially different is the barotropic conversion from K_E to K_M, which is of opposite sign in the two hemispheres. The energy sources and sinks are also qualitatively similar, and the zonal available potential and eddy kinetic energies are close in magnitude. P_E is greater in the Northern Hemisphere, while K_M is greater in the Southern Hemisphere.

The observed summer Northern Hemisphere energy cycle (July) is presented in Figure 5.2a. The baroclinic energy conversions, P_M to P_E and P_E to K_E, still have the same sense, although they are smaller than in January. The weak (barotropic) conversion from K_E to K_M is again present, but the estimate of the conversion between K_M and P_M has changed sign from the January observations. The amounts of the different types of energy are considerably less in summer than in winter. The energy conversions of the model Northern Hemisphere summer (July, Figure 5.2b) are in the same sense as observed, but they are generally of much larger magnitude. This is particularly true of the conversion from P_E to K_E. Furthermore, the amounts of energy in the model simulation are somewhat larger than observed, the discrepancy being the greatest for P_M. Frictional dissipation

in the model is approximately the same as the observed estimate, but the total model generation of P_M and P_E greatly exceeds the estimates of the real atmosphere. In general, the simulated Northern Hemisphere summer circulation appears to be overly vigorous.

Comparing the model energy cycles for Northern Hemisphere summer (July, Figure 5.2b) and Southern Hemisphere summer (February, Figure 5.2c), it is seen that the conversions are generally similar in magnitude and are in the same direction. It should be noted, however, that the conversions P_M to P_E and K_E to K_M are larger in the Southern Hemisphere summer. Both hemispheres contain similar amounts of K_E and P_E, but the Southern Hemisphere K_M and P_M are significantly greater than those of the Northern Hemisphere. The sources and sinks of energy are comparable in the two summer hemispheres, although the generation of P_E by dry diabatic processes is of opposite sign.

Meridional energy transports. This subsection presents the meridional transports of the various components of energy density, viz., sensible heat (internal energy), potential energy, kinetic energy, and the latent energy of condensation of water. These transports are time-averaged and vertically integrated, and are also divided into eddy and zonal-mean components.

The observed zonal-mean transports of the various forms of energy density are presented for February in Figure 5.3a, while the mean model transports are given in Figure 5.3b. The source of all the observed transports reported here is Oort and Rasmusson (1971). The observed mean transport of potential energy is directed opposite to the transports of latent and sensible heat; potential energy is carried northward by the Hadley cell, whereas sensible and latent heat are transported southward. North of 26N, the presence of the Ferrel cell causes this pattern to reverse, although the mean latent heat transport becomes very small. Because the transports of the individual components tend to oppose

each other, the total energy transport is relatively small. It is also consistently in the direction of the potential energy transport. The mean transport of kinetic energy is not depicted, since it is too small to play any role in the overall energy transport. The February zonal-mean energy transports of the model are given in Figure 5.3b. The basic pattern of transports agrees well with the observations, with the potential energy transport again opposing that of sensible and latent heat. However, the transition from northward to southward flow of total (or potential) energy occurs about 8 degrees too far north. In addition, the magnitude of the sensible heat and potential energy transported by the model's Hadley cell is too small, as is the amount of sensible heat flow in northern mid-latitudes. (Note the difference in scale between Figures 5.3a and 5.3b.) The Hadley cell transport of latent heat agrees well with observations.

The observed eddies transport both latent and sensible heat northward in February, the total northward energy flow reaching a broad maximum in northern mid-latitudes (Figure 5.3c). The eddy transports of potential and kinetic energy are both quite small. Although the model results for the latent and sensible heat carried by the eddies (Figure 5.3d) show basic agreement with the observations north of 30N, there are discrepancies. The magnitude of the total model transport is somewhat too large, and the peak in sensible heat flow occurs 4 degrees (one grid point) too far south. Between 30N and the equator, the model's eddies transport sensible heat southwards, while the latent heat transport remains near its peak value. Neither of these features is observed. In the Southern Hemisphere, the (poleward) eddy transports of latent and sensible heat resemble those in the northen hemisphere, although the amount of sensible heat carried is considerably smaller. The potential and kinetic energy transports are again quite small.

It is quite apparent from Figures 5.3a-5.3d that almost all of the potential energy transport is accomplished by the mean flow. In contrast, Figure 5.3e indicates that in the case of kinetic energy, it is the eddies which dominate the transport. The model's eddy kinetic energy flow agrees with the observed only in the grossest sense: the transports are both to the north from about 14N to 62N. Not only does the model transport much more energy than is observed, but it transports kinetic energy southward north of 62N, in contrast to the observations. Also, the double maximum in the observed transport is absent in the model results.

The observed zonal-mean transports of energy in July (Figure 5.4a) strongly resemble the winter transports, with the Hadley cell now shifted southwards and directed towards the Southern Hemisphere. The mean energy transports of the model in July (Figure 5.4b) indicate the same deficiencies present in February, namely that the transports of sensible heat and potential energy are too small. (Note the difference in scale between Figures 5.4a and 5.4b.) Also, the latitude of peak transport of the Hadley cell is located at least 4 degrees too far north. Gauging the strength of the model winter hemisphere Ferrel cell by its transport of potential energy, one concludes from Figures 5.3b and 5.4b that the cell is weaker in July than it is in February.

The observed July eddy transports (Figure 5.4c) are naturally much weaker than in February, with the peak magnitude of northward latent heat transport greater than that of the sensible heat transport. This overall pattern is reproduced in the Northern Hemisphere July model results (Figure 5.4d), although the model peak of northward latent heat transport is too large by almost a factor of two. The position of the peak in sensible heat transport is slightly too far south in the model, although the peak magnitude is correct. Also, the transition from northward to southward energy transport occurs near the equator, as is observed. The flows of latent and sensible heat in the model Southern

(winter) Hemisphere generally resemble those of the February Northern (winter) Hemisphere (Figure 5.3d), with the exception that the July sensible heat transport is a factor of two less than the February transport.

The July eddy transports of kinetic energy, both as simulated and observed, are shown in Figure 5.4e. The only significant observed feature in the Northern (summer) Hemisphere is a peak of northward transport at 34N. This is absent in the model results, which indicate weaker maxima of northward transport at 42N and 58N and maxima of southward transport at 28N and 66N. In the Southern Hemisphere, the model's eddies carry a great deal of kinetic energy southward near 32S, and, further south, an equally large amount northward. Whether the very sizeable convergence of eddy kinetic energy at 40S is realistic or not is a question which cannot be answered with the data presently in hand.

b. Stationary waves in the geopotential height field. The time-averaged departures from zonal symmetry of the basic meteorological fields reflect the lack of such symmetry at the lower boundary. That is, the presence of stationary waves is due to the existence of orography and geographically fixed, asymmetric, heat sources. Thus, in order for a GCM to reproduce the observed three-dimensional structure of the stationary waves, the model must simulate the geographically fixed heat sources and flow over orography in a realistic manner.

In this section results are presented for the stationary (time-averaged) component of the geopotential height, from which the stationary temperature and wind fields may be estimated by using hydrostatic and geostrophic balance respectively. Figure 5.5a shows the observed winter variance around a latitude circle of the stationary geopotential height, summed over the planetary waves (wavenumbers 1-4). The term "stationary" refers to a 90-day average commencing on January 1. This average was computed from NMC analyses for each of the years 1963-1977, and the mean over these years was taken. The corresponding stationary

planetary wave variance for the winter GCM simulation is presented in Figure 5.5b1. "Stationary" here refers to a time-average over the first 90 days of the simulation, which was initialized from data valid for January 1, 1975. The model results show good overall agreement with the observations, with both variances reaching a maximum in the mid-latitude upper troposphere. The model variance is slightly too weak up to the 250 mb level, above which it fails to show the decrease with height apparent in the observations. This failure may be related to the unrealistically low polar temperatures and strong zonal winds at the upper levels. The model stationary planetary wave variance in the Southern (summer) Hemisphere (Figure 5.5b2) is almost an order of magnitude smaller than in the Northern Hemisphere, due to the relative lack of orography and geographically fixed heat sources in the Southern Hemisphere. It should be noted that the zonal variance of the stationary height field in the lowest four wavenumbers is (in winter) several orders of magnitude larger than the variance in higher wavenumbers, indicating that the total stationary variance will strongly resemble the planetary wave variance.

A more detailed description of the stationary waves is afforded by a zonal wavenumber decomposition of the geopotential height field. Figures (5.6a)-(5.6f) present the amplitude and phase[2,3] of wavenumbers 1-3 (separately) for both the observed and simulated winters. Comparison of Figures (5.6a) (15 year mean observations) and (5.6b) (GCM) shows that the amplitude of wavenumber 1 in the GCM agrees well with the observations in that both amplitudes reach a

---

[2] The phase is defined as the relative position of the ridge, i.e. the phase ϕ is defined by writing the wave as $A \cos(k\lambda - \phi)$, where k is the zonal wavenumber and λ the longitude.

[3] The plots of amplitude and phase were constructed from data at only five vertical levels (200 mb, 300 mb, 500 mb, 700 mb and 850 mb). This vertical resolution was not adequate to resolve certain ambiguities in the behavior of the phase as a function of latitute and height. Certain portions of the phase plots hence were left blank.

maximum in the mid-latitude upper troposphere. However, the GCM amplitude does not decrease above 300 mb as does the observed amplitude, and the maximum in the GCM amplitude is both somewhat too strong and located about 6 degrees too far north. The phase of the GCM's wavenumber 1 tilts westward with height in mid-latitudes, but with less slope than is observed. The eastward phase tilt with increasing latitude evident in the observations is almost completely absent in the model. Further, the actual values of the GCM phase are about 30 degrees less than (to the west of) the observed values near the mid-latitude amplitude maximum.

The behavior of the model wavenumber 2 (Figures 5.6c-5.6d) presents a contrast to the wavenumber 1 results in that the phase shows better agreement with the observations than does the amplitude. The simulated amplitude is only half as large as the observed throughout mid-latitudes, although the overall latitude-height structure is similar, with a broad mid-latitude upper tropospheric maximum and one in the sub-tropical upper troposphere. Both the simulated and observed wave phase show a westward tilt with height and with (increasing) latitude in mid-latitudes, although the model phase tends to tilt too rapidly. In the vicinity of the mid-latitude amplitude maximum, the phase of the GCM wave is about 30 degrees too large (too far to the east).

The amplitude and phase of the observed and simulated wavenumber 3 are presented in Figures (5.6e)-(5.6f). The model amplitude agrees well with the observations, both with regard to the overall latitude-height structure and to the maximum amplitude, although the GCM maximum is located about 4 degrees too far north. In the vicinity of the mid-latitude maximum both the GCM phase and the observed phase show a moderate westward tilt with height and eastward tilt with (increasing) latitude. The values of the phase are also in rough agreement. To the north of 60N, the observed phase tilts westward with increasing latitude, while the model phase continues to shift eastward with latitude in the lower

troposphere. In the subtropics, the model captures the observed westward phase shift with height but fails to capture the observed eastward shift with latitude in the upper troposphere.

The observed summer variance of the stationary component of the geopotential height, summed over wavenumbers 1-4, is presented in Figure 5.7a. The corresponding GCM variance is shown in Figure 5.7b1. These quantities were computed in the same manner as for the winter season, except that the averaging period was defined to be the 90 days starting on June 15. (This time period was chosen to correspond to the summer simulation, which was initialized with data valid for June 15, 1979.) The simulated planetary wave variance agrees well with the observations with regard to the location and strength of the three maxima: one in mid-latitudes at about 300 mb, and two in the subtropics, at 850 mb and 200 mb. Discrepancies include the fact that the simulated mid-latitude variance does not decrease above 300 mb, the slight northward displacement in the GCM of the subtropical maximum at 850 mb, and the weakness of the simulated subtropical maximum at 200 mb. It is noteworthy that the Southern (winter) Hemisphere ultra-long wave variance (Figure 5.7b2) is now of the same order of magnitude as the Northern (summer) Hemisphere variance.

The amplitude and phase of the stationary zonal wavenumber 1 in summer is shown in Figures 5.8a for the observations and in Figures 5.8b for the GCM. The latitude-height structure of the observed amplitude is very similar to that of the total planetary wave variance; one mid-latitude maximum in the upper troposphere is present, as are sub-tropical maxima at 850 mb and 200 mb. The model amplitude shows good agreement with the observations, the major discrepancies being the excess strength and southward displacement in the model of the midlatitude maximum. The GCM phase strongly resembles the observed south of 34N, exhibiting strong eastward tilt with height but little tilt with latitude. In mid-latitudes, however, the model phase is less realistic. The

observations show a slight eastward tilt with height and a stronger eastward tilt with (increasing) latitude south of the mid-latitude maximum, and a moderate westward tilt with height and no tilt with latitude just north of the maximum. The phase in the GCM, in contrast, tilts westward with height and eastward with (increasing) latitude through much of the mid-latitude region.

The observed summer amplitude of stationary wavenumber 2 shows a good deal of structure (Figure 5.8c1); there are three distinct amplitude maxima and two distinct minima. The maxima again occur in the upper troposphere in mid-latitudes, and in the subtropics at 850 mb and 200 mb. The structure of the GCM amplitude (Figure 5.8d1) is generally similar, but differences of detail exist. The locations of the maxima are too far north, both upper tropospheric maxima are too strong, and the minima are not as distinct as in the observations. The behavior of the observed phase shows several regimes, and these are present to some extent in the model results. In the upper tropical troposphere, the observed phase tilts little with latitude, and tilts westward with height. The model phase in this region tends to show much less shift with height and much more (westward) tilt with latitude. The observed phase in mid-latitudes tilts eastward with (increasing) latitude in the lower troposphere, and westward in the upper troposphere, up to the latitude of the amplitude maximum. The phase tilts eastward with height throughout this region. North of the amplitude maximum, the phase slopes westward with latitude, but shows little shift with height. The phase of the GCM wave reproduces this structure very well in an overall sense, but the values of the phase tend to be uniformly smaller (wave located too far to the west).

The structure of the observed summer wavenumber 3 amplitude is quite similar to that of the lower wavenumbers (Figures 5.8e), with three distinct maxima again present. In this case, however, the 850 mb maximum is located in mid-latitudes, at 38N. The GCM wave 3 amplitude again follows the pattern quite

well (Figures 5.8f), although the maxima are located slightly too far north, and the upper-tropospheric mid-latitude maximum is somewhat too weak. The observed phase slopes rapidly eastward with latitude in the subtropics, and slopes slowly westward with height. The model phase, however, shows a more rapid westward tilt with height and a westward tilt with latitude. Between 38N and 46N, the observations indicate almost no phase tilt with height and a strong eastward tilt with latitude, while the phase of the GCM shows a strong eastward tilt with height and no tilt with latitude. Between 46N and the mid-latitude amplitude maximum, both observed and simulated phases slope rapidly eastward with latitude, and very little with height. The region near the amplitude maximum is one with little phase change for either the GCM or the real atmosphere.

c. Space-time structure of transient fluctuations-local analysis of variance.

A useful description of the fluctuations in any basic field is afforded by the analysis of local variability discussed by Blackmon (1976). This method portrays the spatially local fluctuations of a particular field by the construction of maps of its RMS deviation in time. The variability due to low frequency motions or that due to higher frequency baroclinic activity can be separated by first filtering the data with a low-pass filter (retaining periods of 10-90 days), or a band-pass filter (retaining fluctuations of 2.5 to 6 days). In the application of this method, an estimate of the annual cycle is removed from the data before either the filtering or the computation of the RMS deviation.

The RMS deviation of the (unfiltered) 500 mb geopotential height in the Northern Hemisphere winter is presented for the observations[4] in Figure 5.9a

[4] Figures 5.9a, 5.10a and 5.11a are taken from Blackmon (1976). In that paper, the winter season was defined to be the period of 120 days commencing on November 15. The data consisted of the NMC analyses, twice daily, for the years 1963 through 1972, from which nine winter seasons were abstracted. The first four harmonics of the annual cycle were removed. The RMS deviations of the filtered and unfiltered fields were computed for each winter, and then averaged.

and for the GCM[5] in Figure 5.9b. The observed map shows a trend of increasing variability with higher latitude, at least up to mid-latitudes. Particularly noticeable are the regions of high variability in the northeast Pacific, in the north Atlantic, and over north-central Asia. The GCM results show the same general trend, although the values of the RMS deviation tend to be less. The observed high in the north Pacific is present in the model, although in much weakened form, while the observed strong north Atlantic high is replaced by a pattern of weaker highs over Newfoundland and off the east coast of Greenland and a low over the northeast Atlantic. In addition, the model shows a region of relatively high variability over the west coast of the United States, a feature that is not observed. The level of noise in the GCM map relative to the observations is to be expected, for the latter represents an average of nine individual atmospheric realizations, whereas the former represents a single (simulated) realization.

The discrepancies between the simulated and observed RMS maps are further elucidated by the separate consideration of the low-pass and band-pass RMS maps. The low-pass filtered geopotential height field gets strong contributions from blocking ridges, or positive anomalies that persist longer than, say 10 days (Blackmon, 1976). Their occurrence in nature is highly variable from one year to the next, so that the RMS low-pass field for any one year (or any one model simulation) may be quite different than the climatological mean. The average RMS low-pass map for the observations (Figure 5.10a) and for the GCM (Figure 5.10b) both strongly resemble their unfiltered counterparts. Thus the discrepancies noted between Figures 5.9a and 5.9b are in large part the

---

[5] Here the winter season is defined as the 90-day period commencing on January 1. The annual cycle was estimated by fitting each 90-day time series with a parabola. The filters used are identical to those of Blackmon (1976).

differences between the climatology of persistent anomalies and their presence or absence in one model simulation.

The band-pass RMS, on the other hand, is closely associated with regions having a high frequency of cyclonic activity, and so indicates the location of the "storm tracks" (Blackmon, et al. 1977). A comparison of the observed band pass RMS (Figure 5.11a) with that of the GCM (Figure 5.11b) shows excellent agreement in terms of both the location and strength of the major areas of cyclonic activity in the north central Pacific and western Atlantic.

The observed total RMS of the summer 500 mb height field[6] is presented in Figure 5.12a. The two oceanic regions of high variability in the winter map (Figure 5.9a) are again present, although they are weaker and their positions have been somewhat shifted. The simulated total RMS summer 500 mb height field (Figure 5.12b) is quite noisy compared to the observations. In the Atlantic, there is an extended region of high RMS, but the RMS is much too small. The GCM shows a rapid succession of highs and lows in the Pacific region where the observations indicate a broad high. The average RMS in this area is also much too small.

The observed summer band-pass RMS height field (Figure 5.13a) shows the two oceanic maxima present on the winter map. The Atlantic maximum has been shifted to the east, and the magnitude of the summer RMS is generally much smaller. The corresponding (Northern Hemispheric) map for the GCM (Figure 5.13b) indicates that the Atlantic maximum has been realistically simulated, both with respect to position and to magnitude. The Pacific maximum, however, is too weak and is located too far to the west.

---

[6] The observed fields (Figures 5.12a, 5.13a) are taken from Blackmon (1976). The summer season was defined there to be the 123-day period from May 15 to September 14. The data base was identical to that mentioned in footnote 4, as was the methodology used to obtain the maps.

The RMS deviation for the 850 mb temperature field for the observations and for the model are shown in Figures 5.14a and 5.14b, respectively[7]. The observations show greater variability over land than over oceans, especially at high latitudes, with no clear indication of the oceanic storm tracks. The most noticeable region of high variability is that over northwestern Canada, reflecting the alternation of high marine and low Arctic air temperatures (Blackmon et al., 1977). Other (less striking) regions of high RMS are Greenland and an area in north-central Asia. The GCM map also shows more variability over land than over water. The maximum in the RMS over northwestern Canada and Greenland are not only present but are in fact unrealistically strong. In addition, the Atlantic storm tracks stand out more in the GCM than in the observations. The observed high over north-central Asia appears over eastern Siberia in the GCM, and also appears too strong. Both the observed and simulated low-pass RMS maps (Figures 5.15a and 5.15b) resemble the total RMS maps, with the exception that the model's Atlantic storm tracks now are not apparent.

The observed band-pass RMS (Figure 5.16a) shows both the presence of high variability over the oceanic storm tracks and in the lee of the Rocky mountains, presumably reflecting the cyclogenetic activity there. The GCM band-pass RMS (Figure 5.16b) shows the presence of both the Pacific and Atlantic storm tracks. The lee-side Rocky mountain maximum does not appear on the simulated map.

Wavenumber-frequency spectra. Space-time spectral analysis is an approach in which the longitude- and time-variance of a field is separated into components of distinct spatial scales (described by wavenumber) and time scales (measured by frequency). The calculations of the wavenumber-frequency spectra

---

[7] The observed RMS deviations are from Blackmon et al. (1977). The annual cycle was estimated from the 850 mb temperature field in that work by fitting a parabola to the time series at each grid point. Otherwise, the methodology is as described in footnote 4.

reported here are described in Straus and Shukla (1981), to which the reader should refer for complete details[8].

The observed winter wavenumber-frequency spectrum of the 500 mb geopotential height field at 50N is shown in Figure 5.17a, and the model results are given in Figure 5.17b. These plots show the spectral density as a function of zonal wavenumber and frequency (in cycles per day). Both the observed and model spectra possess two noteworthy features: (i) the lowest frequencies and wavenumbers have the greatest spectral density, and (ii) a ridge of high spectral density extends diagonally from lower frequencies and wavenumbers to higher frequencies and wavenumbers. These two features are common to many of the spectra that are presented in this paper. The orientation of this ridge is very similar in the model and observed spectra, and is consistent (in a very approximate way) with the Rossby phase speed formula (Pratt, 1977). Hence, this ridge is referred to as the "propagation band" (Pratt, 1975). The major difference between Figures 5.17a and 5.17b is the relatively small magnitude of the model spectral density at low frequencies and low wavenumbers. This shortcoming of the model will be evident in further results (to be presented), and is also a failing of other GCM's (Pratt, 1979).

The dashed lines in Figure 5.17a divide the wavenumber-frequency plane into four domains: (i) low frequency planetary waves (LFPW's), consisting of wavenumbers 1-4 with periods of 7.5 to 90 days, (ii) low frequency synoptic-scale waves (LFSW's), consisting of wavenumber 5-10 with periods of 7.5 to 90 days, (iii) medium frequency planetary waves (MFPW's), consisting of wavenumbers 1-4 with periods of 2.8 to 6.9 days, and (iv) medium frequency synoptic-scale

---

[8] A brief description of the methodology is as follows: The winter (summer) season is defined as the 90-day period commencing on January 1 (June 15). The observational data consist of 15 years (1963-1977) of NMC analyses. Each observed season and model simulation had a separate parabolic estimate of the annual cycle removed from each grid point before the spectra were computed. The reported observational spectra have been averaged over 15 seasons.

waves (MFSW's), consisting of wavenumbers 5-10 with periods of 2.8 to 6.9 days. The latter category is associated with propagating, baroclinically active systems, while the LFSW category may be related to the growth and decay (life cycle) of such systems. There are numerous physical mechanisms capable of explaining the presence of the LFPW's in the atmosphere, including the instability of either axisymmetric or non-axisymmetric mean states, the non-linear transfer of energy from synoptic-scale waves, or the propagation of essentially free modes. Which of these explanations is valid is not known. These categories will be used to compile the space-time spectral summaries presented in a later subsection.

The observed spectrum of 500 mb geopotential height at 30N in winter is given in Figure 5.18a, and the GCM spectrum in Figure 5.18b. The observed spectrum at 30N is less intense than at 50N, although the main features of the two spectra resemble each other. The simulated spectrum at 30N has the same overall shape as the observed, with the magnitudes of the spectral density being generally comparable. The model LFPW's are only moderately too weak, although the discrepancy is more striking for wavenumber 1. The simulated spectrum also shows a peak at wavenumber 6 and frequencies near 0.10 cpd, a feature that is not observed.

The observed (simulated) spectrum of 500 mb height at 50N in summer is given in Figure 5.19a (5.19b), while the spectrum at 30N is shown in Figure 5.20a (5.20b). The observed summer spectra are much weaker than their winter counterparts, particularly at 30N. At 50N, the propagation band has been shifted to higher wavenumbers (consistent with the observations of Pratt, 1975), while at 30N it has ceased to exist altogether. The propagation band of the simulated summer spectrum at 50N does not appear to have shifted from its winter position, although it is not very well defined. In addition, the shape of the model spectrum is quite different than observed, with the model low frequency

peak at wavenumbers 1 and 2 contrasting with the observed peak at wavenumbers 4 and 5. The model spectral density is generally too small. At 30N, the model spectrum does not show any signs of a propagation band, a feature which agrees with the observations. But rather than indicating one low frequency peak at wavenumber 1, the model results show a series of peaks at wavenumbers 1, 3 and 7. Here the low frequency model spectral density is much larger than is observed.

A further useful diagnostic defined in the space-time spectral domain is the net propagation tendency, which measures the extent to which motions of a particular space and time scale propagate preferentially westward or eastward. (This measure is defined so that -1.0 corresponds to pure eastward propagation, +1.0 to pure westward propagation.) The net propagation of the observed (simulated) winter 500 mb geopotential height at 50N is presented in Figure 5.21a (5.21b), and that of the temperature[9] in Figure 5.22a (5.22b).

Both the observed temperature and heights have a net propagation tendency of close to -1.0 in the MFSW region, consistent with the eastward propagation of synoptic-scale systems. On the other hand, it is clear that the observed low frequency planetary waves have little tendency to propagate preferentially in any direction; the values reported for those scales in Figures 5.21a and 5.22a are small and positive for the height field, and small and negative for the temperature field. The observational study of Pratt and Wallace (1976) indicates that this may be due to the coexistence of two dominant low frequency planetary wave modes, one which propagates westward and one which propagates eastward. Although the westward propagating mode is dominated by the height field at 500 mb and the eastward propagating mode is dominated by the

---

[9] The net propagation tendency of the temperature was taken from Pratt and Wallace (1976). The major differences between their methodology and that used in this paper are the definition of the winter season (they define it to be the 132-day period starting November 25), the choice of band width (they use 0.133 cycles per day as opposed to 0.0667 cycles per day used here), and the data base (they used only four years of NMC analyses).

temperature field, both variables contribute to both modes, leading to a certain amount of cancellation in the net propagation tendency. The observed pattern of net propagation tendency is reproduced in the model results for temperature and geopotential (Figures 5.21b and 5.22b). Both fields show almost exclusively eastward propagation in the MFSW scales, while the height (temperature) field shows a slight tendency to propagate westward (eastward) in the LFPW scale. The region of positive net propagation tendency in the model spectrum is, however, not as extensive as in the observations.

In order to provide a background for the space-time spectral analyses of heat and momentum fluxes to be discussed in subsections d and e, spectra of the u and v winds are presented here. The spectrum of the observed 300 mb u-wind (v-wind) in winter at 35N is presented in Figure 5.23a (5.24a), and the simulated spectrum (at 34N) in Figure 5.23b (5.24b). The observed[10] u-wind spectrum is similar to the spectra of the geopotential in that most of the spectral density is concentrated in the LFPW's, and in the appearance of a distinct propagation band. The propagation band of the model spectrum is somewhat disorganized, although the LFPW maximum is well simulated. The spectral density is in general too low, especially for low frequencies at wavenumber 1.

In contrast, the v-wind spectrum is very well simulated by the model. The propagation band is correctly represented as running from wavenumber 5 and lower frequencies to higher wavenumbers and frequencies. (That the low frequency end of the propagation band occurs at wavenumber 5 rather than 1 or 2 is a direct consequence of geostrophic balance.) Also, the magnitude of the simulated spectral density is generally quite realistic, including the values at the maxima. Howevever, the model spectrum does show a peak near wavenumber 7 and a

---

[10] The observed wind spectra are reproduced from Pratt (1977). The methodology of that paper is similar to that described in footnote 9.

frequency of 0.175 cpd, a feature that is not observed. (It is important to note that some features may appear more localized in frequency in the GCM spectra than in Pratt's observed spectra because of the difference in band width alluded to in Footnote 9.)

Space-time spectral summaries. In order to obtain a representation of the vertical and meridional structure of the wavenumber-frequency spectra, it is useful to be able to summarize each spectrum by a few parameters. It is for this purpose that the four space-time categories of the previous subsection (low frequency planetary waves, low frequency synoptic-scale waves, medium frequency planetary waves, and medium frequency synoptic-scale waves) were introduced The parameters to be discussed in this subsection are derived by integrating the spectral density over these four space-time regimes.

The latitude-height structure of the observed winter LFPW variance is shown in Figure 5.25a. This variance reaches a maximum slightly above the 300 mb level at about 64N, and shows a decrease above this level. The GCM variance (Figure 5.25b) has a similar structure, except that the variance increases up to at least 200 mb. In addition, the model variance is somewhat too small throughout the northern hemispheric extratropical domain.

The observed winter LFSW variance (Figure 5.26a) reaches a fairly sharp maximum at 300 mb near 46N. The structure of the simulated variance (Figure 5.26b) is again similar to this, although the maximum is much more diffuse in both the vertical and meridional directions. As before, the model variance is not large enough south of 62N, whereas north of this latitude it is too large.

Figure (5.27a) presents the observed winter MFPW variance. Its structure is seen to be quite similar to the LFPW variance, except that the maximum is pushed further northwards. The magnitude of the MFPW variance, on the other hand, is considerably less than that of the LFPW's. The deficiencies of the

model MFPW variance (Figure 5.27b) are quite similar to the deficiencies of the model LFPW variance; the model variance is generally too small, and does not show the observed decrease above 300 mb.

In contrast to these results, the simulated MFSW variance (Figure 5.28b) agrees quite well with the observations (Figure 5.28a). Not only is the model variance almost as large as is observed, but it also shows the observed decrease above the 300 mb maximum.

The observed summer variances in the LFPW, LFSW, MFPW and MFSW categories are presented in Figures 5.29a, 5.30a, 5.31a and 5.32a, respectively. In general, the latitude-height structures of the variance are quite similar to the corresponding winter results, except that the 300 mb maxima have moved somewhat farther north, and the magnitude of the summer variances is somewhat less. The summer LFSW variance does not fit this pattern, however, since the winter maximum at 300 mb has moved up to at least 200 mb in summer, and the magnitude of the variance has decreased only slightly.

Figures 5.29b, 5.30b 5.31b and 5.32b give the GCM results for the variances in the LFPW, LFSW, MFPW and MFSW categories. All the model variances increase with height up to at least 200 mb, so that except for the LFSW's, their structure is not in agreement with the observations. In addition, the model medium frequency (MFPW, MFSW) variances show indications of two maxima at 200 mb. The magnitudes of the planetary wave (LFPW, MFPW) variances are too small over the whole northern hemispheric extratropical domain, while in the case of the synoptic-scale wave (LFSW, MFSW) variances, the simulated magnitudes are too small in the vicinity of the observed maximum but are too large far to the south and north of this region.

d. Northward eddy transport of heat. The analysis of meridional energy transports presented in subsection a indicated that the total vertically integrated

northward transport of heat by the eddies was fairly realistic in both the winter and summer simulations. In this subsection, the northward flux of heat is diagnosed in much more detail. The first part discusses latitude-height cross sections of both stationary and transient zonally-averaged meridional heat fluxes, while the geographical structure of the local transient heat flux and its breakdown into low-pass and band-pass components are studied in the second part. Some representative space-time spectra are presented in the third part.

Stationary and transient eddy heat flux. The observed (simulated) time mean February heat flux due to the stationary eddies is shown as a function of latitude and pressure level[11,12] in Figure 5.33a (5.33b). The agreement between the model results and the observation is quite good. The observed mid-latitude maximum of positive heat flux is well reproduced, as is the secondary maximum at 200 mb. Discrepancies include the presence of a sizeable negative heat flux in the model subtropics at 200 mb (which is not observed), the incorrect sign of the model heat flux north of 70N in the lower troposphere, and the slight equatorward displacement of the 200 mb maximum in the model results.

The time mean heat flux due to the transient eddies in February is given for the model[12] in Figure 5.34b and for the observations in Figure 5.34a. It is important to note that no prefiltering of the data has been done before computing the transient component, so that this component includes a contribution due to the annual cycle. Both the observed broad maximum of positive flux in the mid-latitude lower troposphere and the weaker maximum near 200 mb are well reproduced by the model. Several differences exist, however. The region of

---

[11] The observed results for the stationary and transient heat flux are taken from Oort and Rasmusson (1971). Their definitions of stationary and transient eddy fluxes have been adhered to in computing the model statistics.

[12] The apparent maximum in the lower troposphere between 30N and 38N is an artifact of the reduction of the fields below the Himalayas.

large positive heat flux in the model penetrates higher than is observed, and the upper tropospheric maximum is unrealistically weak in the model.

The stationary eddy heat flux in July is very weak for both the model (Figure 5.35b) and the observations (Figure 5.35a). However, the model results show several features that are not observed, including maxima of negative flux in the subtropical lower troposphere, a maximum of positive flux at high latitudes in the lower troposphere, and a strong maximum of postive flux at the mid-latitude tropopause. The transient eddy heat flux in July, shown for the observations (model) in Figure 5.36a (5.36b), is much stronger. The model reproduces well the observed broad maximum of positive flux in mid-latitudes, although the peak values in the model seem slightly too large. Further, the maximum of positive flux near the tropopause in mid-latitudes is very weak in the model results.

Local covariance analysis. The observed local transient northward heat flux at 850 mb in winter, as reported by Blackmon et al. (1977) is shown in Figure 5.37a. This quantity is given by the covariance of northward velocity with temperature, where each field has had the annual cycle removed in the manner described in subsection c. The Atlantic and Pacific storm tracks correspond to regions of high (positive) covariance, and other (positive) maxima occur over the Gulf of Alaska, the east coast of Iceland, and southern Russia. Minima (areas of relatively large negative flux) are seen over western Canada and northwestern Russia. The simulated northern hemispheric winter covariance of transient heat flux at 850 mb (Figure 5.37b) shows some similarity to the observations. Both major oceanic storm tracks stand out clearly, although the heat flux associated with the one in the Atlantic is somewhat too small. The maxima near the Gulf of Alaska and in southern Russia are present, although their magnitudes, orientations and precise positions do not agree with the

observations. The observed minimum over western Canada is very weak in the model results.

The observed low-pass and band-pass transient 850 mb heat fluxes (obtained from the covariances of the filtered v-wind and temperature fields) are shown in Figures (5.38a) and (5.39a). The band-pass heat flux is dominated by the major oceanic storm tracks, while the low-pass results show the other major features that were present in Figure 5.37a. Two features that appear as part of the storm tracks in Figure 5.37a, but which are seen to correspond to lower frequency phenomena in Figure 5.38a, are the maxima of heat flux over the eastern United States and over southeast Asia. These two features are present in the simulated 850 mb low-pass heat flux (Figure 5.38b), whose resemblance to the total simulated transient heat flux (Figure 5.37b) is close but not as close as in the observations. The simulated band-pass heat flux (Figure 5.39b) is dominated by the major oceanic storm tracks, which agree very well with the observations (Figure 5.39a) both with regard to position and intensity.

The observed local transient heat flux in winter at 300 mb and 200 mb (Figures 5.40a and 5.41a) present an interesting contrast with one another. (Lau, 1978). There are maxima in the northward heat flux over the western oceans at both levels, but the heat fluxes over western North America and western Europe show an abrupt change in going from large and equatorward at 300 mb to large and poleward at 200 mb. The simulated winter transient heat fluxes at 300 mb and 200 mb (Figures 5.40b and 5.41b) show some evidence of this sharp transition. The 200 mb heat flux resembles the observations to the extent that it is maximum over the western oceans and western continents, but the peak values of the heat flux (except over North America) are unrealistically low. In addition, the model results indicate an area of very strong equatorward flux in the eastern Pacific and one of more moderate equatorward flux further west. Neither of these are observed. The simulated 300 mb heat flux reaches

a maximum of negative values over western North America with a peak magnitude that agrees with the observations. Thus, in this region the model reproduces the change of sign of the heat flux. The 300 mb heat flux reproduces the observed (positive) maxima off the East coasts of North America and Asia, although they are too weak. The observed large, equatorward flux over Western Europe at 300 mb is not present in the simulated results.

Wavenumber-frequency cospectra. The behavior of the transient heat flux can be farther described by its wavenumber-frequency cospectrum, which expresses the longitude- and time-covariance of v and T in terms of contributions from different wavenumbers and frequencies. The model cospectra reported here were calculated in a manner entirely analagous to the wavenumber-frequency variance spectra described in subsection c. The observed cospectra are taken from Pratt (1975)[13]. Figures 5.42a and 5.43a show the observed winter heat flux cospectra at 50N at 850 mb and 200 mb, respectively. The corresponding cospectra of the GCM are given in Figures 5.42b and 5.43b. Both the observed and simulated 850 mb heat flux at 50N show a distinct propagation band, with the maximum covariance for wavenumbers 4-5 and for low frequencies. The model cospectrum, in general, looks quite realistic, the main exception being the lack of covariance near the low frequency end of the propagation band.

In contrast, the GCM heat flux cospectrum at 200 mb, 50N, looks quite unrealistic. The observed cospectrum again shows a well-defined propagation band, with a maximum covariance at wavenumber 4, at low frequencies. There is also a slight secondary maximum at wavenumbers 7-8 and frequencies near .30, space and time scales which are associated with cyclones. The propagation band so evident in the observations is not present in the GCM cospectrum, which is dominated by very large values at wavenumber 3 near frequencies of 0.10 cpd.

---

[13] The methodology used by Pratt (1975) is similar to that described in footnote 9.

In addition, the low frequency cospectrum for wavenumber 2 is sizeable and negative, indicating a relatively large southward heat transport by these scales of motion. It is worth noting that the weak secondary maximum in the synoptic-scale region is evident in the model results.

The summer heat flux cospectrum at 850 mb, 50N (Figure 5.44a) also indicates the presence of a propagation band, but with its low frequency end shifted to higher wavenumbers compared to the corresponding winter cospectrum. The magnitudes of the heat flux are of course also much less than in winter. This decrease in magnitude and shift to higher wavenumber is captured by the GCM summer cospectrum at 850 mb, 50N (Figure 5.44b), which agrees well qualitatively with the observations. There are some differences in detail, with the observations showing low frequency peaks at wavenumbers 4 and 6, whereas maxima in the simulated cospectrum occur at wavenumbers 6 and 7.

The propagation band of the observed 200 mb cospectrum at 50N (Figure 5.45a) is not noticeably weaker than its winter counterpart, although it is shifted towards higher wavenumbers. The simulated spectrum (Figure 5.45b) is similar to the observed only in that there is some indication of a propagation band present. The GCM cospectra show a large drop in peak magnitudes in going from winter to summer, and the maximum values in the summer cospectra appear at very low frequencies in wavenumbers 2 and 5. These features do not correspond to the observations.

e. Northward eddy transport of momentum-stationary and transient eddy momentum flux. The time mean momentum flux due to the stationary eddies in February is shown (as a function of latitude and pressure level) for the observations[14] in Figure 5.46a, and for the GCM in Figure 5.46b. The observations

[14] The observed results for stationary and transient momentum flux are taken from Oort and Rasmusson (1971). Their definitions of stationary and transient eddy fluxes have been adhered to in computing the model statistics.

are dominated by large positive (northward) values of the flux in the upper troposphere at mid-latitudes, and large negtive (southward) values farther north. The peak northward flux in the model upper troposphere in mid-latitudes is larger than observed, while the observed region of large southward flux is almost completely missing in the GCM results.

The observed time mean momentum flux due to transient eddies for February is shown in Figure 5.47a. It is dominated by a large peak in northward flux slightly north of 30N at the 200 mb level. The only other feature of note is the relatively small peak of negative (southward) flux at 200 mb at the equator. The model results (Figure 5.47b) also show a large maximum of positive flux, and its position is correct. However, it is too weak by a factor of two. A small maximum of southward flux at 200 mb over the equator is also present in the model, but it is too weak. A feature present in the GCM results which is not observed is the region of negative flux in the upper troposphere between 54 and 70N.

The behavior of the GCM's time mean momentum flux due to the stationary eddies for July is quite unrealistic (Figures 5.48a-b). The observations show a peak of northward flux at 200 mb at about 30N, while in the GCM results this peak is completely missing. The (small) maxima of negative flux in the model upper troposphere do not have their counterpart in the observations. In contrast to the stationary eddy flux of momentum, the model transient eddy flux of momentum behaves more realistically. The observations (Figure 5.49a) show three important features: a large maximum of positive flux at 200 mb at 45N, a smaller (positive) maximum at 200 mb just south of the equator, and a broad upper tropospheric maximum of negative flux north of 60N. The GCM results (Figure 5.49b) show the same basic features, located approximately in the correct positions. However, the positive maxima are too small, and the negative maximum too large in magnitude.

Local covariance analysis. The observed local transient northward flux of momentum at 250 mb in winter, as reported by Lau et al. (1978), is shown in Figure 5.50a. This quantity is given by the covariance of northward velocity with eastward velocity. The covariance of the band-pass filtered fields is given in Figure 5.51a. The main features of these two observed fields are similar, although the magnitude of the band-pass covariance is considerably less than that of the total covariance. One feature that is prominent in both maps is the dipole structure that appears over the western and central Atlantic with poleward fluxes south of about 45N and equatorward fluxes north of this. This feature implies a large convergence of momentum flux into the storm track region (defined by the maximum RMS of the 500 mb band-pass height field), which is indicated in the figures by the dashed arrows. A similar feature appears in the Pacific. Another important feature is the large northward flux apparent over the western parts of continents, particularly the United States. The GCM local winter covariance at 200 mb is shown in Figure 5.50b, and the band-pass local covariance in Figure 5.51b. The simulated map of local covariance shows dipole patterns over North America and the Eastern Pacific, off the east coast of Asia, and over Western Europe. Clearly the simulated convergence of momentum flux is not realistic. The Pacific and Atlantic storm tracks seem to be marked by almost no convergence of momentum flux, in contrast to the observations. The GCM band-pass covariance has dipole-like patterns in the Atlantic (although it is south of the storm track) and in the eastern Pacific, but they are too weak. The maximum over western North America is present in the GCM results but it is too weak.

The observed winter covariance of westward and northward velocities at 500 mb (taken from Blackmon et al., 1977) is given in Figure 5.52a, and the band-pass variance in Figure 5.53a. The map of total covariance shows a general pattern of momentum flux convergence into mid-latitudes, although the dipole-like

structures evident at 250 mb are not clear here. Features which the model covariances (Figure 5.52b) capture are the peaks of poleward flux over the extreme western oceans and western continents (although the magnitude of the model flux is generally too small), and the tongue of equatorward flux near Greenland.

The observed winter band-pass variance at 500 mb is similar to the 250 mb covariance, with distinct dipole-like patterns over the western oceans, and a large poleward flux over the western United States. The GCM band-pass covariance (Figure 5.53b) at 500 mb is much more realistic than at 200 mb. The dipole pattern observed in the Atlantic is evident in the model results, although it is too extensive. In the Pacific, the observed dipole pattern is also evident in the model results, but it appears to be too diffuse.

Wavenumber-frequency cospectra. The transient momentum flux can be further examined by means of wavenumber-frequency cospectra, exactly analagous to the heat flux cospectra described in subsection d. The observed winter wavenumber-frequency cospectrum of northward and eastward velocities at 300 mb, 35N (taken from Pratt, 1975) is shown in Figure 5.54a, and the GCM cospectrum (at 34N) is shown in Figure 5.54b. Both the observed and the simulated cospectra show a clear propagation band. The observed cospectrum peaks at wavenumber 5, at a frequency of 0.10 cpd, whereas the model results show two low frequency peaks, at wavenumbers 2 and 5. The presence of a double peak makes the slope of the model propagation band ambiguous at the low frequency, low wavenumber end. The observed region of negative (equatorward) flux at low frequencies and wavenumbers 8 and 9 is present in the model, although the choice of contours in Figure 5.54b obscures this somewhat. The secondary peak at wavenumber 7 and frequencies near 0.175 cpd. does not appear in the observations.

Balance of transient eddy flux convergence and ageostrophic acceleration in the local momentum budget. In the zonally-averaged budget of zonal momentum, the contribution of the Coriolis acceleration due to the time-mean meridional ageostrophic wind is very weak. However, this is no longer true in the framework of a local budget (Lau, 1978). In fact, locally the advection of zonal momentum by the time-mean circulation is basically balanced by the ageostrophic Coriolis acceleration, the horizontal convergence of transient momentum flux playing a less important role. This (two-dimensional) convergence is calculated from observations for winter at 250 mb in Lau (1978), and is presented here in Figure 5.55a. This should be contrasted to the Coriolis acceleration accompanying the time-mean meridional ageostrophic flow shown in Figure 5.56a. In the vicinity of the two major jet streams (indicated in Figure 5.56a by the solid arrows) the ageostrophic acceleration dominates the transient flux contribution, causing a local acceleration in the jet entry regions and a local deceleration in the jet exit regions. In the area of the North American-Atlantic jet stream, the transient fluxes work to oppose these accelerations. Their effect in the region of the Japan jet is not as systematic. It should be pointed out that the dominance of the ageostrophic term is seen also over large portions of Europe and Asia.

The corresponding GCM results for the convergence of transient momentum flux and for the ageostrophic Coriolis acceleration at 285 mb for the month of February are shown in Figures 5.55b and 5.56b. Figure 5.56b also shows the model's jet streams. It is apparent that the Pacific jet is correctly located, but that the Atlantic jet is not oriented towards the northeast as in the observations. In comparing the model results to those that are observed, it is the relationship of the terms in the momentum budget to the jet streams that will be considered. (Note also that the observed results are obtained from 11 winter seasons, each winter being defined as the 120 day period starting on

15 November, whereas the model results represent an average over one month only.) The ageostrophic Coriolis acceleration in the GCM acts very realistically in relation to the jets, causing an acceleration over eastern Asia and off the southern coast of the United States, and causing a decceleration in the jet exit regions. The magnitude of these accelerations is quite realistic for the Atlantic jet, but is too weak in the Pacific. The horizontal convergence of transient momentum flux is realistic in the sense that it is of the observed magnitude, approximately a factor of two less than the ageostrophic accelerations. Otherwise the patterns show differences. The observed convergence (acceleration) in the Atlantic is replaced in the model with a divergence, while the observed convergence over western North America appears in the eastern Pacific in the GCM. The observed divergence over Japan is realistically simulated, but the observed divergence downstream is replaced in the model by a region of convergence. Overall, the model's transient momentum flux convergence does not have a consistent relationship to the positions of the jets.

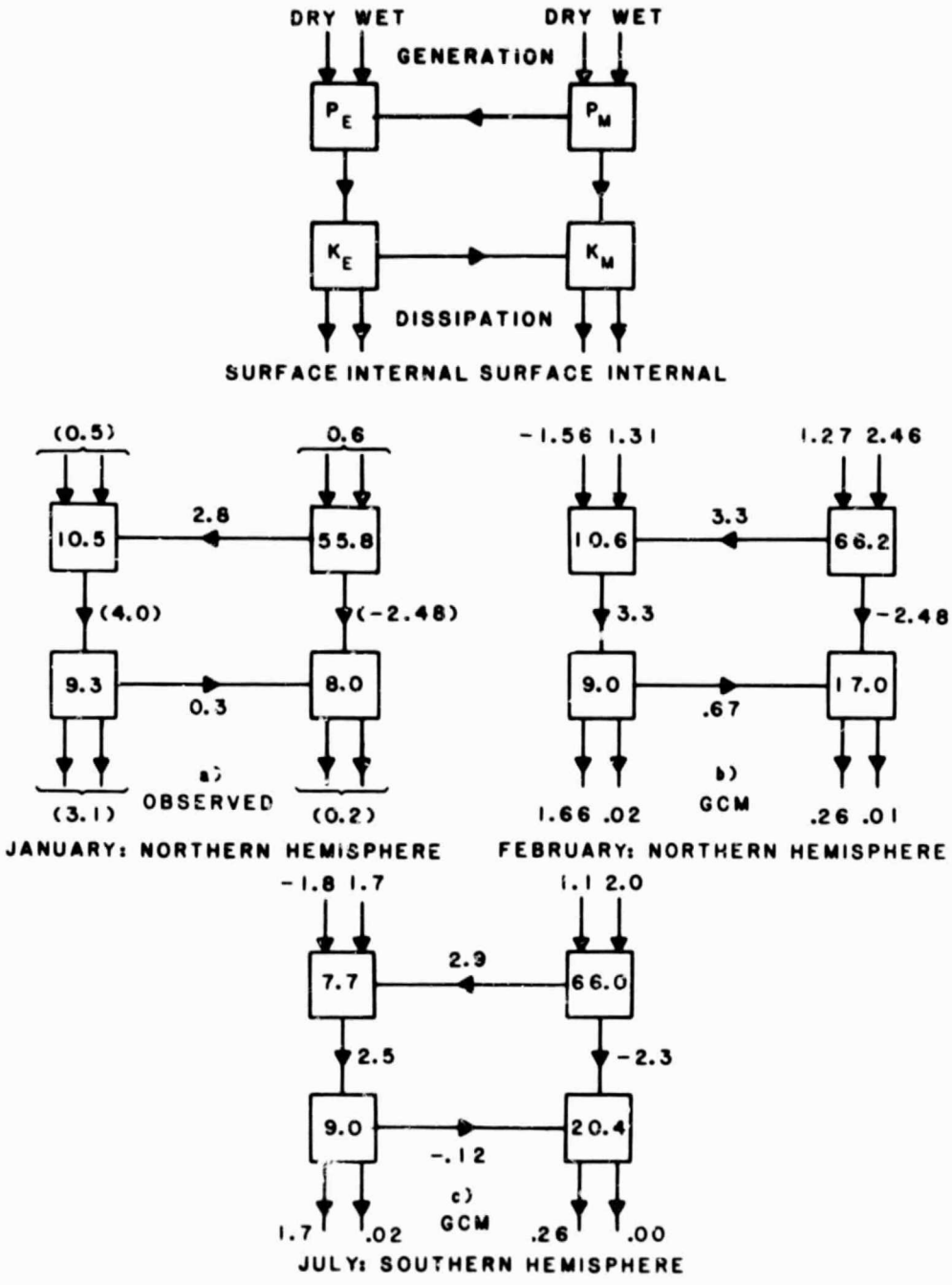

Figure 5.1 Energy cycles for the observed and simulated winter hemispheres, computed in the mixed space-time domain. P_M is the zonal-mean available potential energy, P_E the eddy available potential energy, K_E the eddy kinetic energy, and K_M the zonal-mean kinetic energy. The energies are quoted in units of 10^5 joules/m^2, the transformations and sources and sinks in units of watts/m^2. (a) Observed Northern Hemisphere, January, (b) GCM Northern Hemisphere, February, (c) GCM Southern Hemisphere, July. (Values in parentheses are very approximate.)

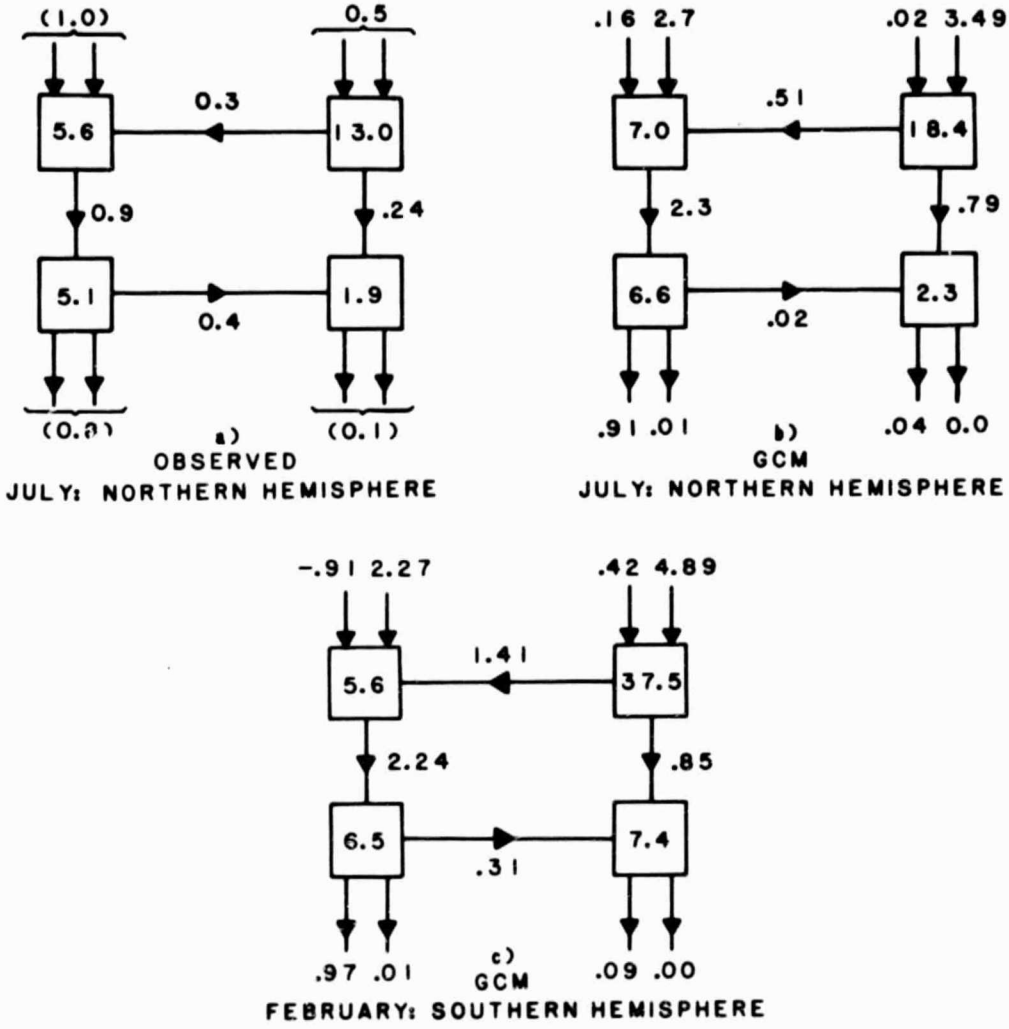

Figure 5.2 Energy cycles for the observed and simulated summer hemispheres, computed as in Figure 5.1. (a) Observed Northern Hemisphere, July, (b) GCM Northern Hemisphere, July, (c) GCM Southern Hemisphere, February. (Values in parentheses are very approximate)

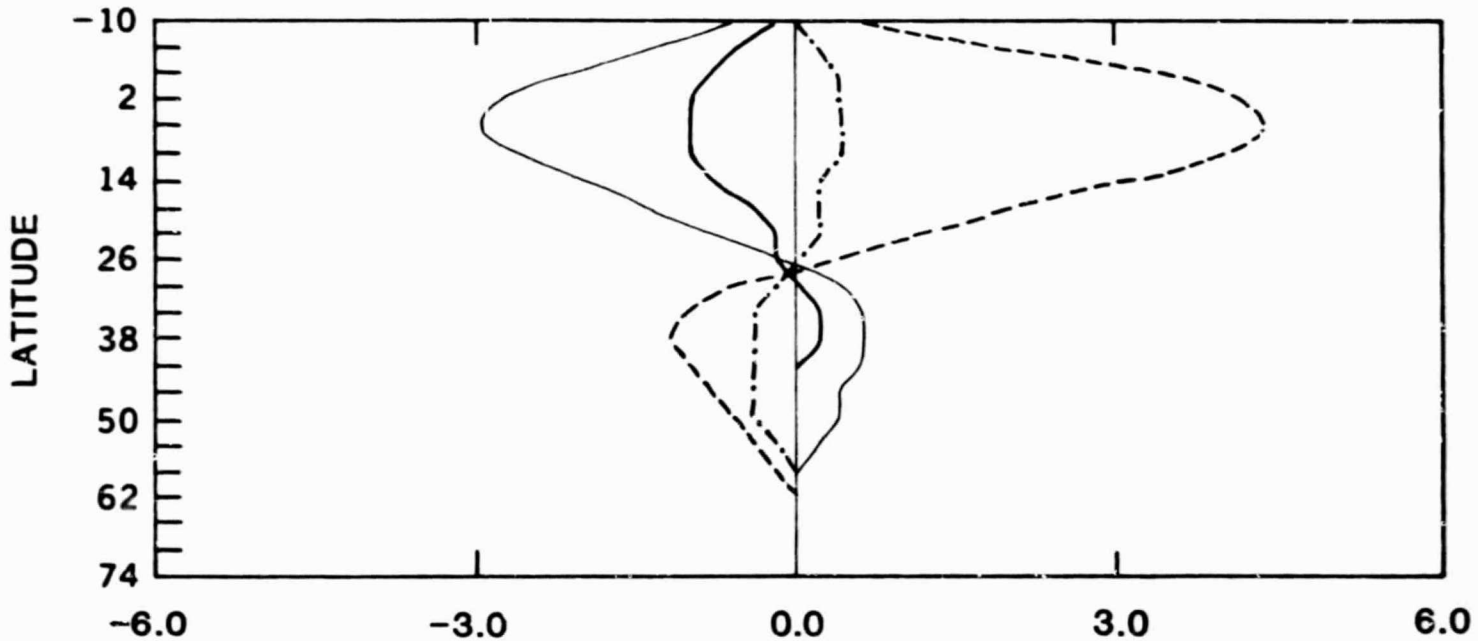

Figure 5.3a Observed meridional mean energy transports for February, units of 10^{20} calories/day. The internal energy is indicated by the light solid line, the latent heat by the heavy solid line, the potential energy by the dashed line, the kinetic energy by the dotted line, and the total energy by the dashed-dotted line. In this plot and in some of those that follow, the kinetic energy transport is too small to be shown, and where the other transports are not shown they are extremely small.

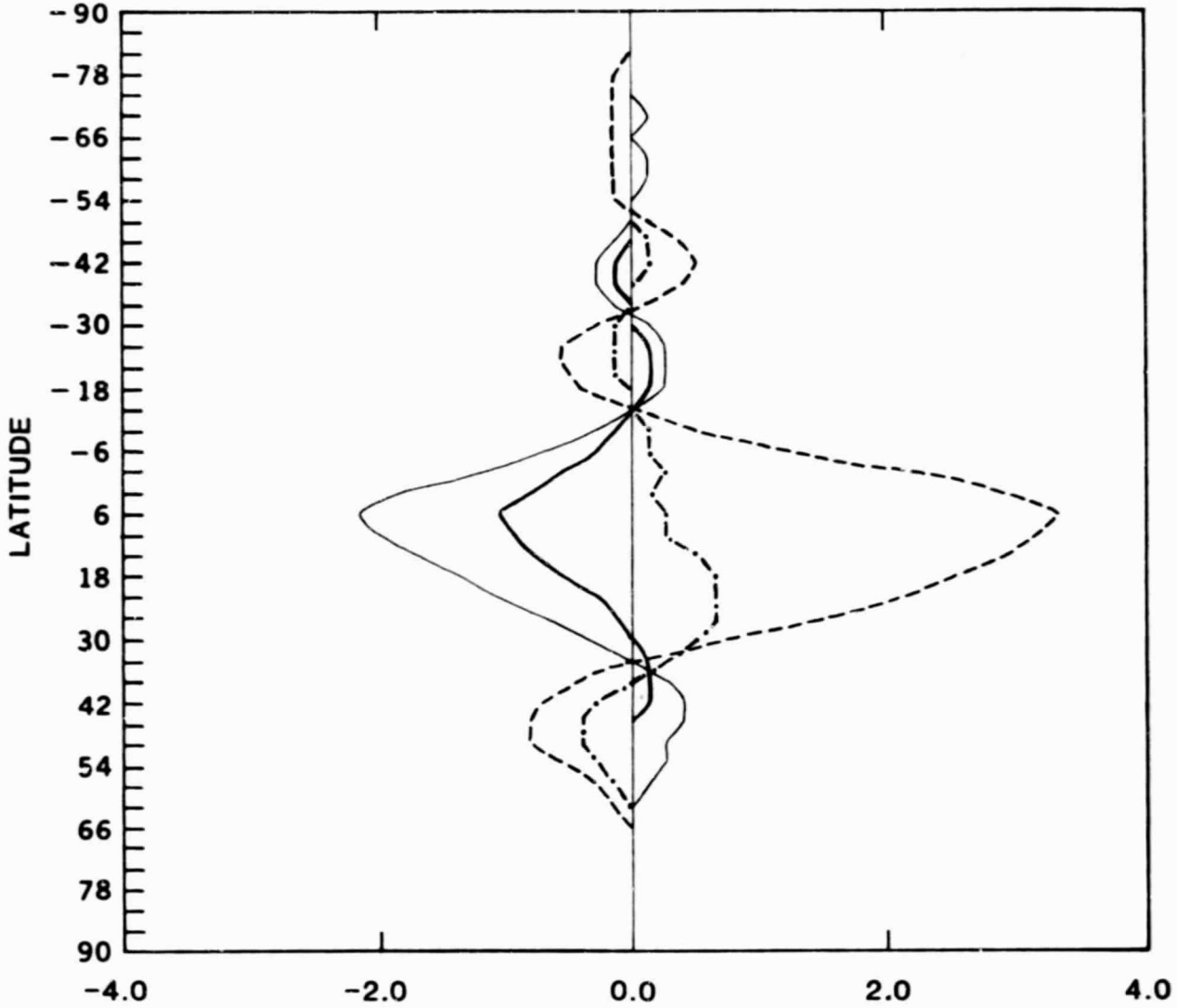

Figure 5.3b GCM meridional mean energy transports for February, units of 10^{20} calories/day, given as in Figure 5.3a. Where transports are not shown, they are extremely small.

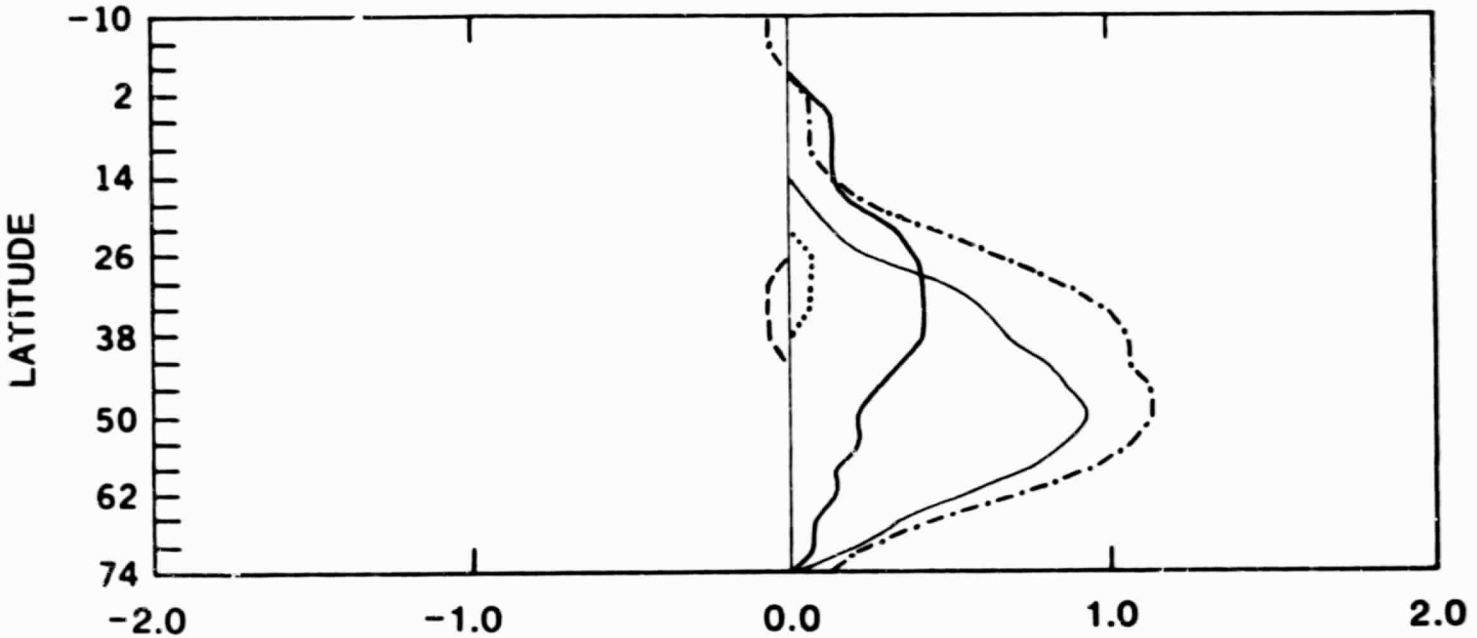

Figure 5.3c Observed meridional eddy energy transports for February, units of 10^{20} calories/day, given as in Figure 5.3a. Where transports are not shown, they are extremely small.

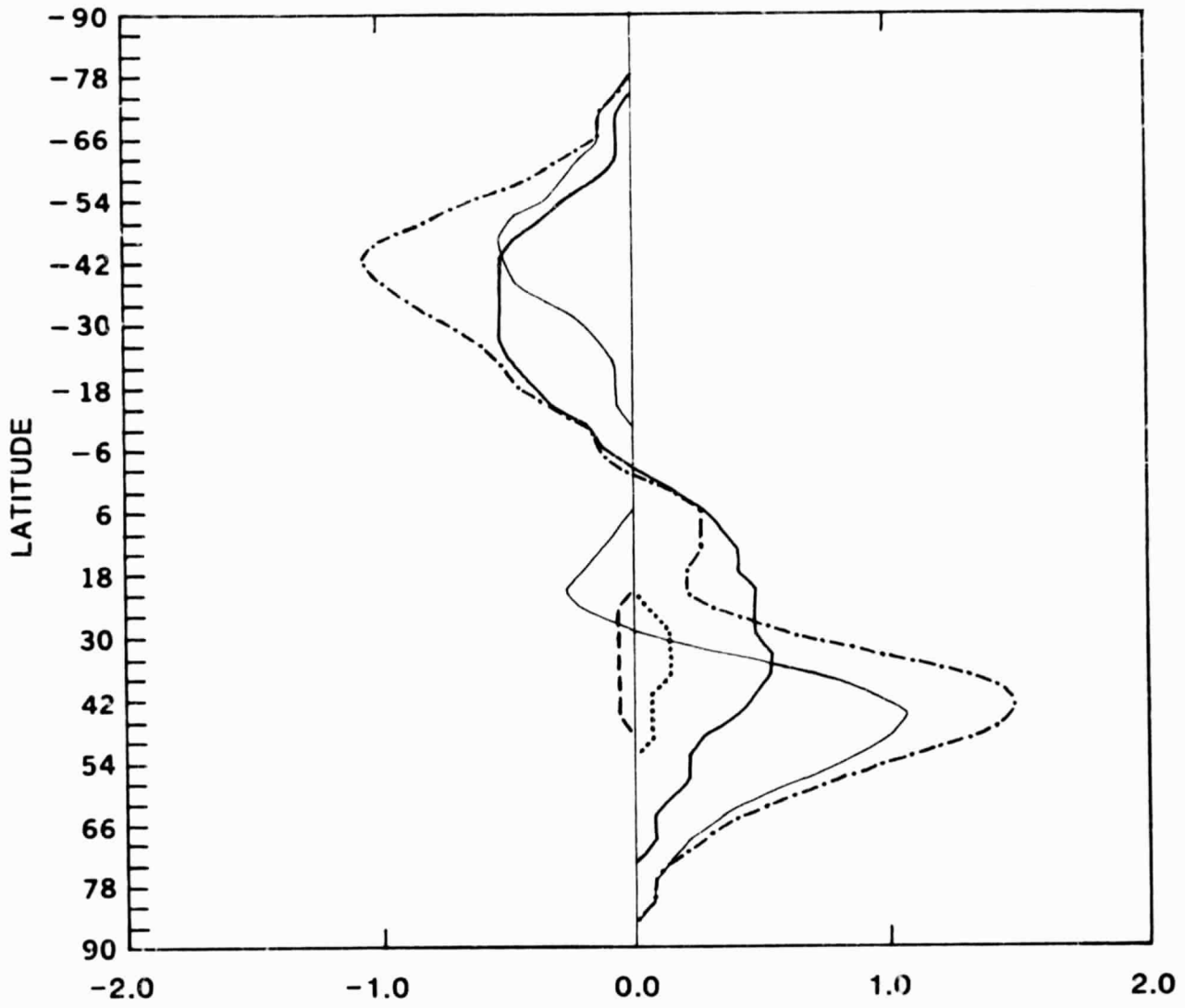

Figure 5.3d GCM meridional eddy energy transports for February, units of 10^{20} calories/day, given as in Figure 5.3a. Where transports are not shown, they are extremely small.

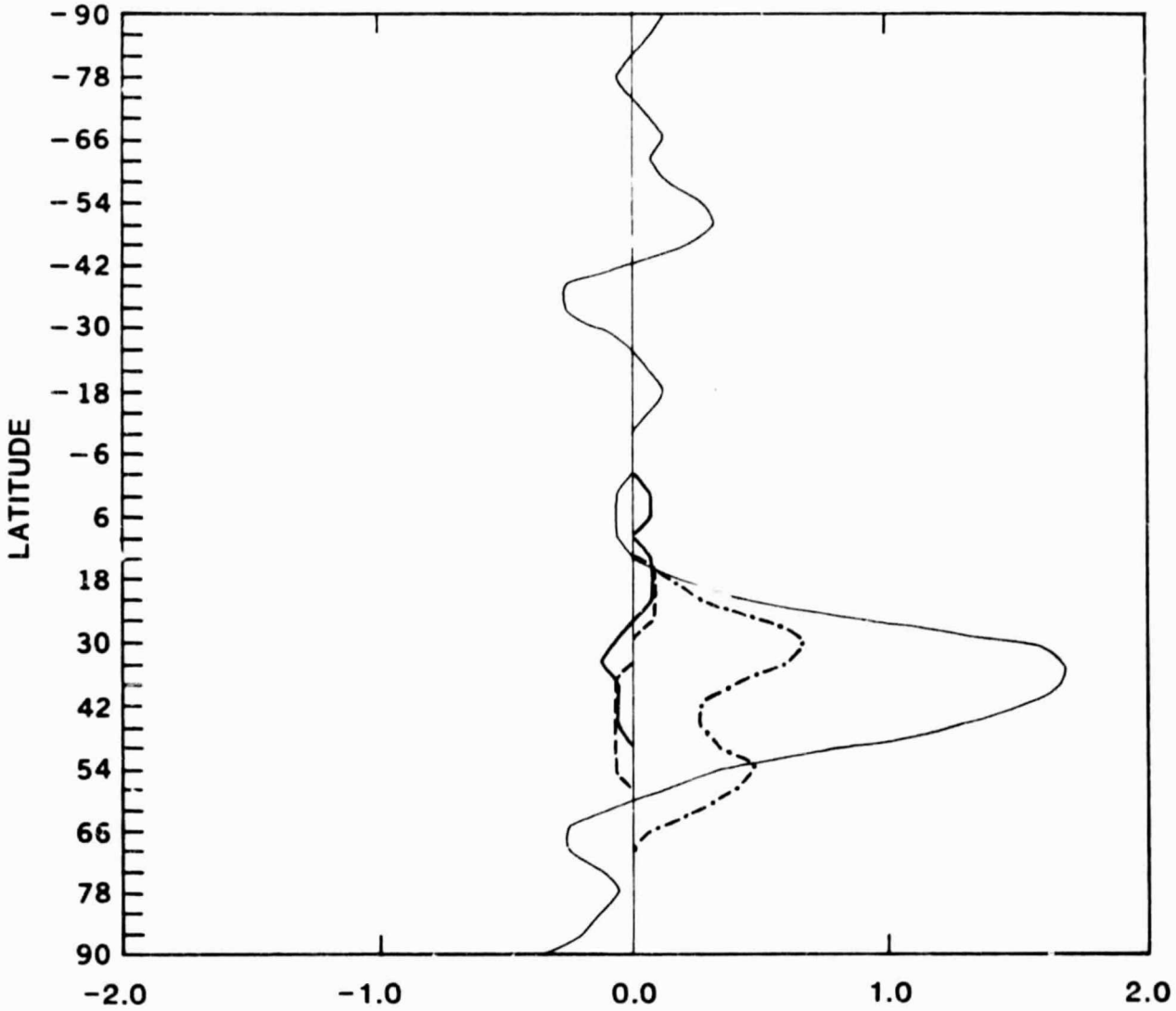

Figure 5.3e Meridional transports of kinetic energy for February, in units of 10^3 m^3/sec^3. The GCM eddy transport is indicated by the light solid line, the GCM mean transport by the dashed line, the observed eddy transport by the dashed-dotted line, the observed mean transport by the heavy solid line. The observations extend only from -10 to +74 degrees of latitude. Where

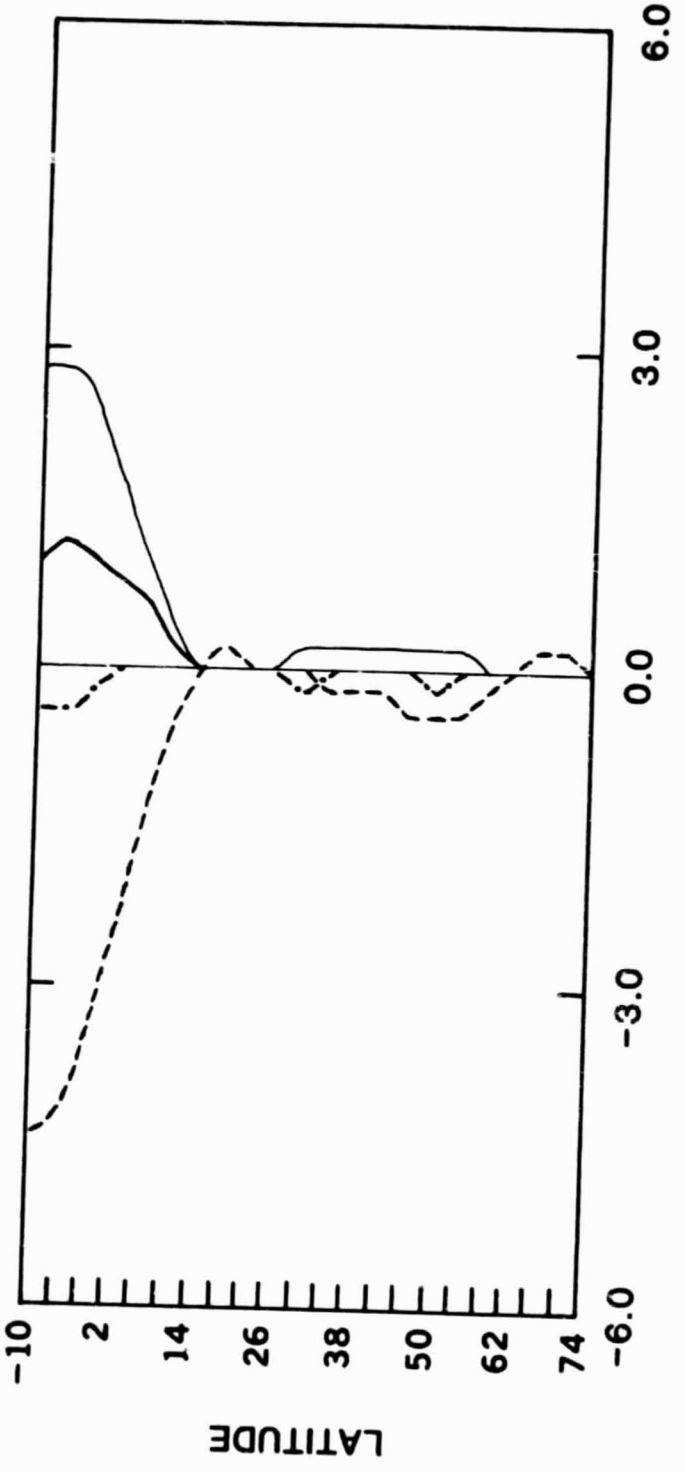

Figure 5.4a Observed meridional mean energy transports for July, units of 10^{20} calories/day, given as in Figure 5.3a. Where transports are not shown, they are extremely small.

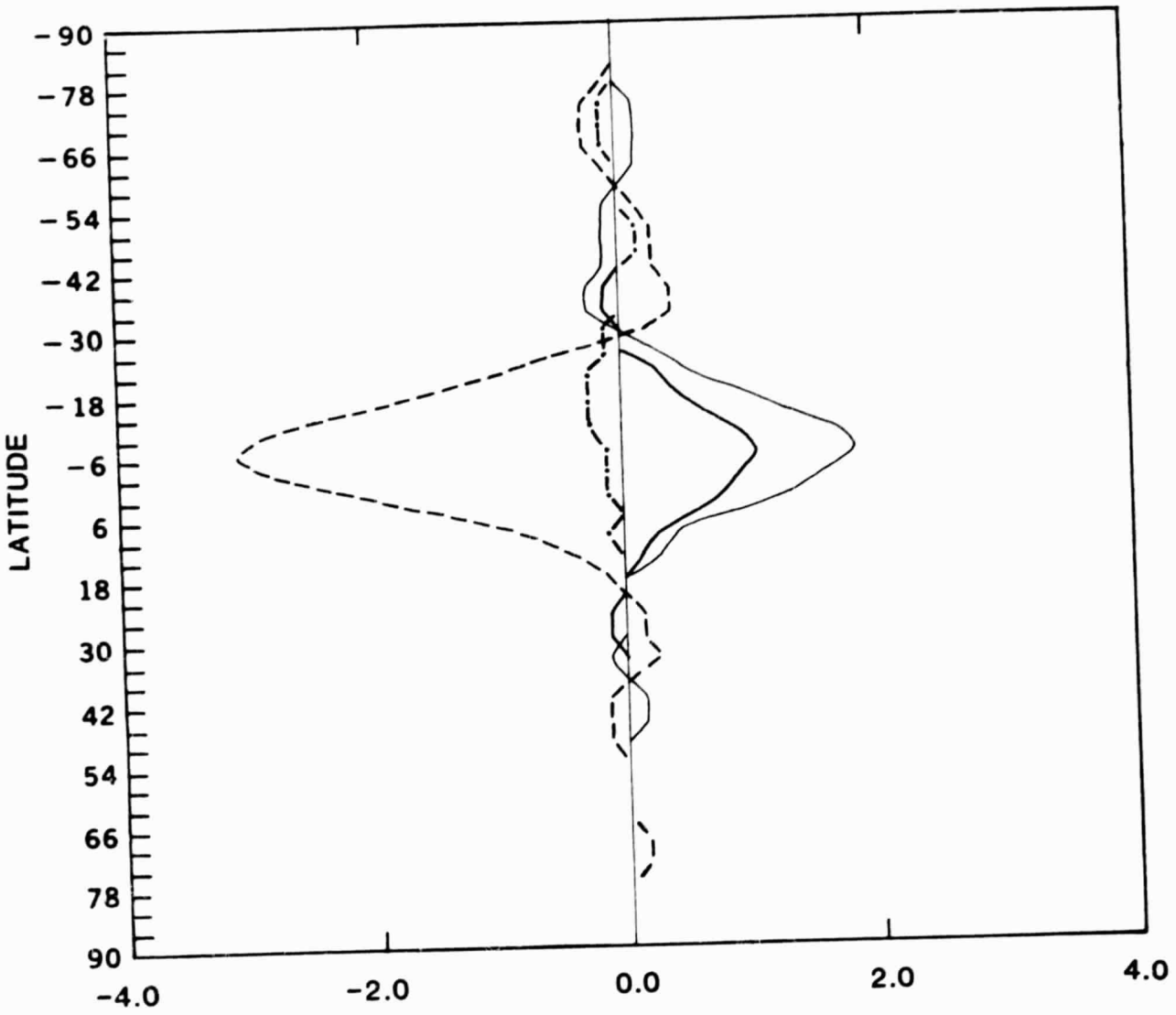

Figure 5.4b GCM meridional mean energy transports for July, units of 10^{20} calories/day, given as in Figure 5.3a. Where transports are not shown, they are extremely small.

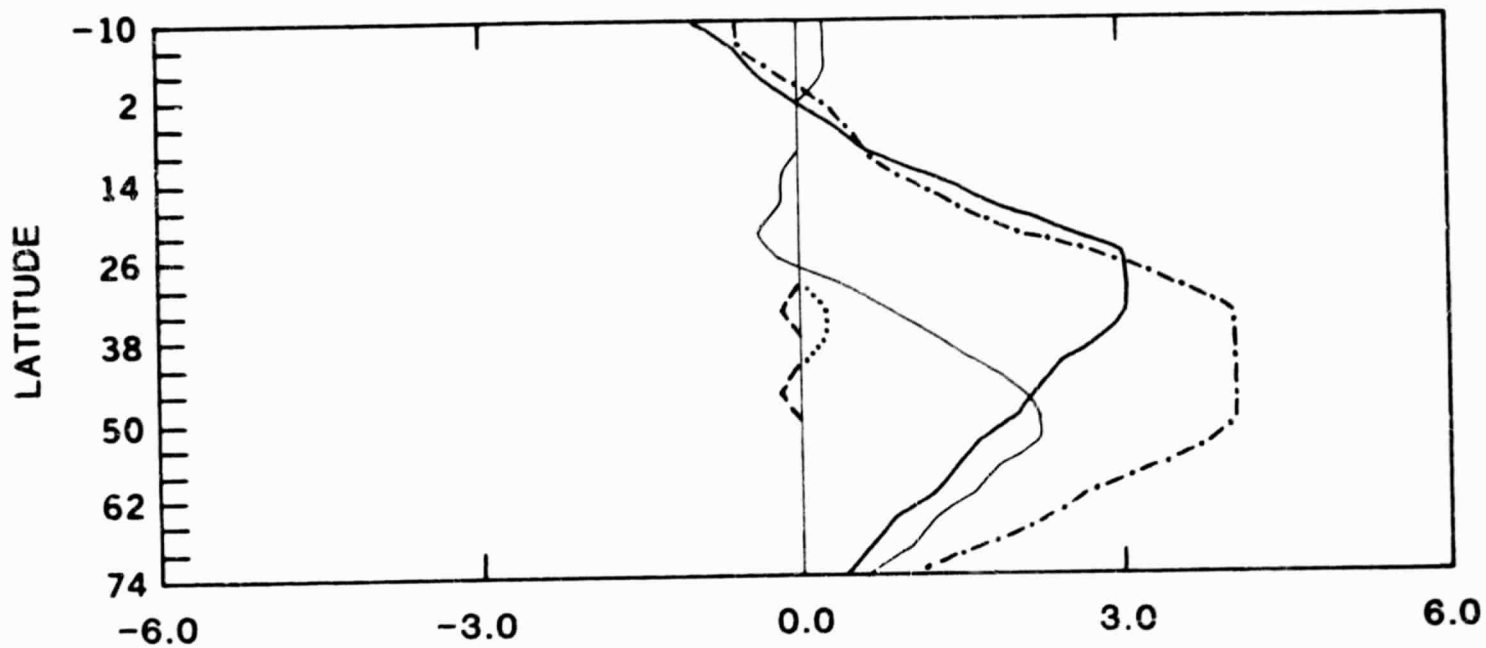

Figure 5.4c Observed meridional eddy energy transports for July, units of 10^{19} calories/day, given as in Figure 5.3a. Where transports are not shown, they are extremely small.

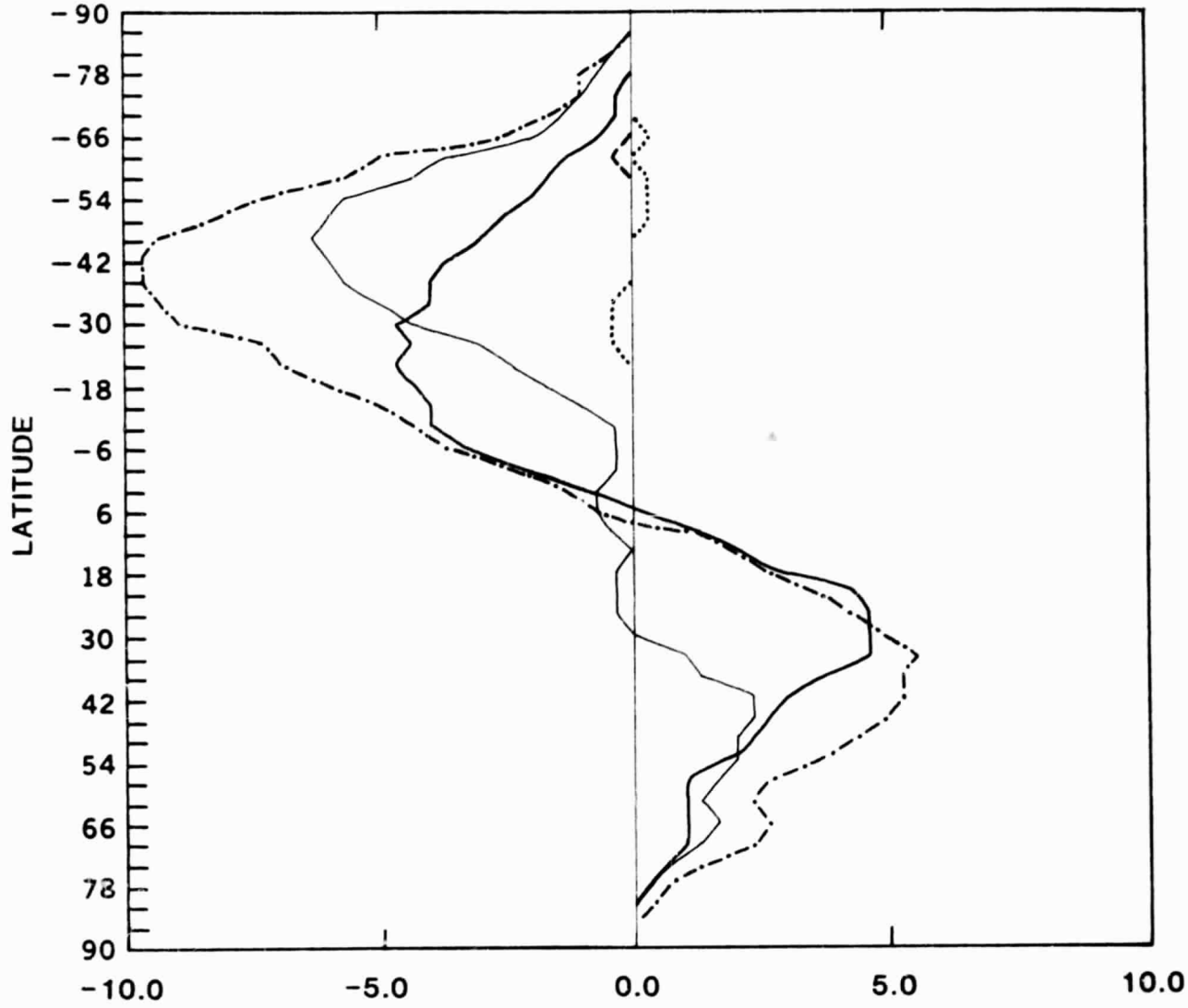

Figure 5.4d GCM meridional eddy energy transports for July, units of 10^{19} calories/day, given as in Figure 5.3a. Where transports are not shown, they are extremely small.

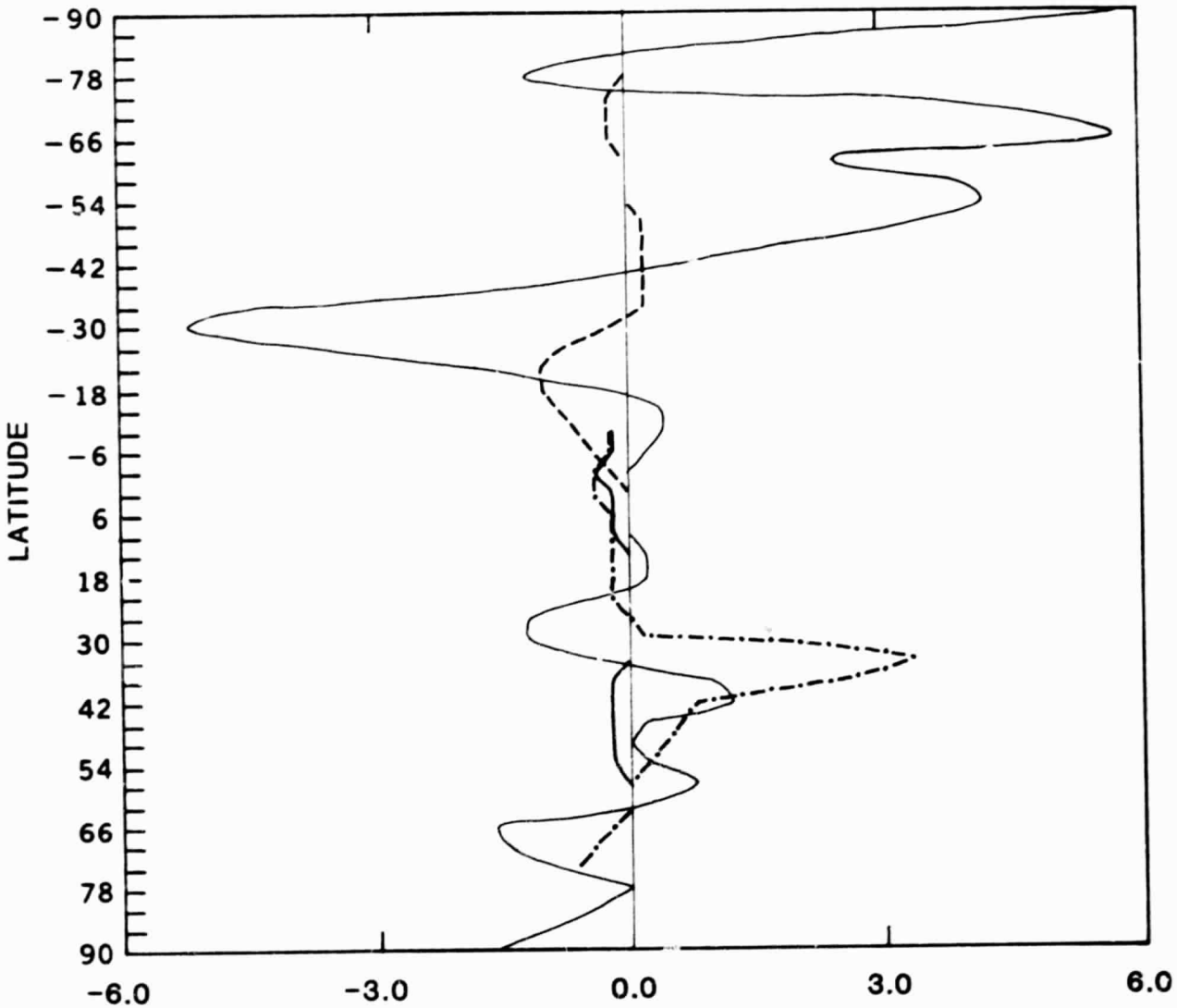

Figure 5.4e Meridional transports of kinetic energy for July, in units of 10^2 m^3/sec^3, given as in Figure 5.3e. Where transports are not shown, they are extremely small.

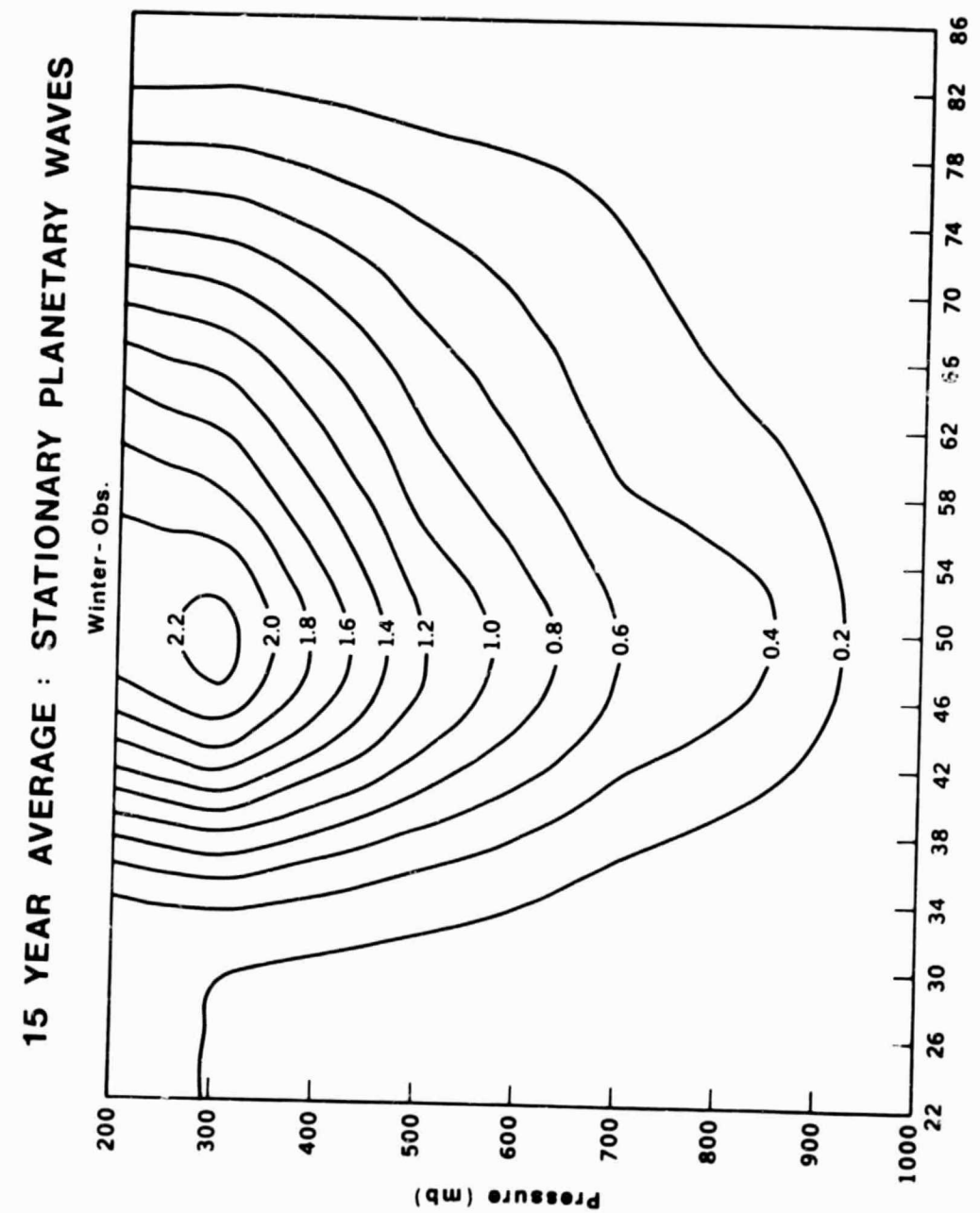

Figure 5.5a Observed winter stationary planetary wave variance of the geopotential height in the Northern Hemisphere. Units of 10^4 m^2.

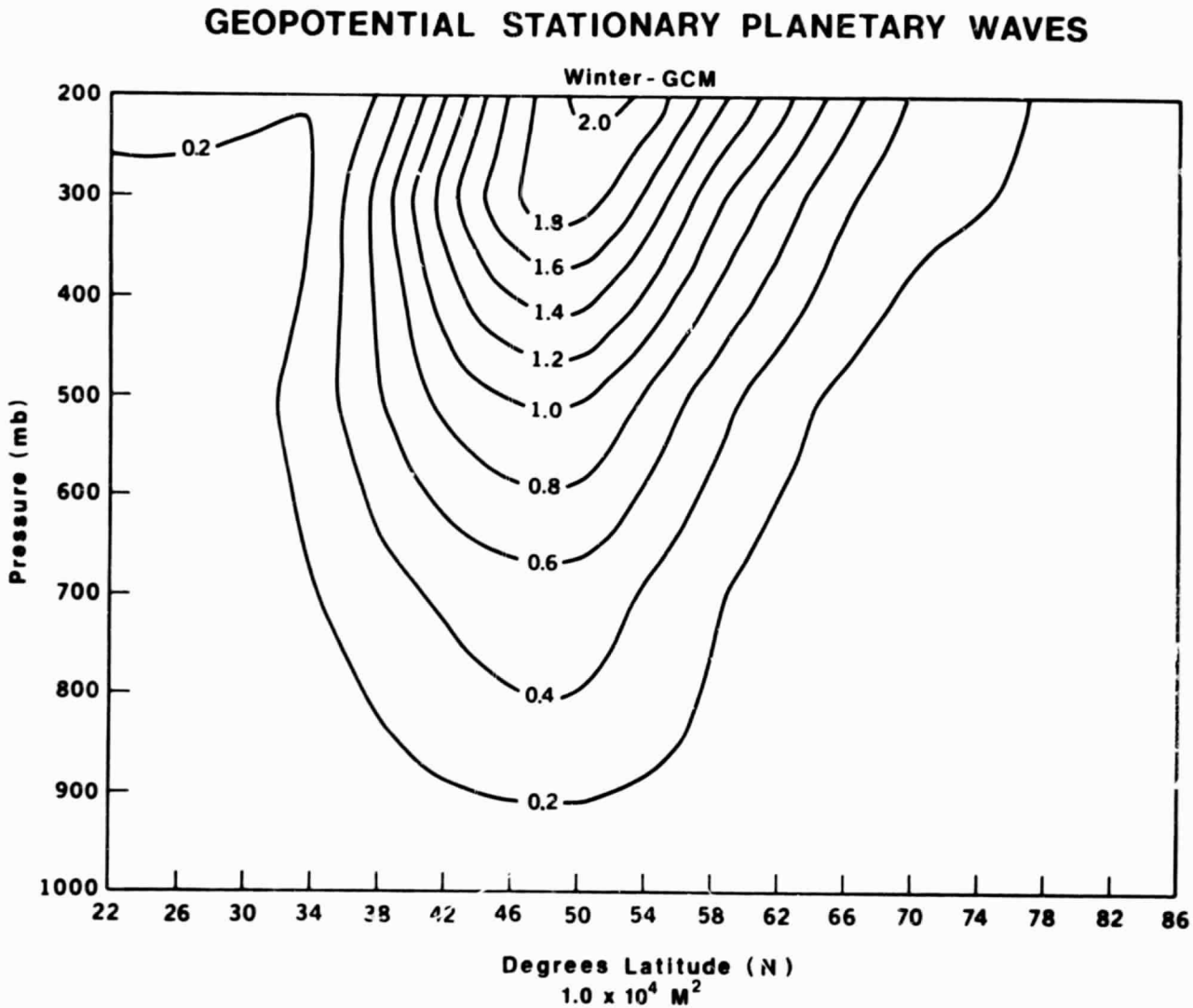

Figure 5.5b1 GCM winter stationary planetary wave variance of the geopotential height in the Northern Hemisphere. Units of 10^4 m^2.

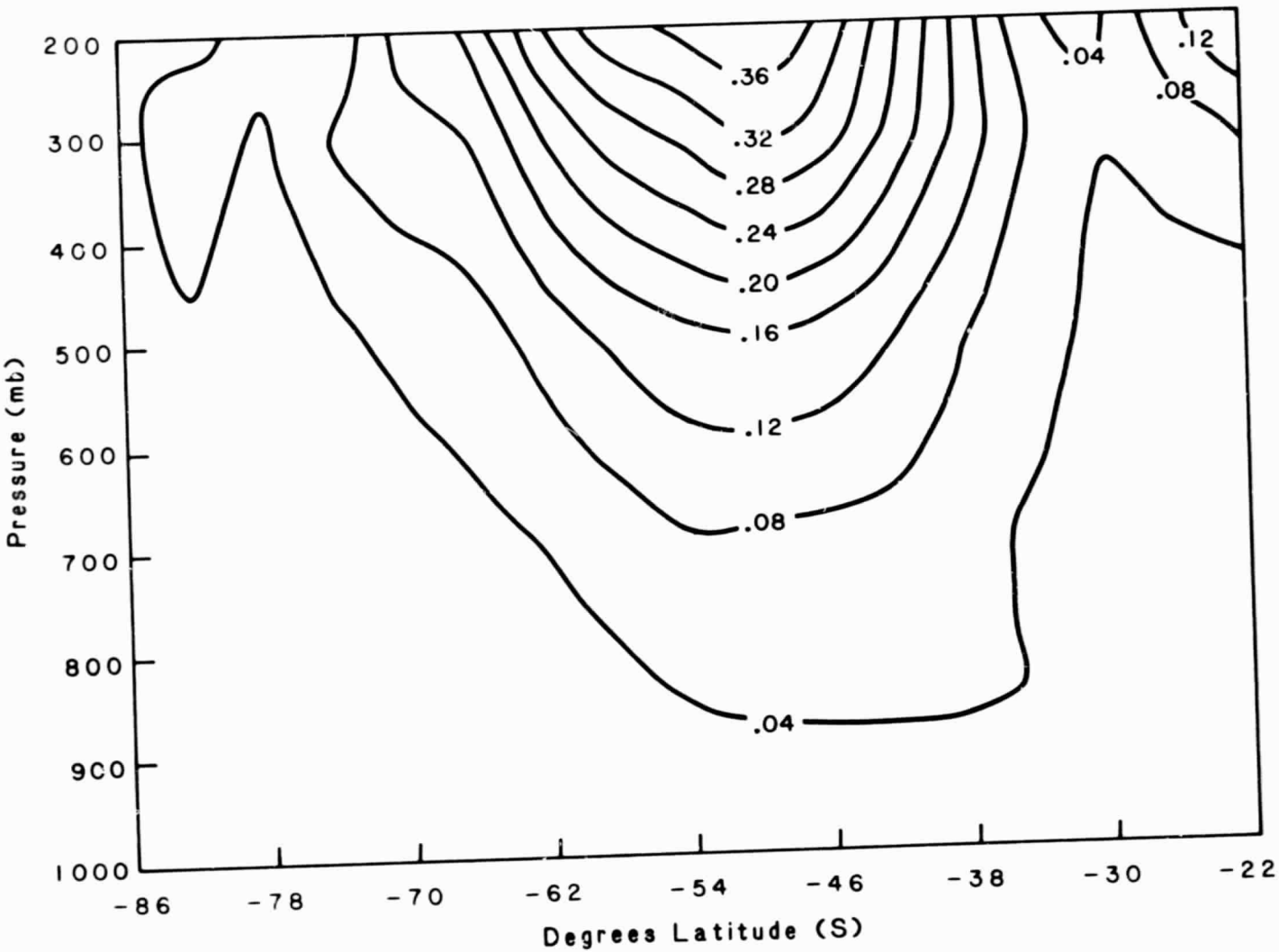

Figure 5.5b2 GCM winter stationary planetary wave variance of the geopotential height in the Southern Hemisphere. Units of 10^4 m^2.

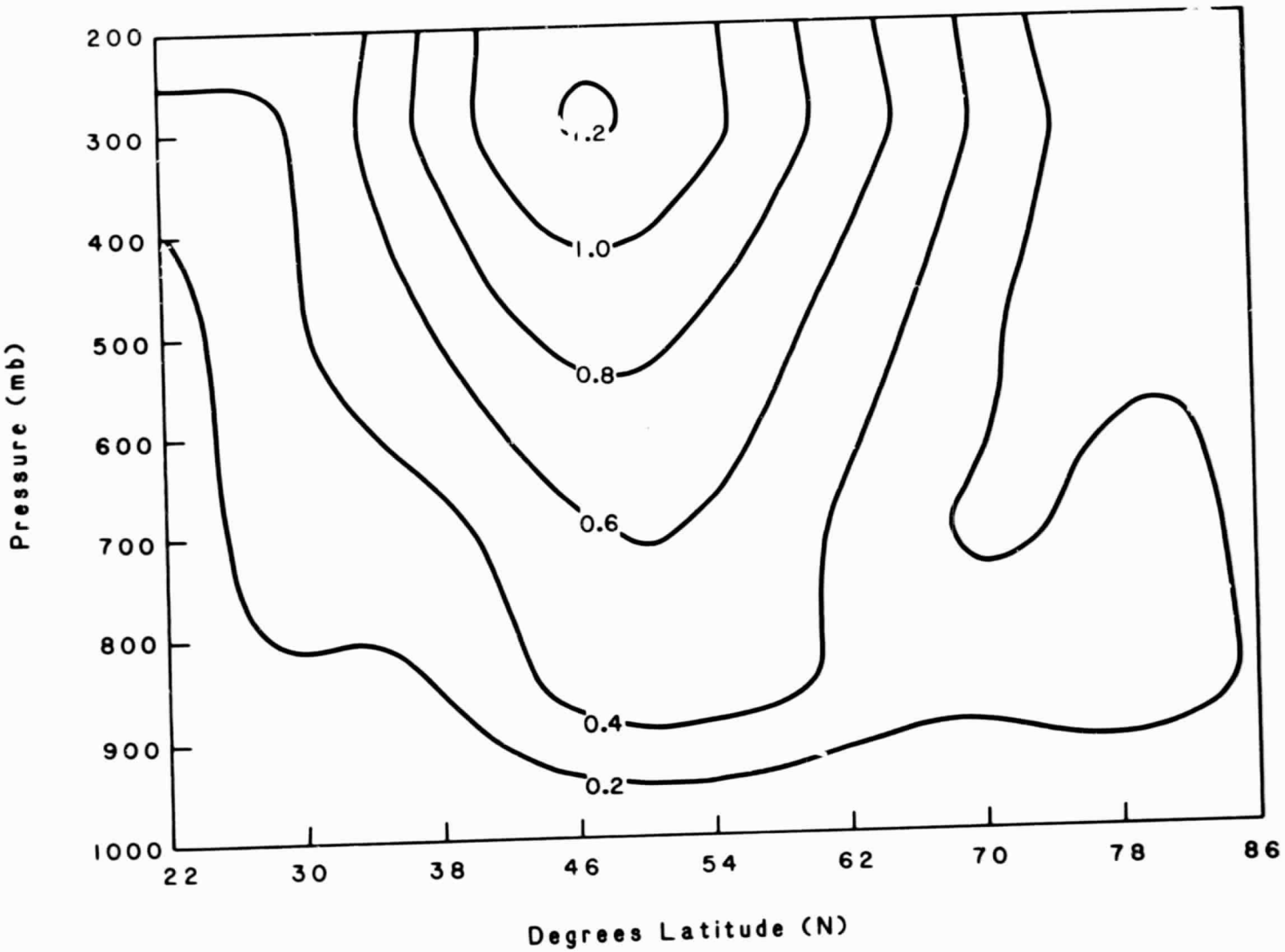

Figure 5.6a1 Observed winter amplitude of the geopotential height, stationary wavenumber 1, in the Northern Hemisphere, units of 10^2 m.

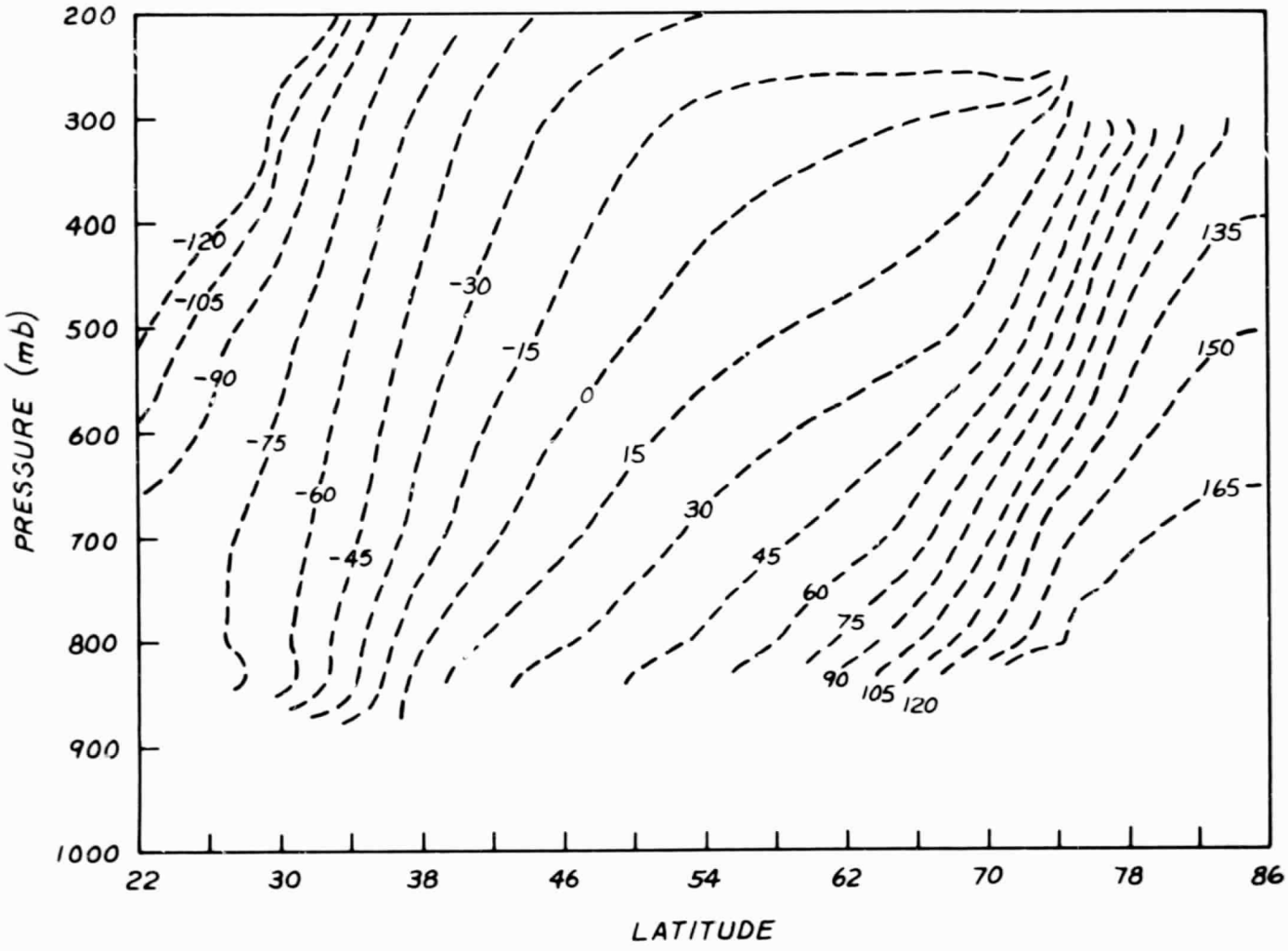

Figure 5.6a2 Observed winter phase of the geopotential height, stationary wavenumber 1, in the Northern Hemisphere, units of degrees. The phase is relative, so that the longitude of the ridge is the phase divided by the wavenumber.

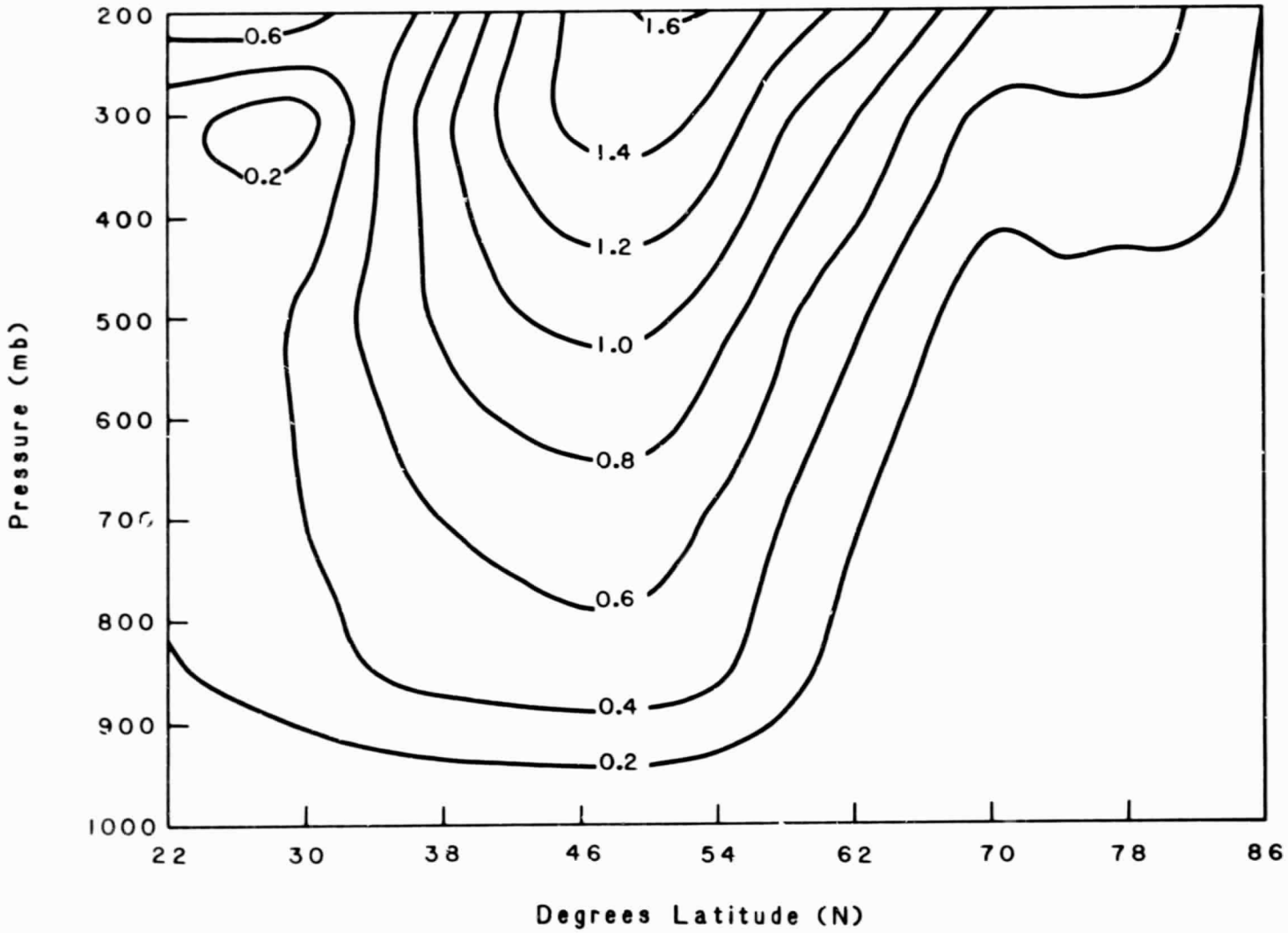

Figure 5.6b1 GCM winter amplitude of the geopotential height, stationary wave-number 1, in the Northern Hemisphere, units of 10^2 m.

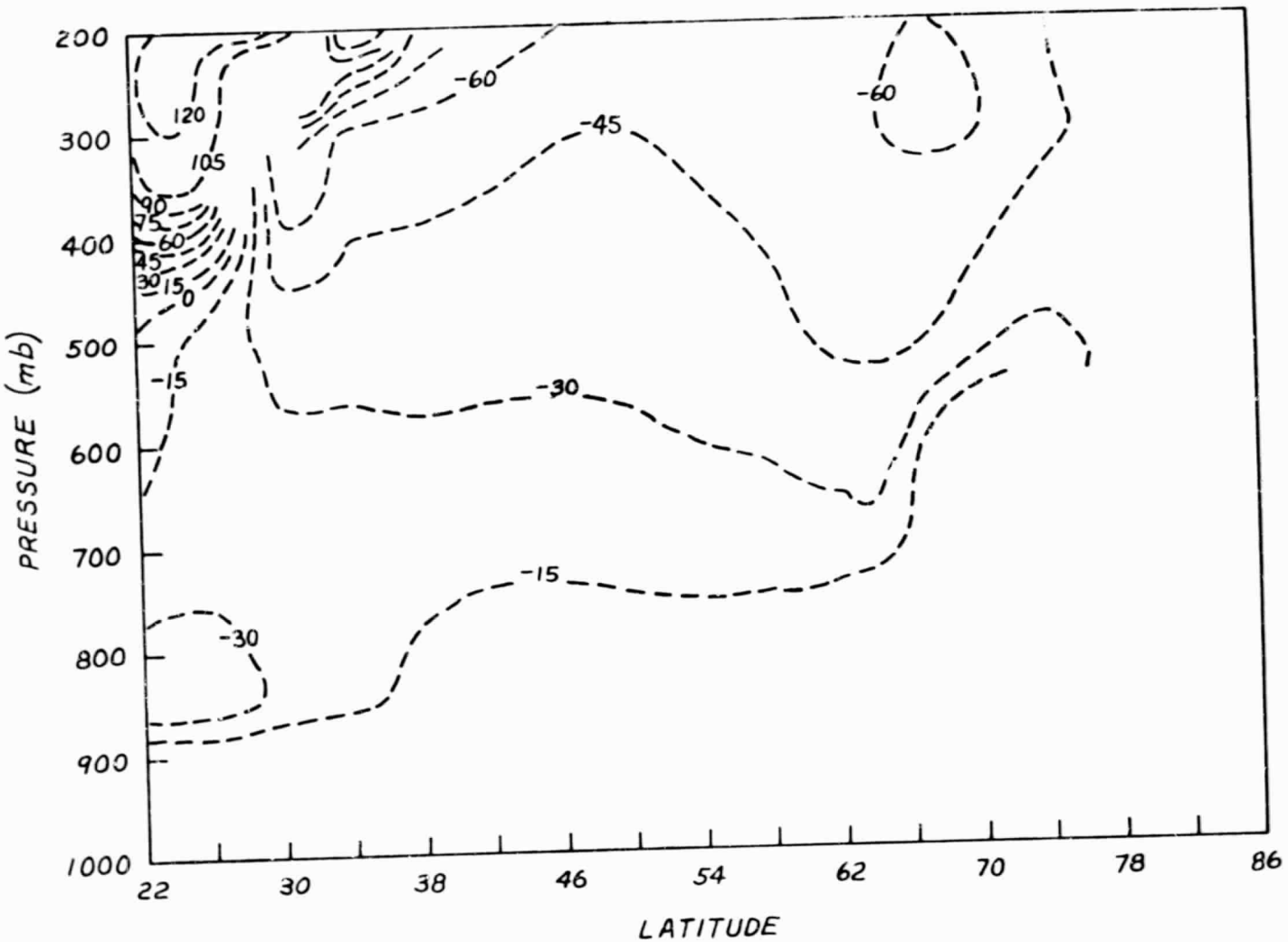

Figure 5.6b2 GCM winter phase of the geopotential height, stationary wavenumber 1, in the Northern Hemisphere, units of degrees. The phase is relative, so that the longitude of the ridge is the phase divided by the wavenumber.

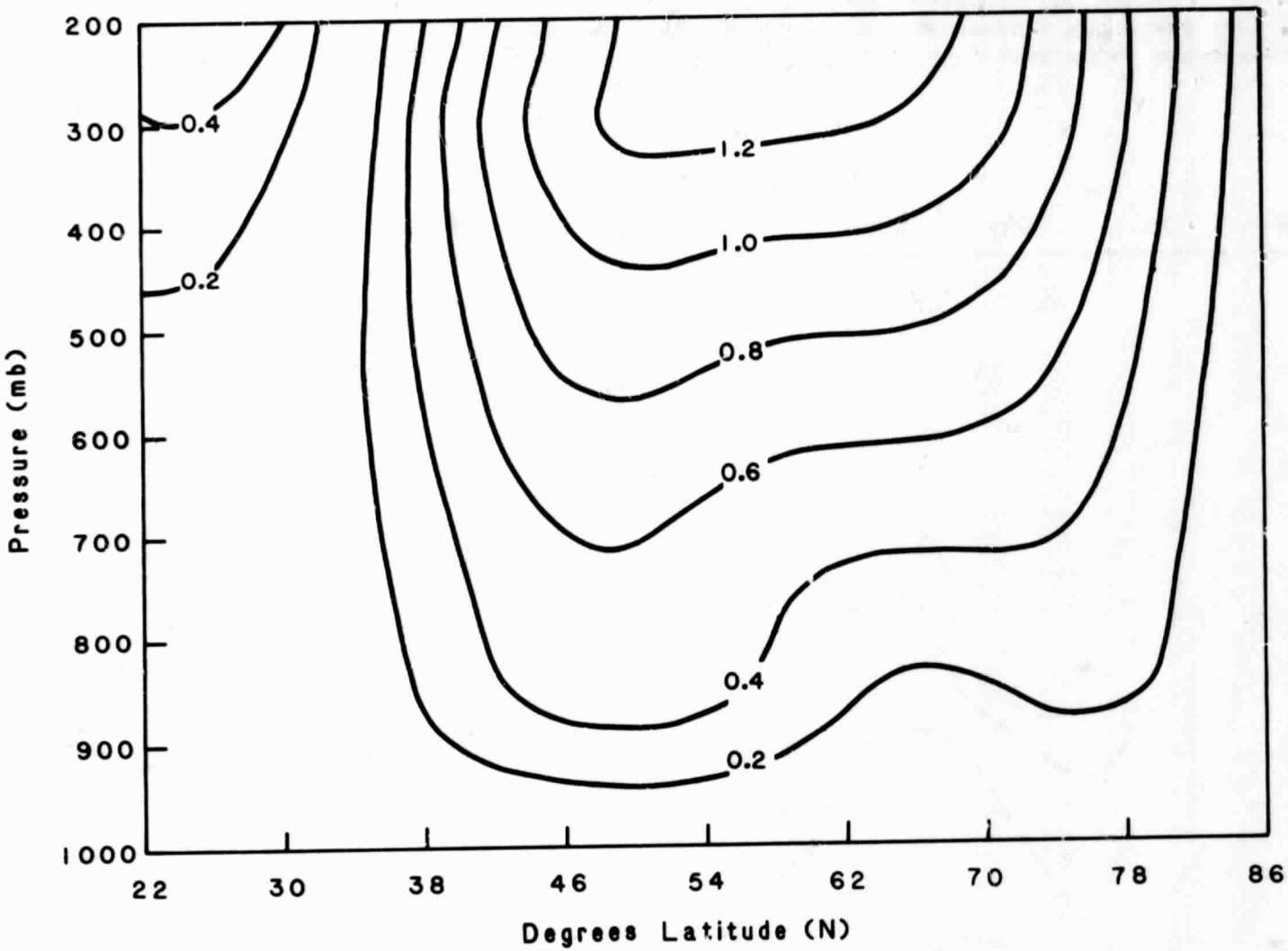

Figure 5.6c1 Observed winter amplitude of the geopotential height, stationary wavenumber 2, in the Northern Hemisphere, units of 10^2 m.

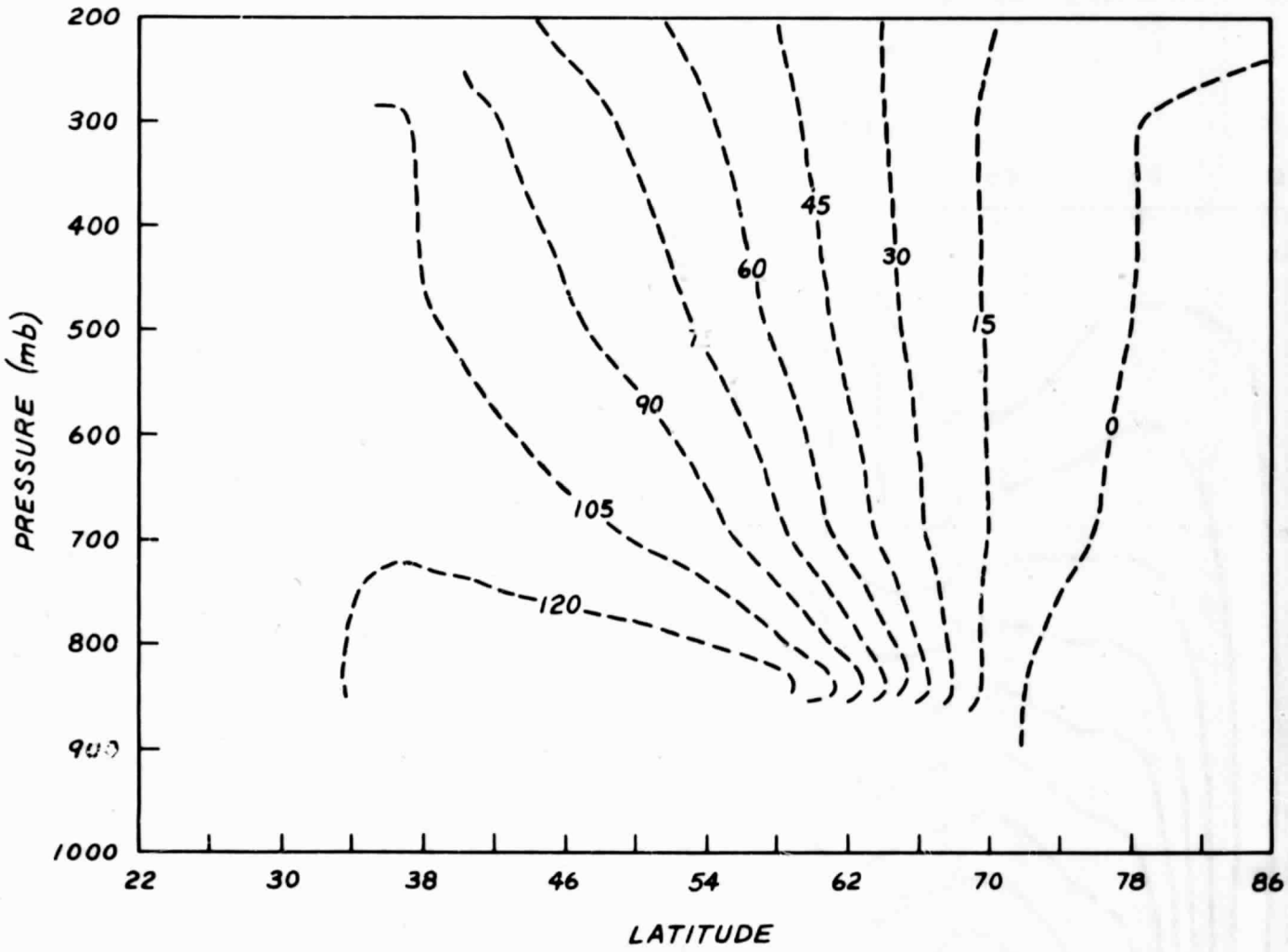

Figure 5.6c2 Observed winter phase of the geopotential height, stationary wavenumber 2, in the Northern Hemisphere, units of degrees. The phase is relative, so that the longitude of the ridge is the phase divided by the wavenumber.

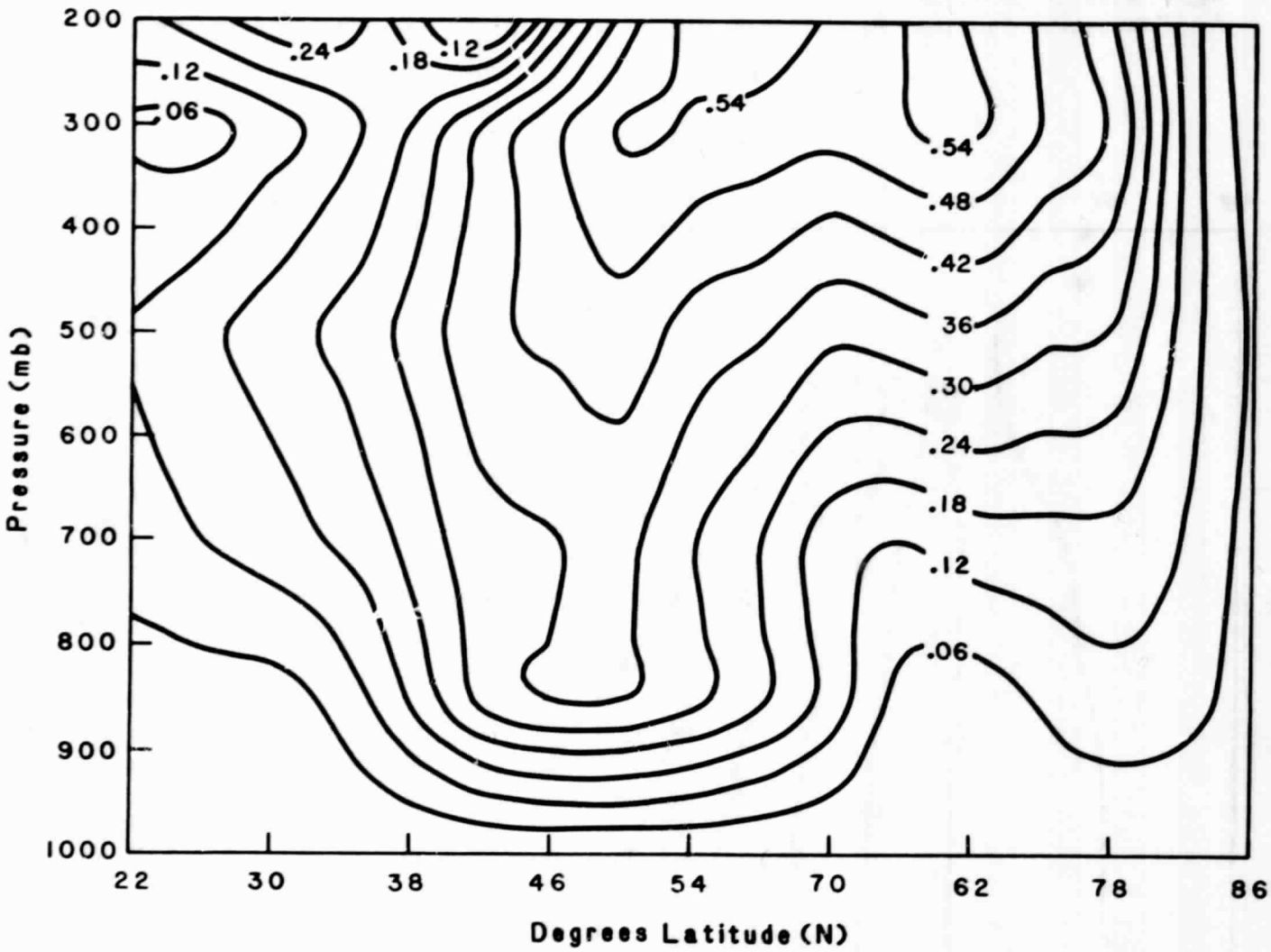

Figure 5.6d1 GCM winter amplitude of the geopotential height, stationary wavenumber 2, in the Northern Hemisphere, units of 10^2 m.

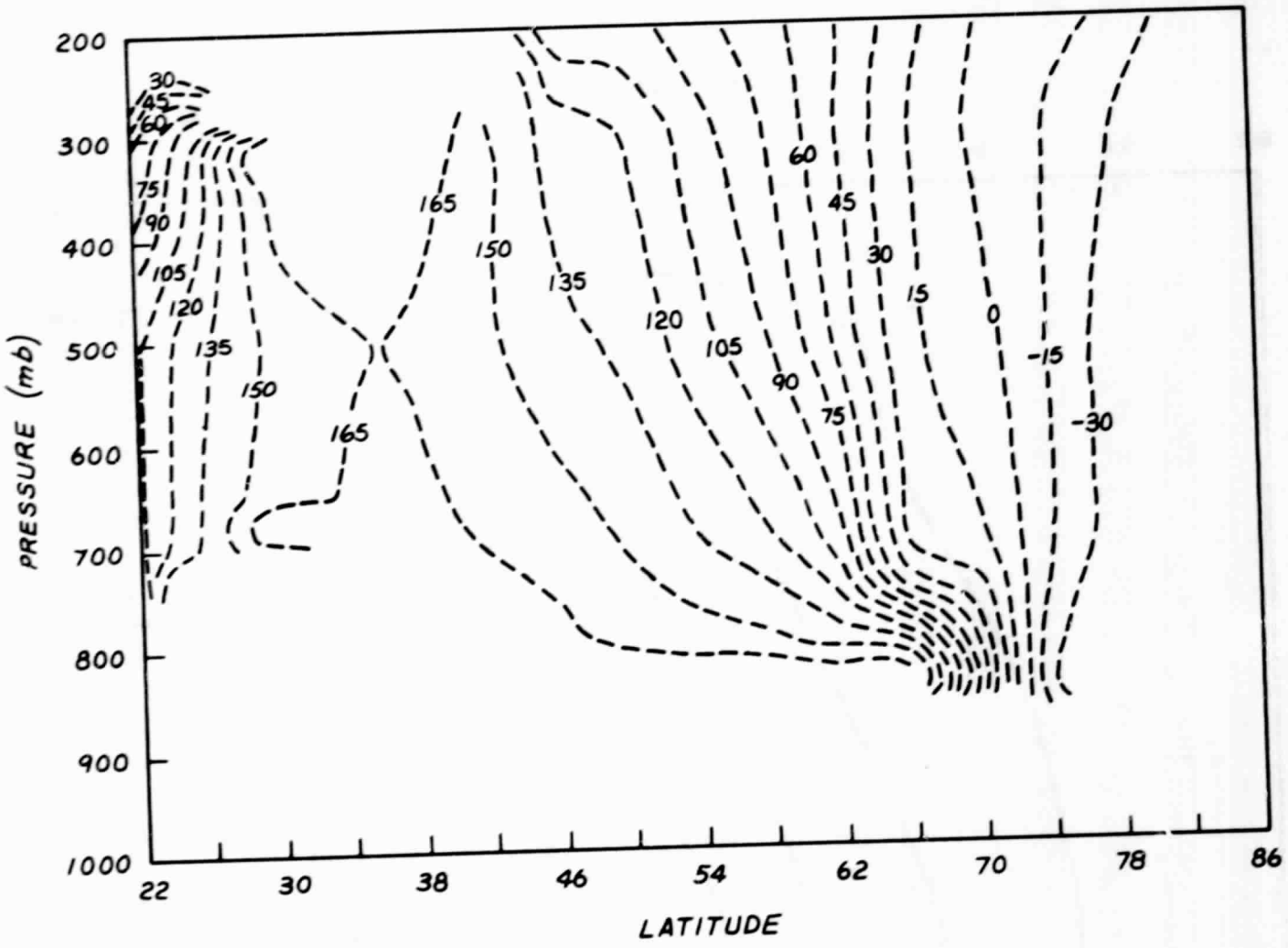

Figure 5.6d2 GCM winter phase of the geopotential height, stationary wavenumber 2, in the Northern Hemisphere, units of degrees. The phase is relative, so that the longitude of the ridge is the phase divided by the wavenumber.

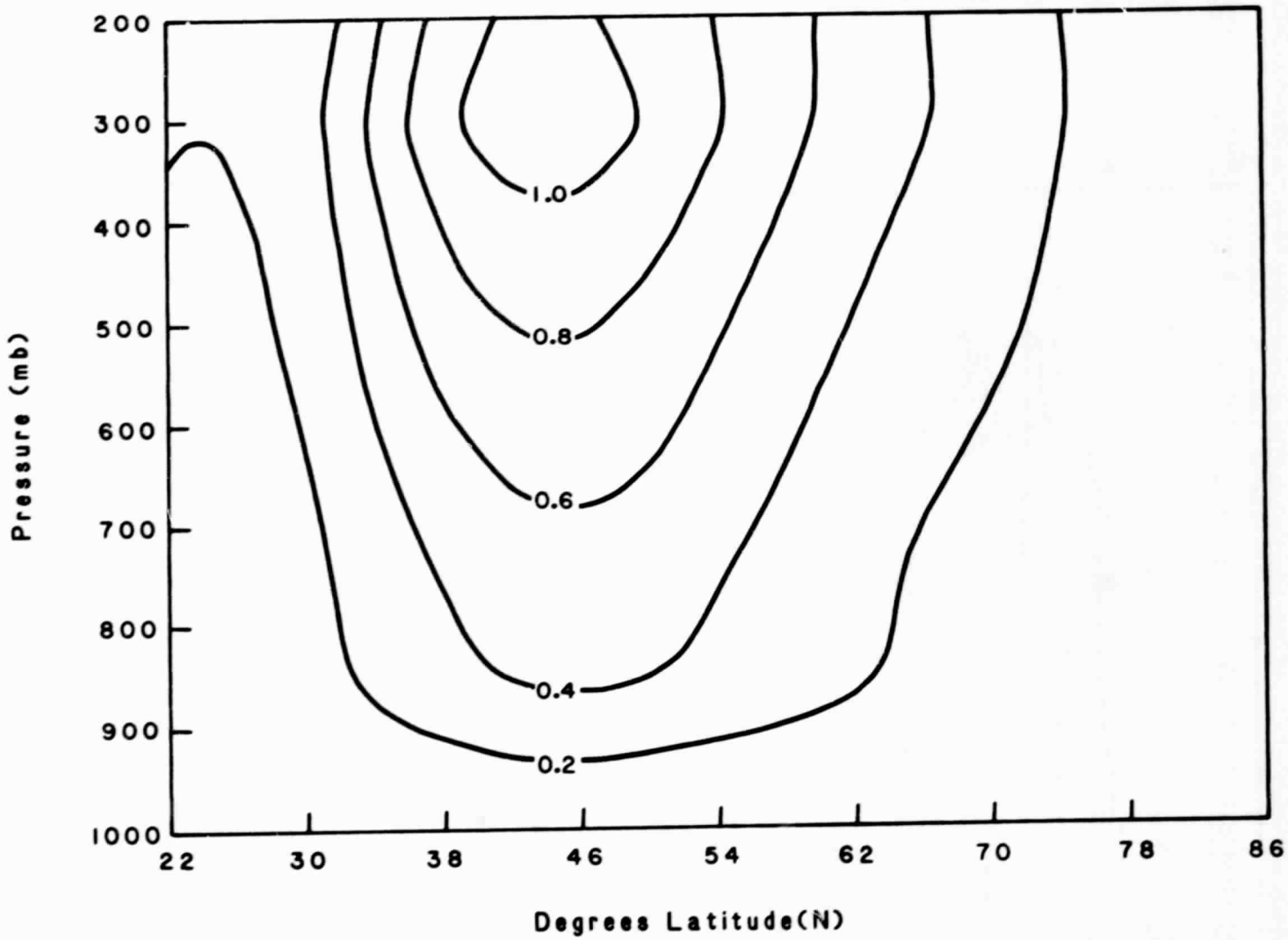

Figure 5.6e1 Observed winter amplitude of the geopotential height, stationary wavenumber 3, in the Northern Hemisphere, units of 10^2 m.

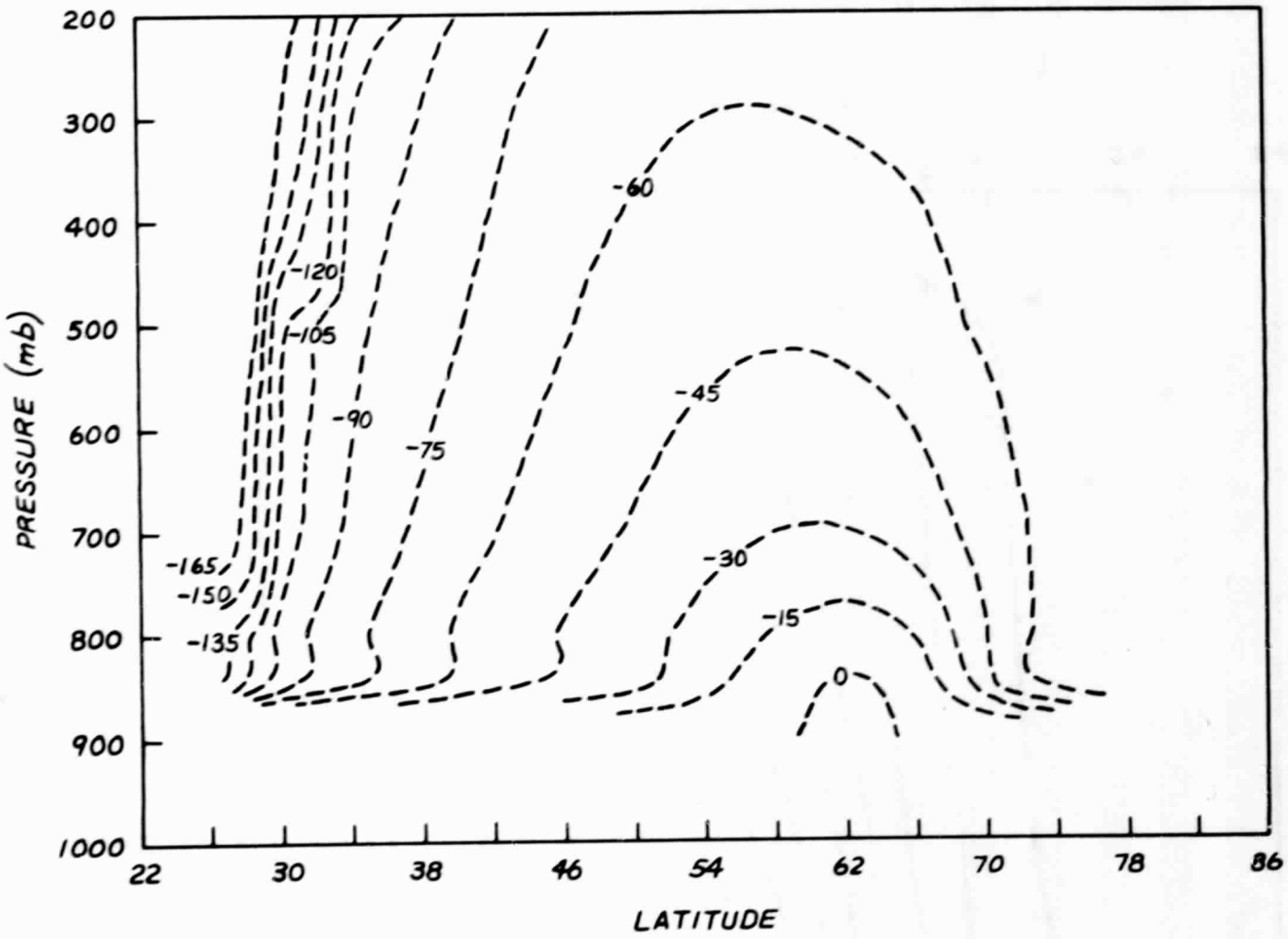

Figure 5.6e2 Observed winter phase of the geopotential height, stationary wavenumber 3, in the Northern Hemisphere, units of degrees. The phase is relative, so that the longitude of the ridge is the phase divided by the wavenumber.

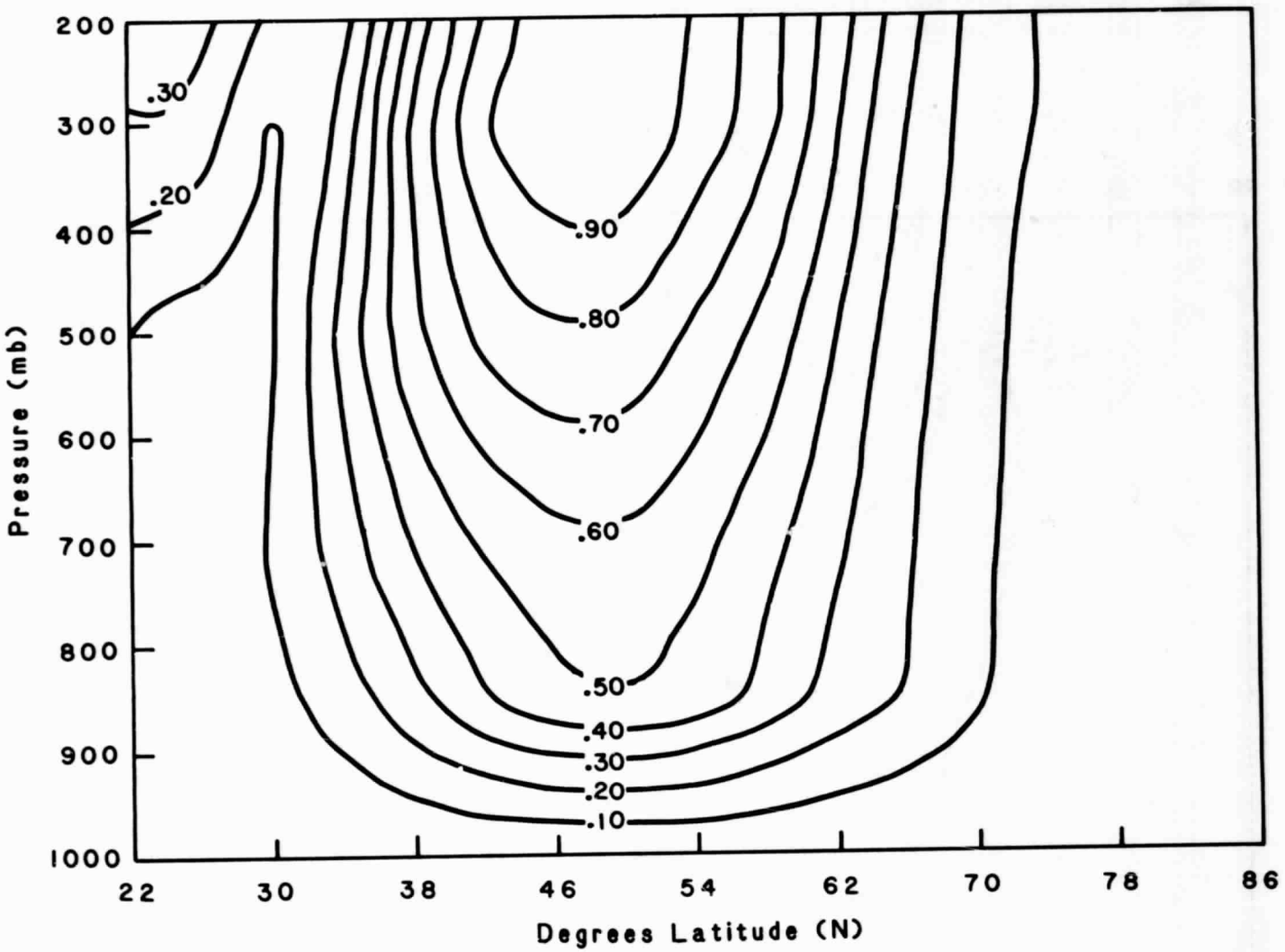

Figure 5.6f1 GCM winter amplitude of the geopotential height, stationary wavenumber 3, in the Northern Hemisphere, units of 10^2 m.

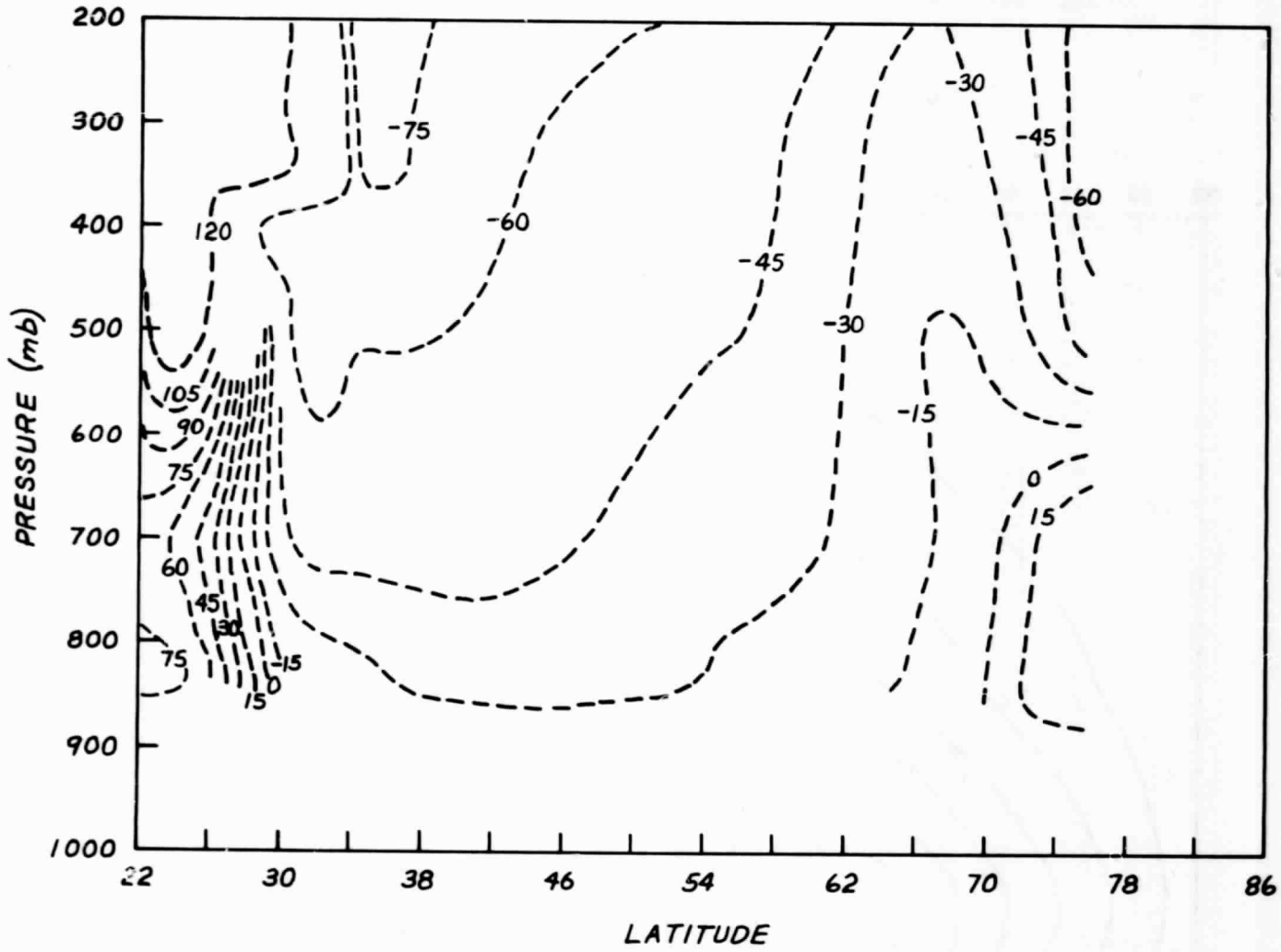

Figure 5.6f2 GCM winter phase of the geopotential height, stationary wavenumber 3, in the Northern Hemisphere, units of degrees. The phase is relative, so that the longitude of the ridge is the phase divided by the wavenumber.

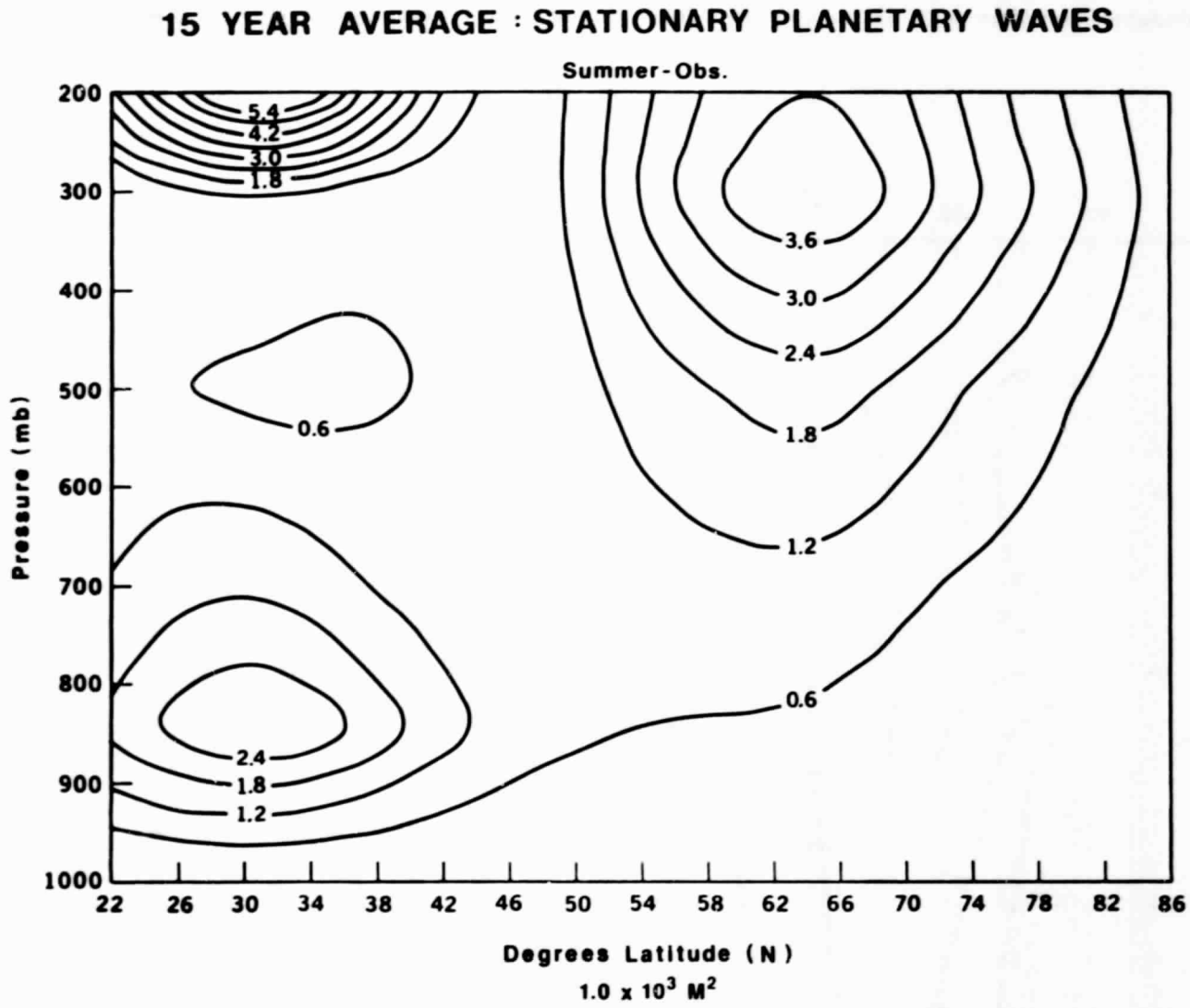

Figure 5.7a Observed summer stationary planetary wave variance of the geopotential height in the Northern Hemisphere. Units of 10^3 m^2.

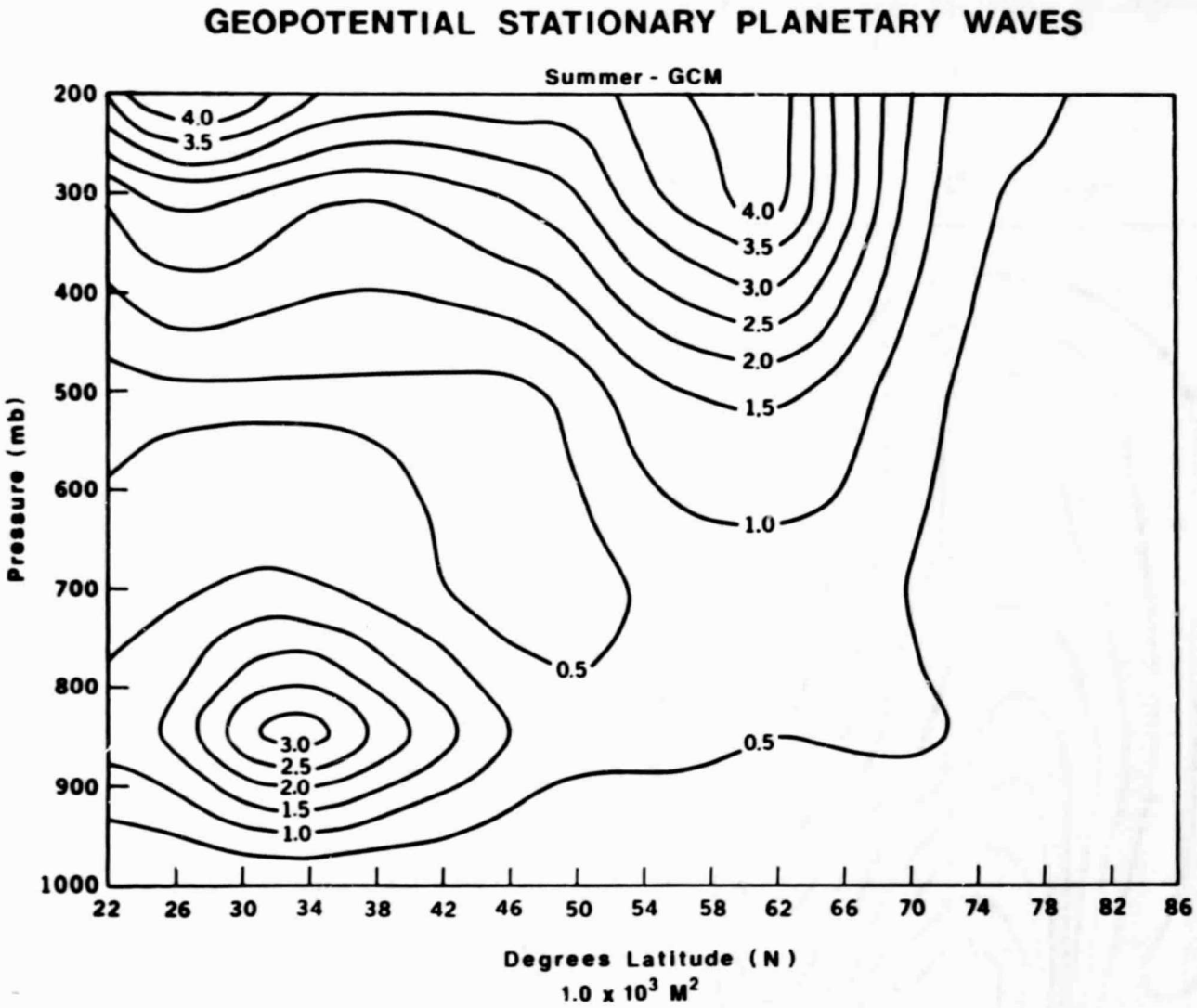

Figure 5.7b1 GCM summer stationary planetary wave variance of the geopotential height in the Northern Hemisphere. Units of 10^3 m^2.

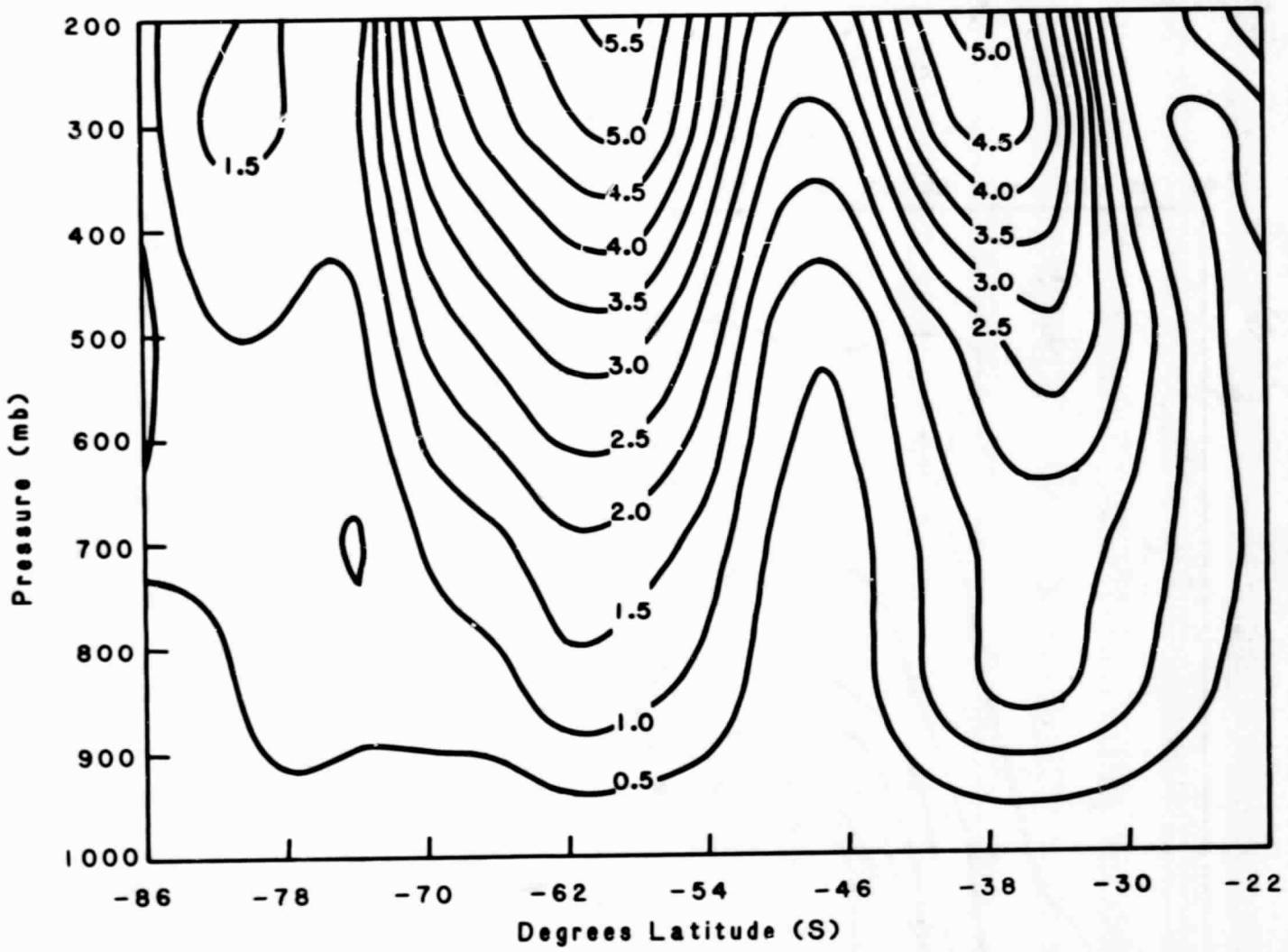

Figure 5.7b2 GCM summer stationary planetary wave variance of the geopotential height in the Southern Hemisphere. Units of 10^3 m^2.

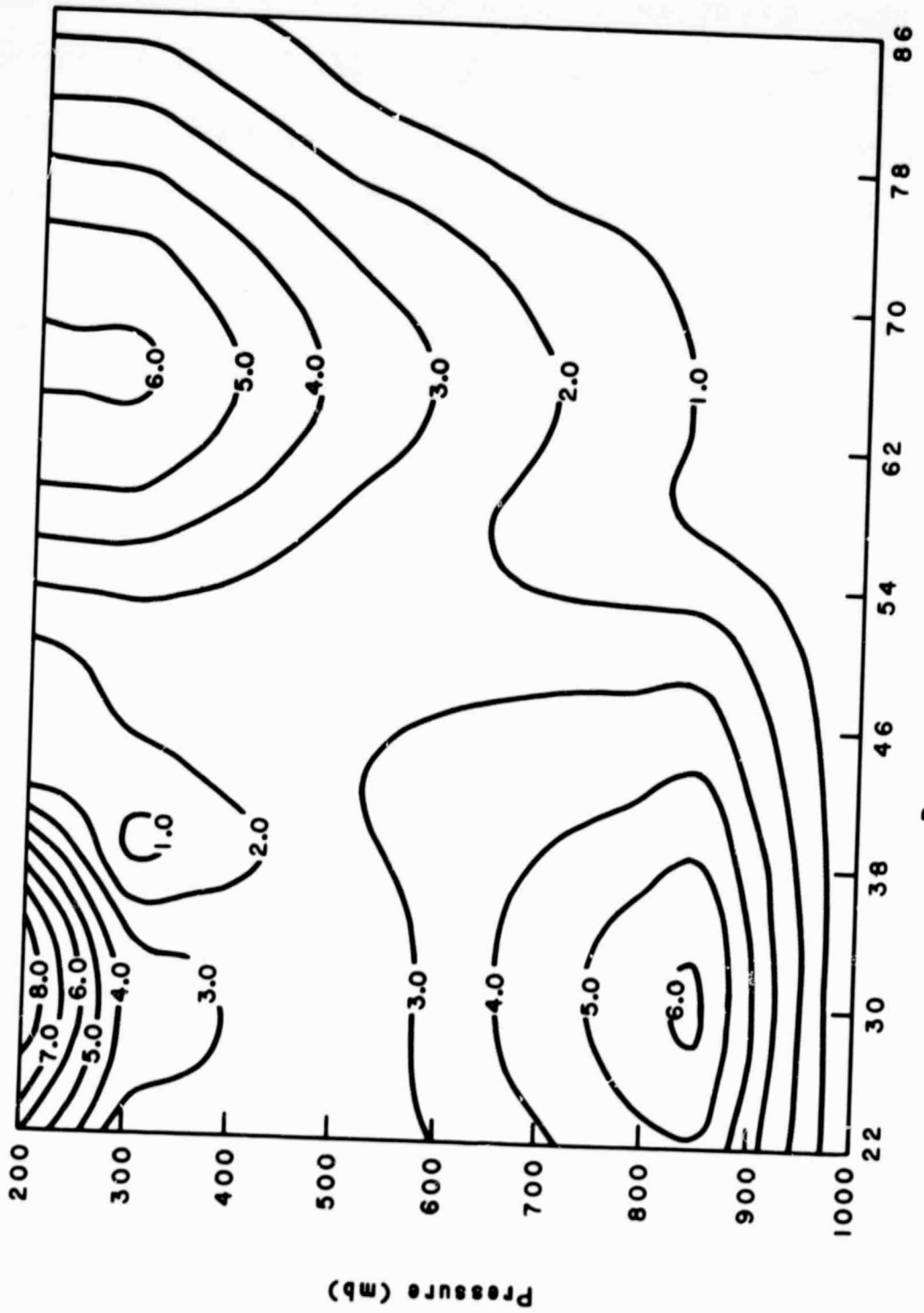

Figure 5.8a1 Observed summer amplitude of the geopotential height, stationary wavenumber 1, in the Northern Hemisphere. Units of 10 m.

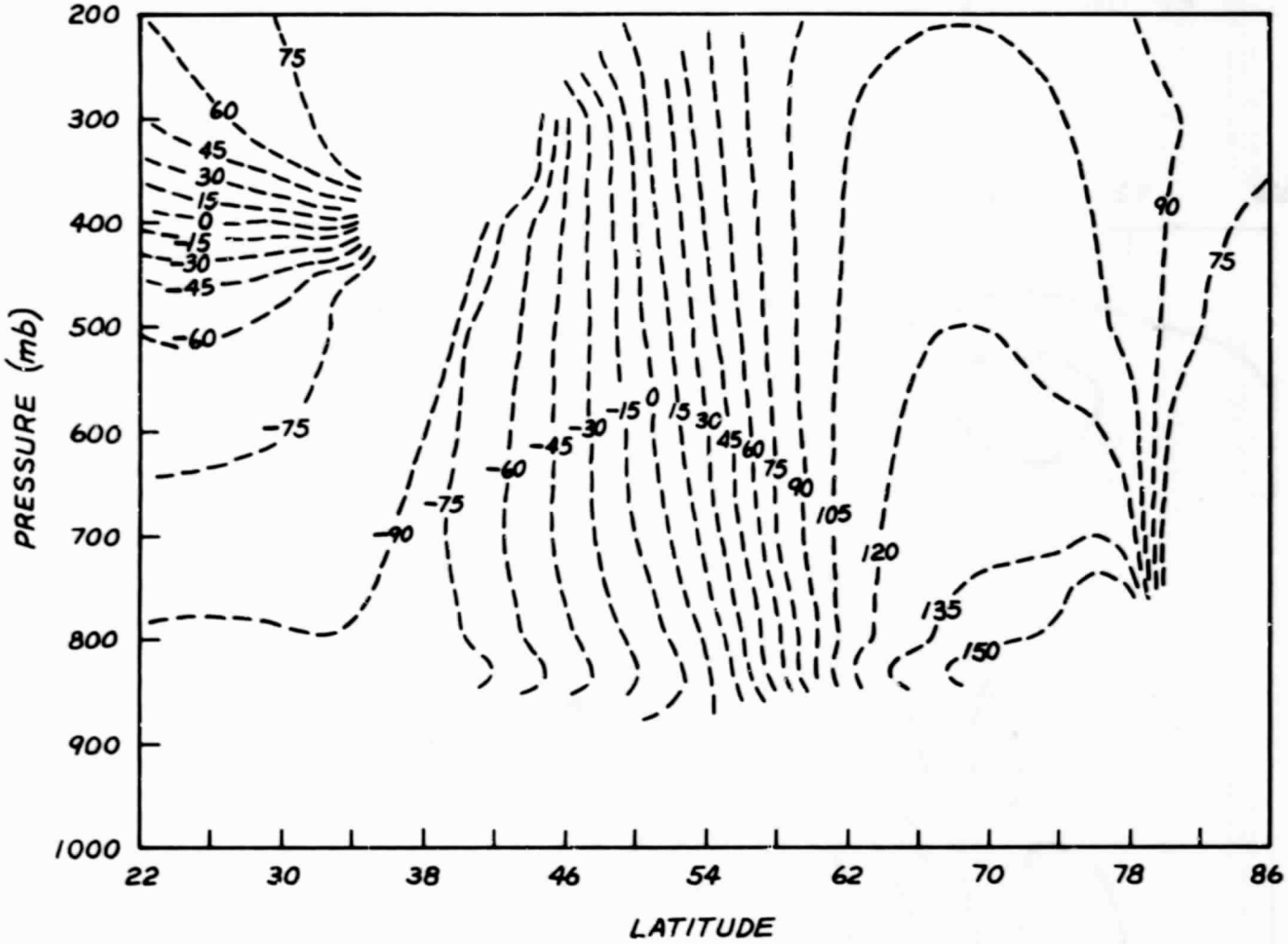

Figure 5.8a2 Observed summer phase of the geopotential height, stationary wavenumber 1, in the Northern Hemisphere, units of degrees. The phase is relative, so that the longitude of the ridge is the phase divided by the wavenumber.

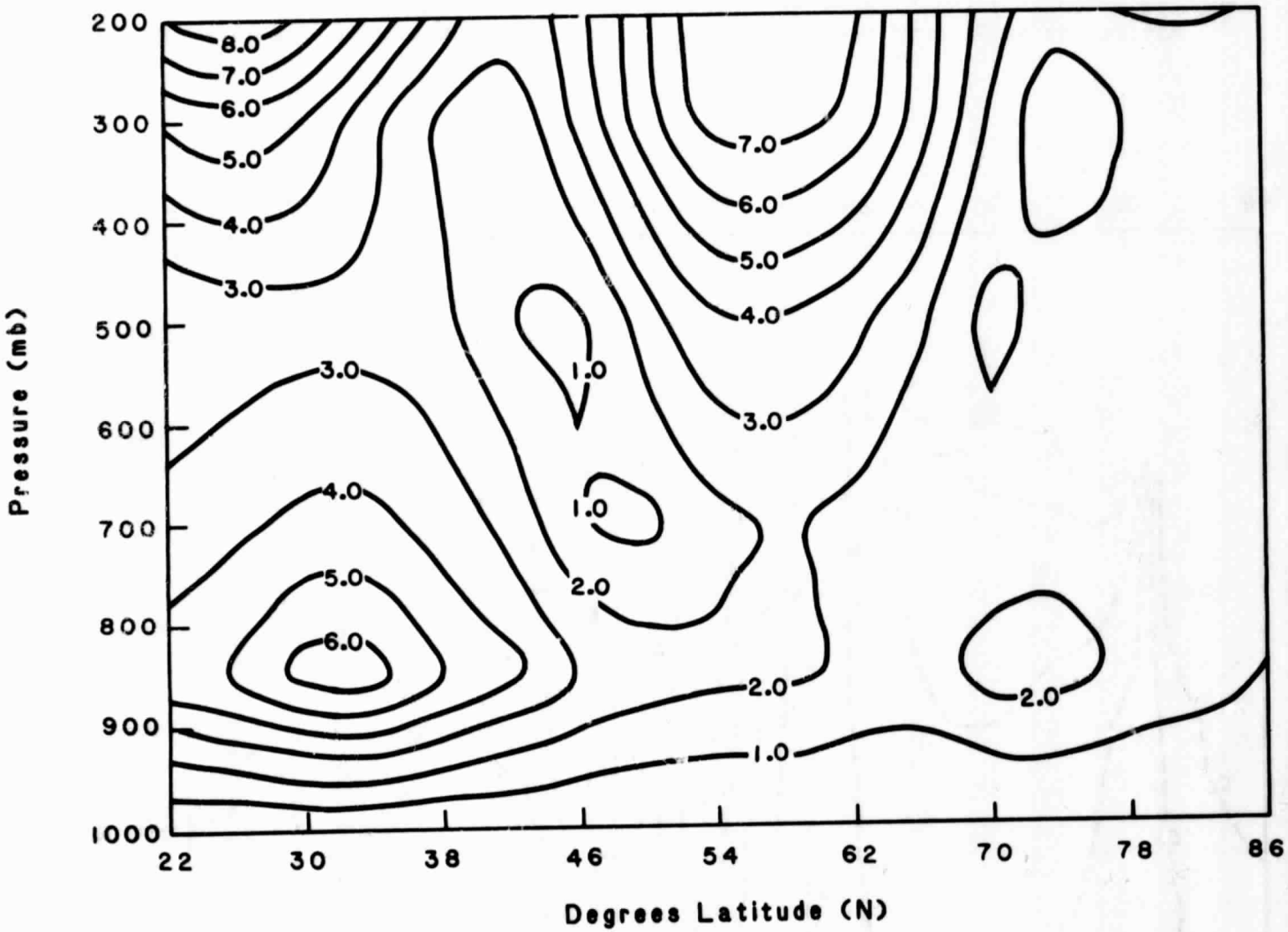

Figure 5.8b1 GCM summer amplitude of the geopotential height, stationary wavenumber 1, in the Northern Hemisphere, units of 10 m.

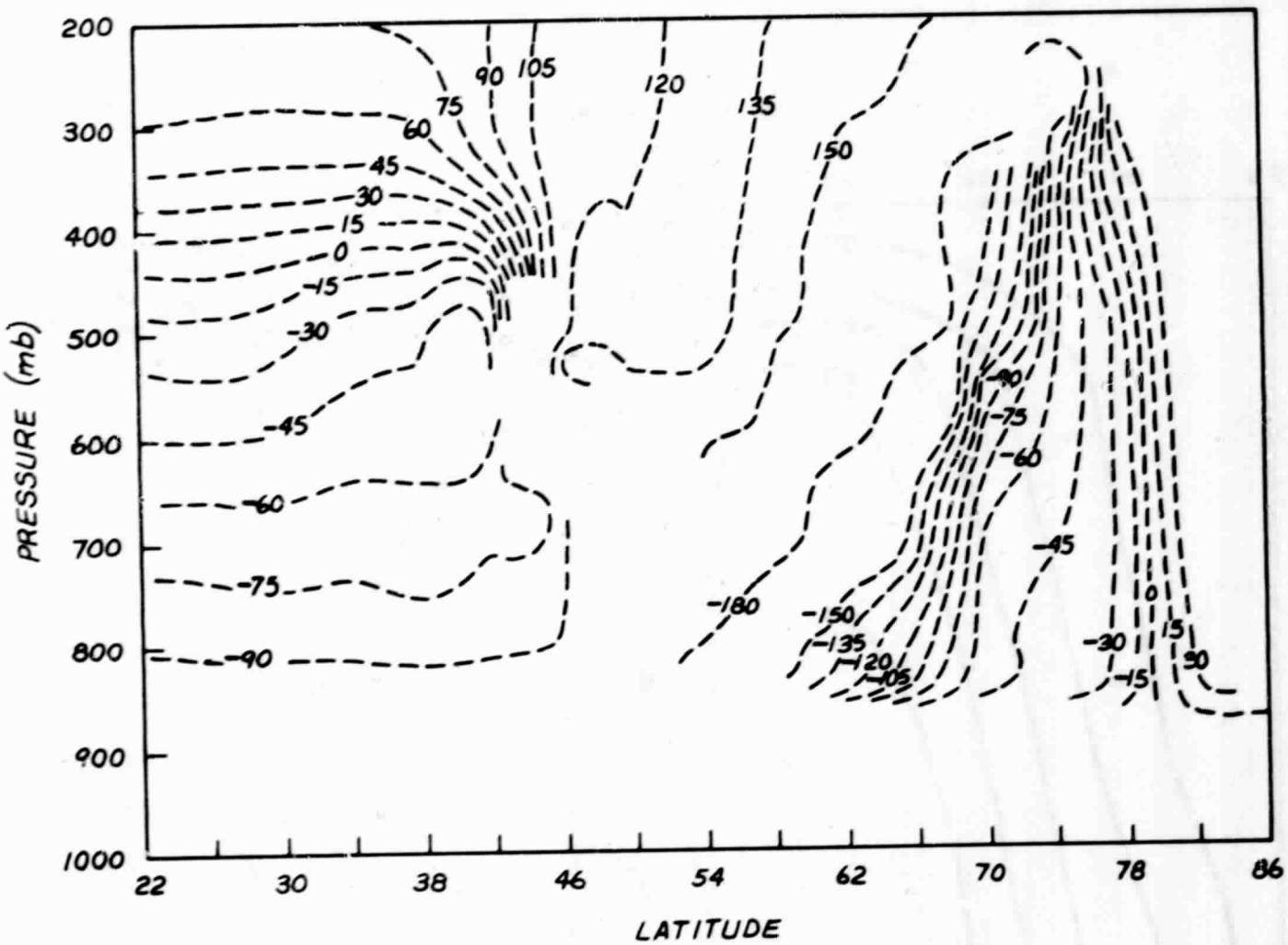

Figure 5.8b2 GCM summer phase of the geopotential height, stationary wavenumber 1, in the Northern Hemisphere, units of 10 m. The phase is relative, so that the longitude of the ridge is the phase divided by the wavenumber.

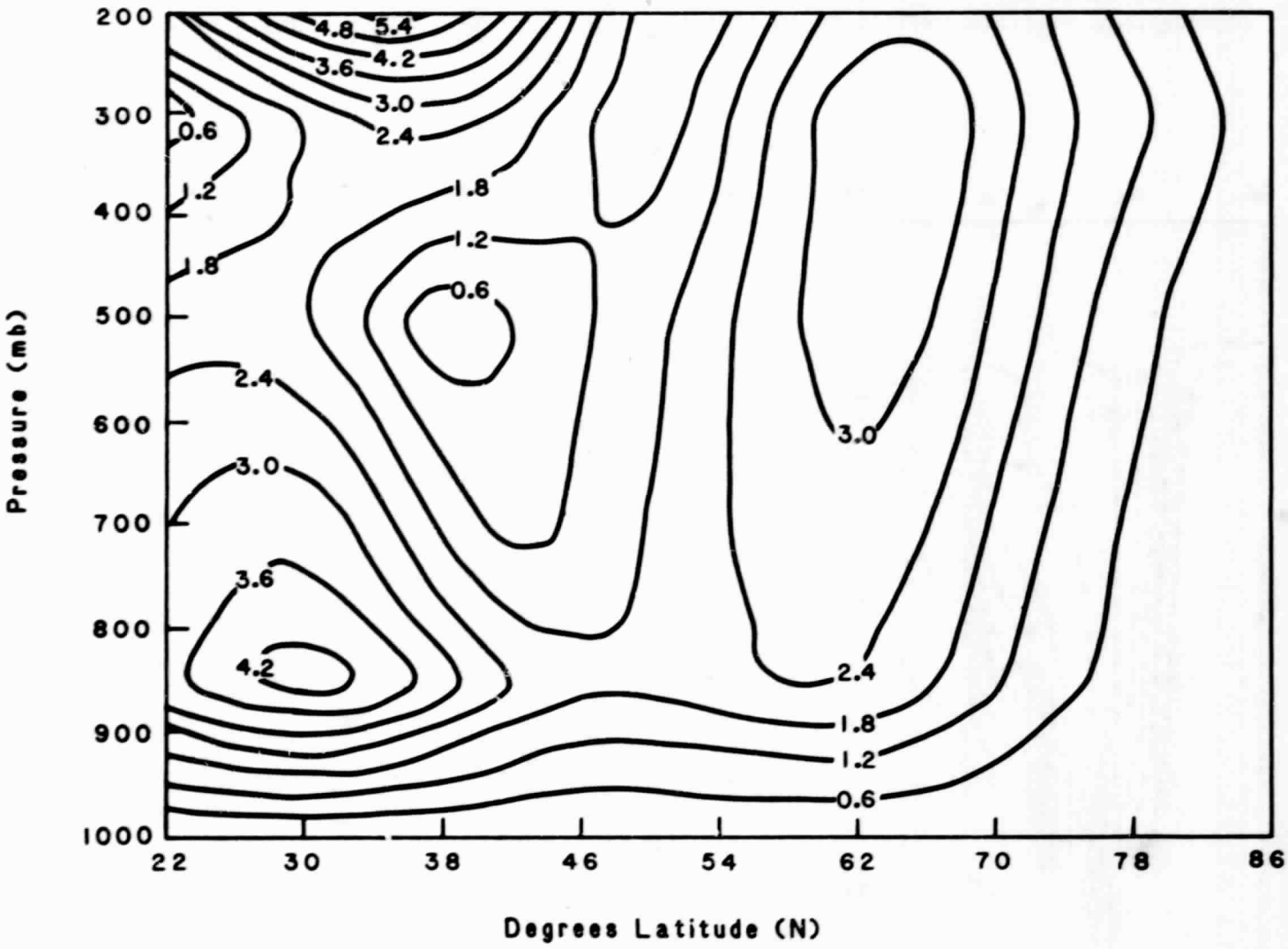

Figure 5.8c1 Observed summer amplitude of the geopotential height, stationary wavenumber 2, in the Northern Hemisphere, units of 10 m.

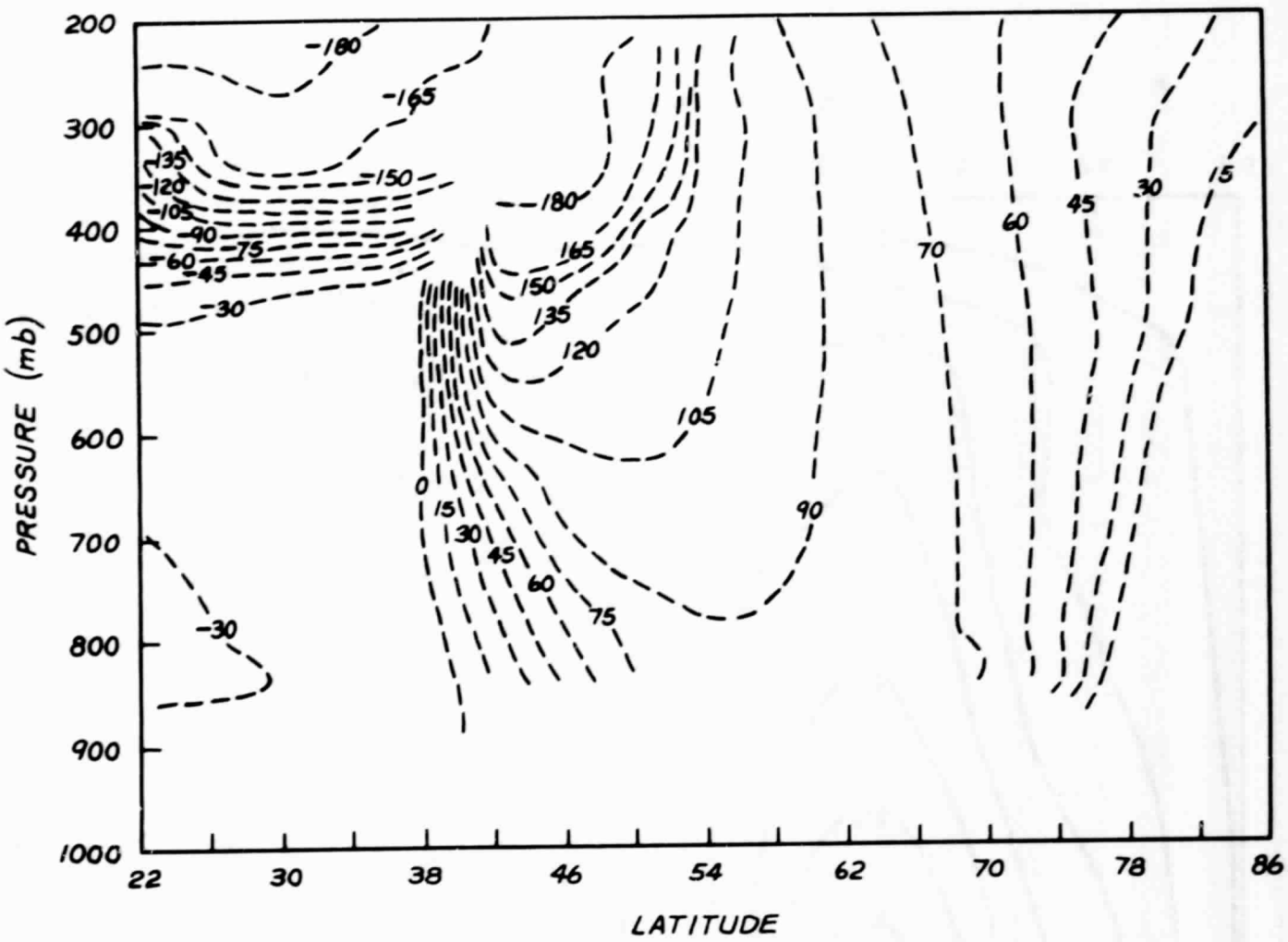

Figure 5.8c2 Observed summer phase of the geopotential height, stationary wavenumber 2, in the Northern Hemisphere, units of degrees. The phase is relative, so that the longitude of the ridge is the phase divided by the wavenumber.

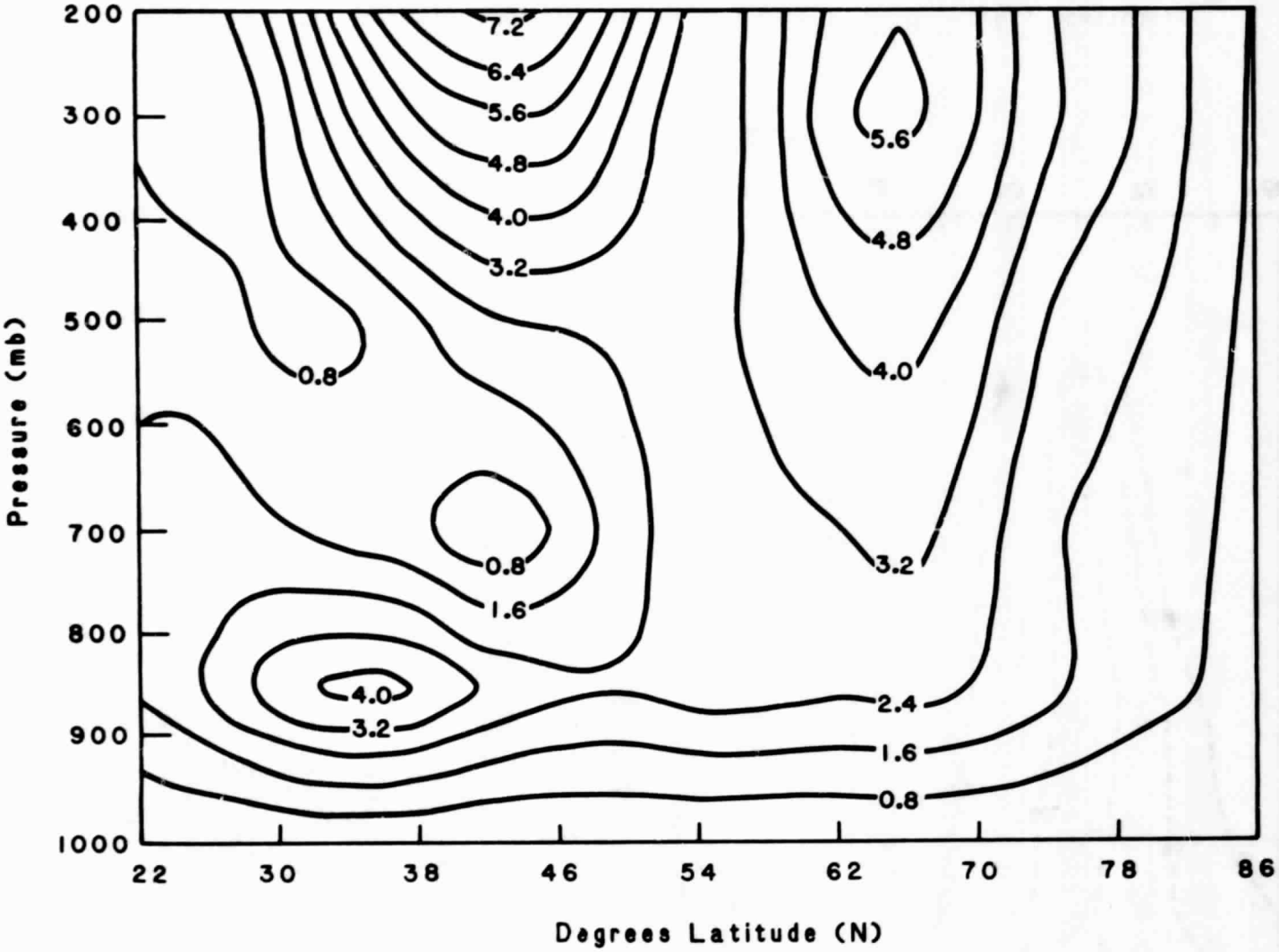

Figure 5.8d1 GCM summer amplitude of the geopotential height, stationary wavenumber 2, in the Northern Hemisphere, units of 10 m.

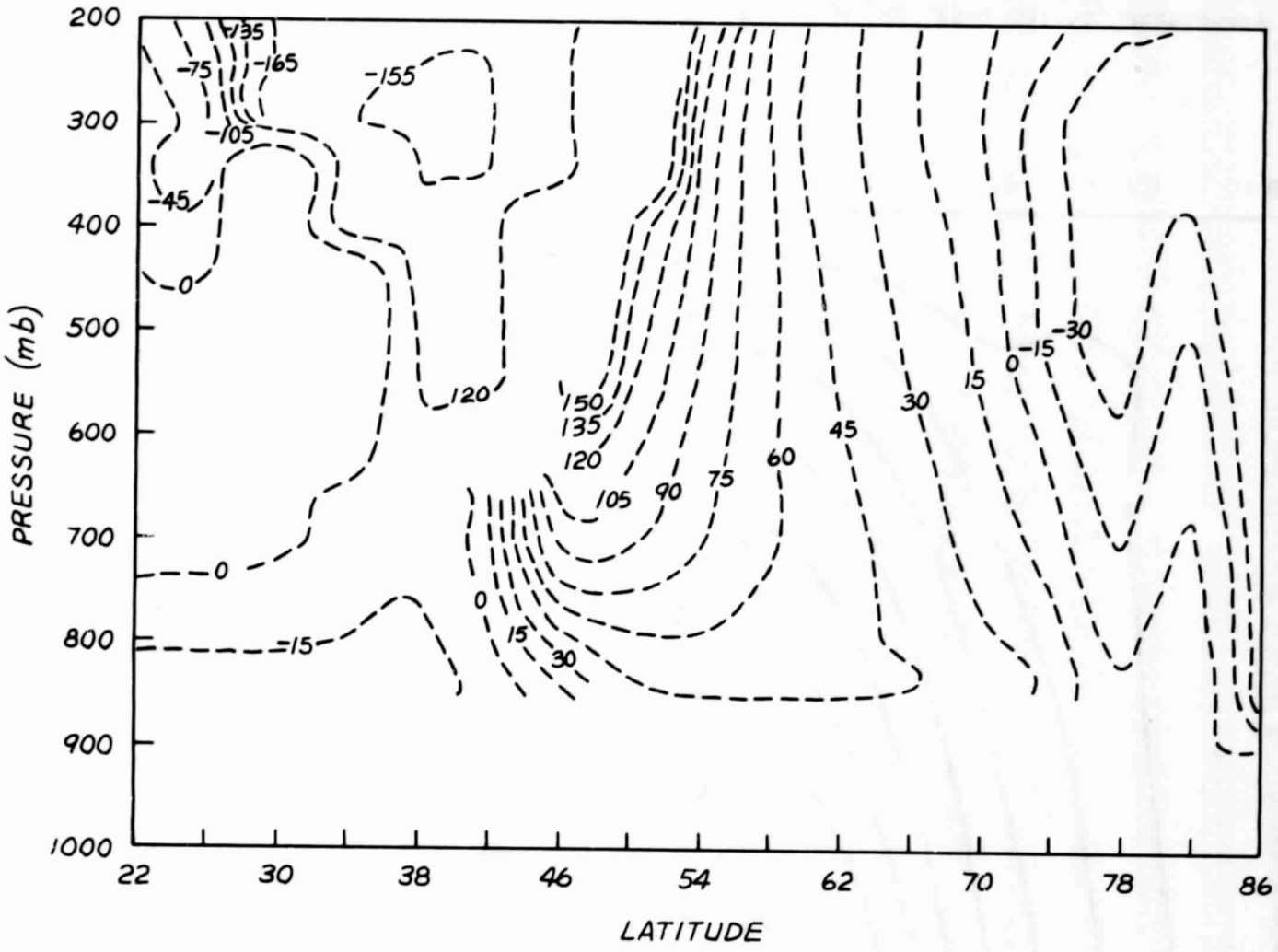

Figure 5.8d2 GCM summer phase of the geoptential height, stationary wavenumber 2, in the Northern Hemisphere, units of degrees. The phase is relative, so that the longitude of the ridge is the phase divided by the wavenumber.

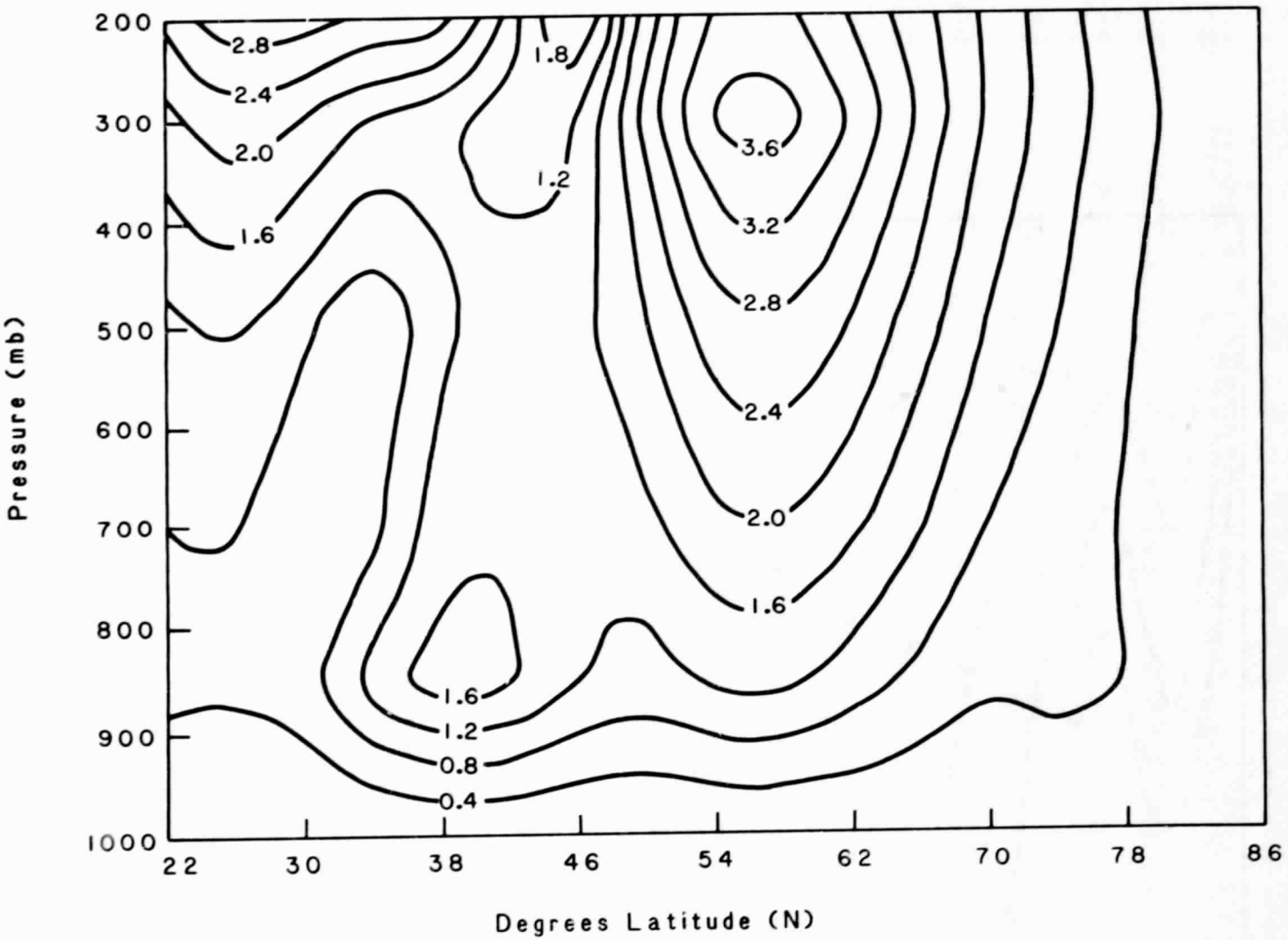

Figure 5.8e1 Observed summer amplitude of the geopotential height, stationary wavenumber 3, in the Northern Hemisphere, units of 10 m.

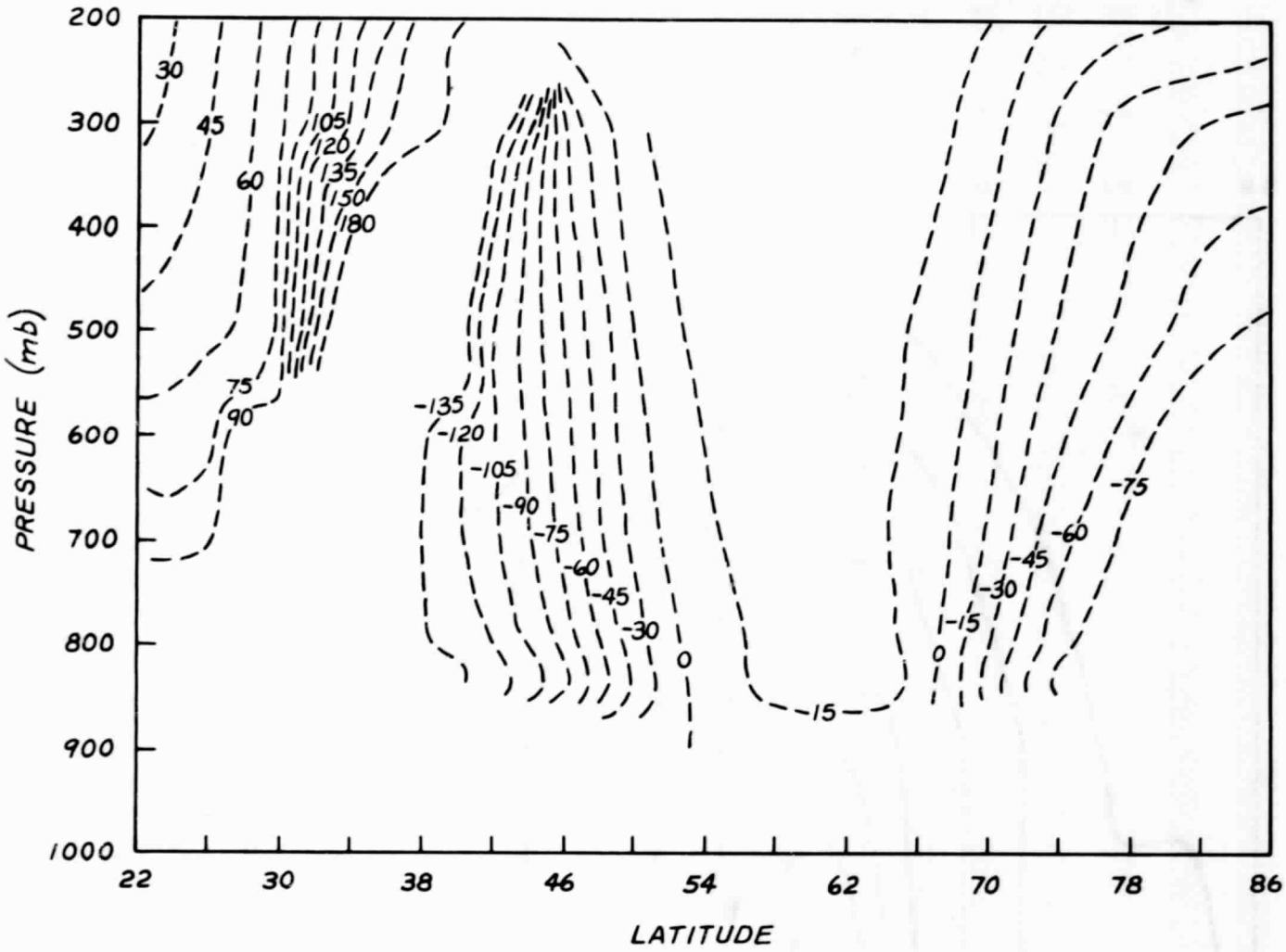

Figure 5.8e2 Observed summer phase of the geopotential height, stationary wavenumber 3, in the Northern Hemisphere, units of degrees. The phase is relative, so that the longitude of the ridge is the phase divided by the wavenumber.

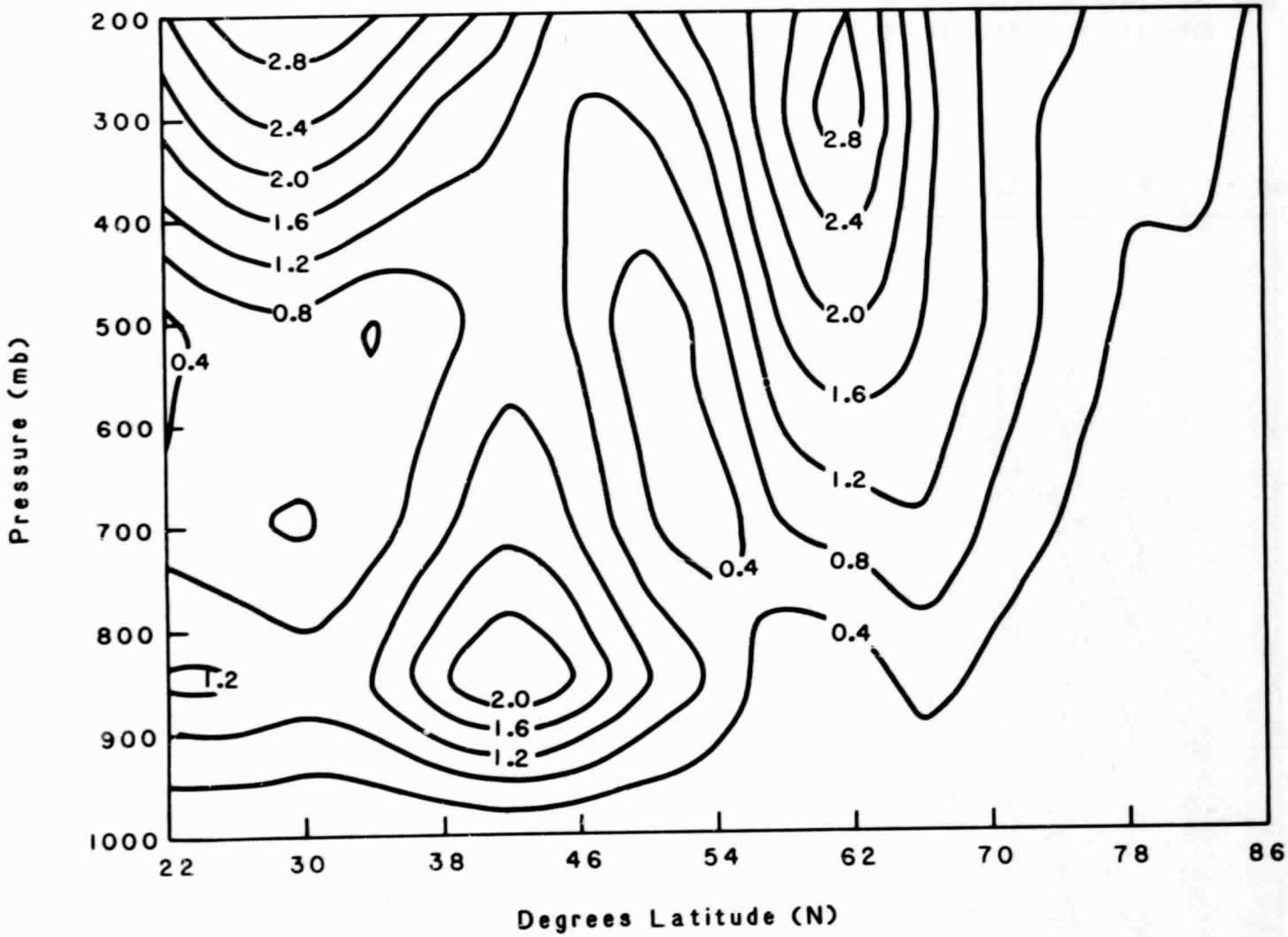

Figure 5.8f1 GCM summer amplitude of the geopotential height, stationary wavenumber 3, in the Northern Hemisphere, units of 10 m.

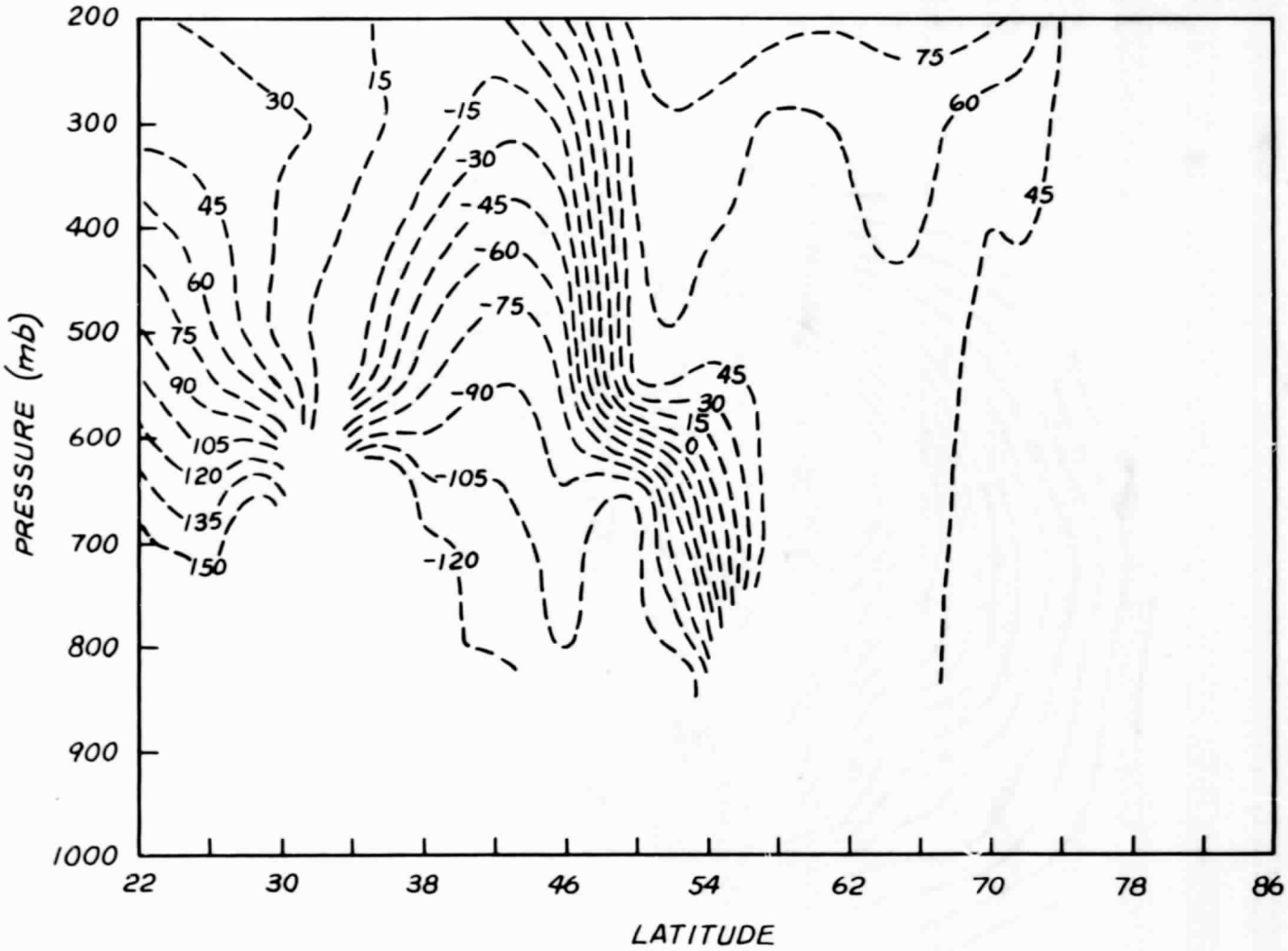

Figure 5.8f2 GCM summer phase of the geopotential height, stationary wavenumber 3, in the Northern Hemisphere, units of degrees. The phase is relative, so that the longitude of the ridge is the phase divided by the wavenumber.

Figure 5.9a Observed RMS deviation of the winter 500 mb geopotential height field (Northern Hemisphere), units of m. Contour interval is 10m.

Figure 5.9b GCM RMS deviation of the winter 500 mb geopotential height field (Northern Hemisphere), units of m. Contour interval is 10 m.

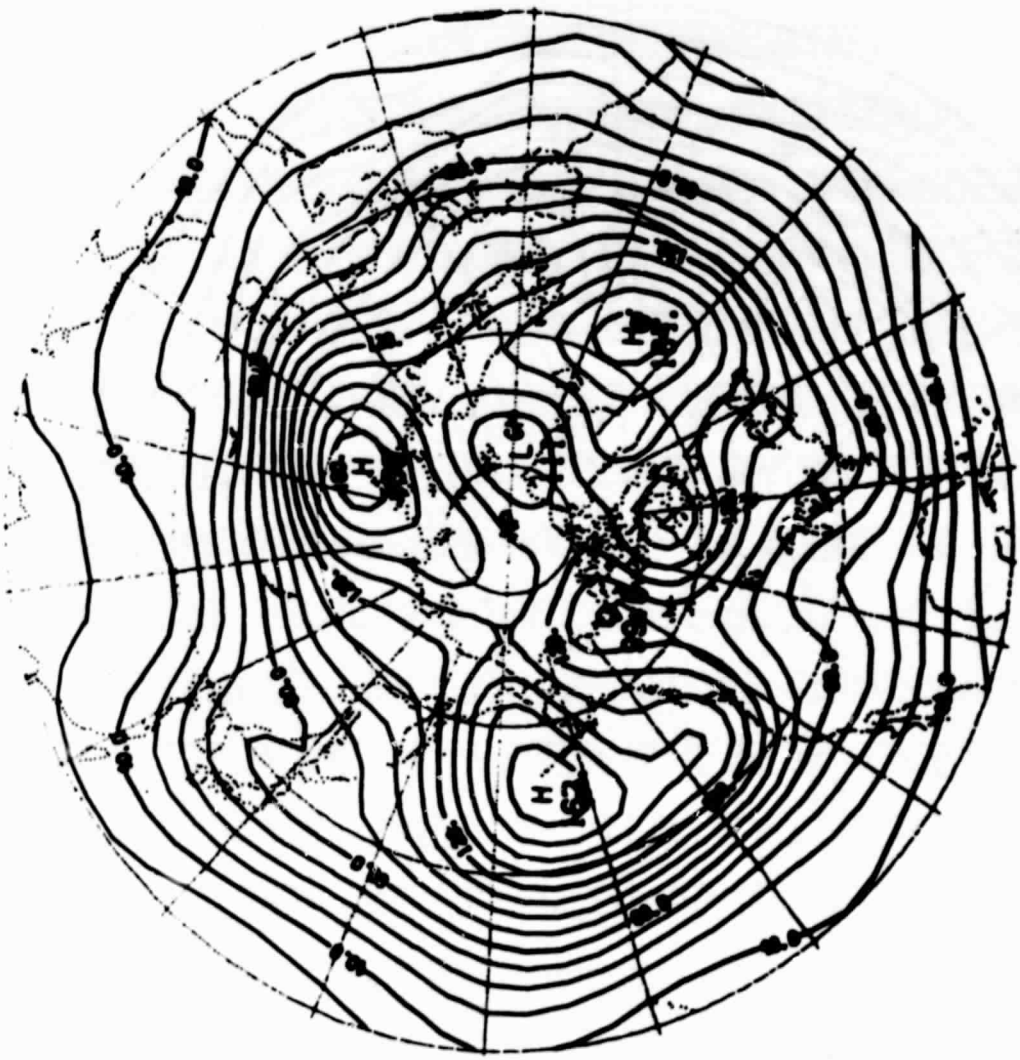

Figure 5.10a Observed RMS deviation of the winter 500 mb low-pass geopotential height field (Northern Hemisphere), units of m. Contour interval is 10 m.

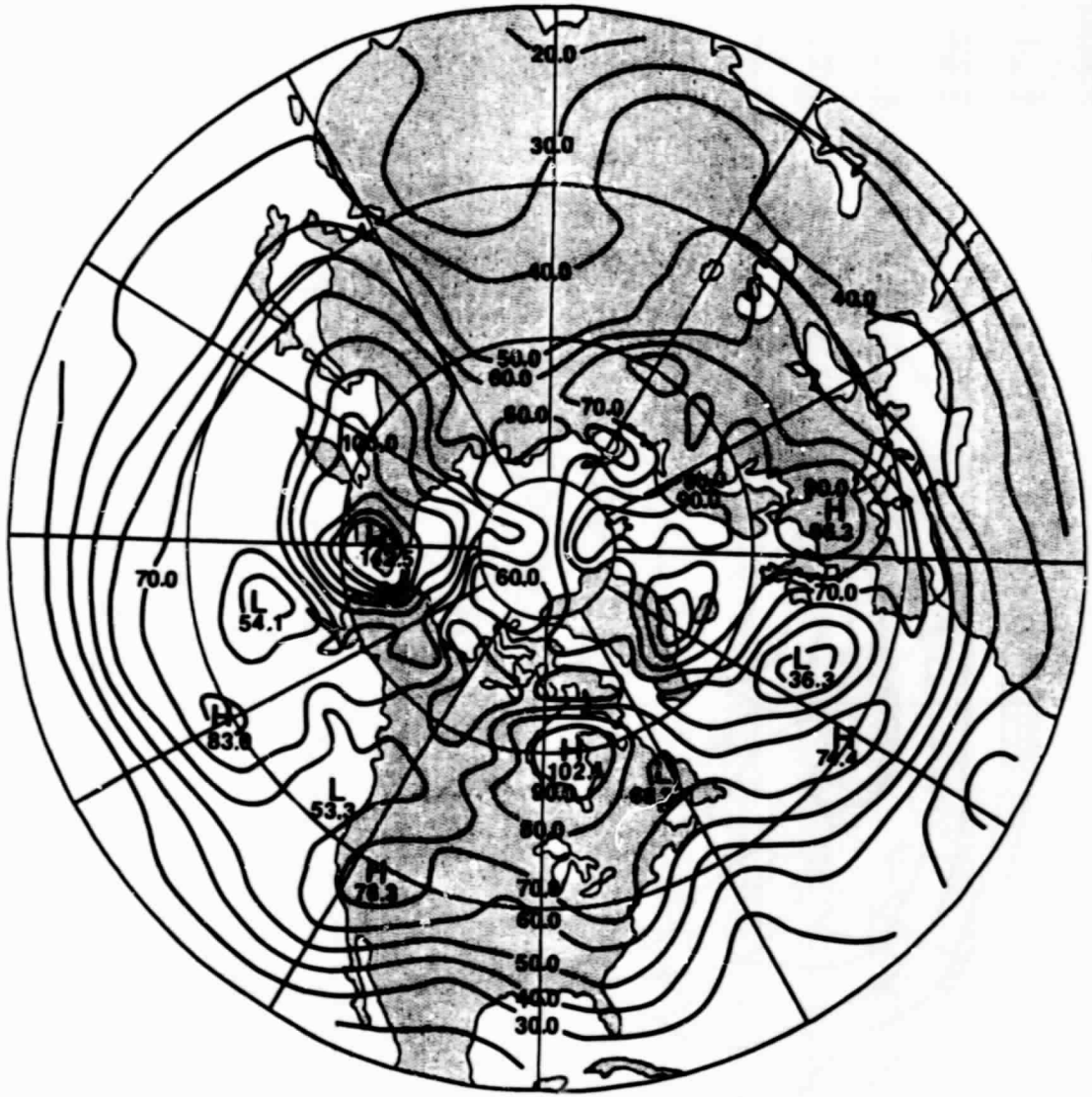

Figure 5.10b GCM RMS deviation of the winter 500 mb low-pass geopotential height field (Northern Hemisphere), units of m. Contour interval is 10 m. (Several contours have been omitted in the immediate vicinity of very sharp maxima or minima.)

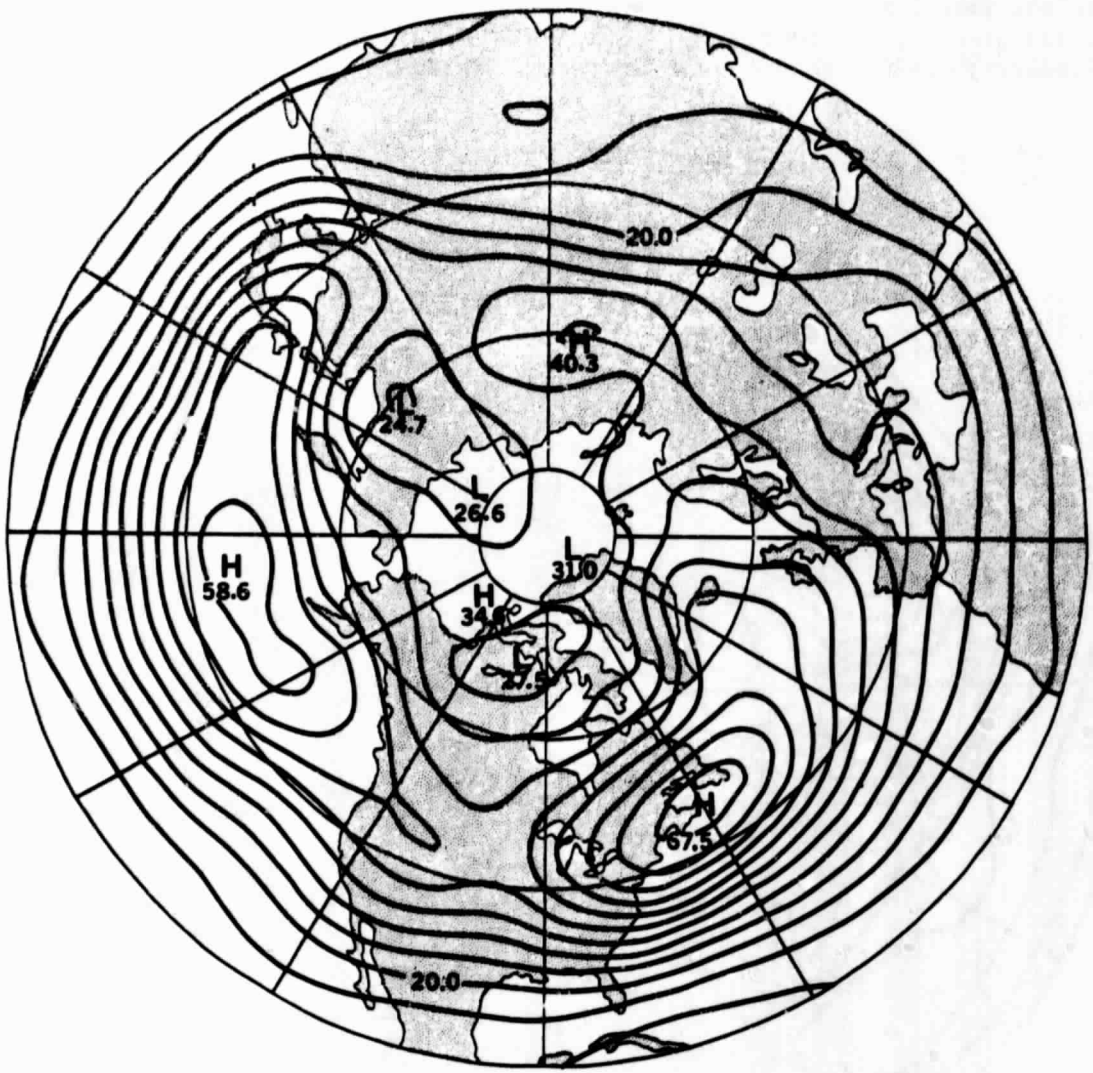

Figure 5.11a Observed RMS deviation of the winter 500 mb band-pass geopotential height field (Northern Hemisphere), units of m. Contour interval is 5 m.

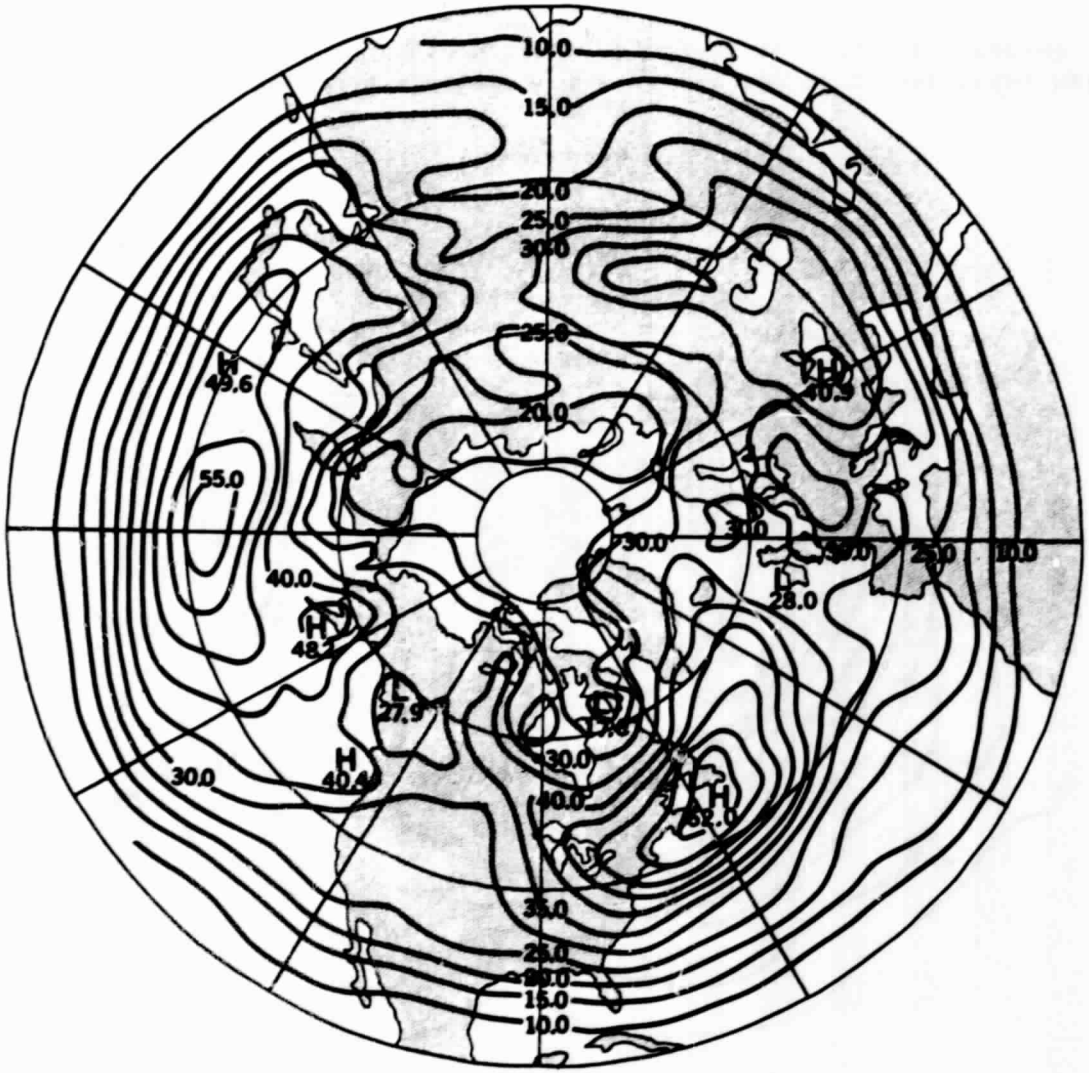

Figure 5.11b GCM RMS deviation of the winter 500 mb band-pass geopotential height field (Northern Hemisphere), units of m. Contour interval is 5 m.

Figure 5.12a Observed RMS deviation of the summer 500 mb geopotential height field (Northern Hemisphere), units of m. Contour interval is 10 m.

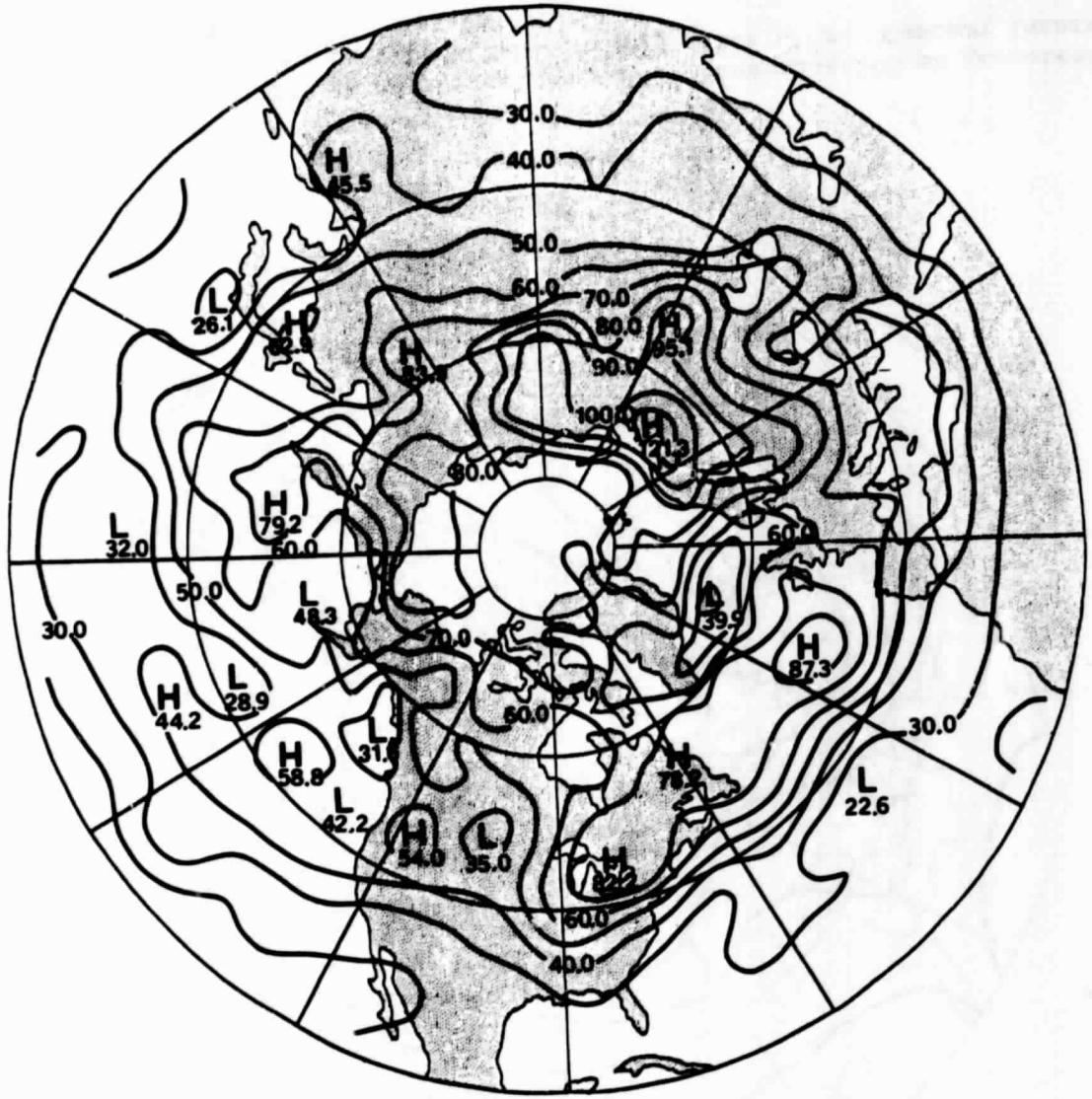

Figure 5.12b GCM RMS deviation of the summer 500 mb geopotential height field (Northern Hemisphere), units of m. Contour interval is 10 m. (Several contours have been omitted in the immediate vicinity of very sharp maxima or minima.)

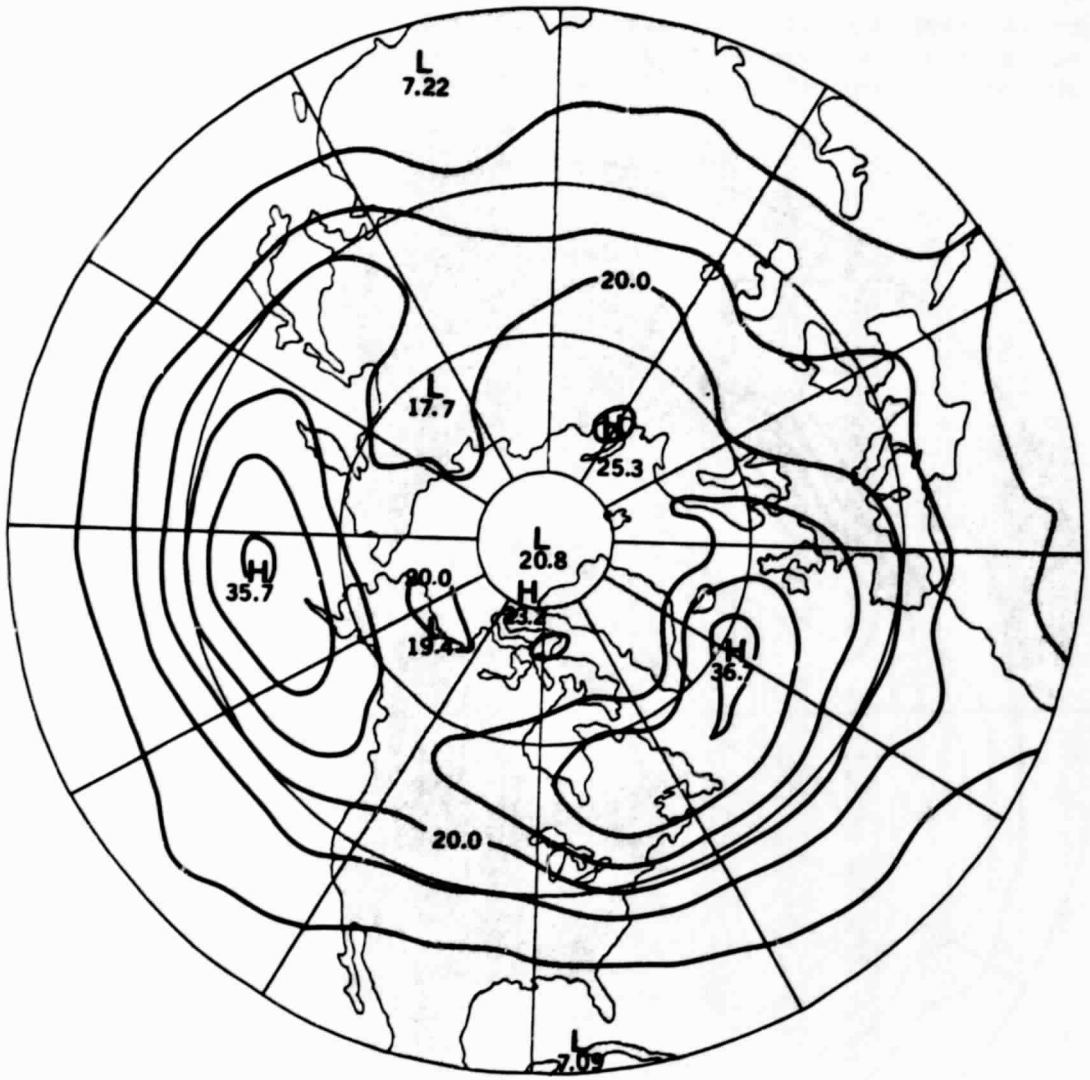

Figure 5.13a Observed RMS deviation of the summer band-pass 500 mb geopotential height field (Northern Hemisphere), units of m. Contour interval is 5 m.

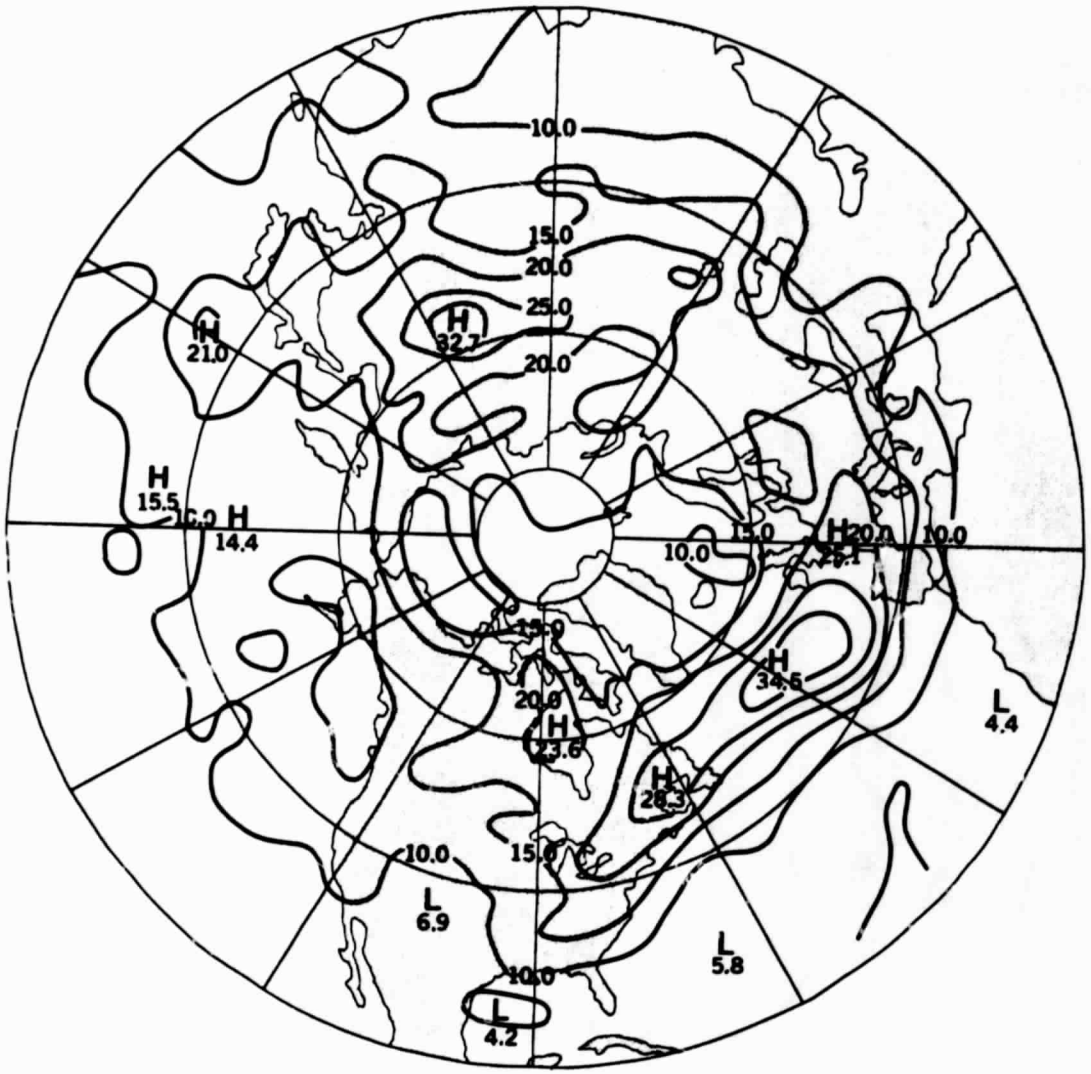

Figure 5.13b GCM RMS deviation of the summer band-pass 500 mb geopotential height field (Northern Hemisphere), units of m. Contour interval is 5 m.

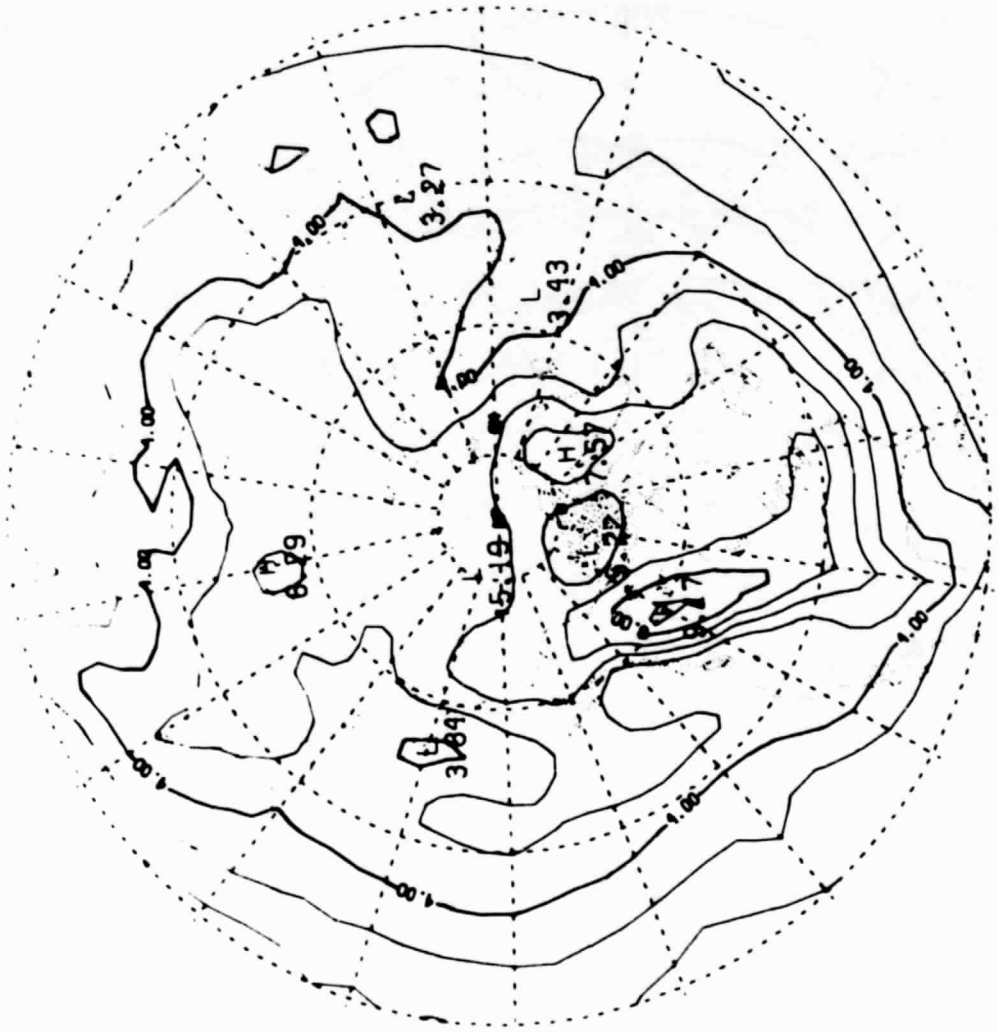

Figure 5.14a Observed RMS deviation of the winter 850 mb temperature field (Northern Hemisphere), units of degrees K. Contour interval is 1 degree.

Figure 5.14b GCM RMS deviation of the winter 850 mb temperature field (Northern Hemisphere), units of degrees K. Contour interval is 1 degree. (Several contours have been omitted in the immediate vicinity of very sharp maxima or minima.)

Figure 5.15a Observed RMS deviation of the winter low-pass 850 mb temperature field (Northern Hemisphere), units of degrees K. Contour interval is 0.5 degrees.

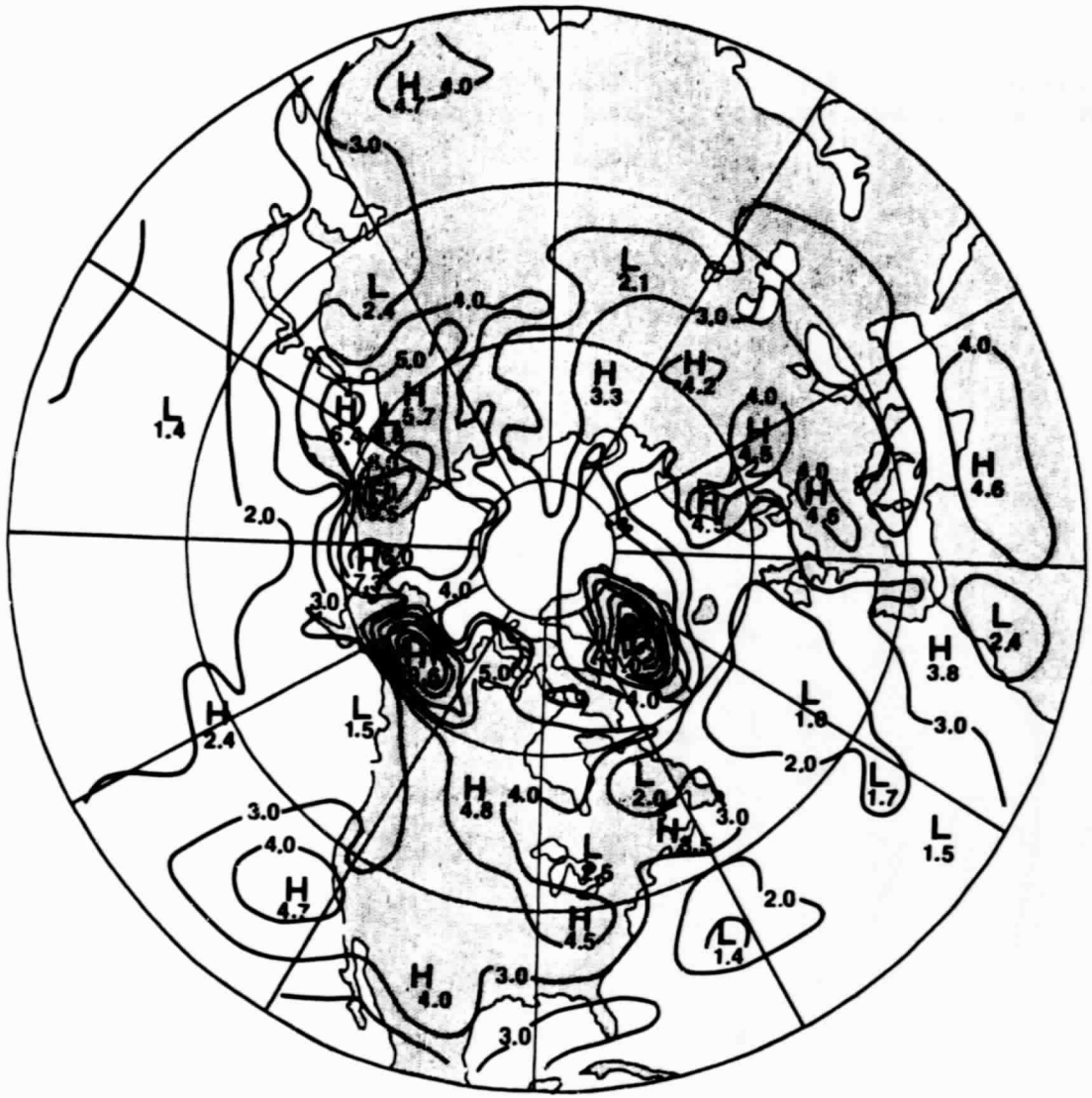

Figure 5.15b GCM RMS deviation of the winter low-pass 850 mb temperature field (Northern Hemisphere), units of degrees. Contour interval is 0.5 degrees. (Several contours have been omitted in the immediate vicinity of very sharp maxima or minima.)

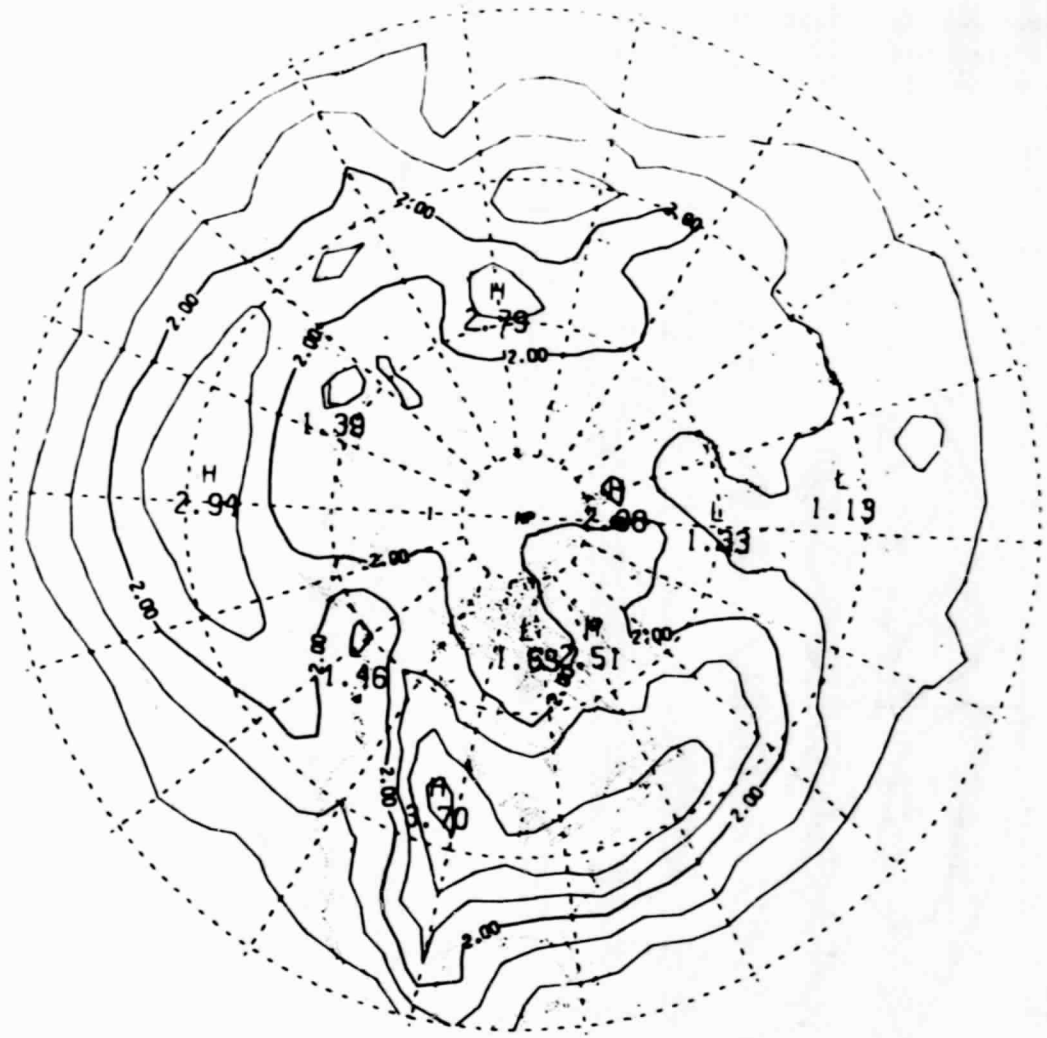

Figure 5.16a Observed RMS deviation of the winter band-pass 850 mb temperature field (Northern Hemisphere), units of degrees K. Contour interval is 0.5 degrees.

Figure 5.16b GCM RMS deviation of the winter band-pass 850 mb temperature field (Northern Hemisphere), units of degrees K. Contour interval is 0.5 degrees. (Several contours have been omitted in the immediate vicinity of very sharp maxima or minima.)

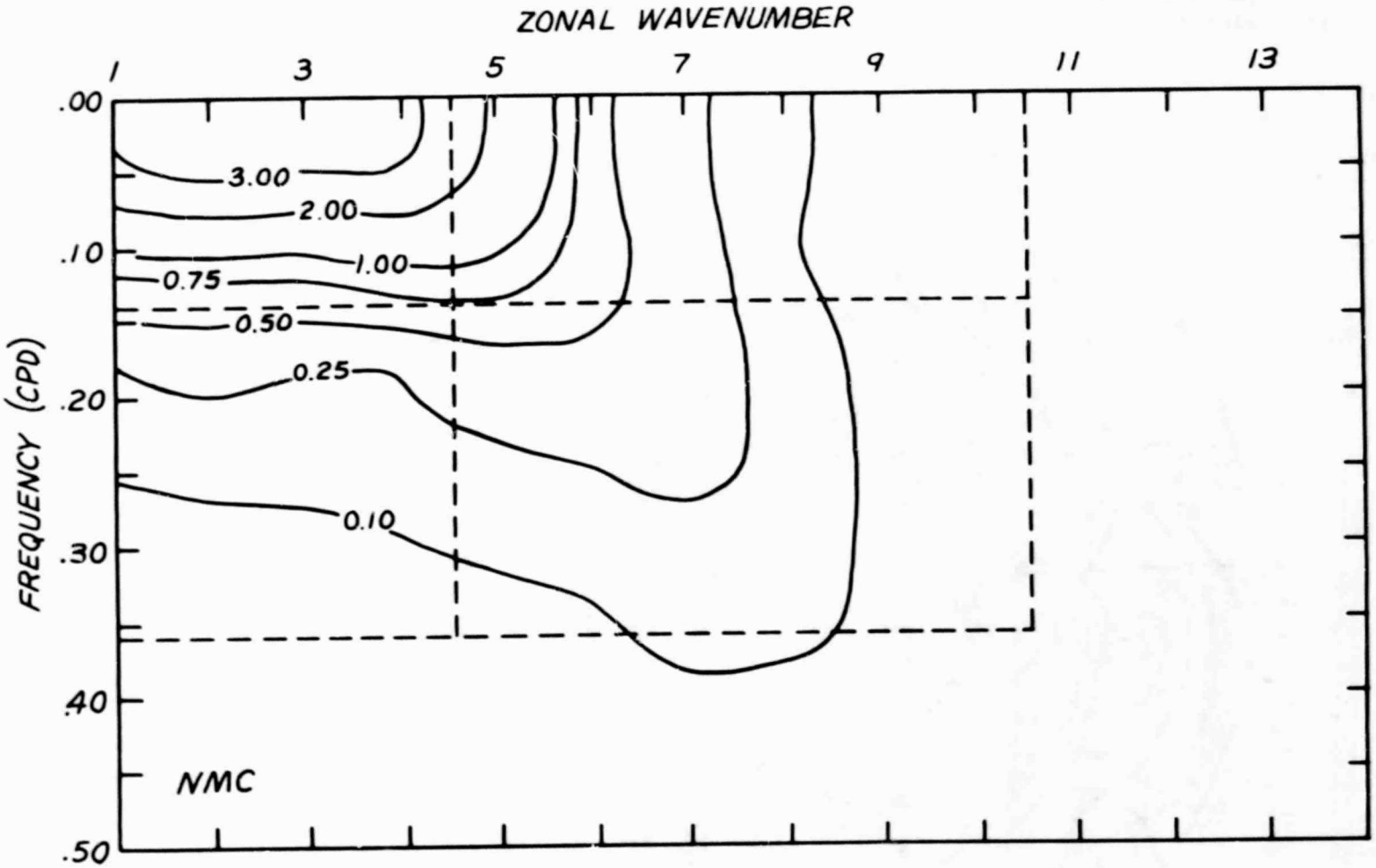

Figure 5.17a Observed wavenumber-frequency spectral density of winter 500 mb geopotential height of 50N, in units of 10^3 m^2/cpd. The spectral density is defined as the variance in a given frequency band divided by 2π times the width of that band. The presence of a non-zero spectral density at zero frequency is an artefact introduced for the sake of the visual clarity of the plot.

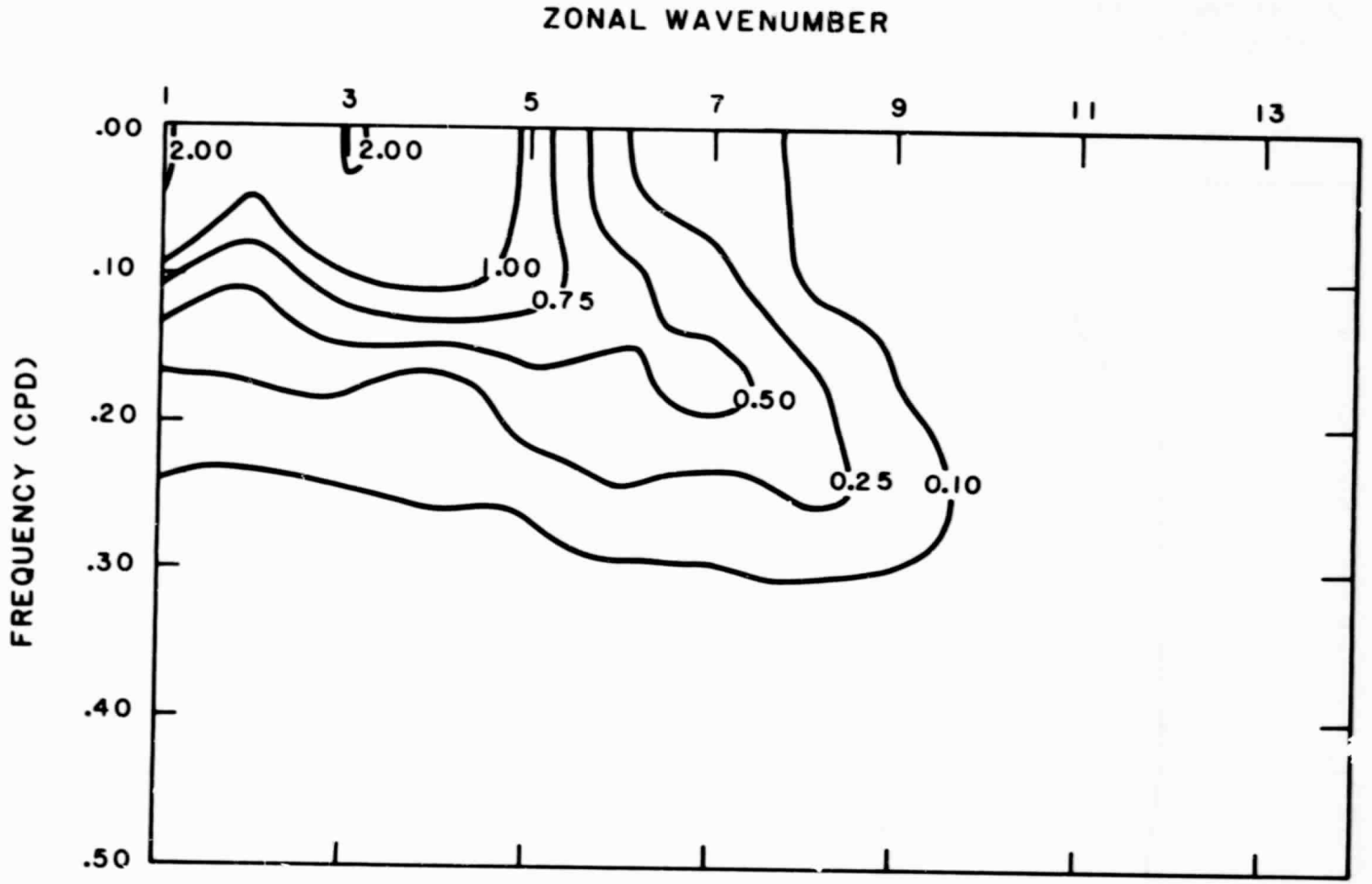

Figure 5.17b GCM wavenumber-frequency spectral density of winter 500 mb geopotential height at 50N, in units of 10^3 m^2/cpd. Otherwise as in Figure 5.17a.

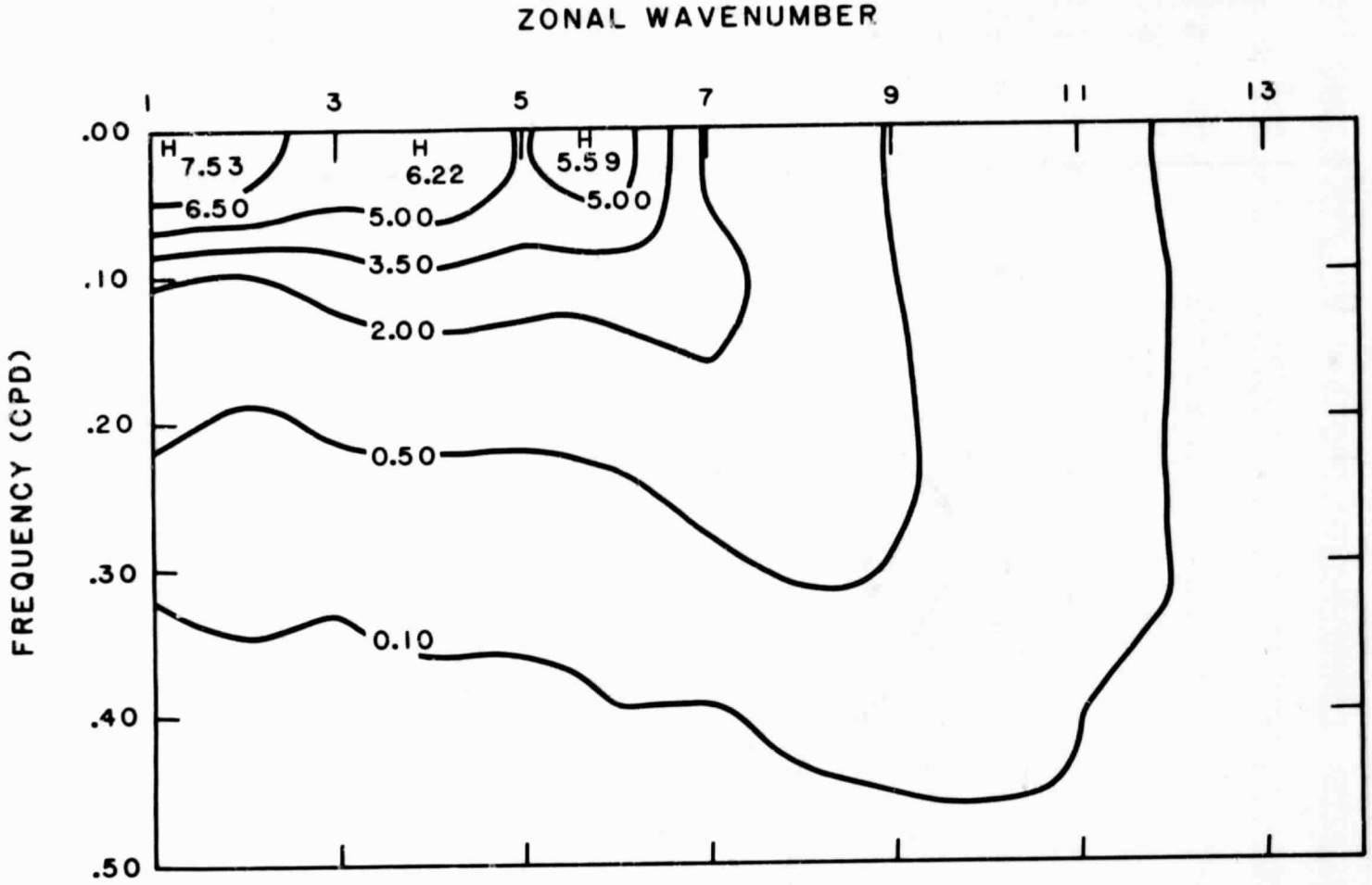

Figure 5.18a Observed wavenumber-frequency spectral density of winter 500 mb geopotential height at 30N, in units of 10^2 m^2/cpd. Otherwise as in Figure 5.17a.

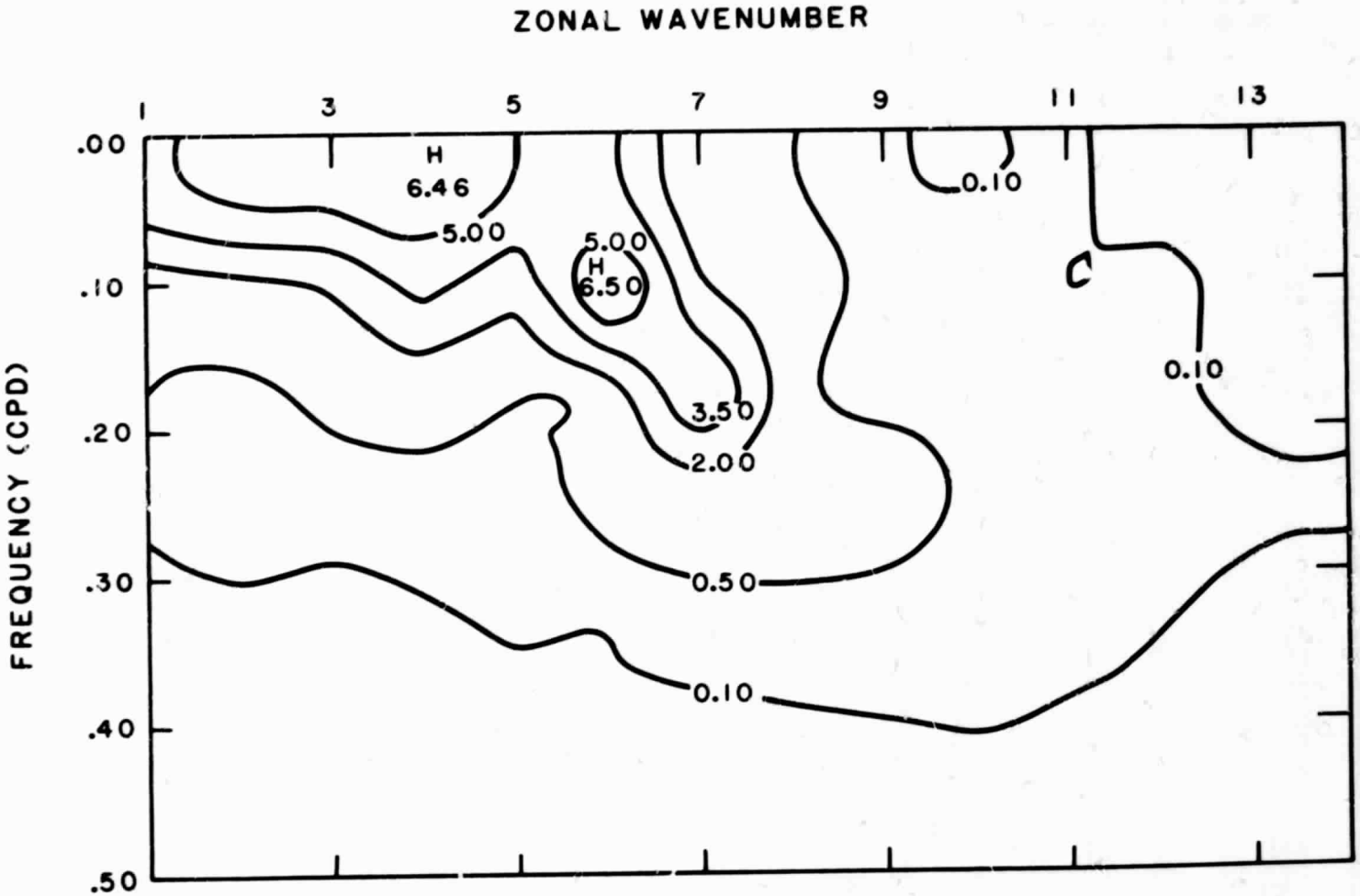

Figure 5.18b GCM wavenumber-frequency spectral density of winter 500 mb geopotential height at 30N, in units of 10^2 m^2/cpd. Otherwise as in Figure 5.17a.

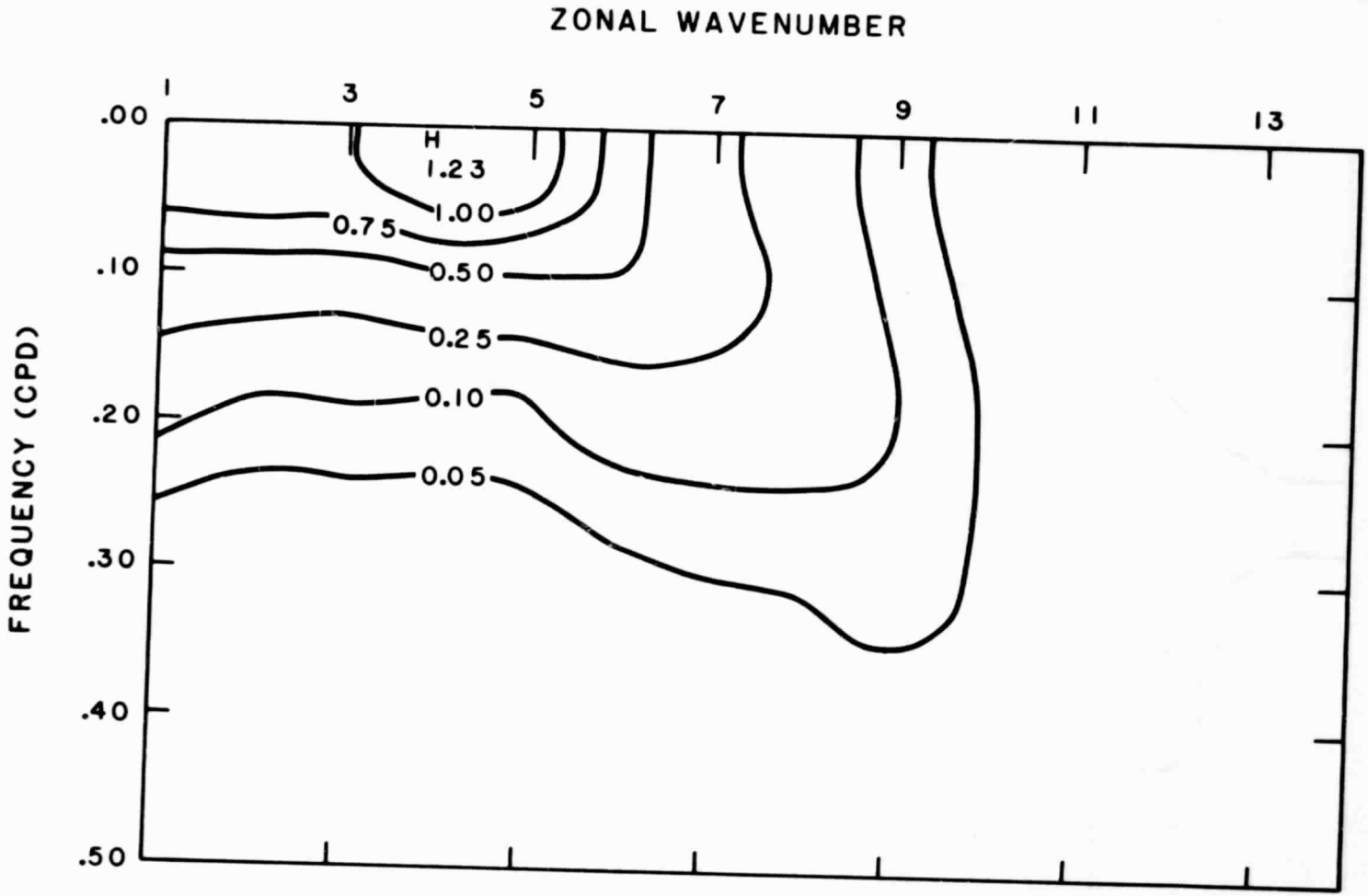

Figure 5.19a Observed wavenumber-frequency spectral density of summer 500 mb geopotential height at 50N, in units of 10^3 m^2/cpd. Otherwise as in Figure 5.17a.

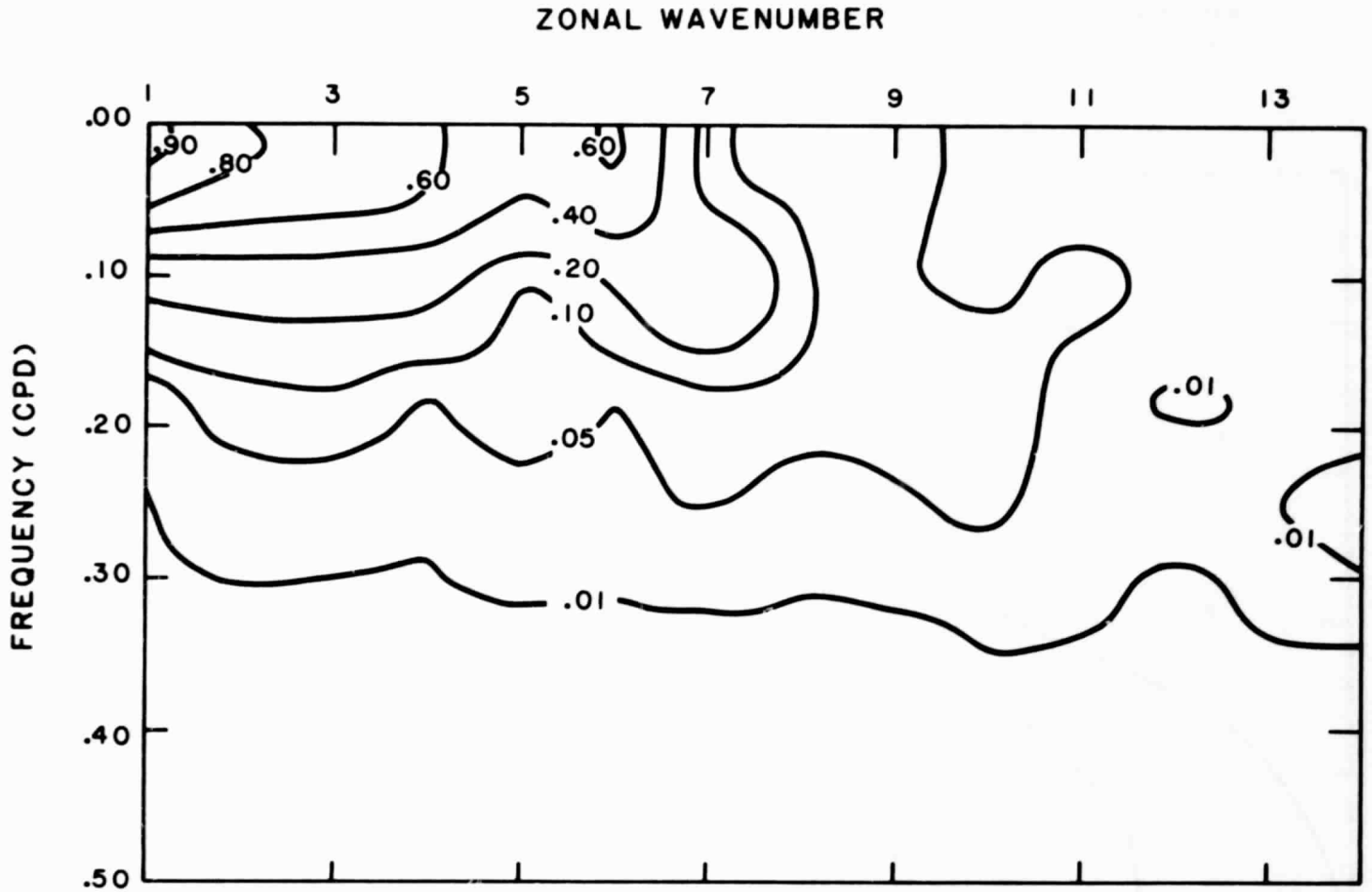

Figure 5.19b GCM wavenumber-frequency spectral density of summer 500 mb geopotential height at 50N, in units of 10^3 m^2/cpd. Otherwise as in Figure 5.17a.

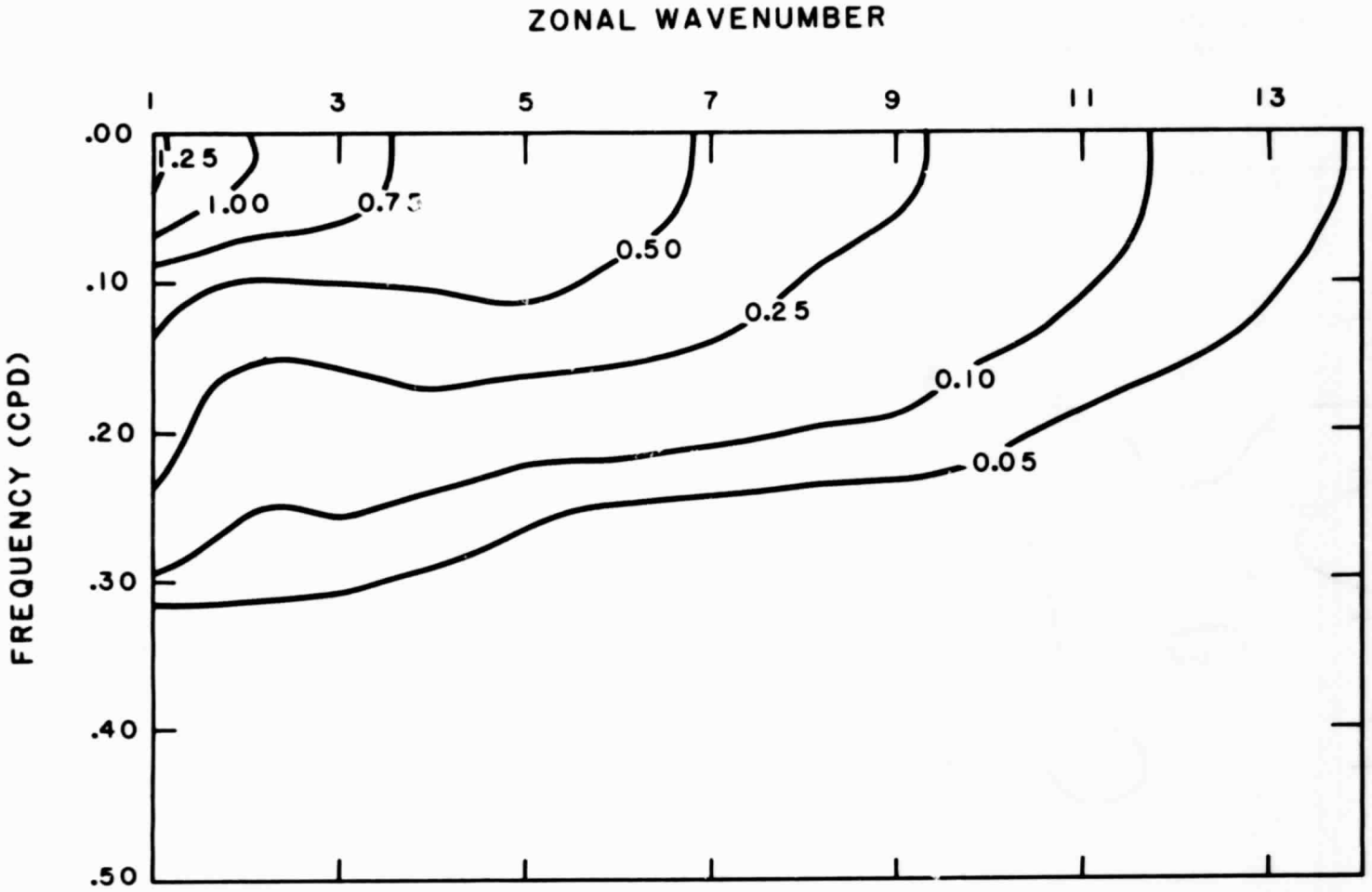

Figure 5.20a Observed wavenumber-frequency spectral density of summer 500 mb geopotential height at 30N, in units of 10^2 m^2/cpd. Otherwise as in Figure 5.17a.

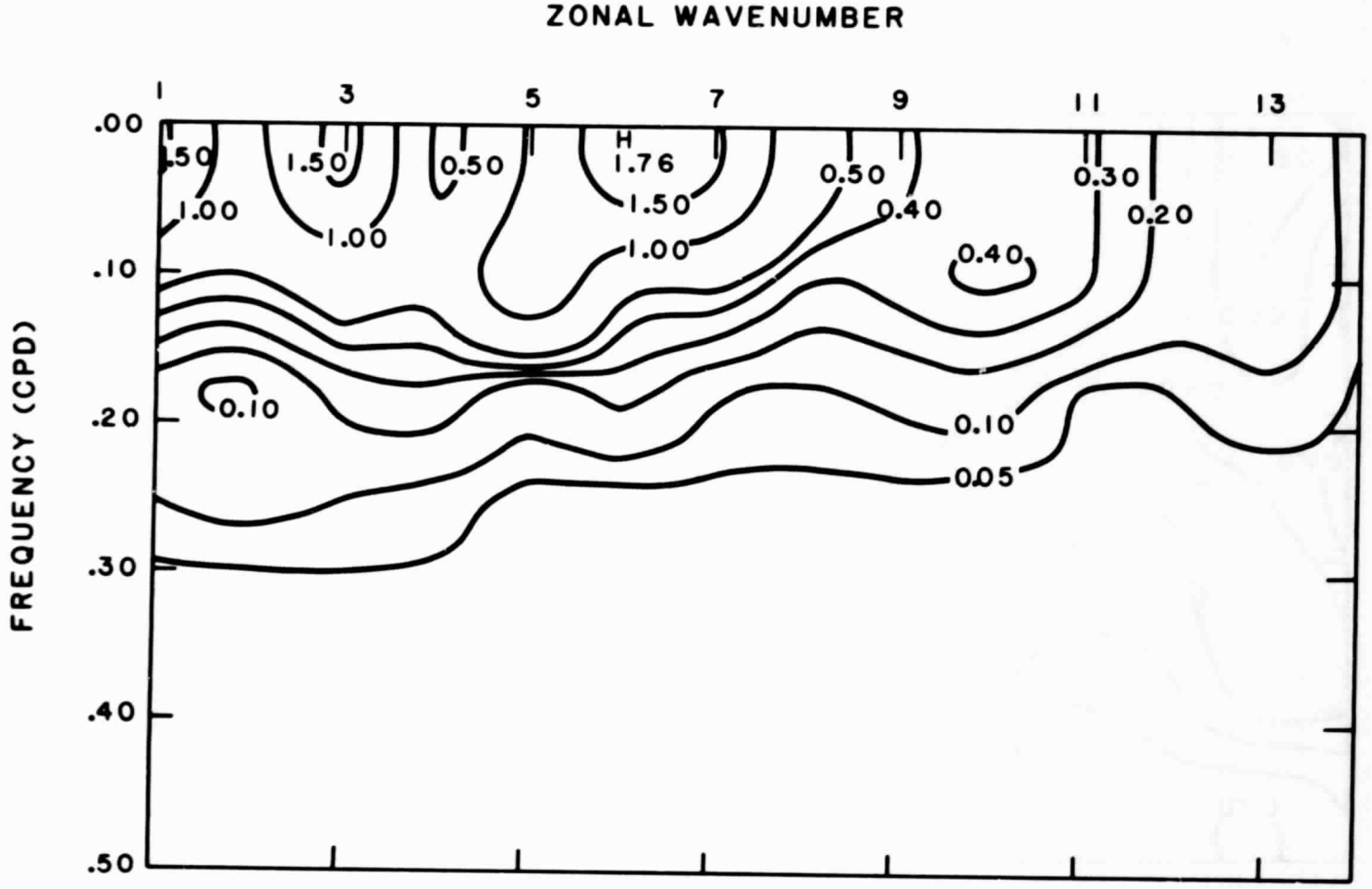

Figure 5.20b GCM wavenumber-frequency spectral density of summer 500 mb geopotential height at 30N, in units of 10^2 m^2/cpd. Otherwise as in Figure 5.17a.

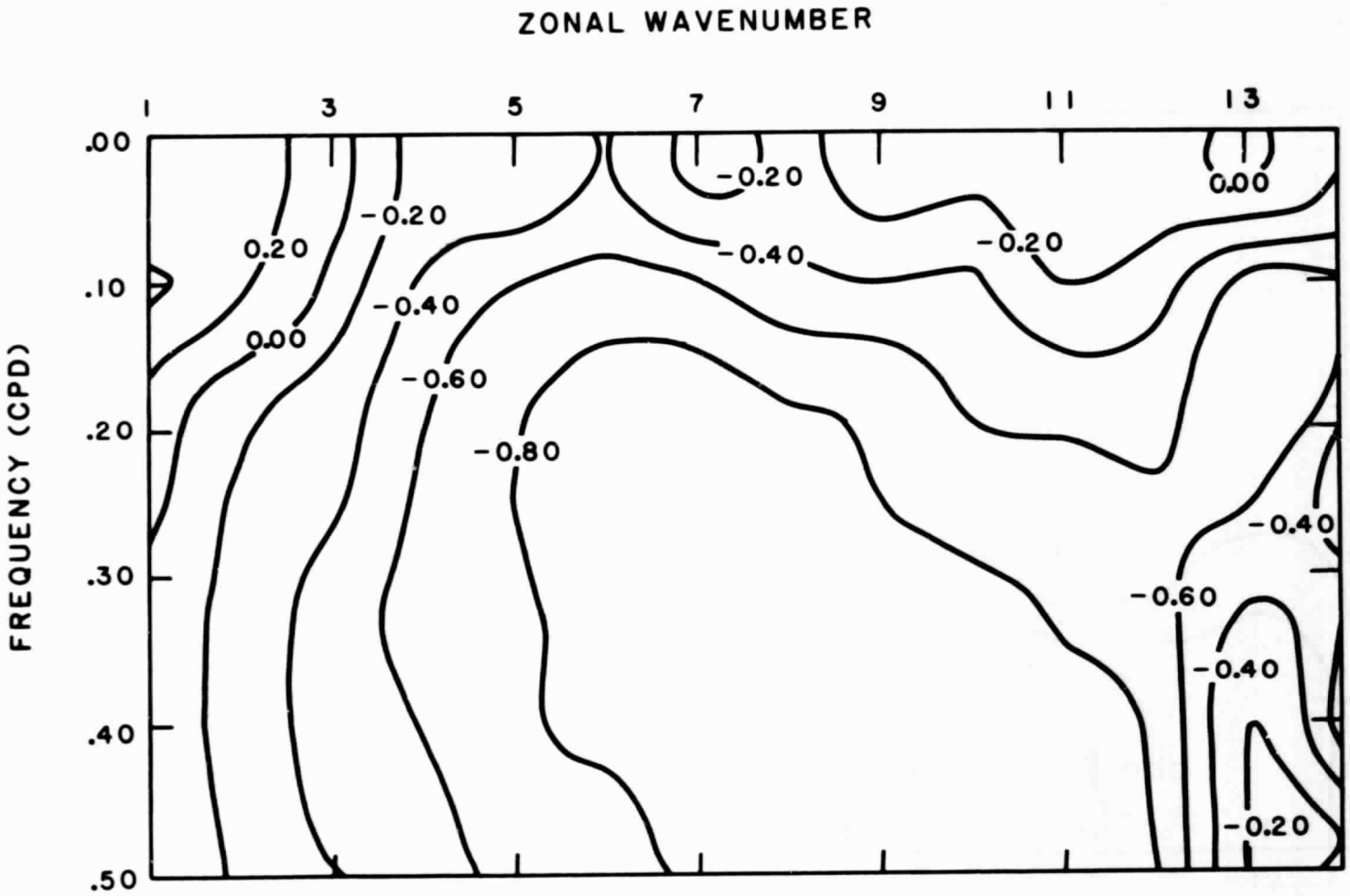

Figure 5.21a Observed wavenumber-frequency net propagation tendency of winter 500 mb geopotential height at 50N, dimensionless.

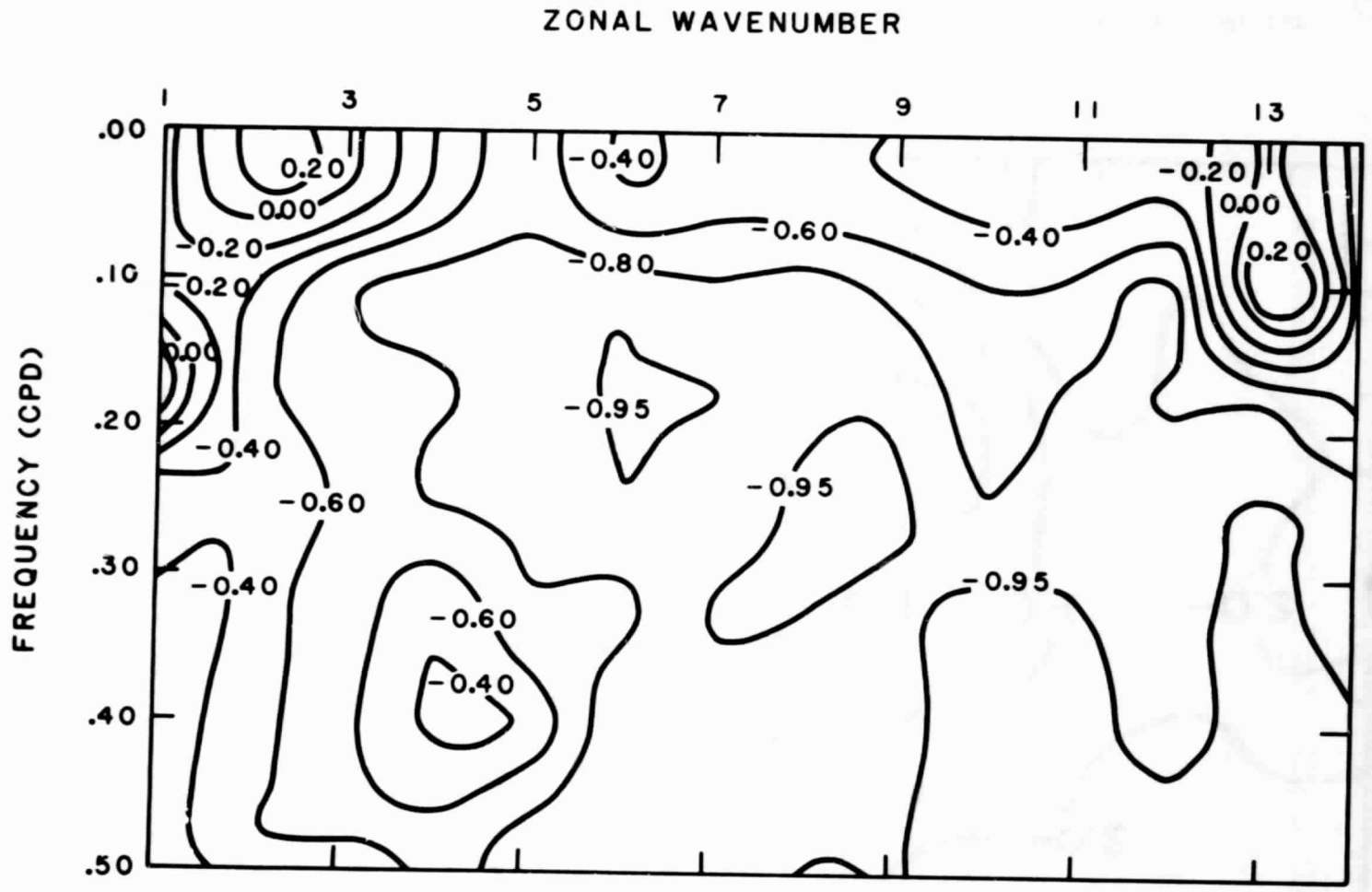

Figure 5.21b GCM wavenumber-frequency net propagation tendency of winter 500 mb geopotential height at 50N, dimensionless.

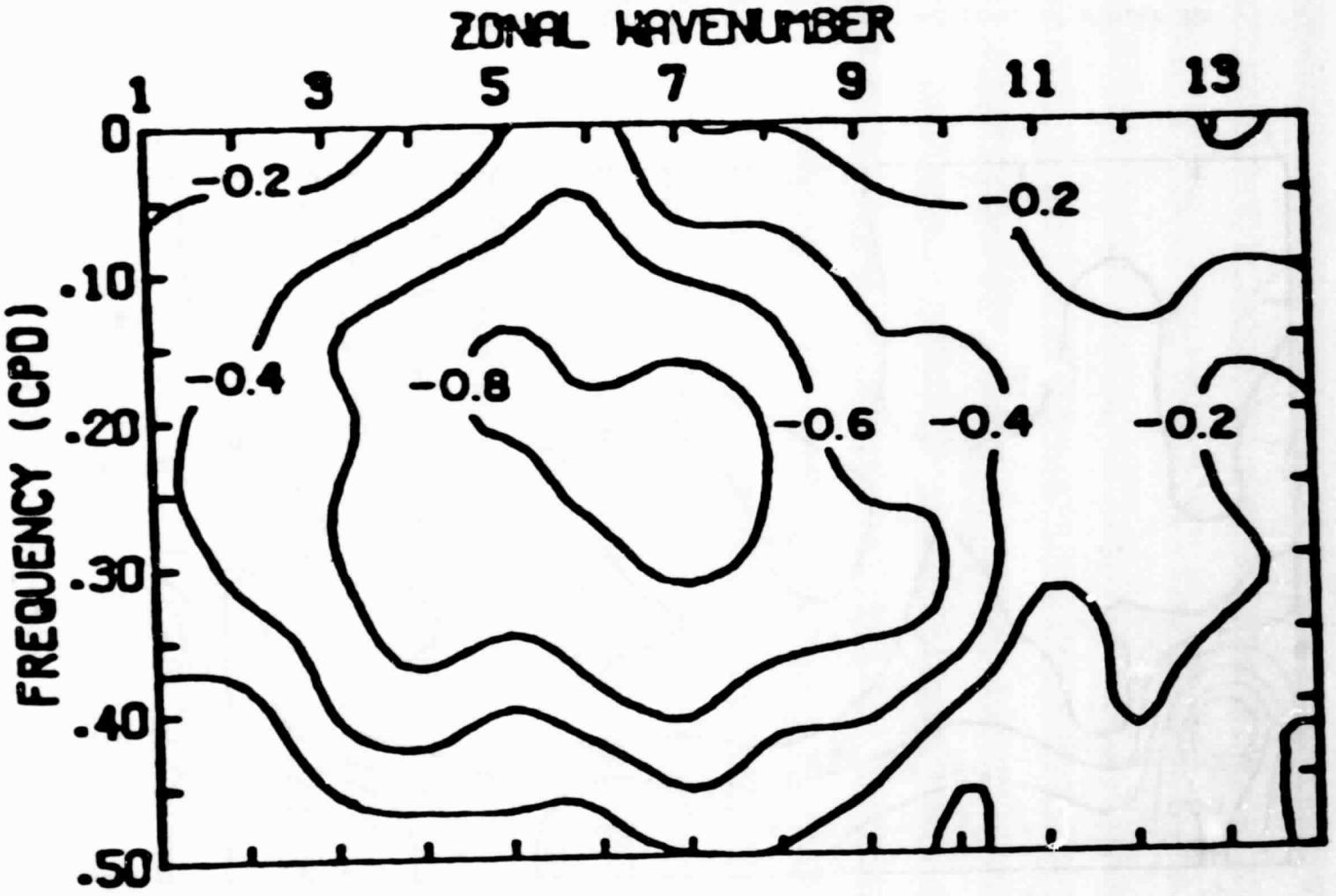

Figure 5.22a Observed wavenumber-frequency net propagation tendency of winter 500 mb temperature at 50N, dimensionless.

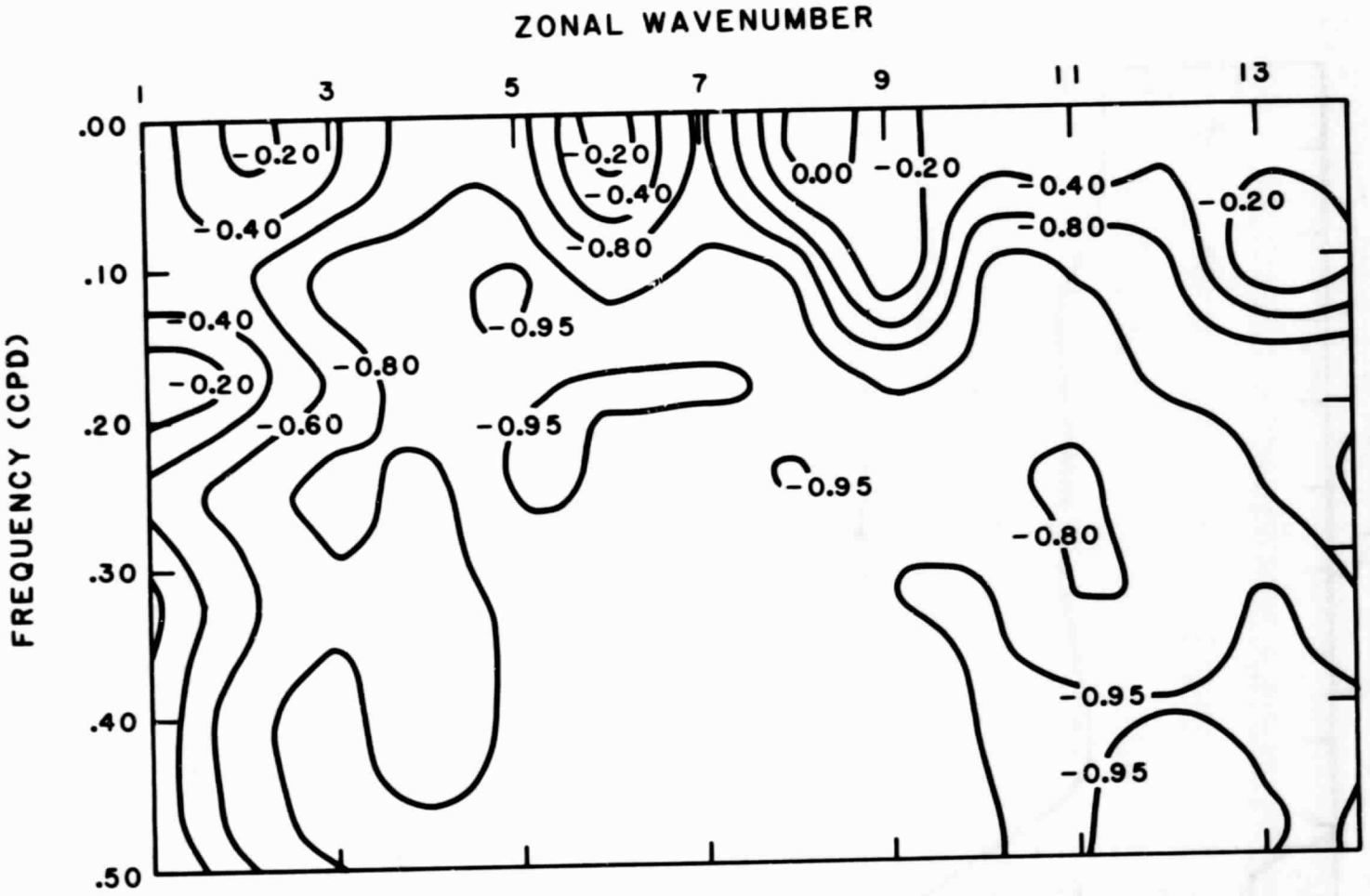

Figure 5.22b GCM wavenumber-frequency net propagation tendency of winter 500 mb temperature at 50N, dimensionless.

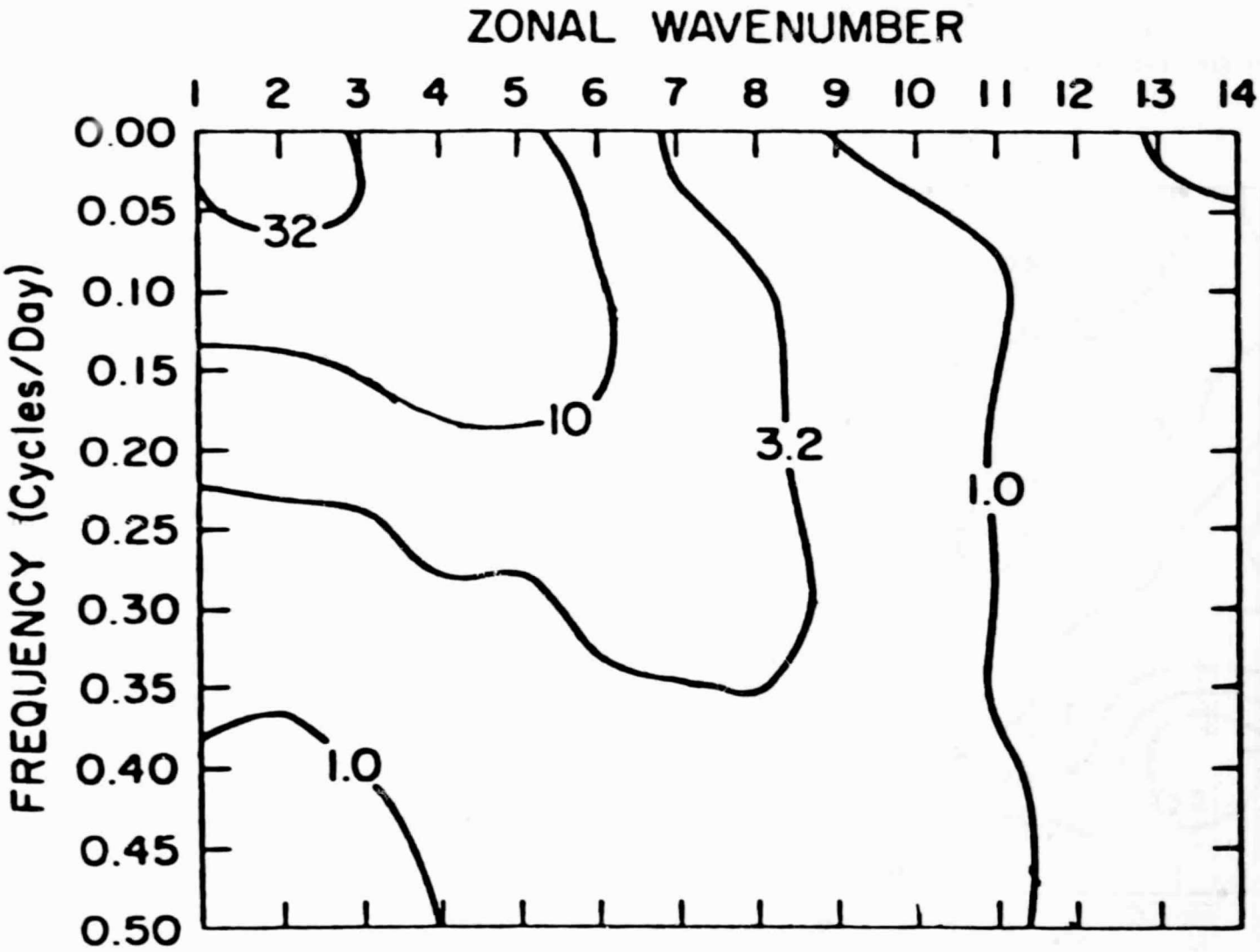

Figure 5.23a Observed wavenumber-frequency spectral density of winter 300 mb u-wind at 35N, in units of m^2s^{-2}/cpd. Otherwise as in Figure 5.17a.

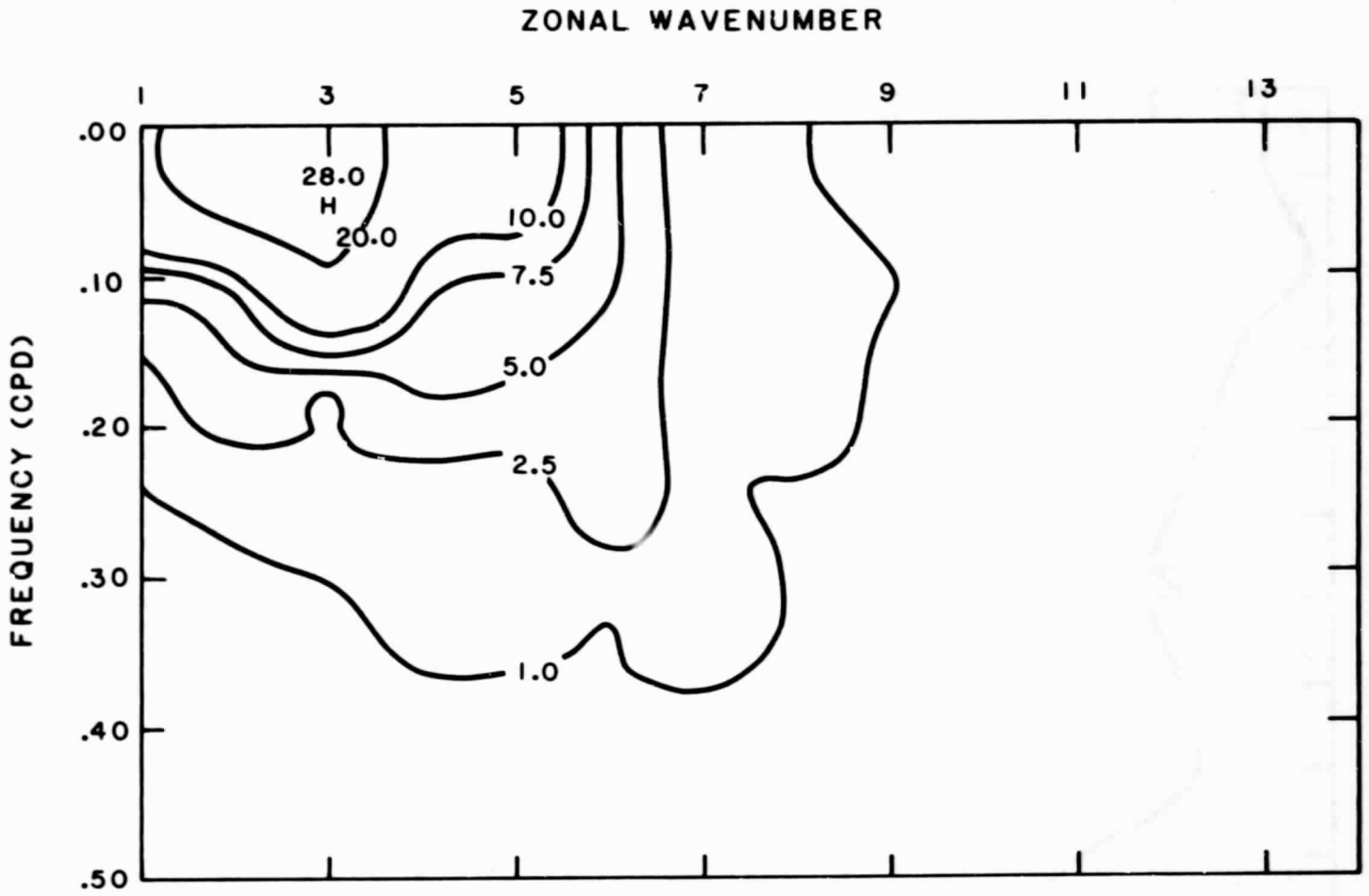

Figure 5.23b GCM wavenumber-frequency spectral density of winter 300 mb u-wind at 34N, in units of m^2s^{-2}/cpd. Otherwise as in Figure 5.17a.

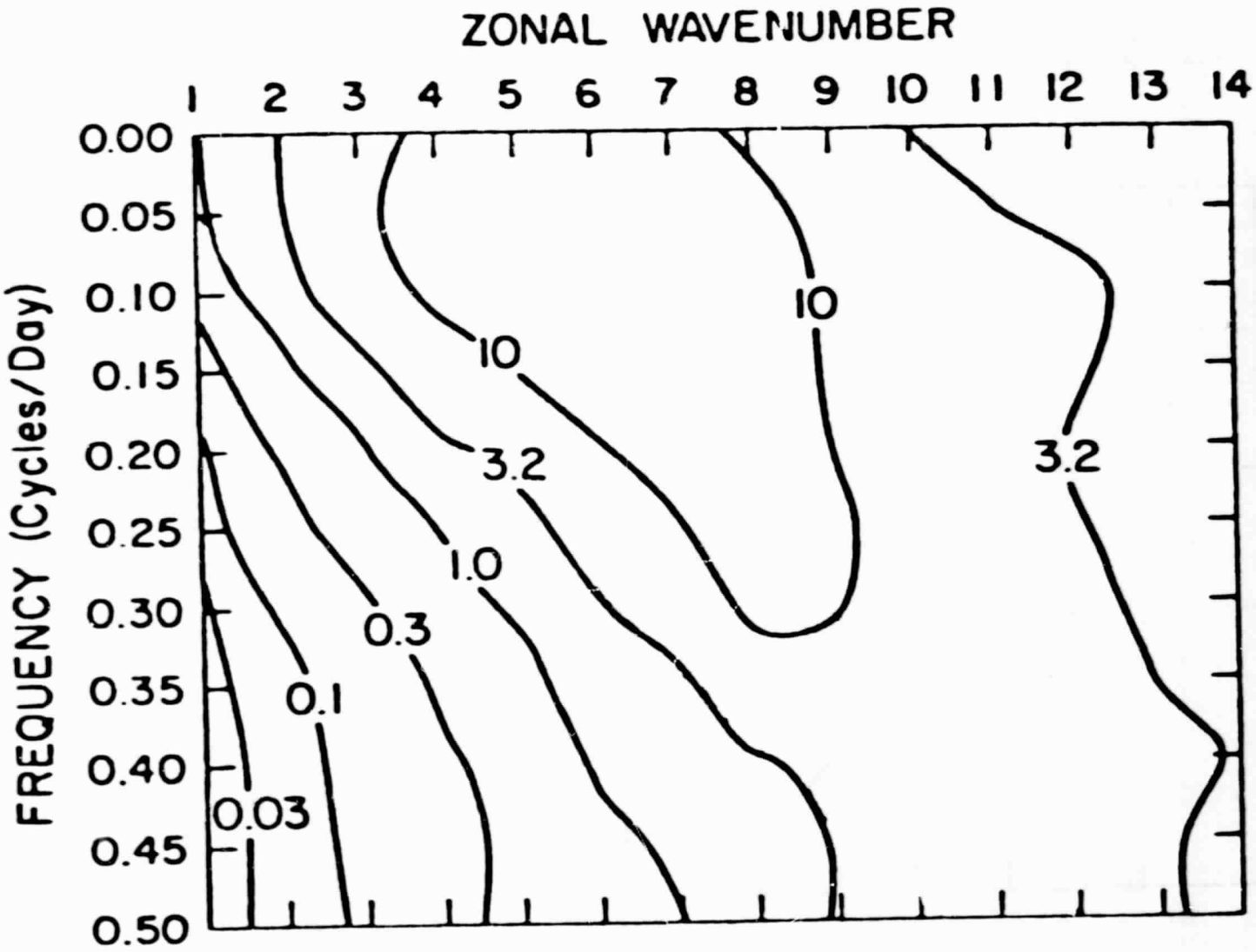

Figure 5.24a Observed wavenumber-frequency spectral density of winter 300 mb v-wind at 35N, in units of m^2s^{-2}/cpd. Otherwise as in Figure 5.17a.

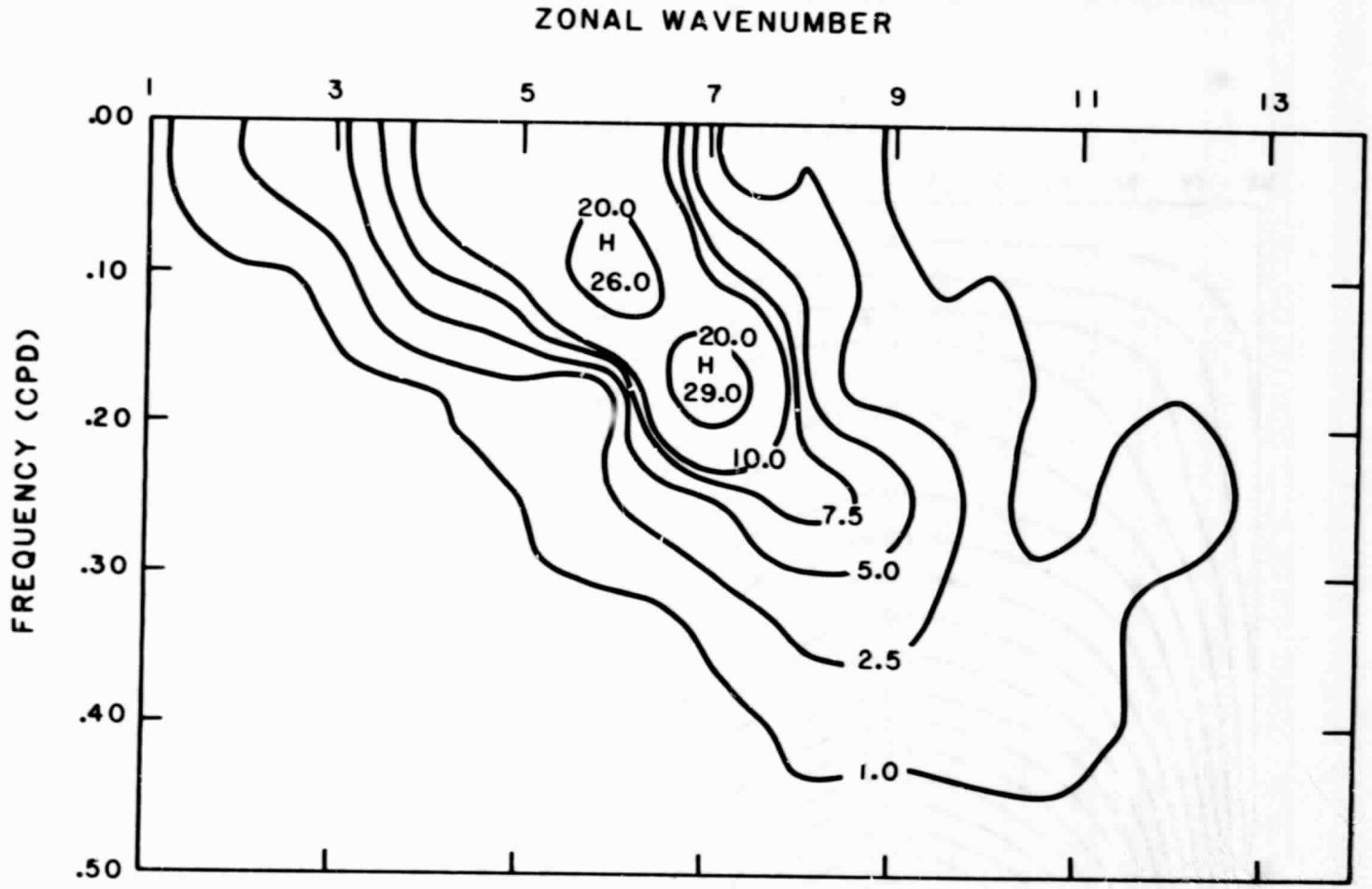

Figure 5.24b GCM wavenumber-frequency spectral density of winter 300 mb v-wind at 34N, in units of m^2s^{-2}/cpd. Otherwise as in Figure 5.17a.

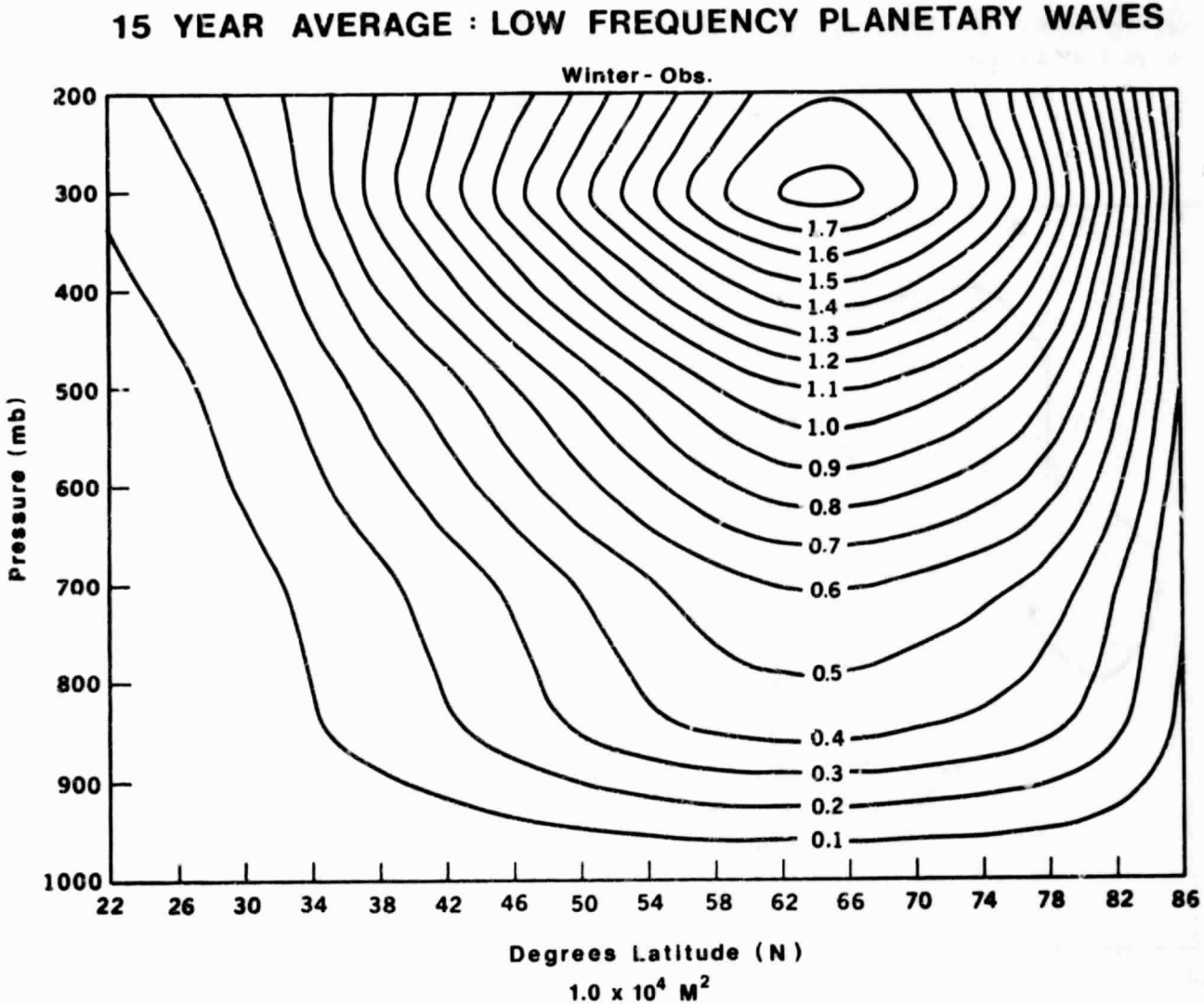

Figure 5.25a Observed winter geopotential height variance in low-frequency planetary waves, in units of $10^4 m^2$ (Northern Hemisphere). Contour interval is .1 x $10^4 m^2$.

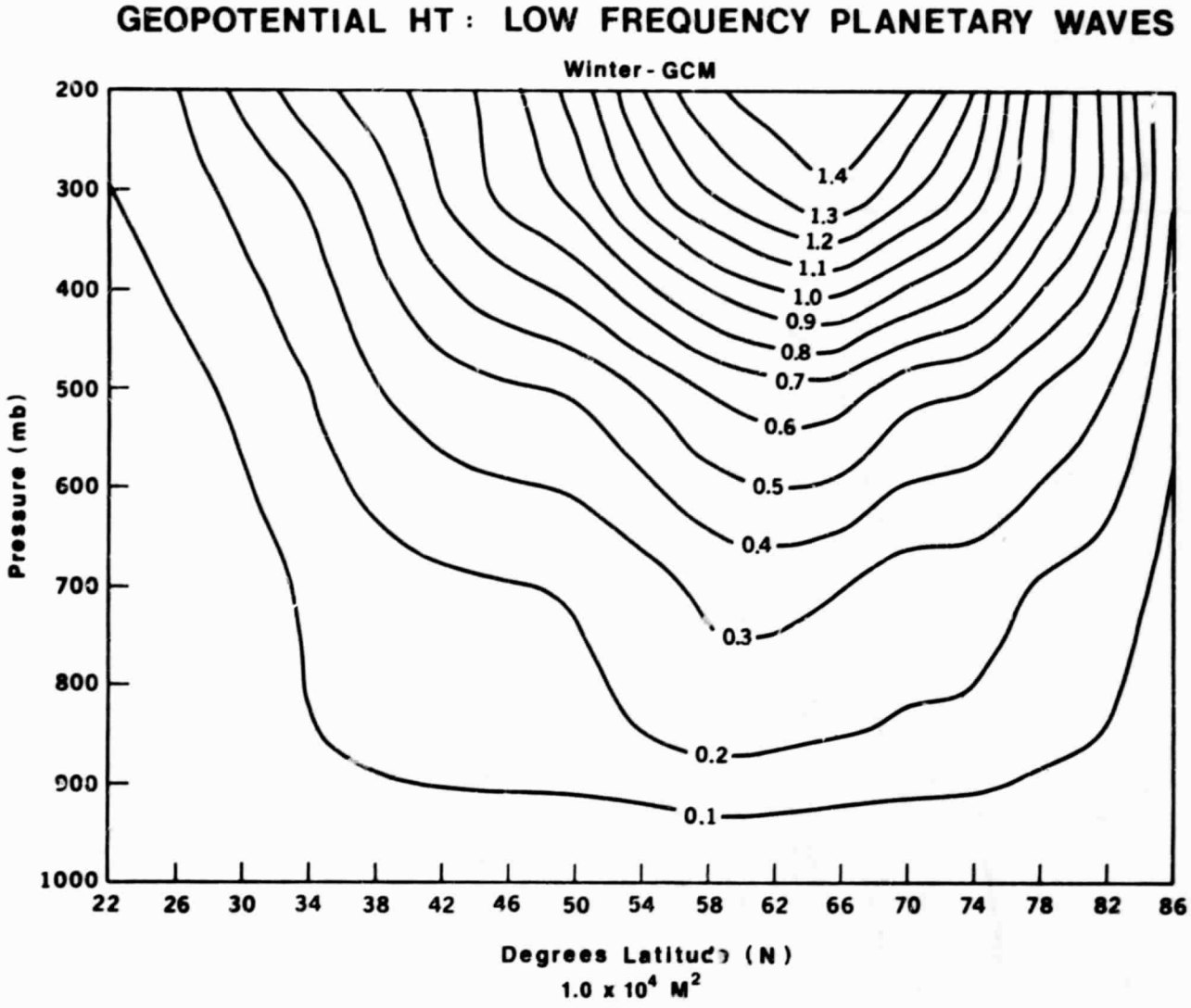

Figure 5.25b GCM winter geopotential height variance in low-frequency planetary waves, in units of $10^4 m^2$ (Northern Hemisphere). Contour interval is .1 x 10^4 m^2.

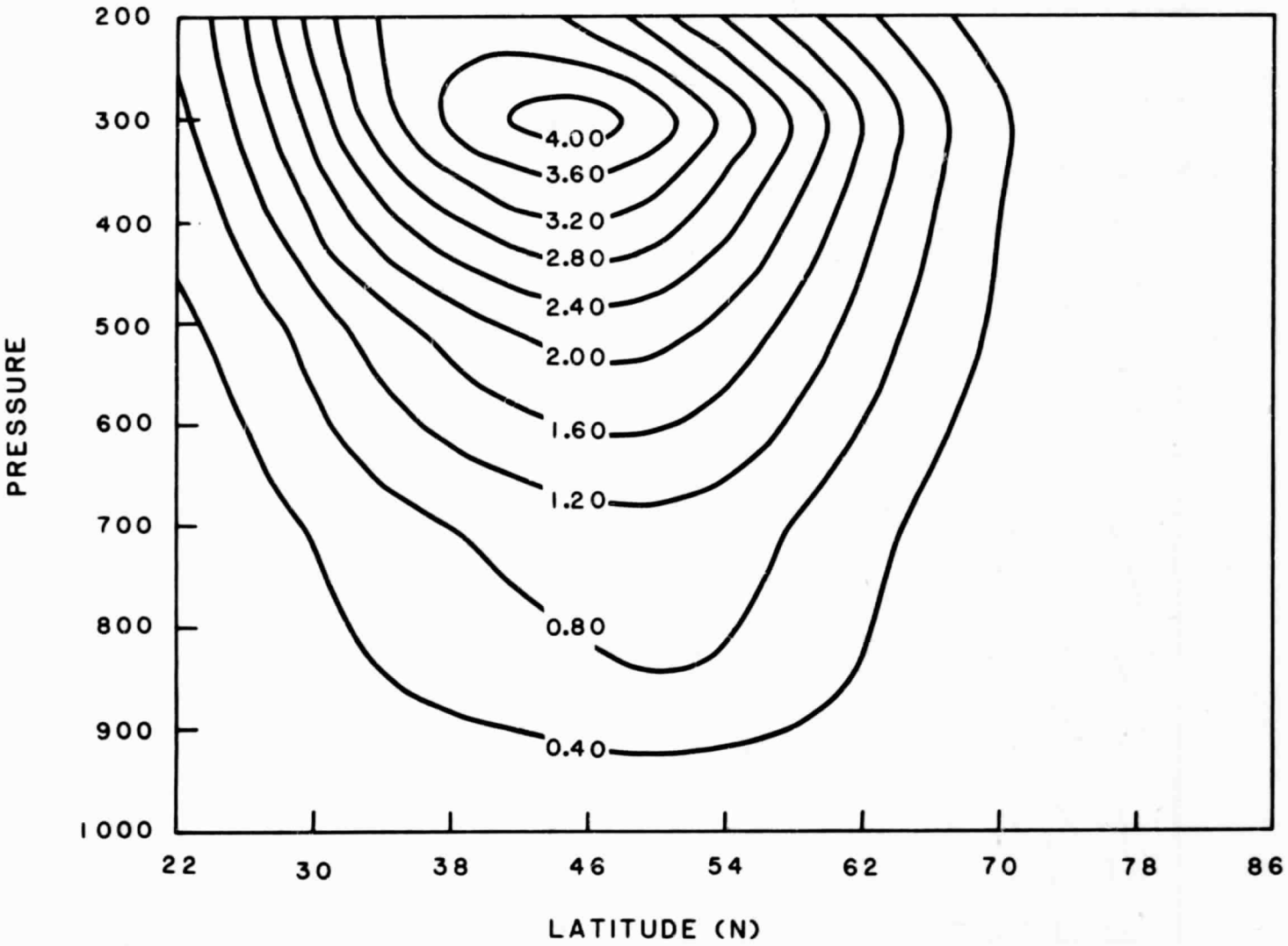

Figure 5.26a Observed winter geopotential height variance in low-frequency synoptic-scale waves, in units of $10^3 m^2$ (Northern Hemisphere). Contour interval is .4 x $10^3 m^2$.

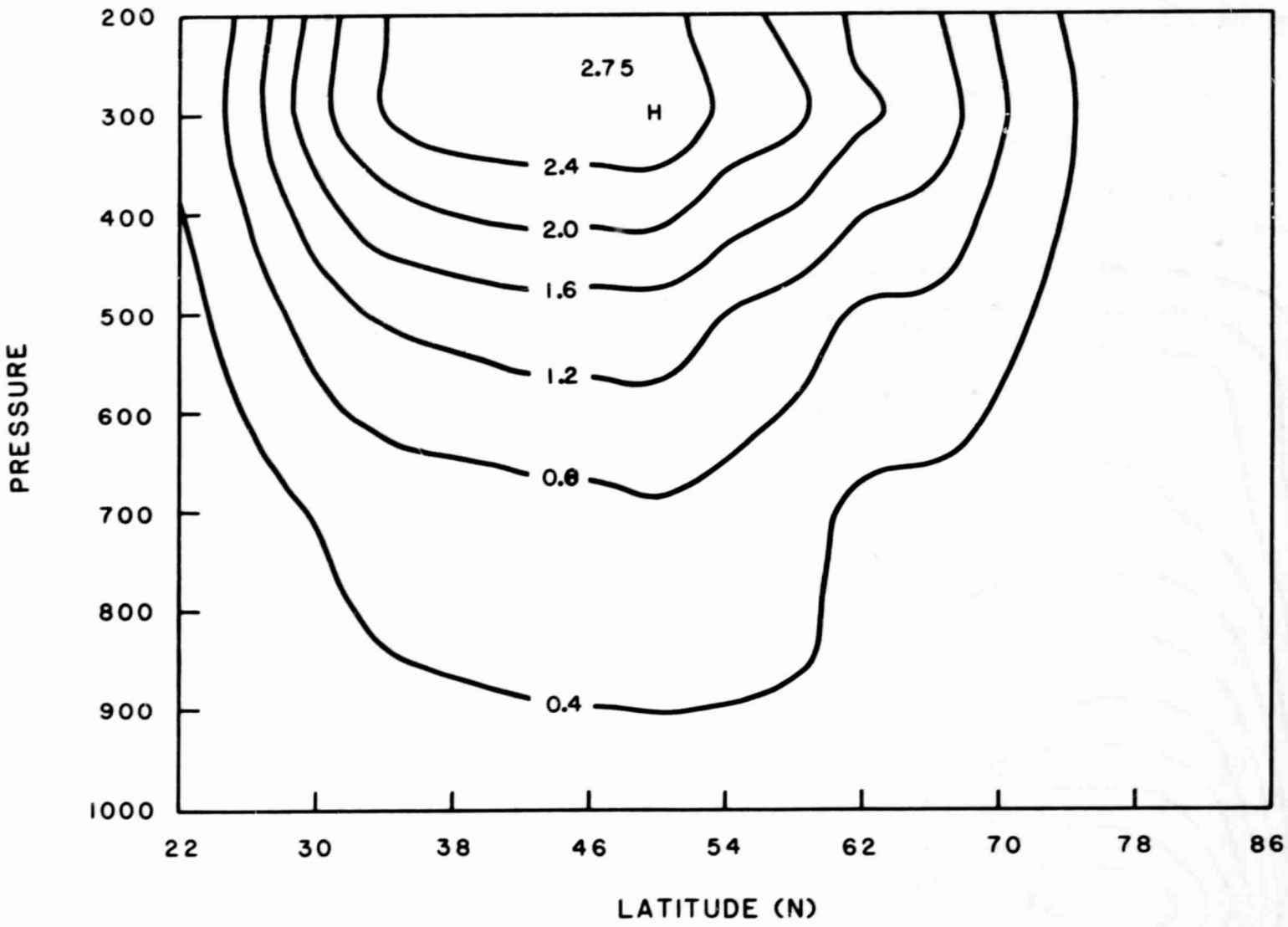

Figure 5.26b GCM winter geopotential height variance in low-frequency synoptic-scale waves, in units of $10^3 m^2$ (Northern Hemisphere). Contour interval is .4 x 10^3 m^2.

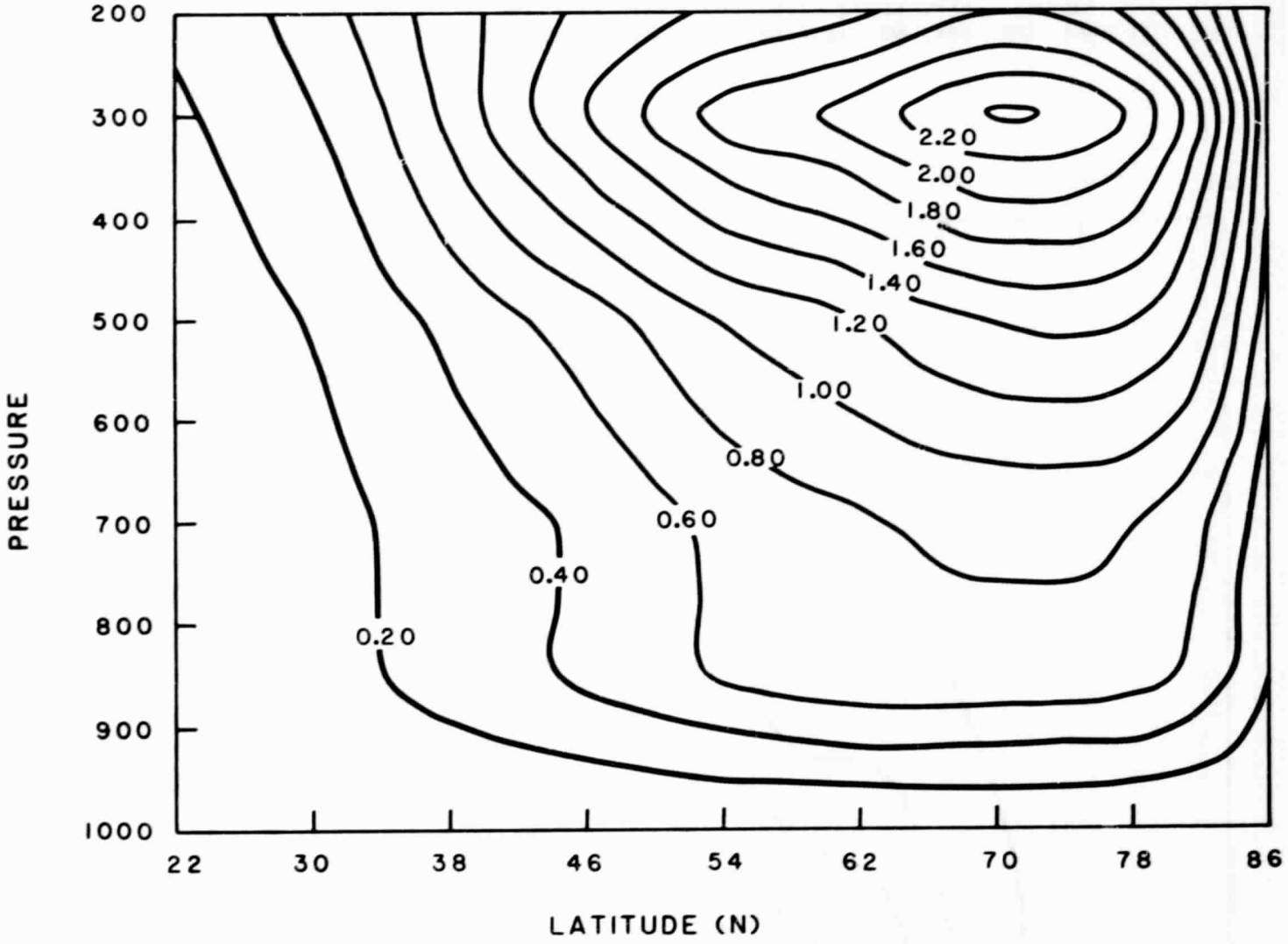

Figure 5.27a Observed winter geopotential height variance in medium-frequency planetary waves, in units of 10^3 m^2 (Northern Hemisphere). Contour interval is .2 x 10^3 m^2.

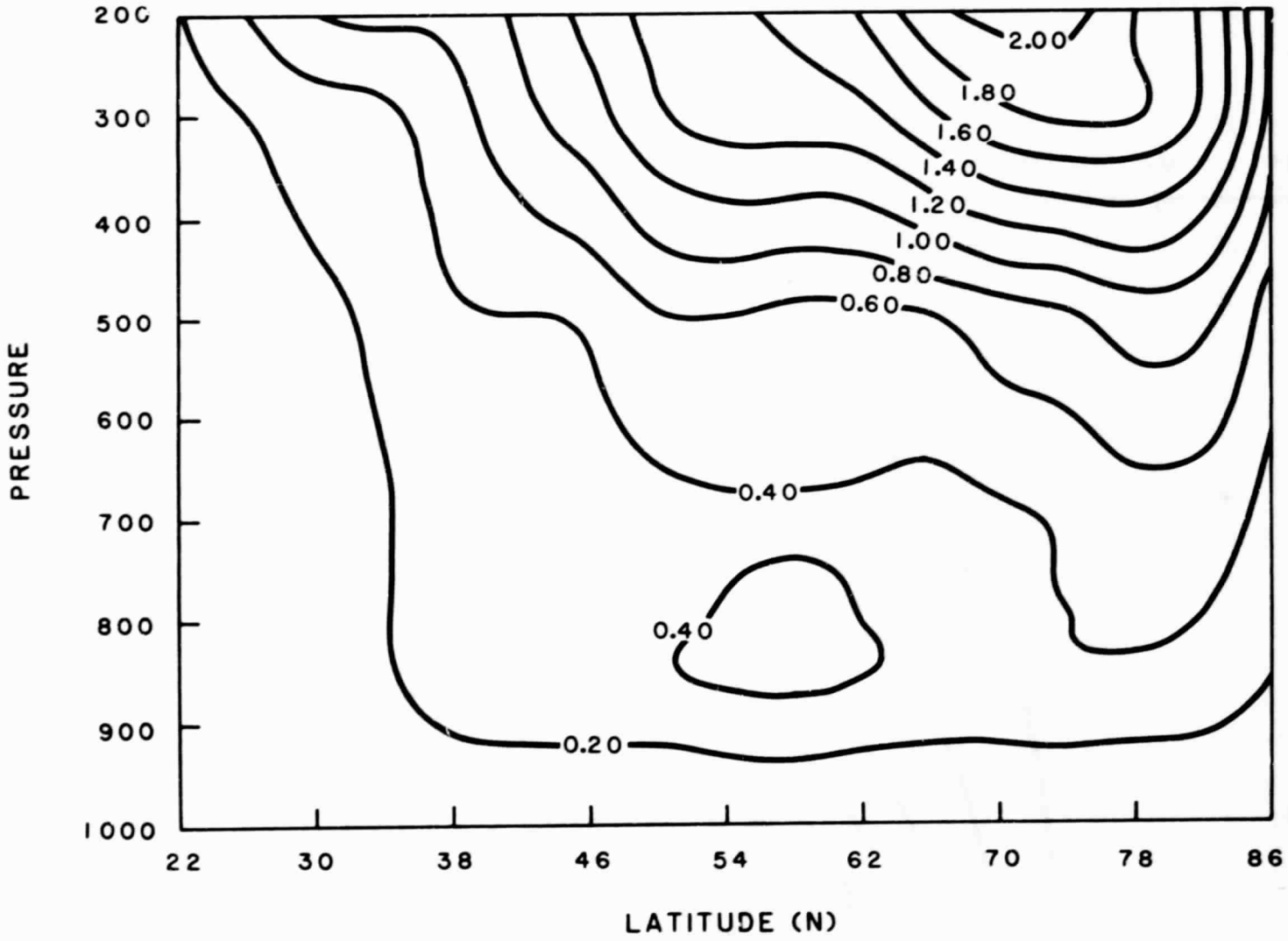

Figure 5.27b GCM winter geopotential height variance in medium-frequency planetary waves, in units of 10^3 m^2 (Northern Hemisphere). Contour interval is .2 x 10^3 m^2.

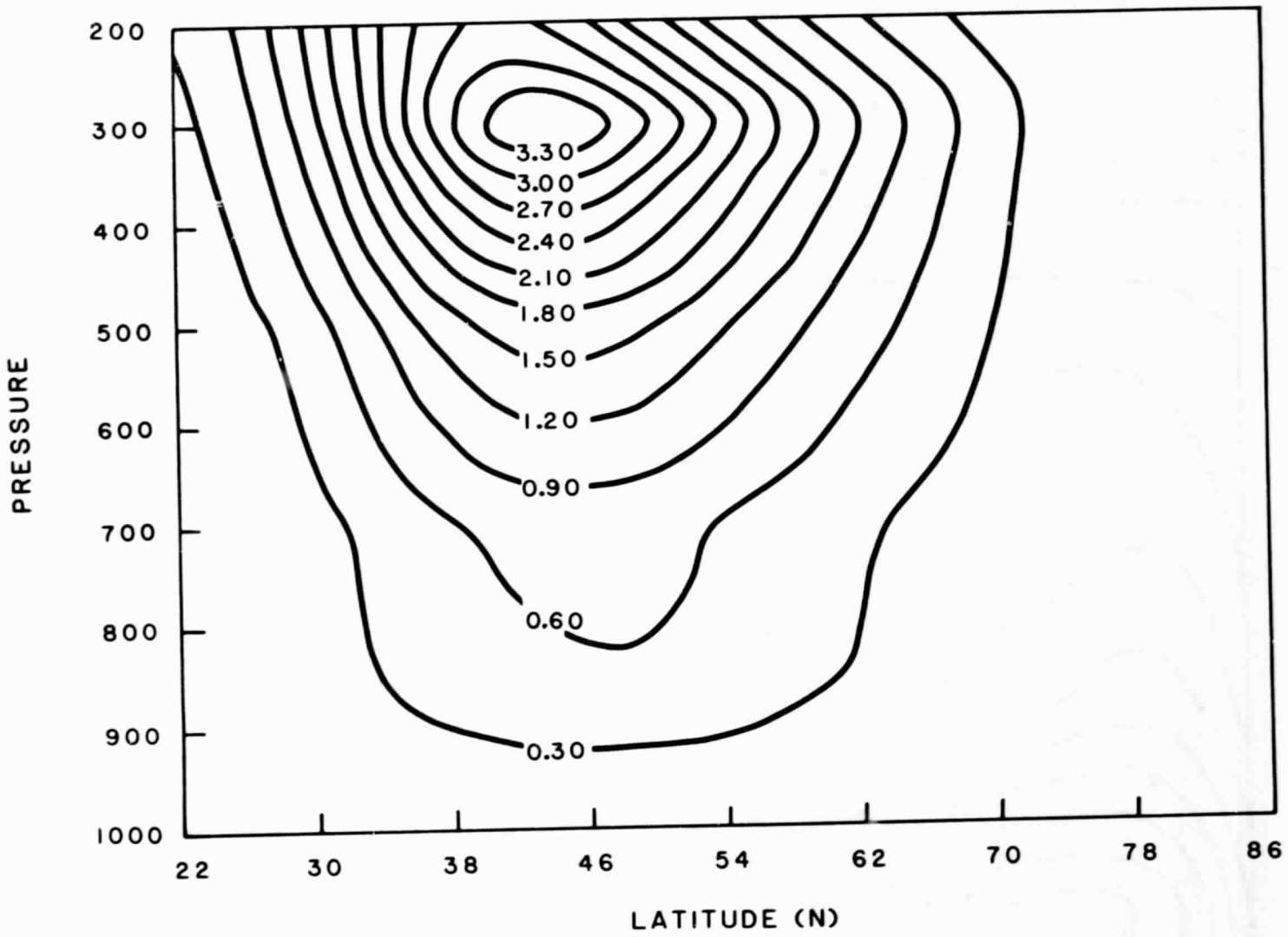

Figure 5.28a Observed winter geopotential height variance in medium-frequency synoptic-scale waves, in units of 10^3 m^2 (Northern Hemisphere). Contour interval is .3 x 10^3 m^2.

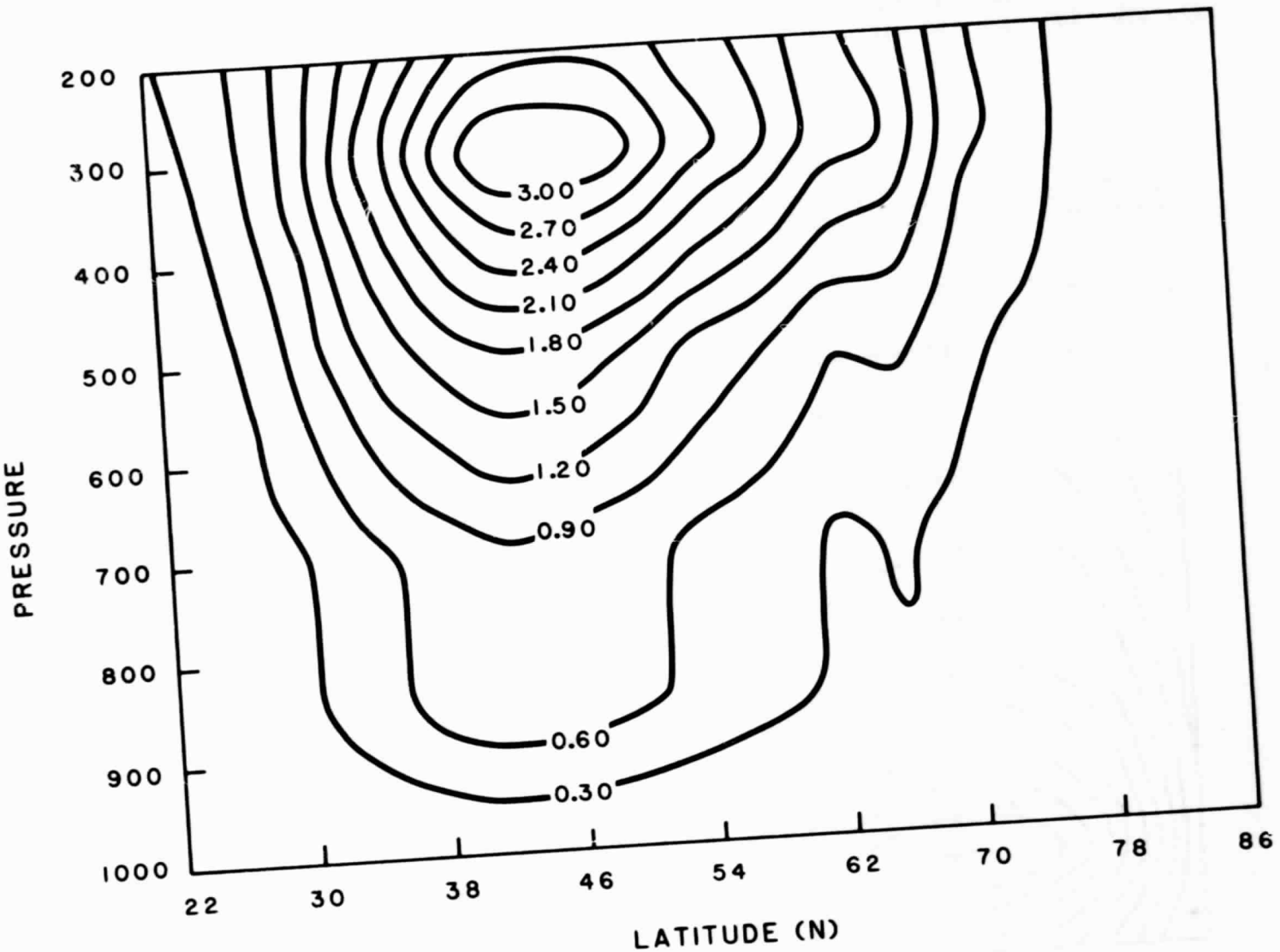

Figure 5.28b GCM winter geopotential height variance in medium-frequency synoptic-scale waves, in units of 10^3 m^2 (Northern Hemisphere). Contour interval is .3 x 10^3 m^2.

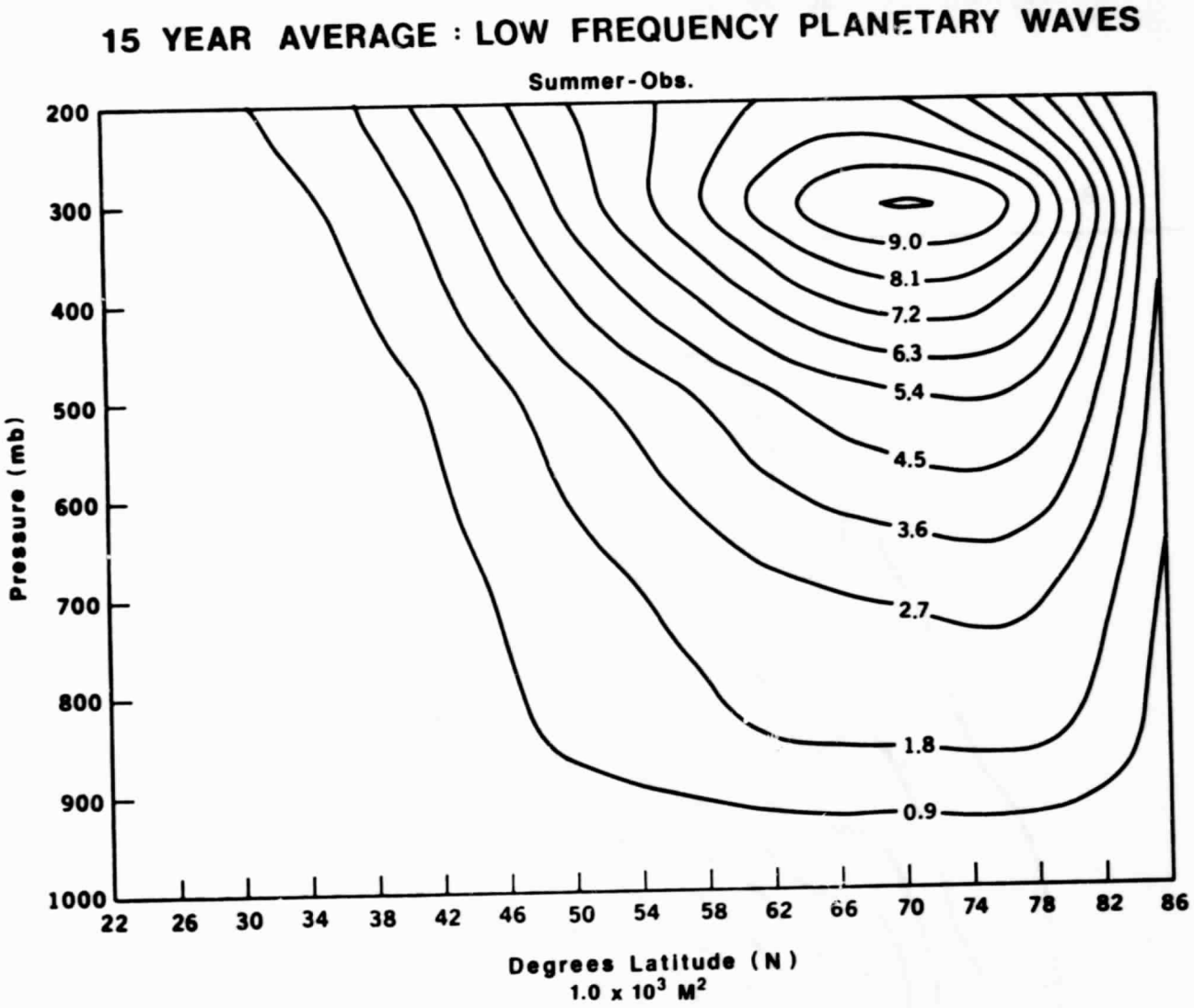

Figure 5.29a Observed summer geopotential height variance in low-frequency planetary waves, in units of 10^3 m^2 (Northern Hemisphere). Contour interval is .9 x 10^3 m^2.

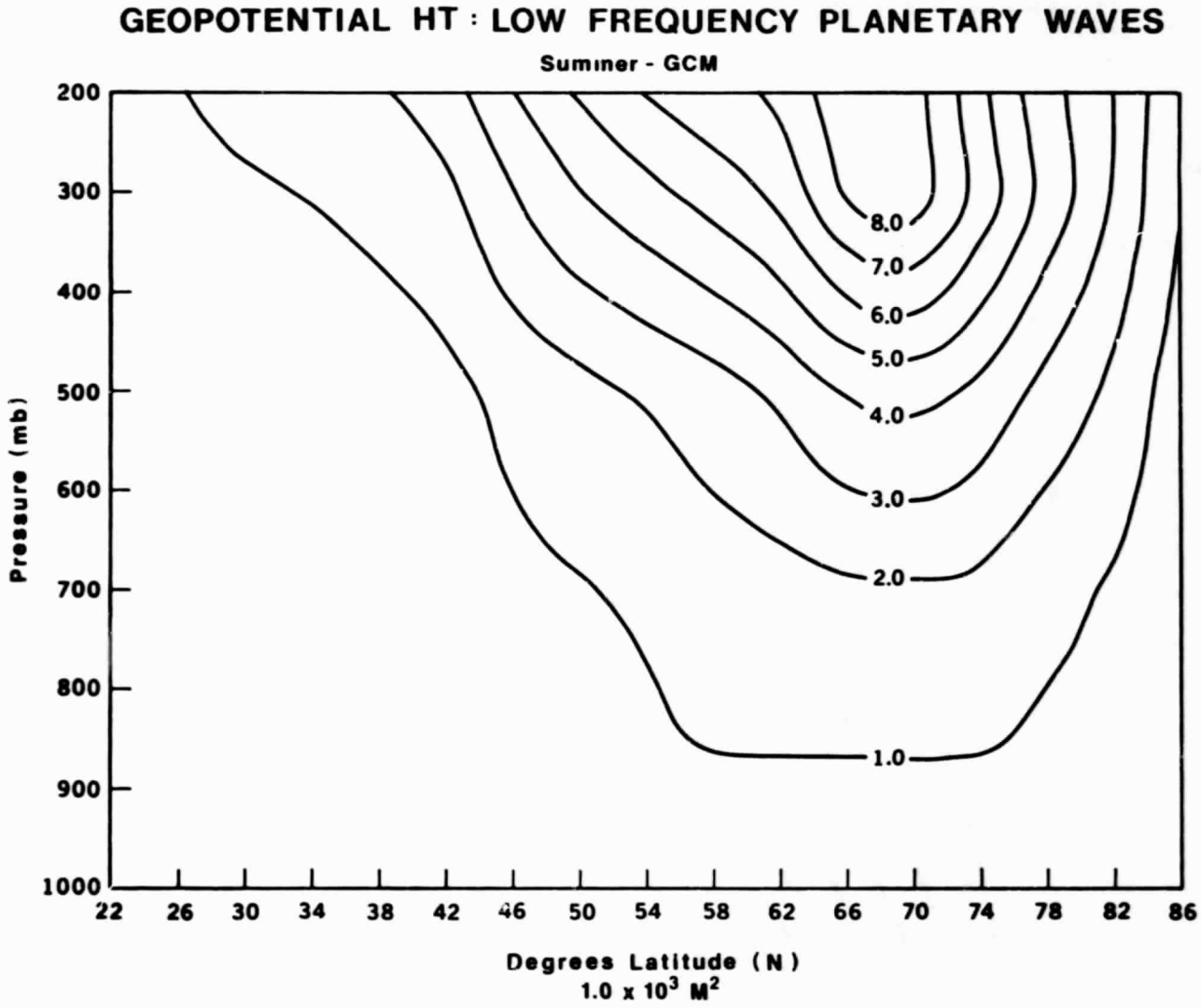

Figure 5.29b GCM summer geopotential height variance in low-frequency planetary waves, in units of 10^3 m^2 (Northern Hemisphere). Contour interval is 1.0 x 10^3 m^2.

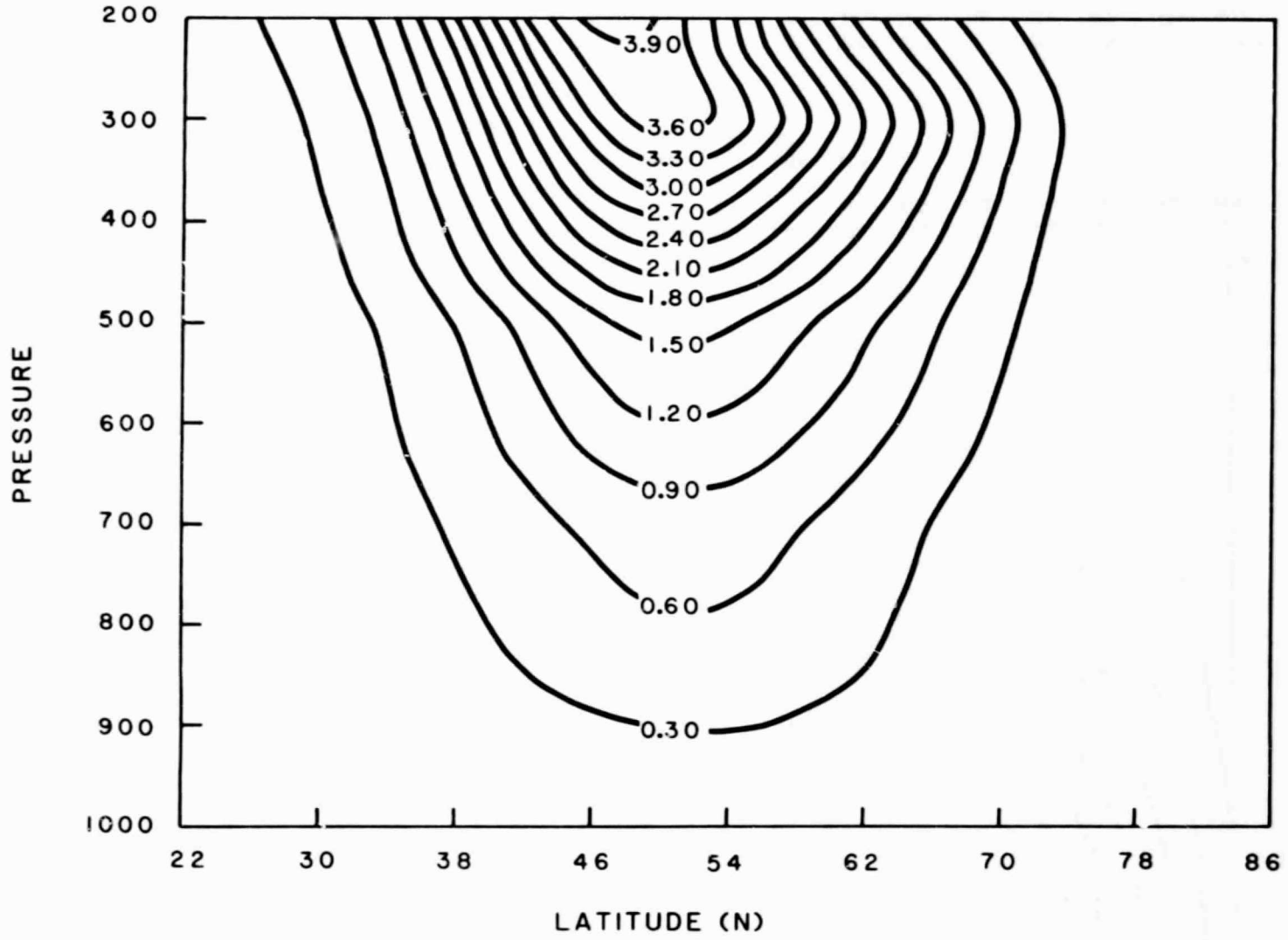

Figure 5.30a Observed summer geopotential height variance in low-frequency synoptic-scale waves, in units 10^3 m^2 (Northern Hemisphere). Contour interval is .3 x 10^3 m^2.

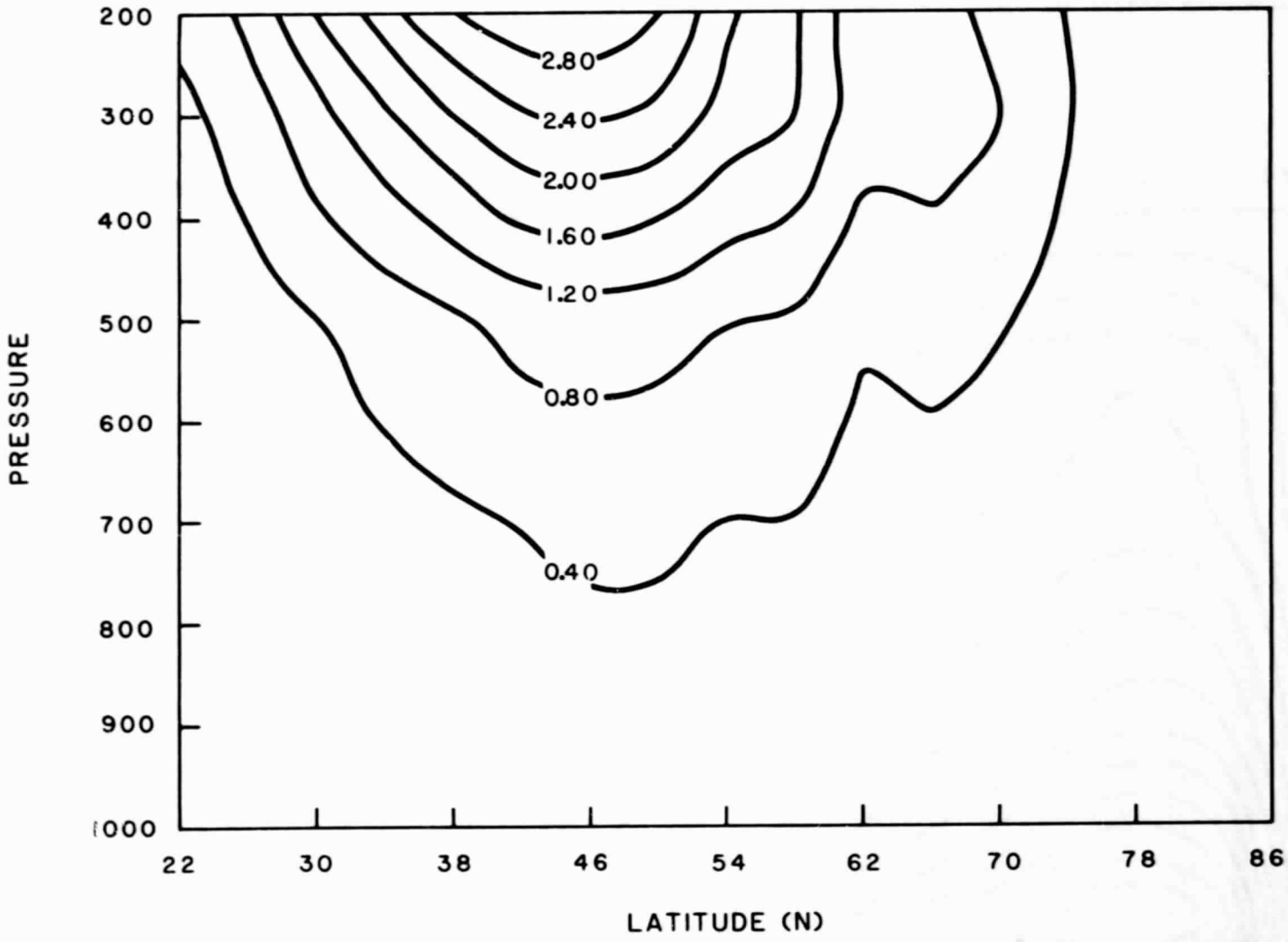

Figure 5.30b GCM summer geopotential height variance in low frequency synoptic-scale waves, in units of 10^3 m^2 (Northern Hemisphere). Contour interval is .4 x 10^3 m^2.

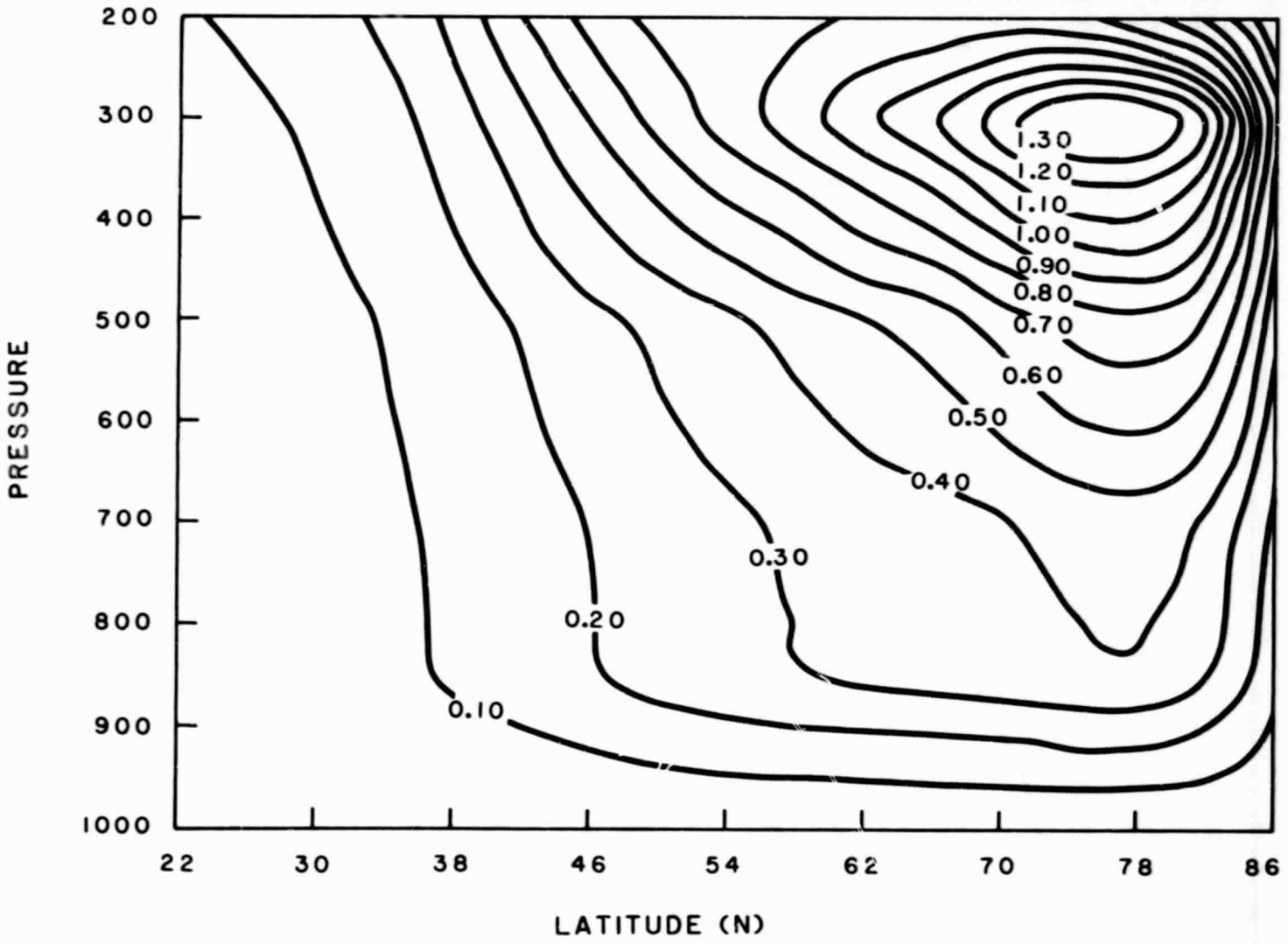

Figure 5.31a Observed summer geopotential height variance in medium frequency planetary waves, in units of 10^3 m^2 (Northern Hemisphere). Contour interval is .1 x 10^3 m^2.

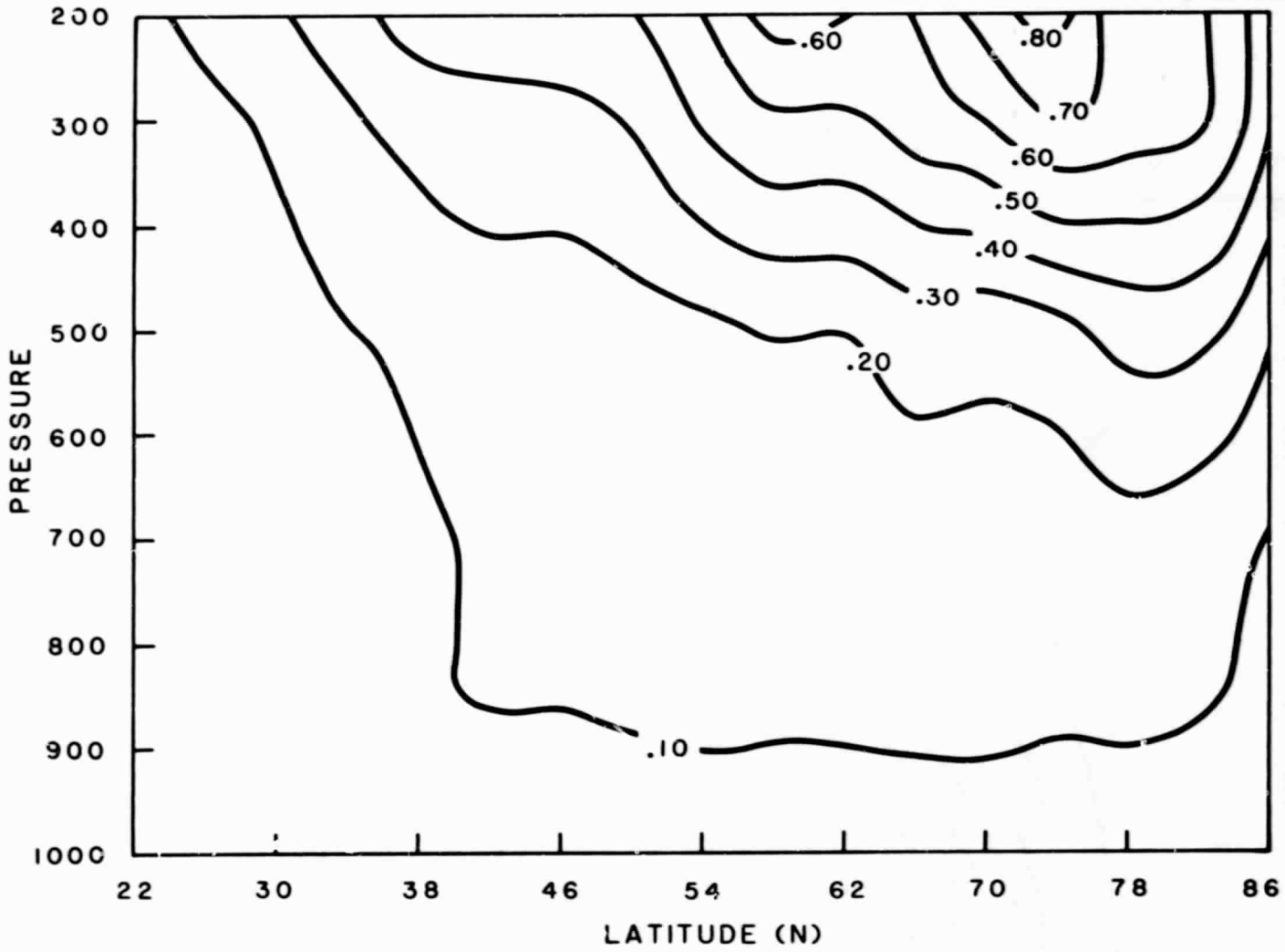

Figure 5.31b GCM summer geopotential height variance in medium frequency planetary waves, in units of 10^3 m^2 (Northern Hemisphere). Contour interval is 0.1 x 10^3 m^2.

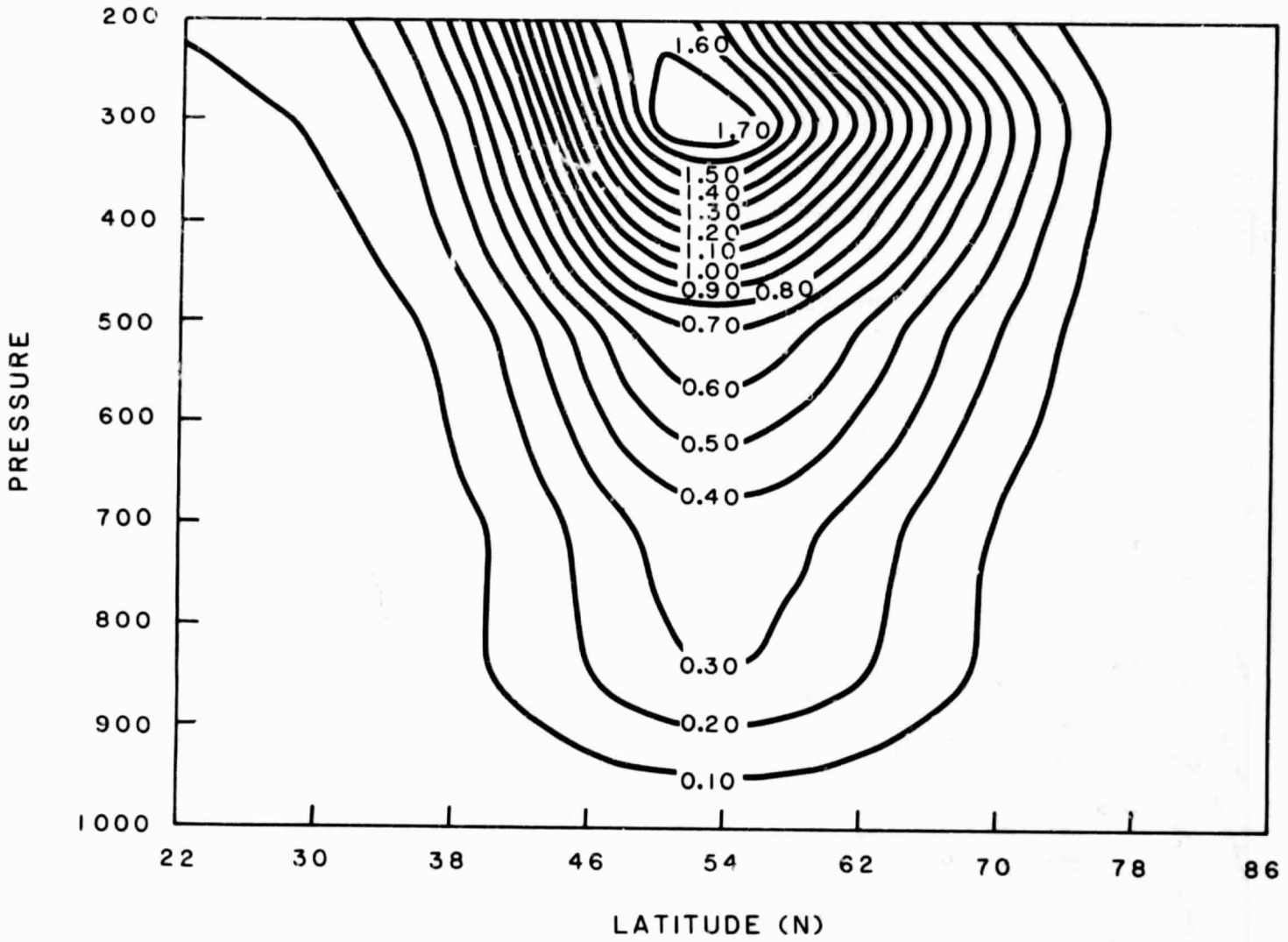

Figure 5.32a Observed summer geopotential height variance in medium frequency synoptic-scale waves, in units of 10^3 m^2 (Northern Hemisphere). Contour interval is .1 x 10^3 m^2.

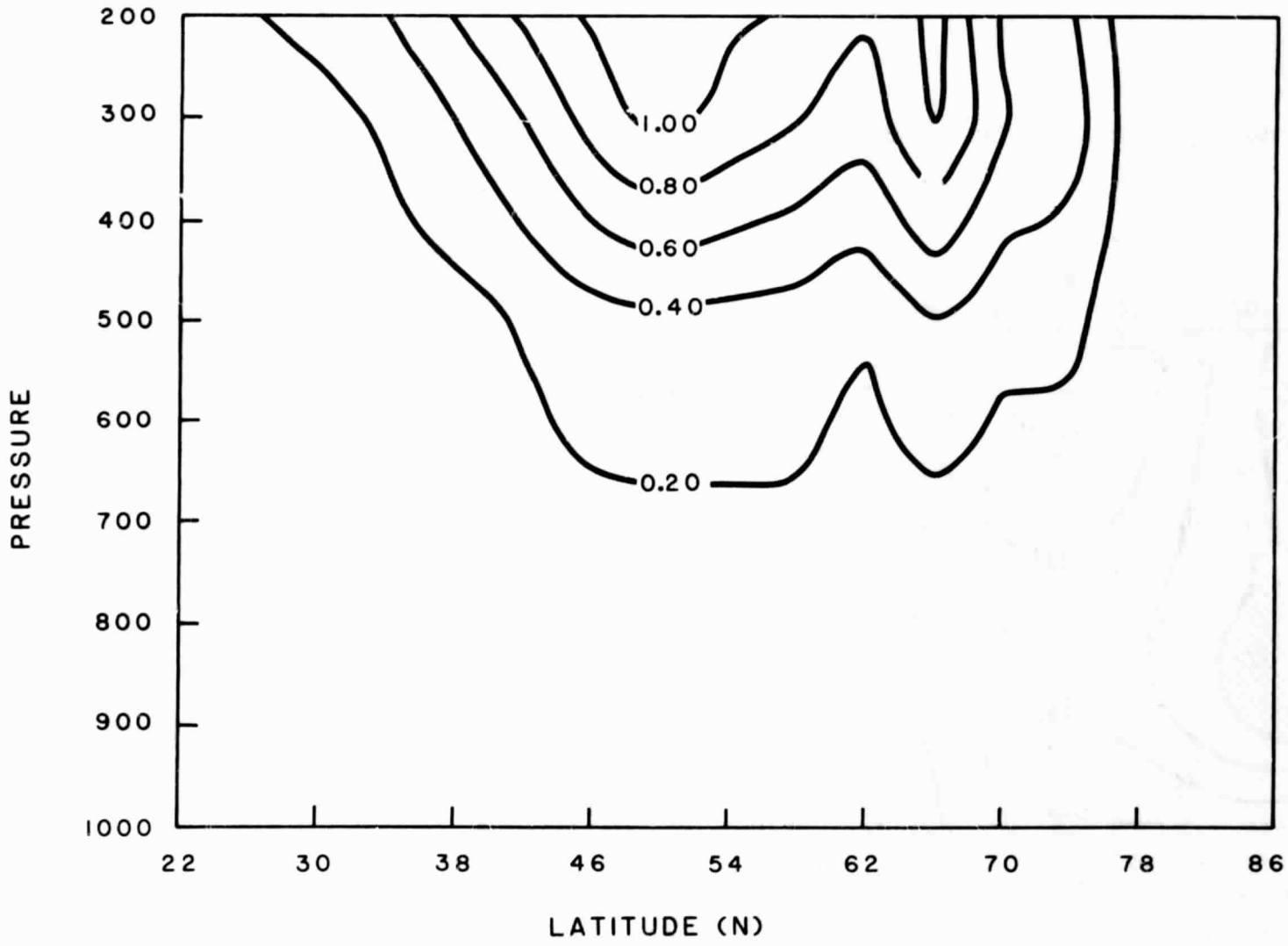

Figure 5.32b GCM summer geopotential height variance in medium frequency synoptic-scale waves, in units of 10^3 m^2 (Northern Hemisphere). Contour interval is .2 x 10^3 m^2.

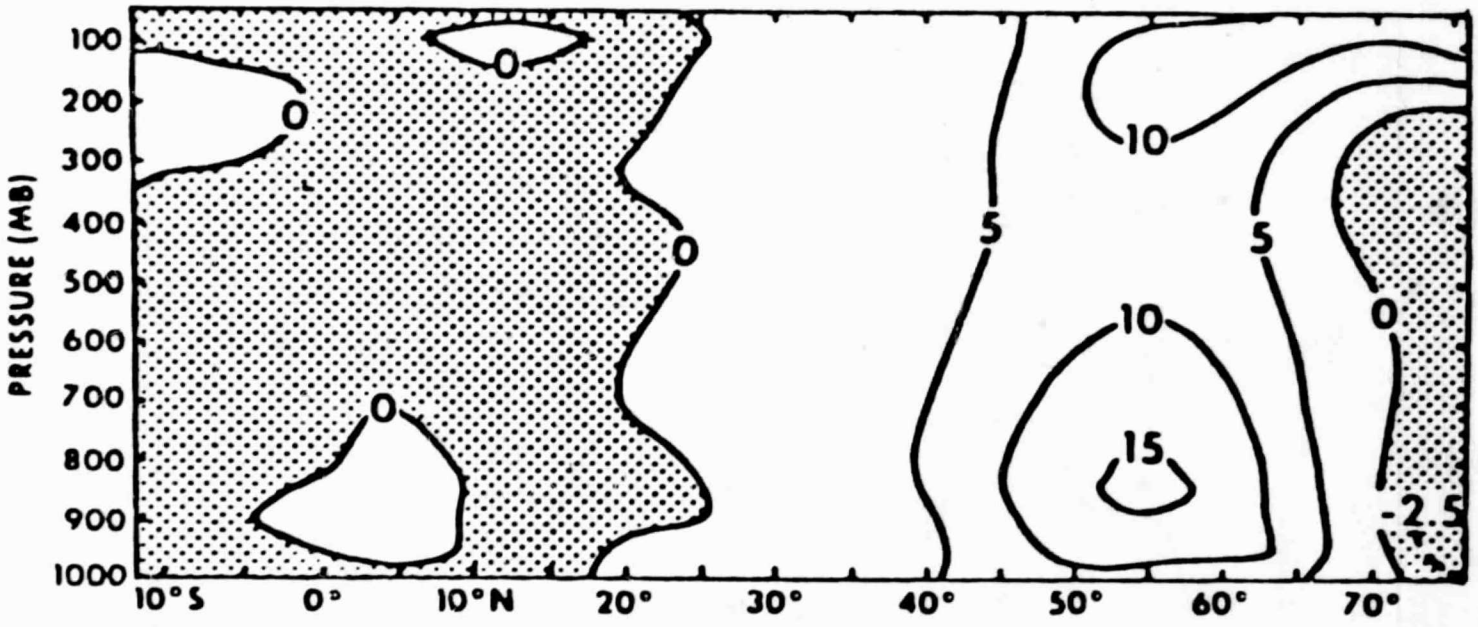

Figure 5.33a Observed February stationary eddy heat flux, in units of °K m/sec.

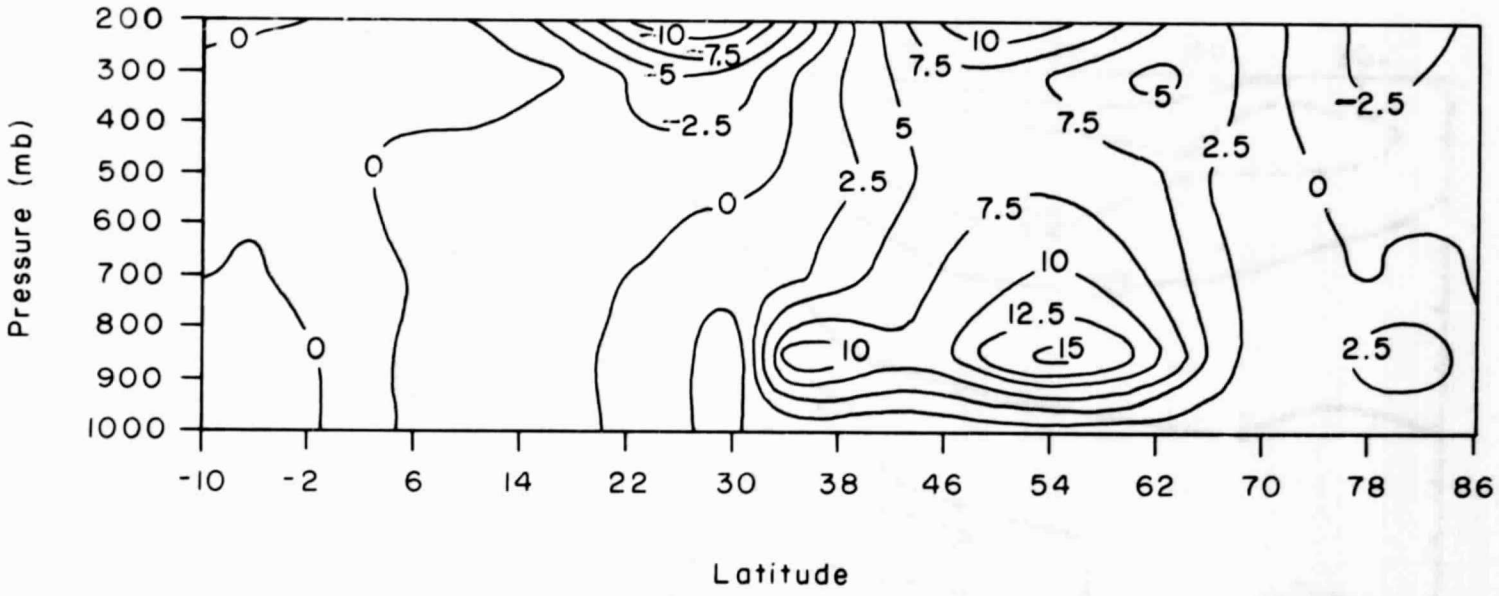

Figure 5.33b GCM February stationary eddy heat flux, in units of °K m/sec.

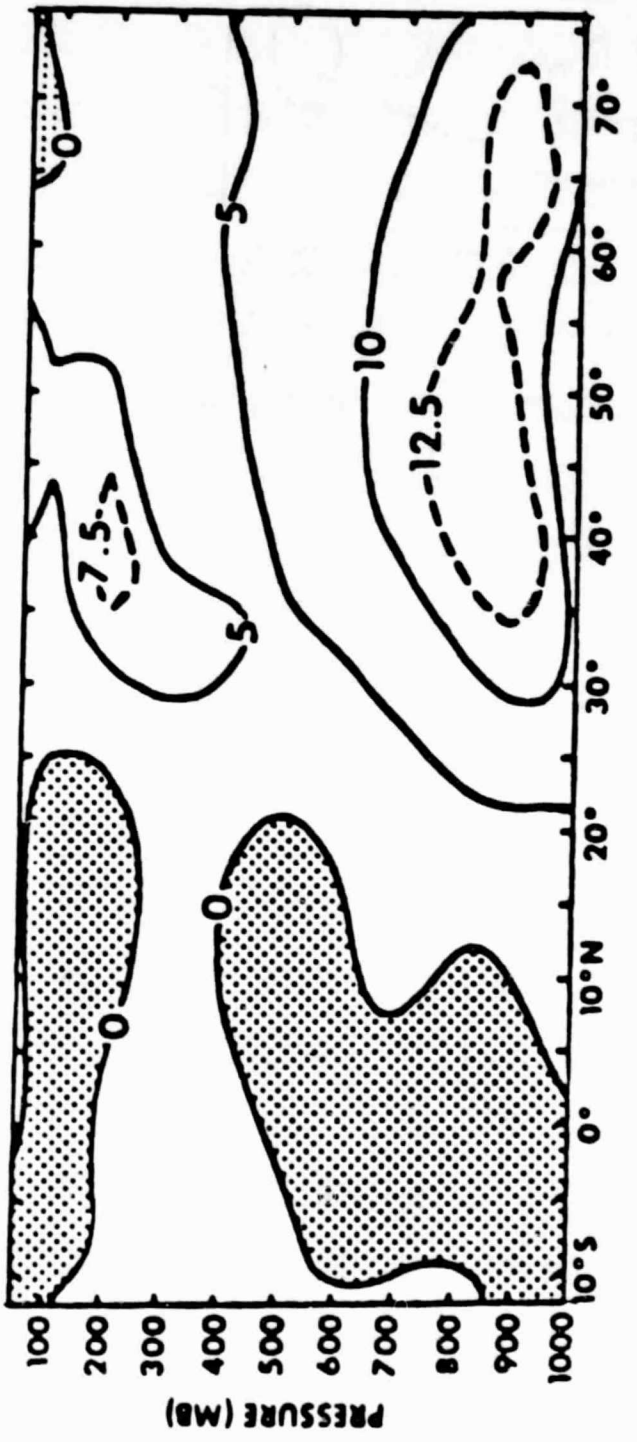

Figure 5.34a Observed February transient eddy heat flux, in units of °K m/sec.

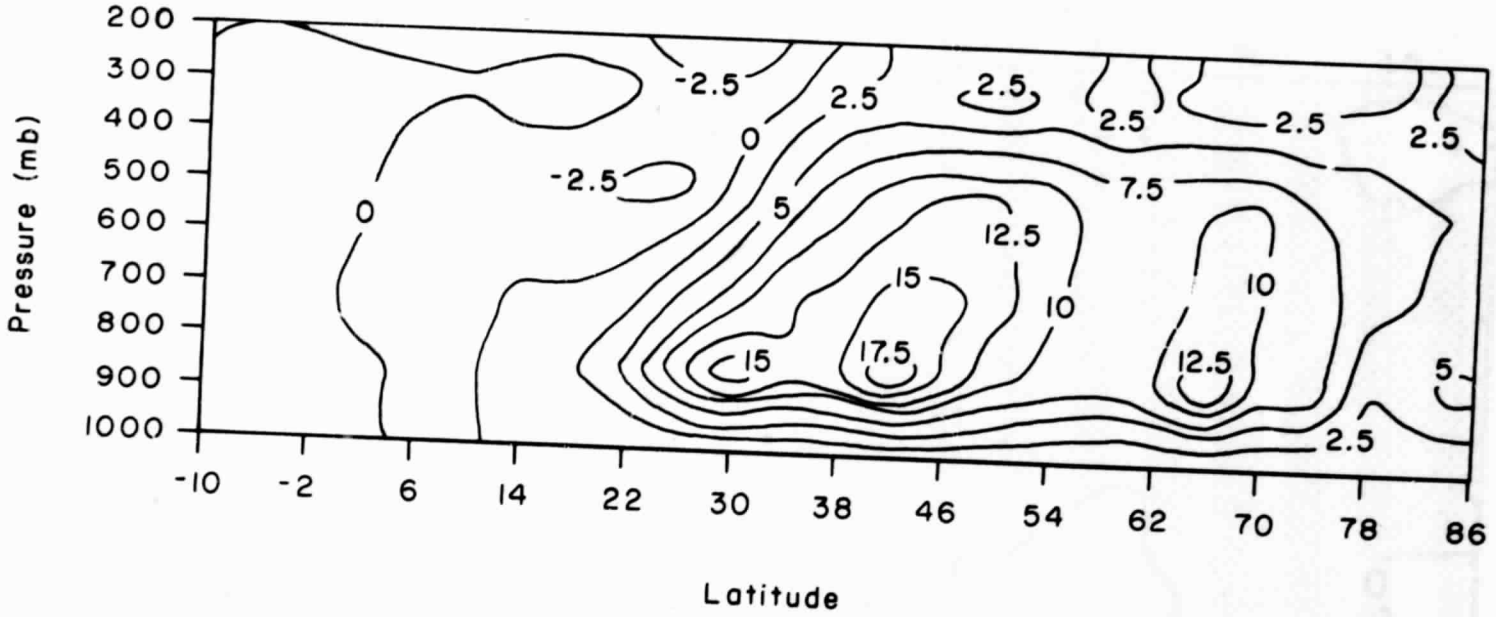

Figure 5.34b GCM February transient eddy heat flux, in units of °K m/sec.

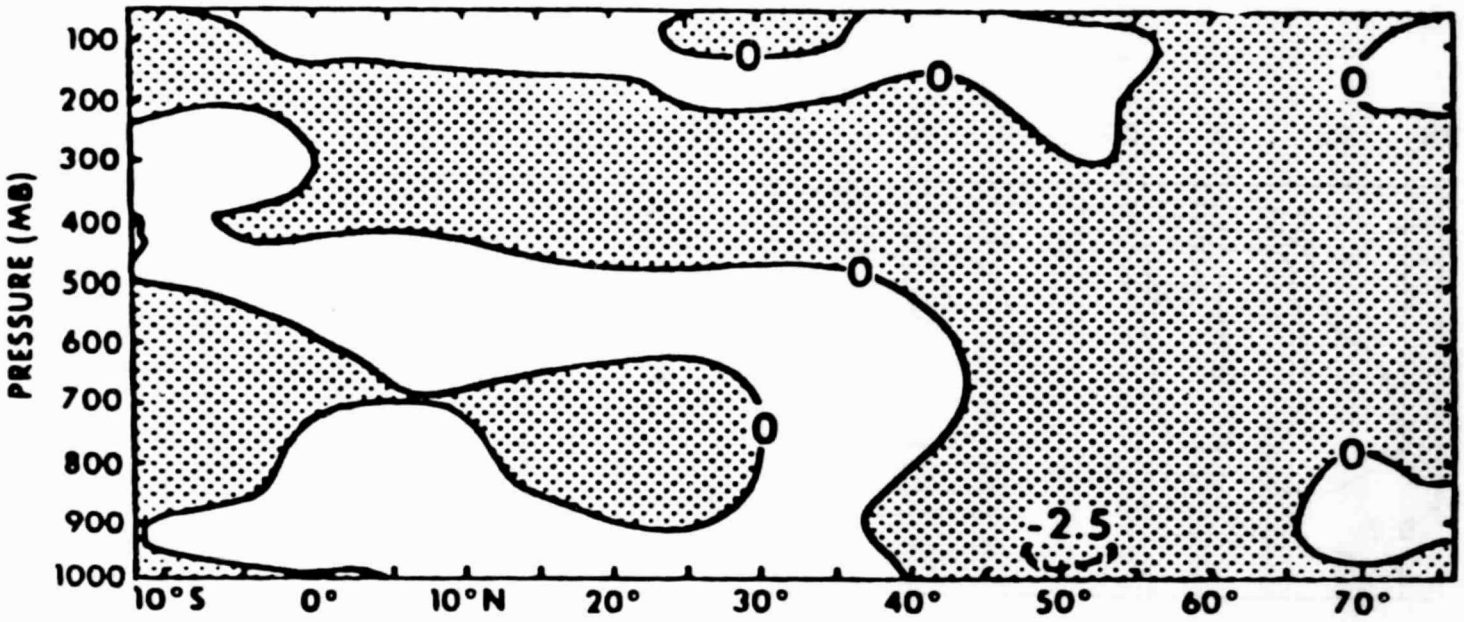

Figure 5.35a Observed July stationary eddy heat flux, in units of °K m/sec.

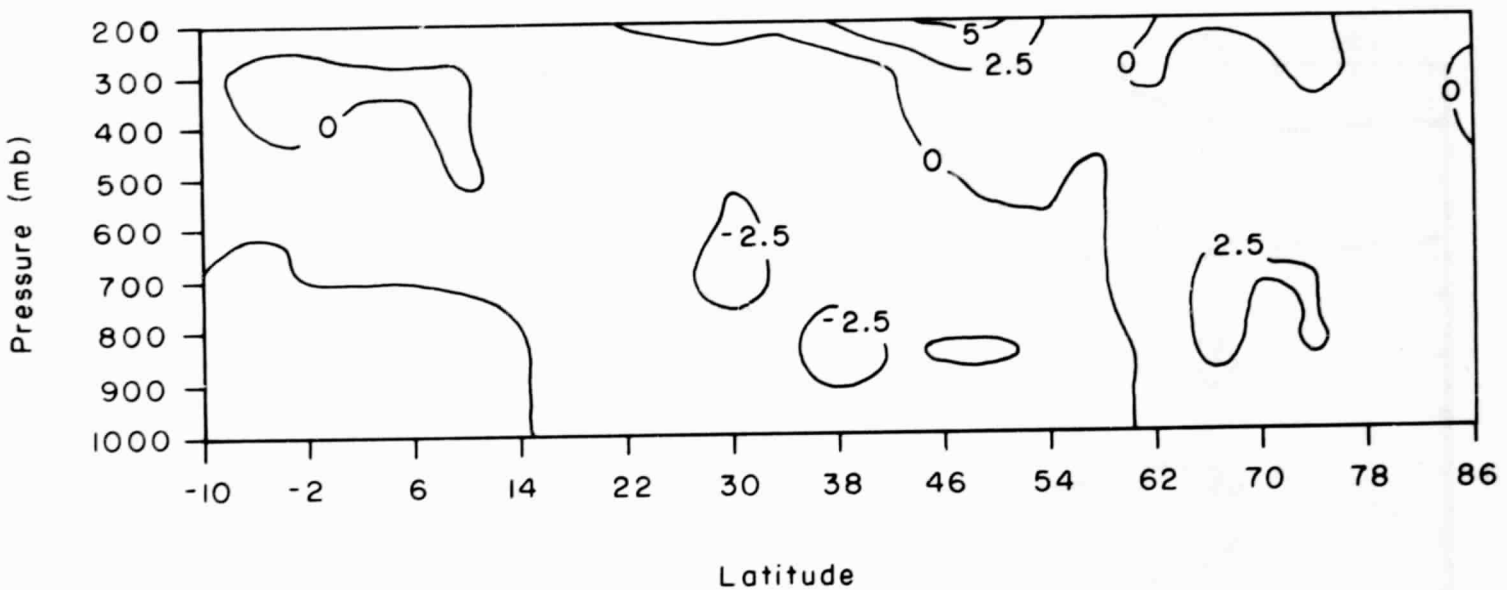

Figure 5.35b GCM July stationary heat flux, in units of °K m/sec.

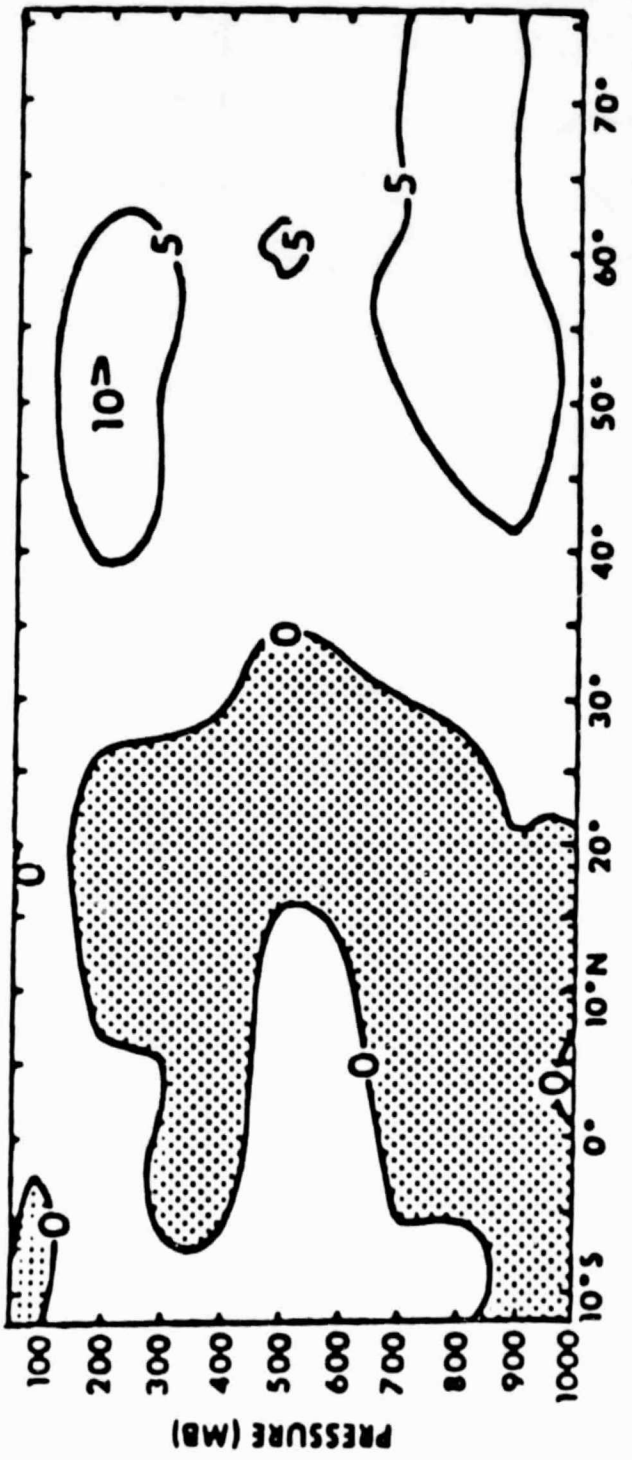

Figure 5.36a Observed July transient eddy heat flux, in units of °K m/sec.

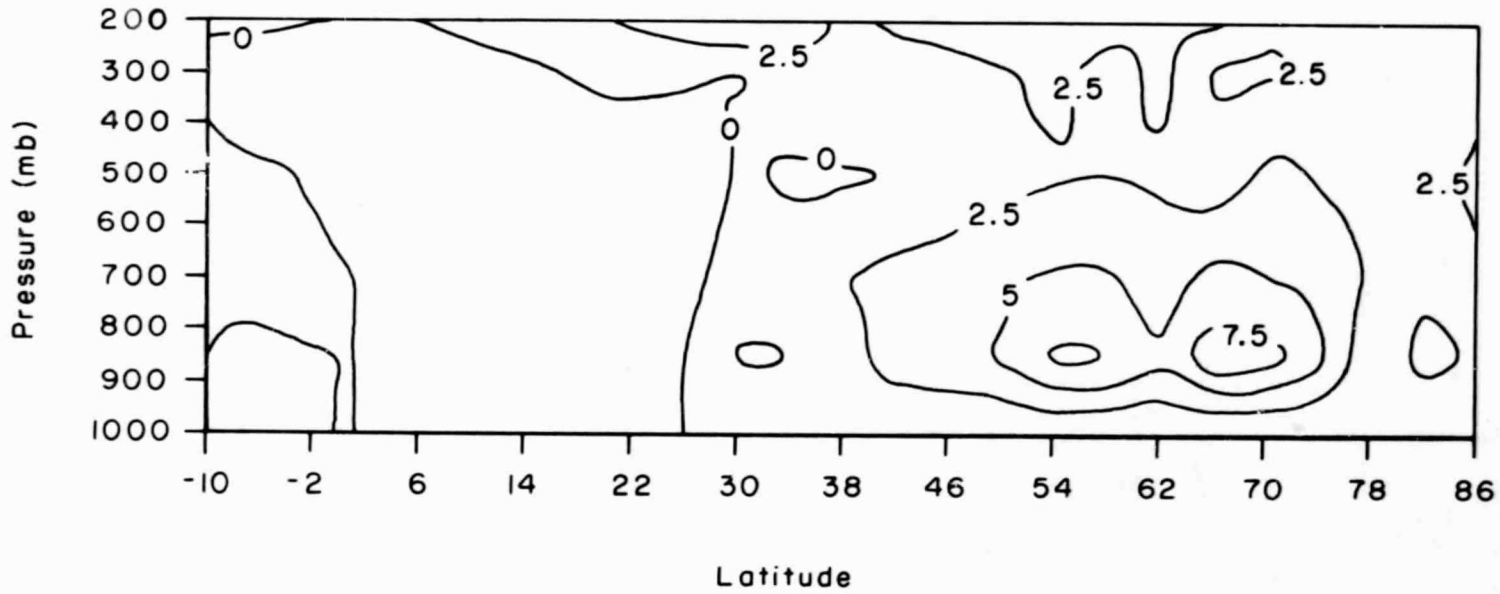

Figure 5.36b GCM July transient eddy heat flux, in units of °K m/sec.

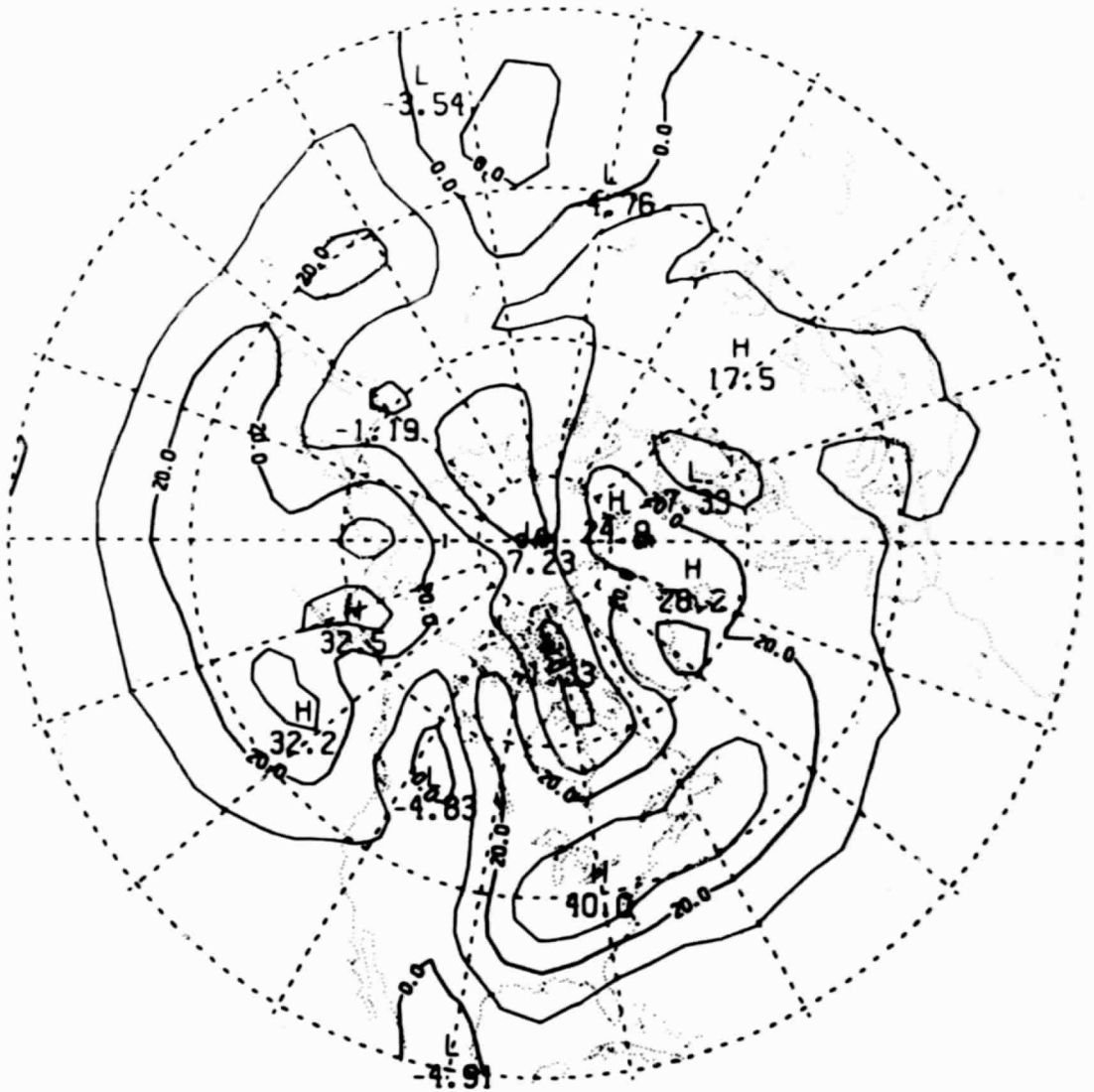

Figure 5.37a Observed winter local transient heat flux at 850 mb, in units of °K m/sec. Contour interval is 10°K m/sec (Northern Hemisphere).

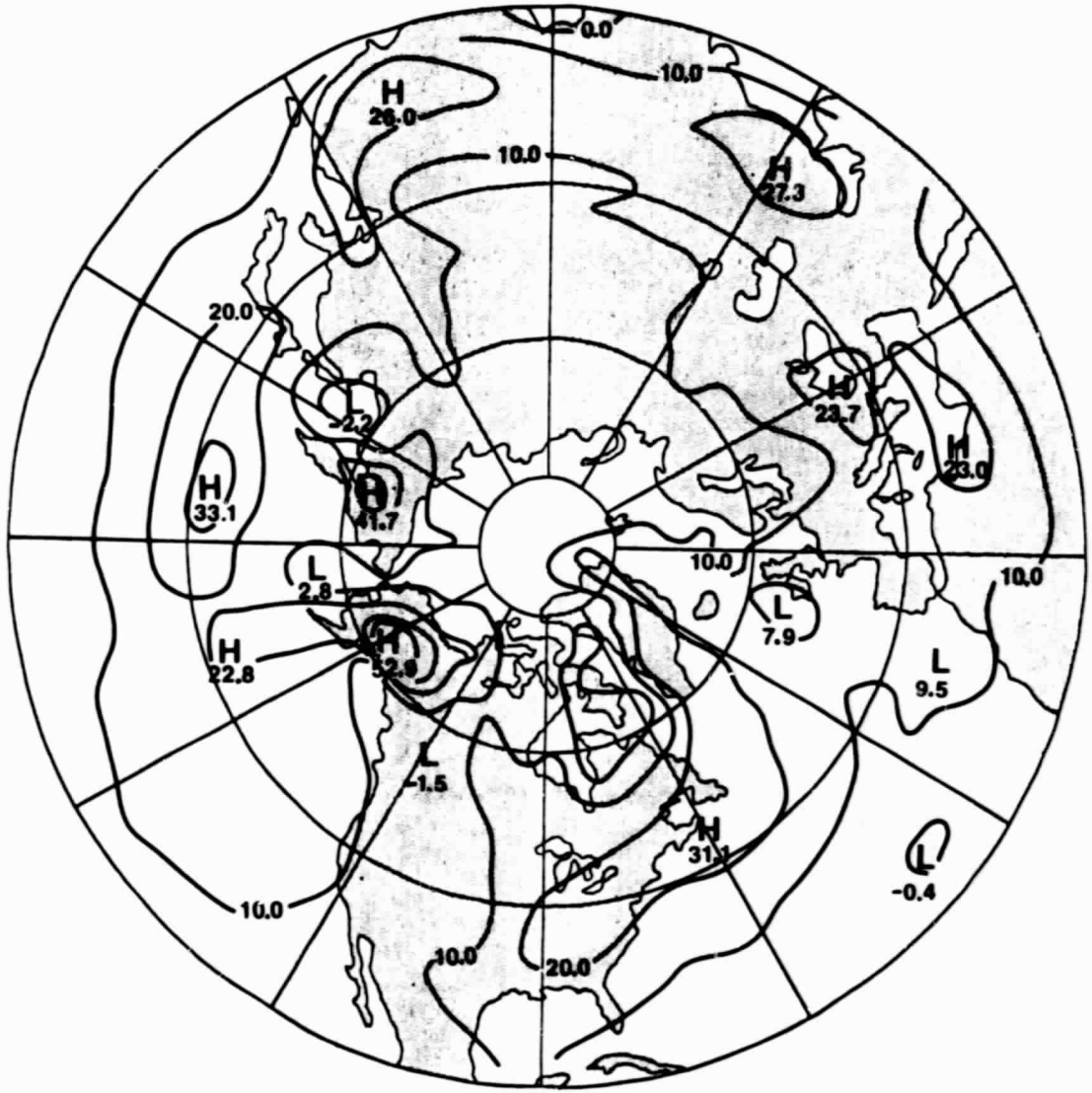

Figure 5.37b GCM winter local transient heat flux at 850 mb, in units of °K m/sec. Contour interval is 10°K m/sec (Northern Hemisphere). (Several contours have been omitted in the immediate vicinity of very sharp maxima or minima.)

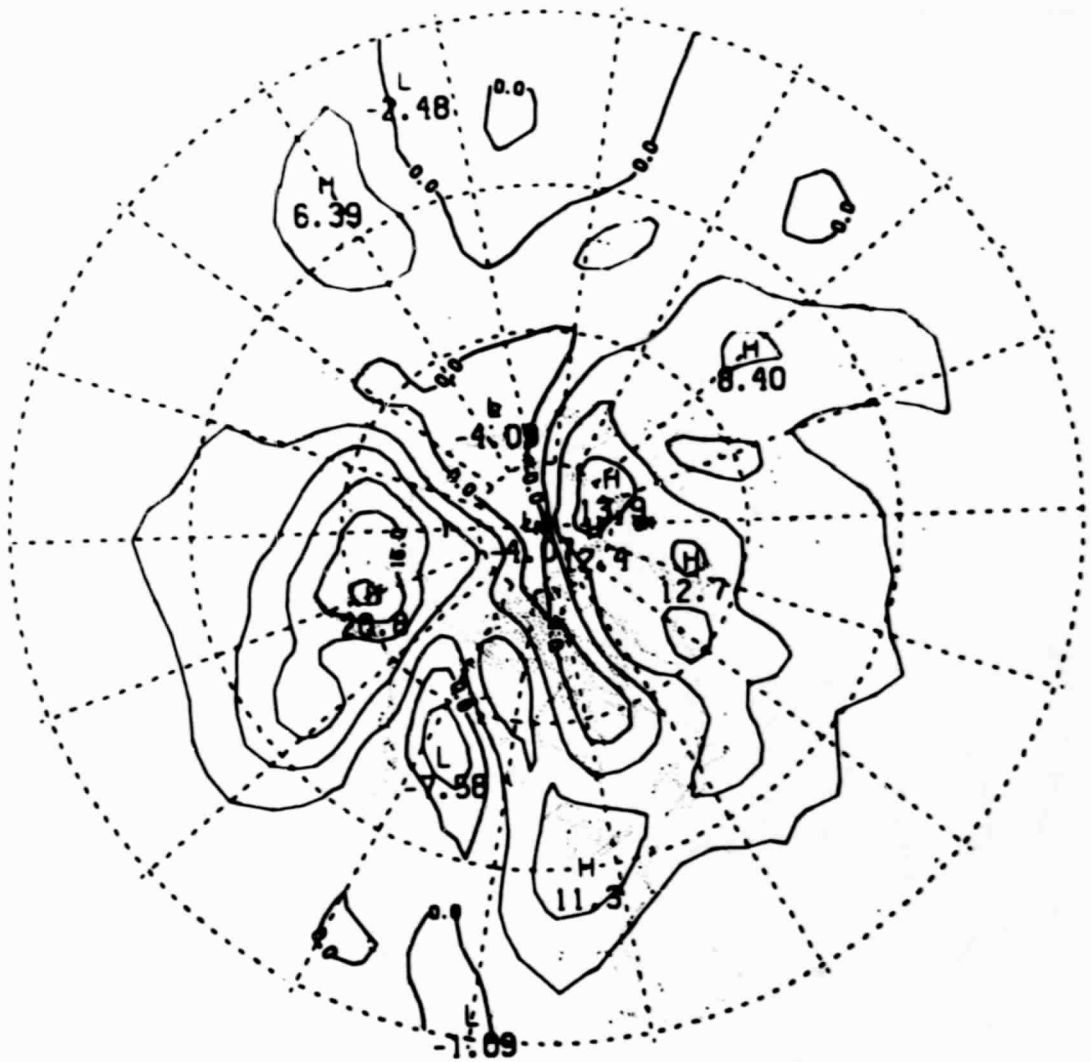

Figure 5.38a Observed winter local low-pass transient heat flux at 850 mb, in units of °K m/sec. Contour interval is 4°K m/sec (Northern Hemisphere).

Figure 5.38b GCM winter local low-pass transient heat flux at 850 mb, in units of °K m/sec. Contour interval is 4°K m/sec (Northern Hemisphere). (Several contours have been omitted in the immediate vicinity of very sharp maxima or minima.)

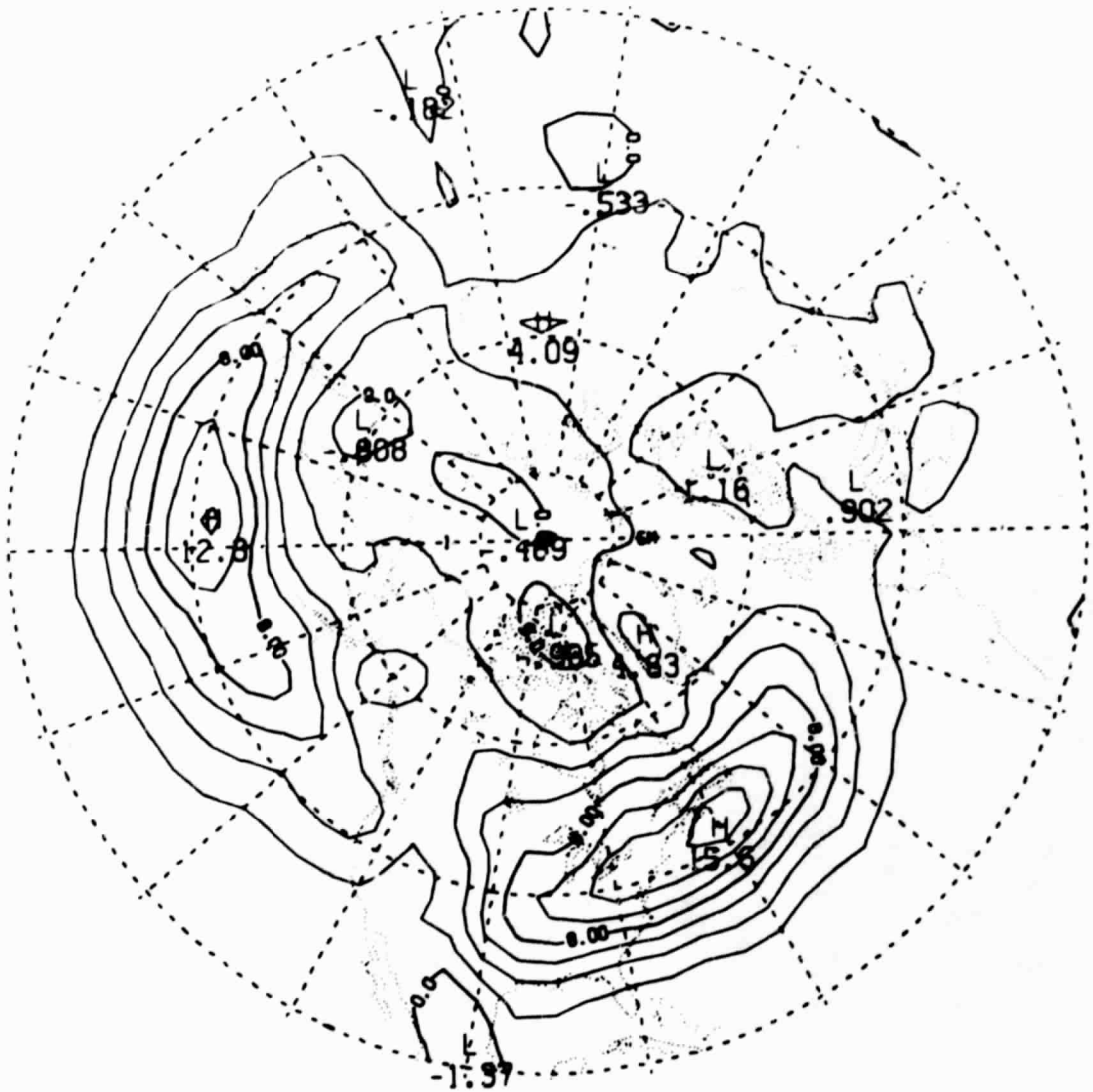

Figure 5.39a Observed winter local band-pass transient heat flux at 850 mb, in units of °K m/sec. Contour interval is 2°K m/sec (Northern Hemisphere).

Figure 5.39b GCM winter local band-pass transient heat flux at 850 mb, in units of °K m/sec. Contour interval is 2°K m/sec (Northern Hemisphere).

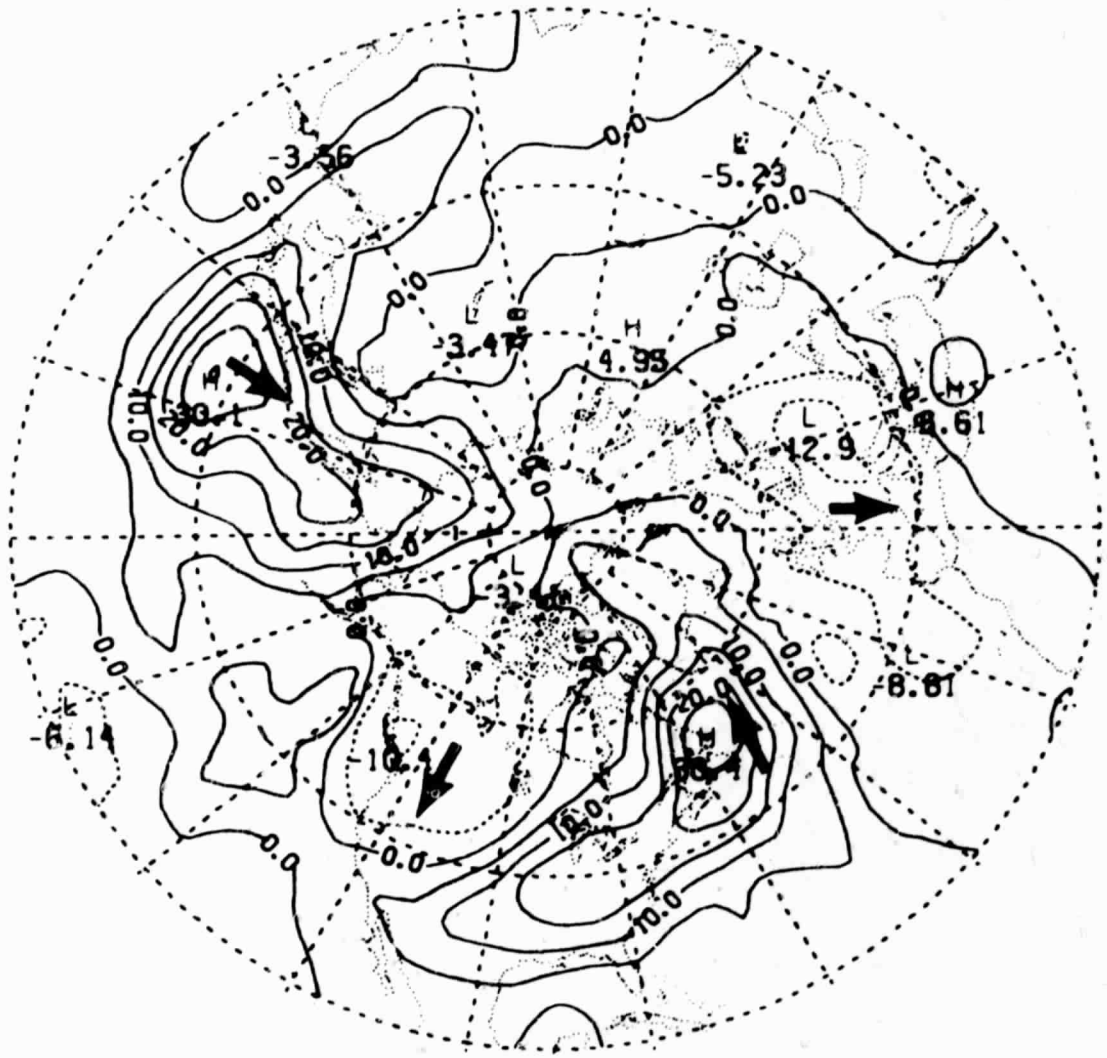

Figure 5.40a Observed winter local transient heat flux at 300 mb, in units of °K m/sec. Contour interval is 5°K m/sec (Northern Hemisphere).

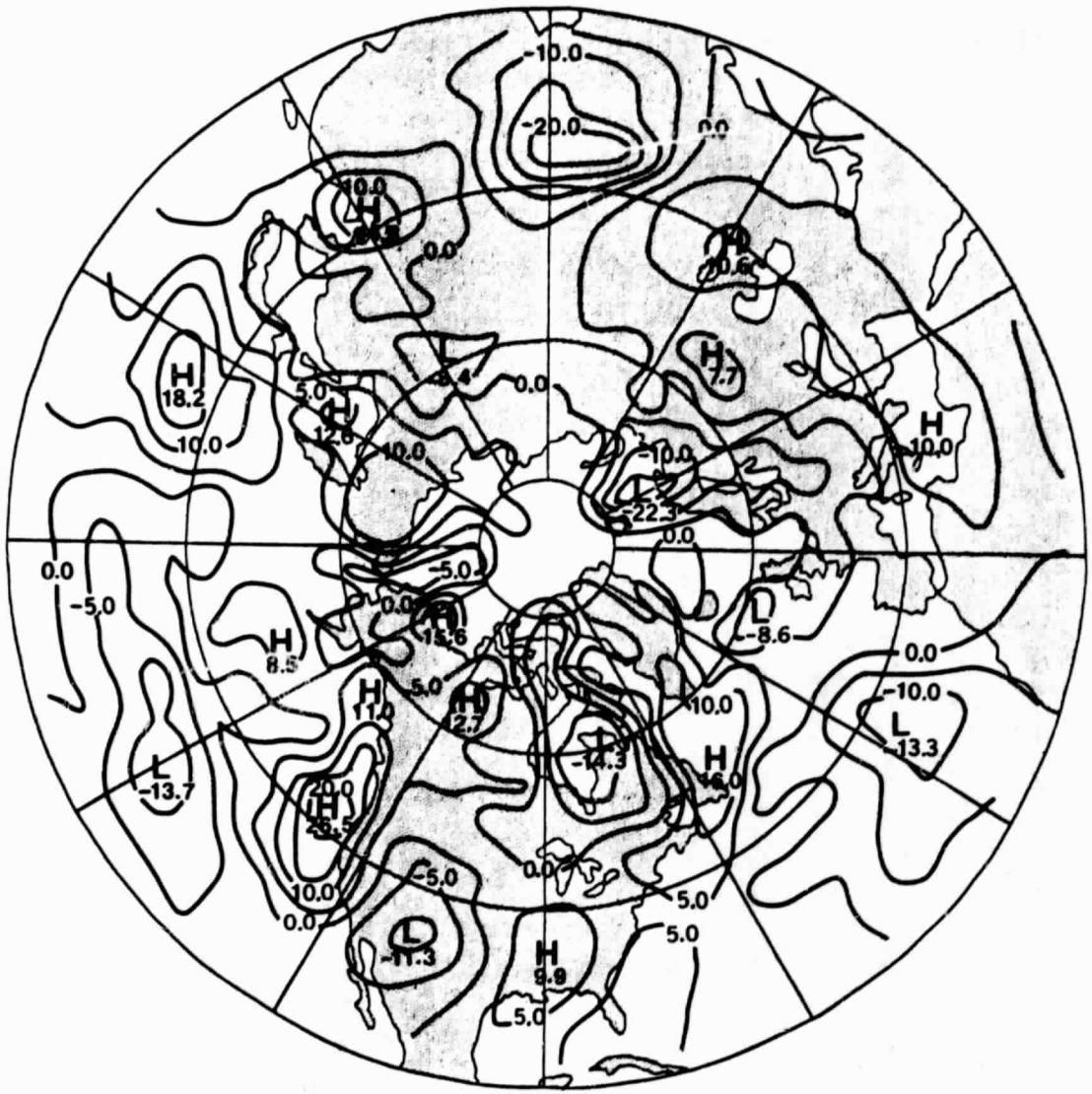

Figure 5.40b GCM winter local transient heat flux at 300 mb, in units of °K m/sec. Contour interval is 5°K m/sec (Northern Hemisphere). (Several contours have been omitted in the immediate vicinity of very sharp maxima or minima.)

Figure 5.41a Observed winter local transient heat flux at 200 mb, in units of °K m/sec. Contour interval is 5°K m/sec (Northern Hemisphere).

Figure 5.41b GCM winter local transient heat flux at 200 mb, in units of °K m/sec. Contour interval is 5°K m/sec (Northern Hemisphere).

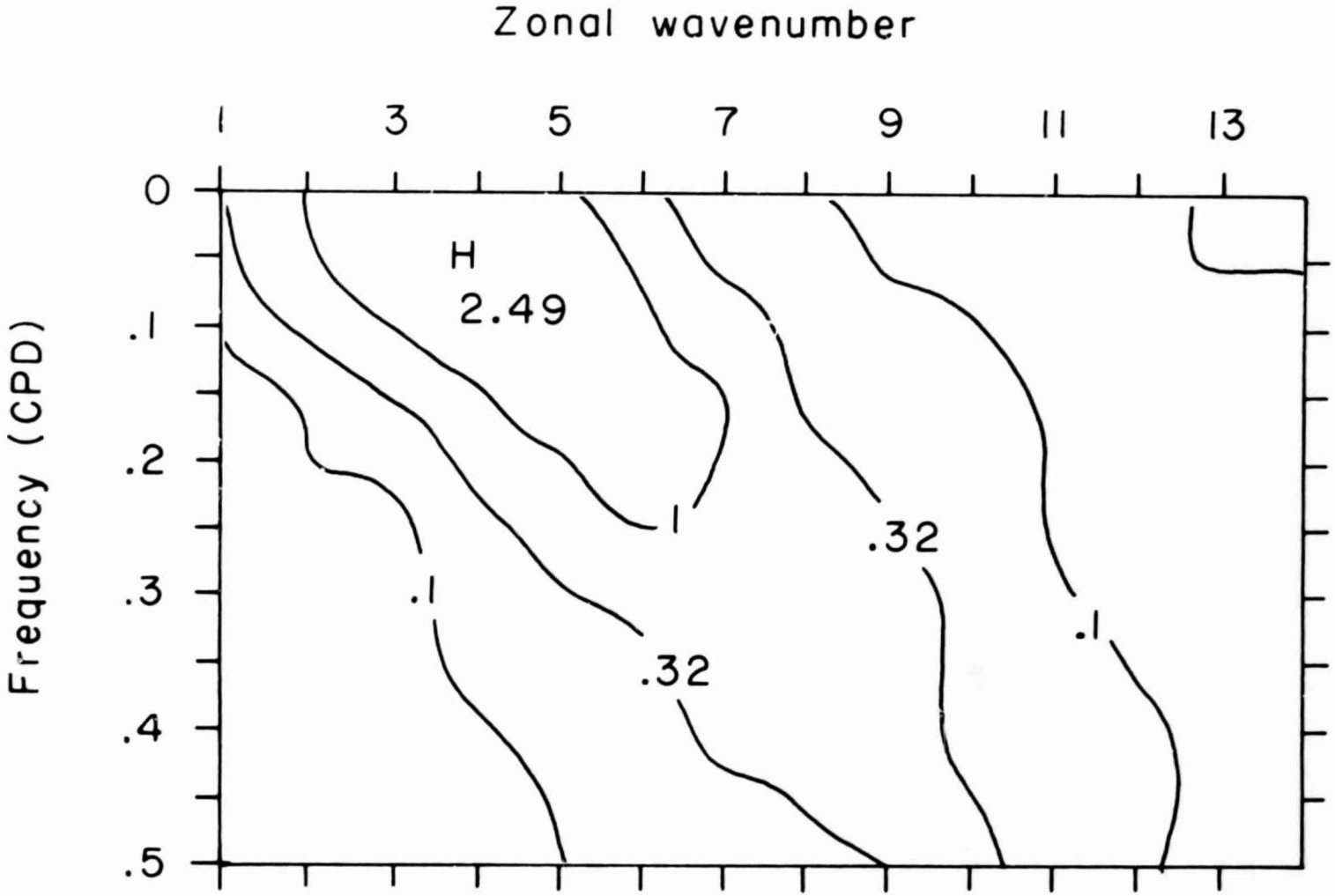

Figure 5.42a Observed wavenumber-frequency cospectral density of winter 850 mb heat flux at 50N, in units of °K m/sec/cpd. The cospectral density is defined as the covariance in a given frequency band divided by 2π times the width of that band. The presence of a non-zero spectral density at zero frequency is an artifact introduced for the sake of the visual clarity of the plot.

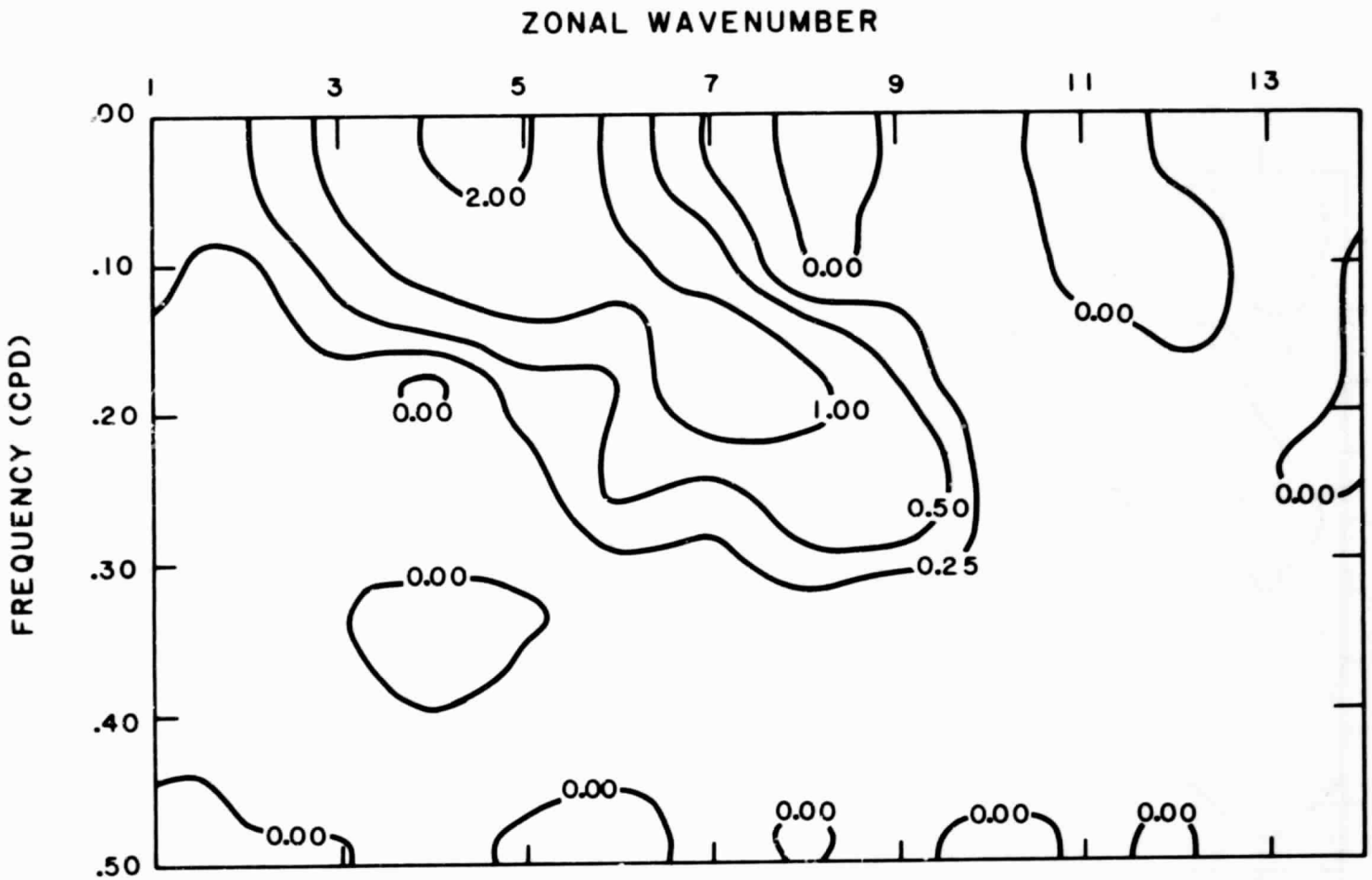

Figure 5.42b GCM wavenumber-frequency cospectral density of winter 850 mb heat flux at 50N, in units of °K m/sec/cpd. Otherwise as in Figure 5.42a.

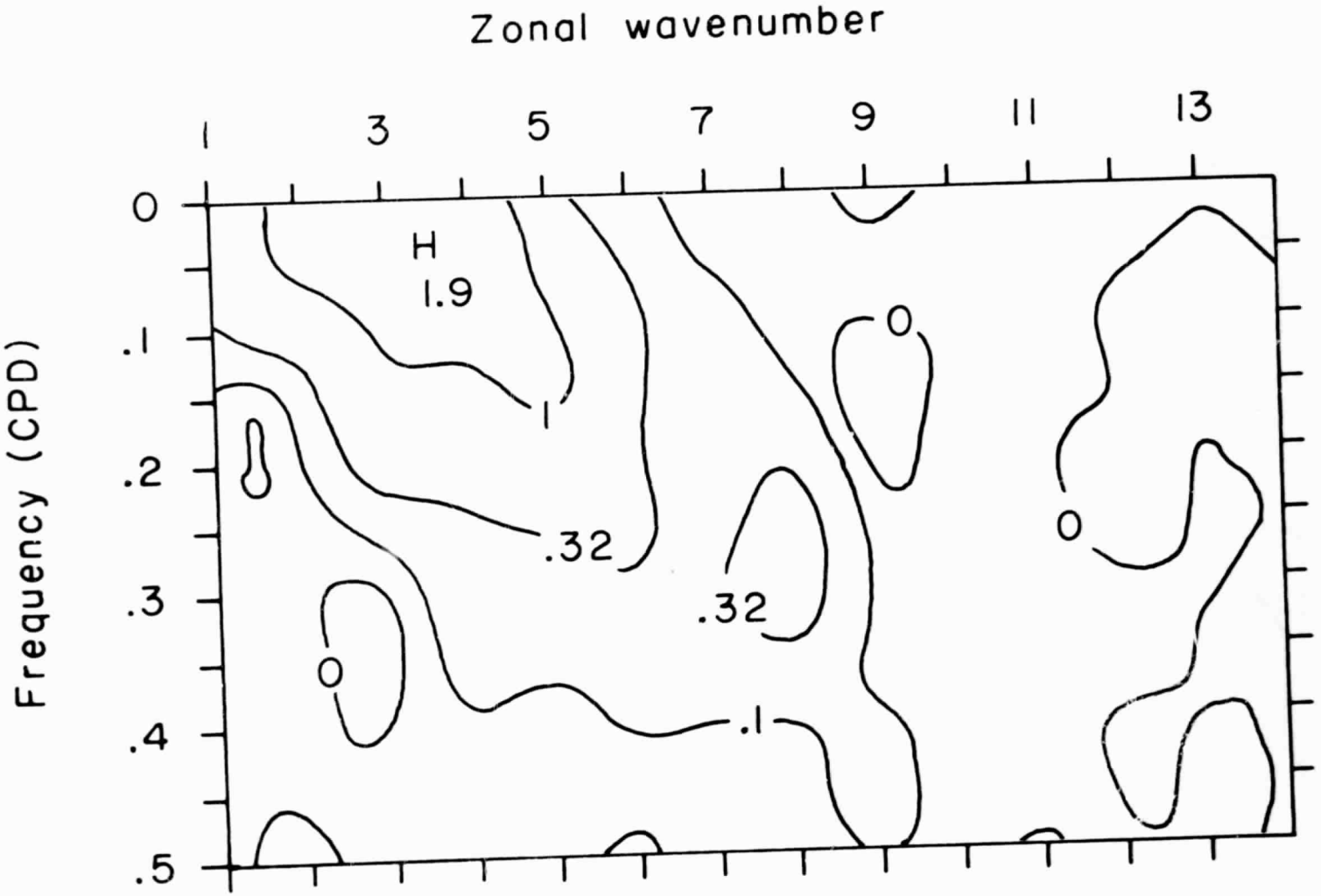

Figure 5.43a Observed wavenumber frequency cospectral density of winter 200 mb heat flux at 50N, in units of °K m/sec/cpd. Otherwise as in Figure 5.42a.

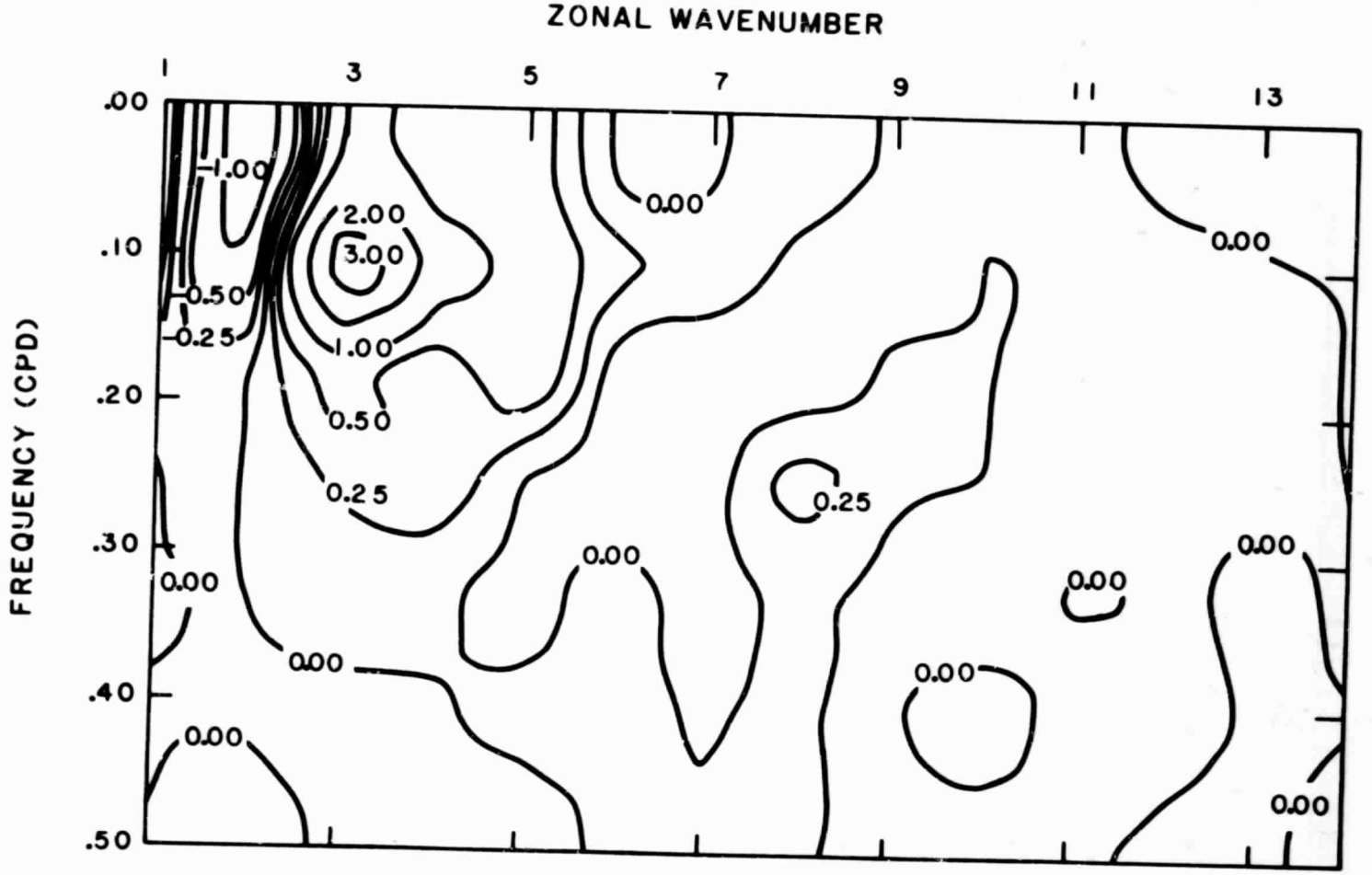

Figure 5.43b GCM wavenumber-frequency cospectral density of winter 200 mb heat flux at 50N, in units of °K m/sec/cpd. Otherwise as in Figure 5.42a.

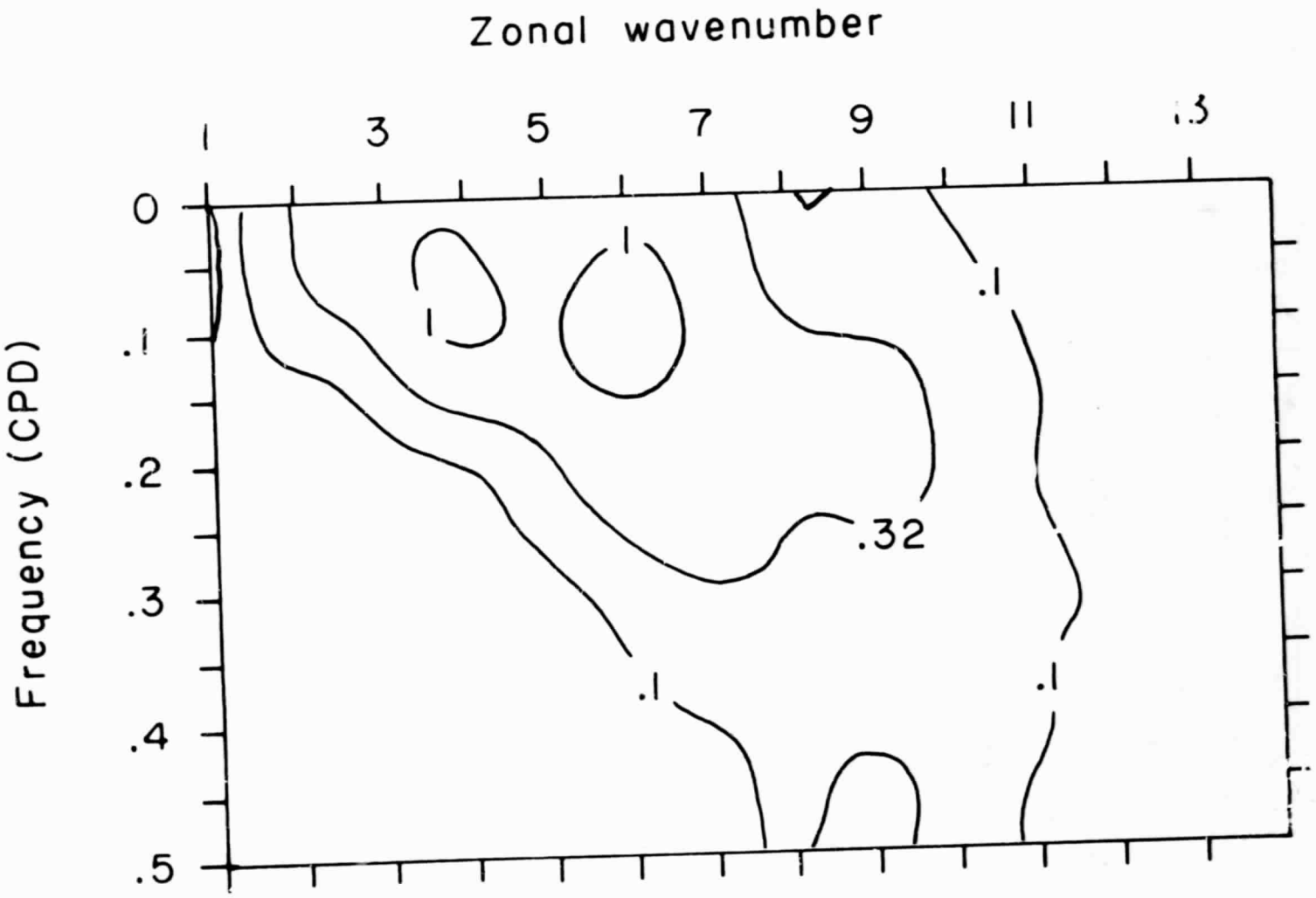

Figure 5.44a Observed wavenumber-frequency cospectral density of summer 850 mb heat flux at 50N, in units of °K m/sec/cpd. Otherwise as in Figure 5.42a.

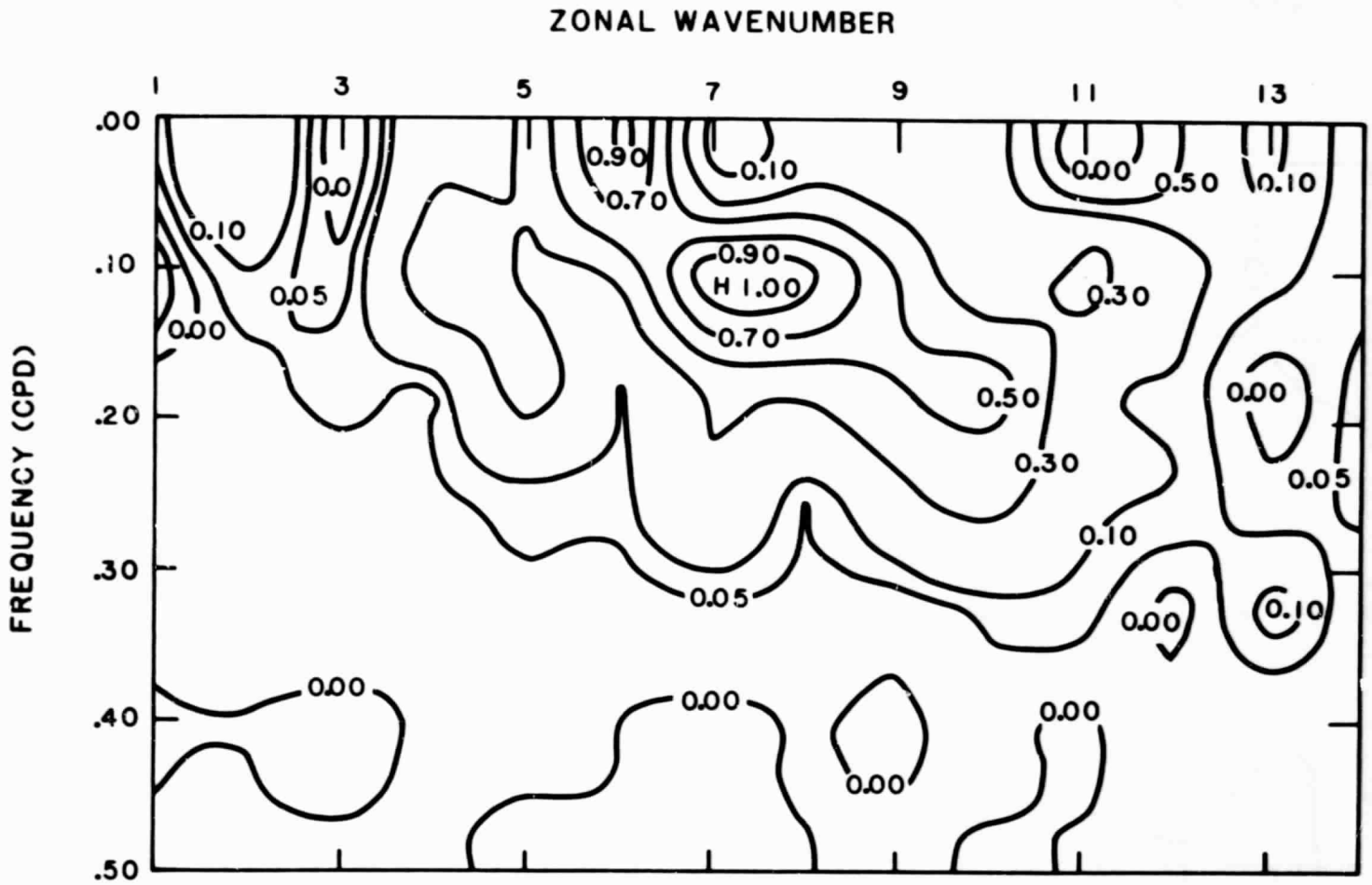

Figure 5.44b GCM wavenumber-frequency cospectral density of summer 850 mb heat flux at 50N, in units of °K m/sec/cpd. Otherwise as in Figure 5.42a.

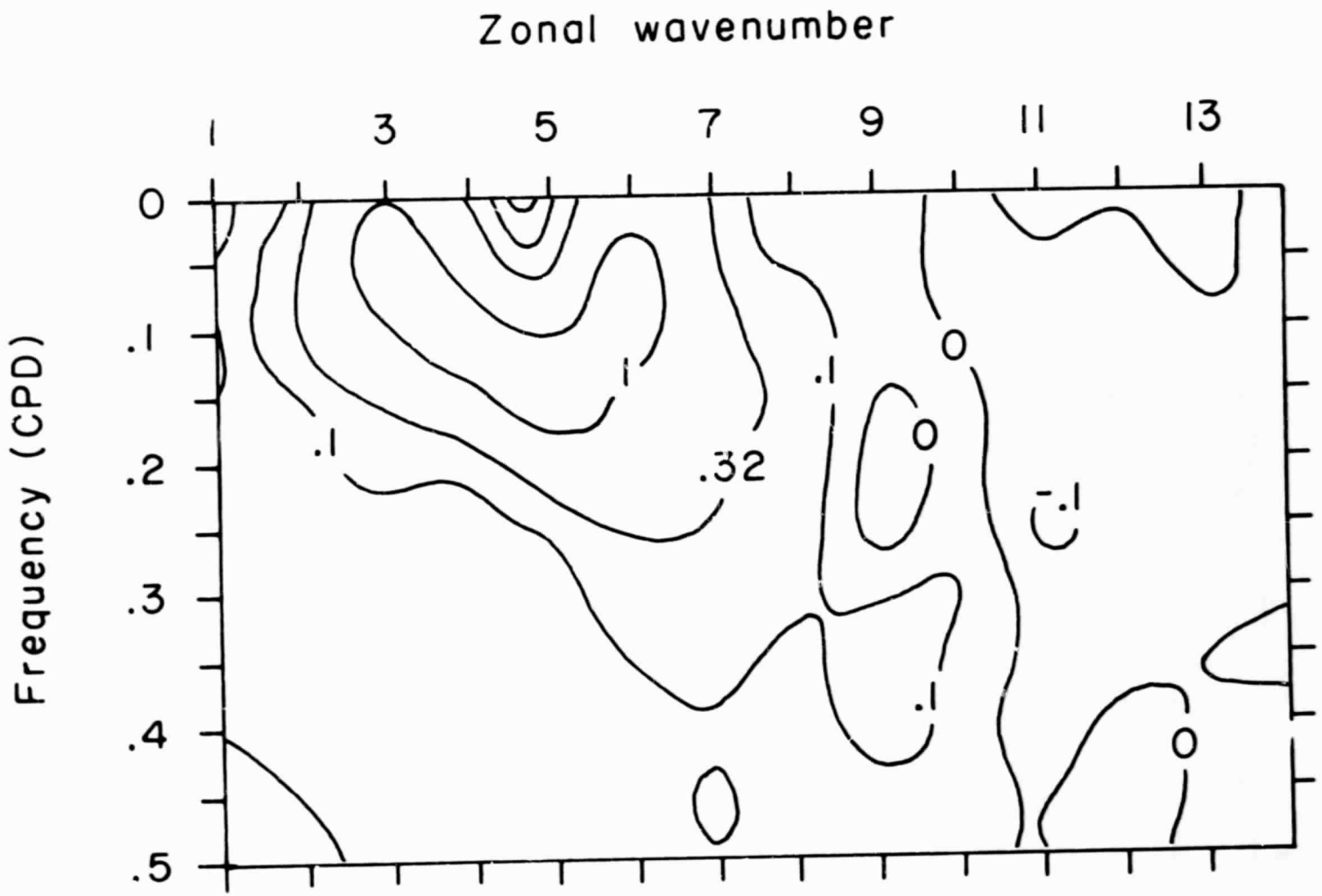

Figure 5.45a Observed wavenumber-frequency cospectral density of summer 200 mb heat flux at 50N, in units of °K m/sec/cpd. Otherwise as in Figure 5.42a.

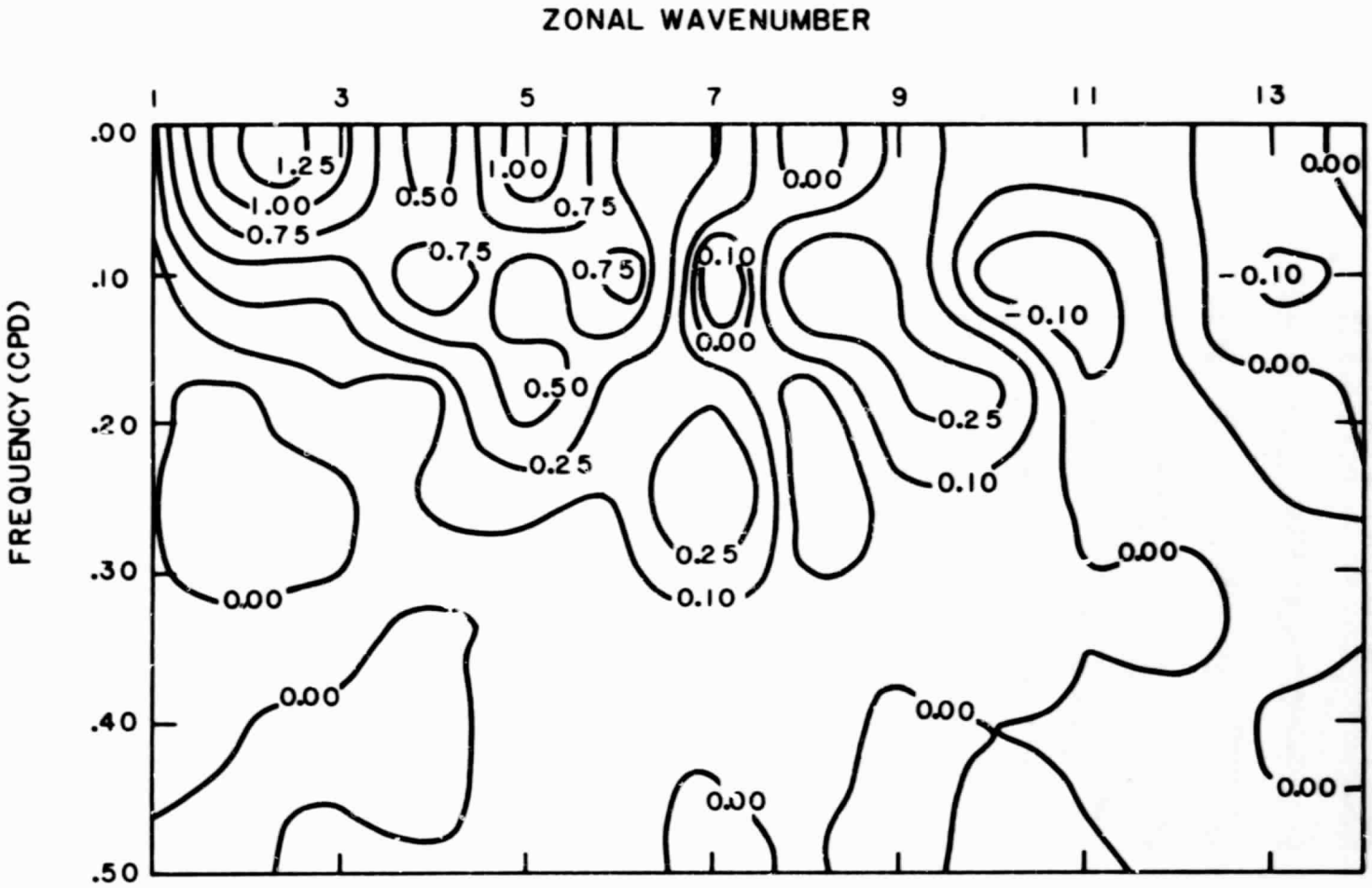

Figure 5.45b GCM wavenumber-frequency cospectral density of summer 200 mb heat flux at 50N, in units of °K m/sec/cpd. Otherwise as in Figure 5.42a.

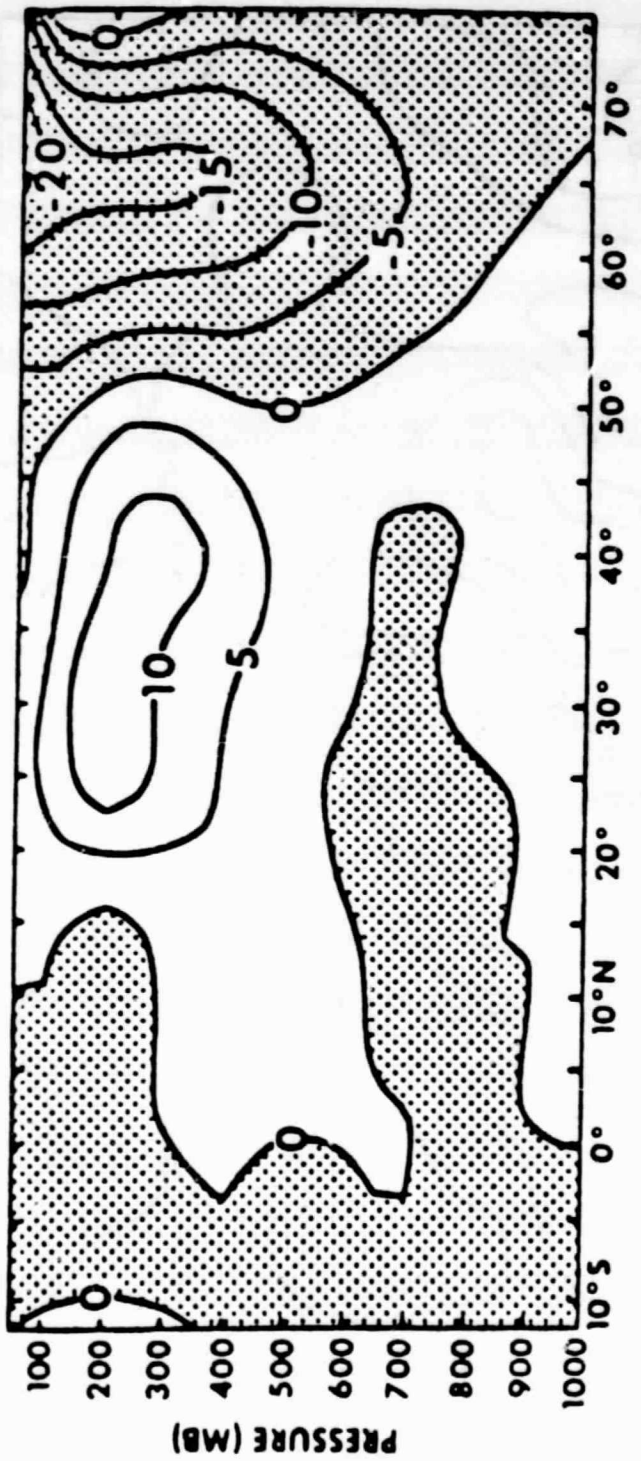

Figure 5.46a Observed February stationary eddy momentum flux, in units of $(m/sec)^2$.

C-3

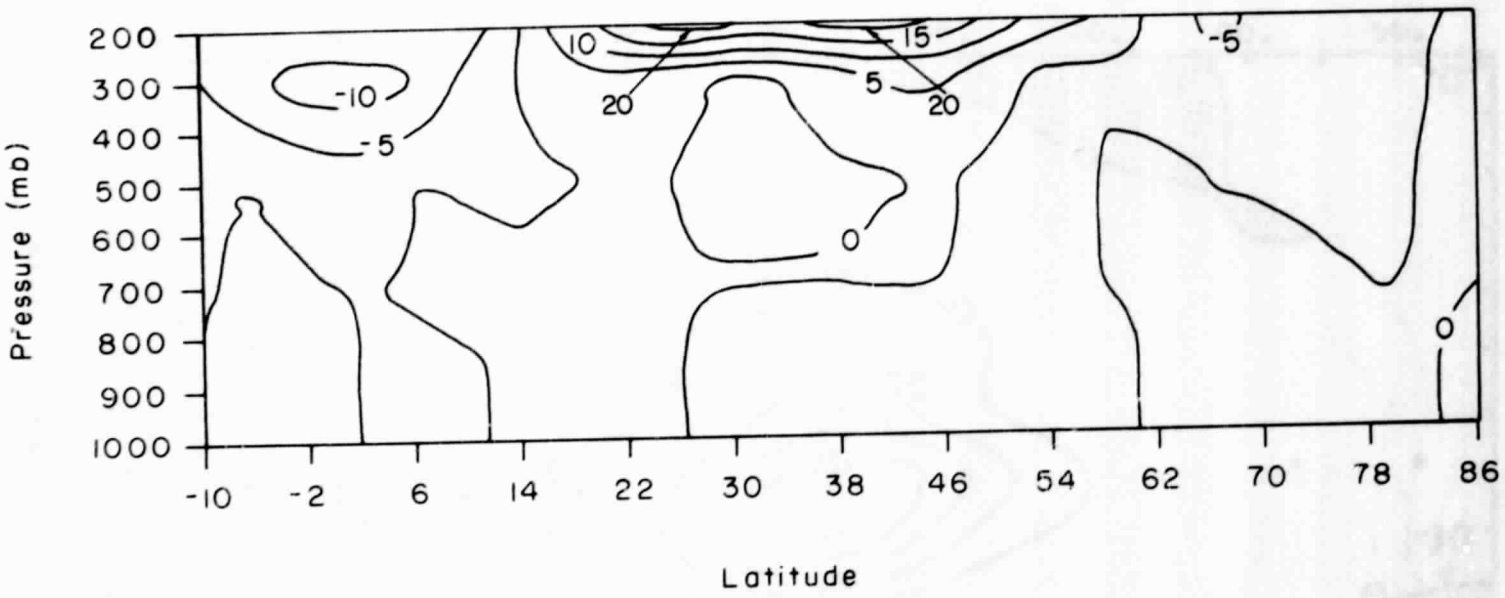

Figure 5.46b GCM February stationary eddy momentum flux, in units of $(m/sec)^2$.

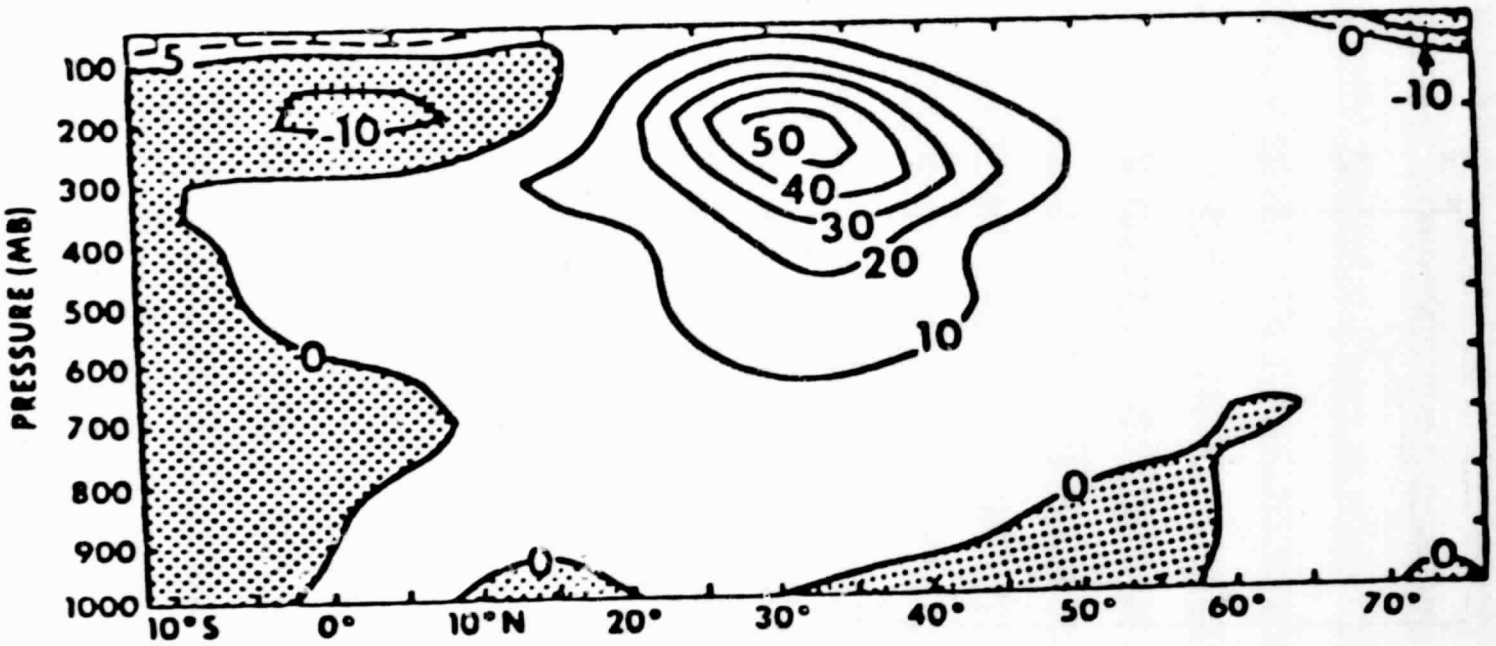

Figure 5.47a Observed February transient eddy momentum flux, in units of $(m/sec)^2$.

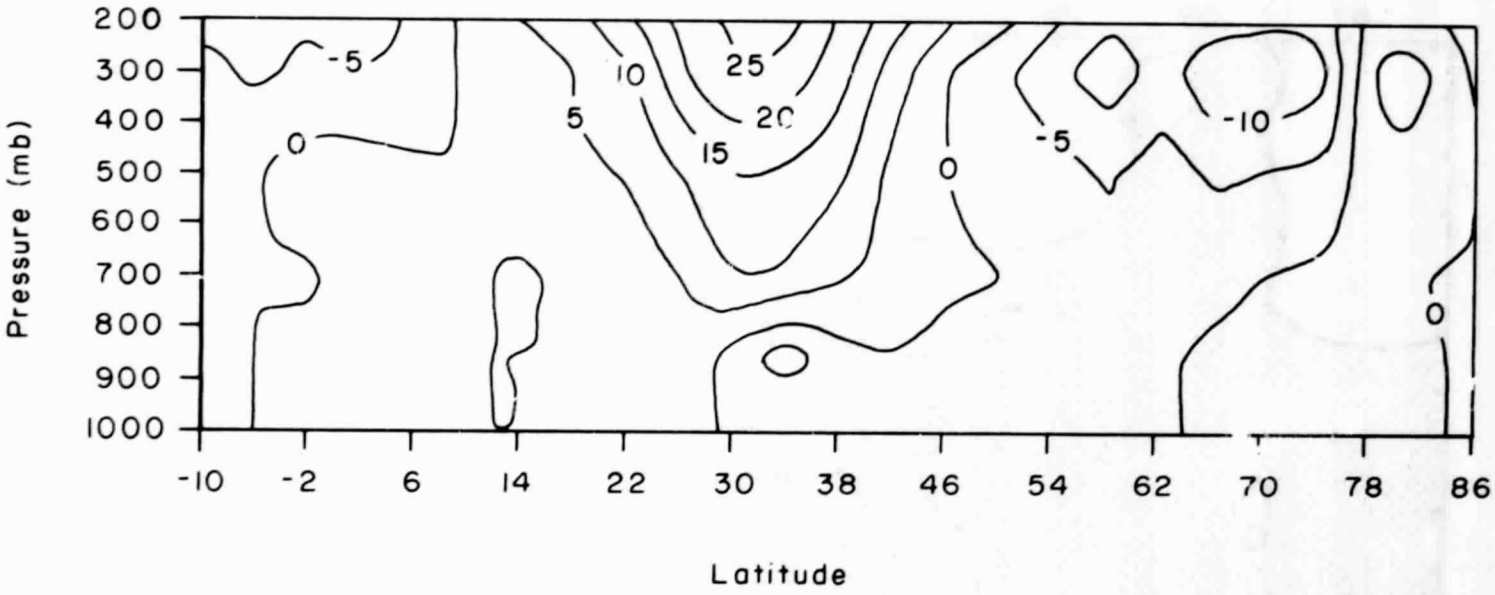

Figure 5.47b GCM February transient eddy momentum flux, in units of $(m/sec)^2$.

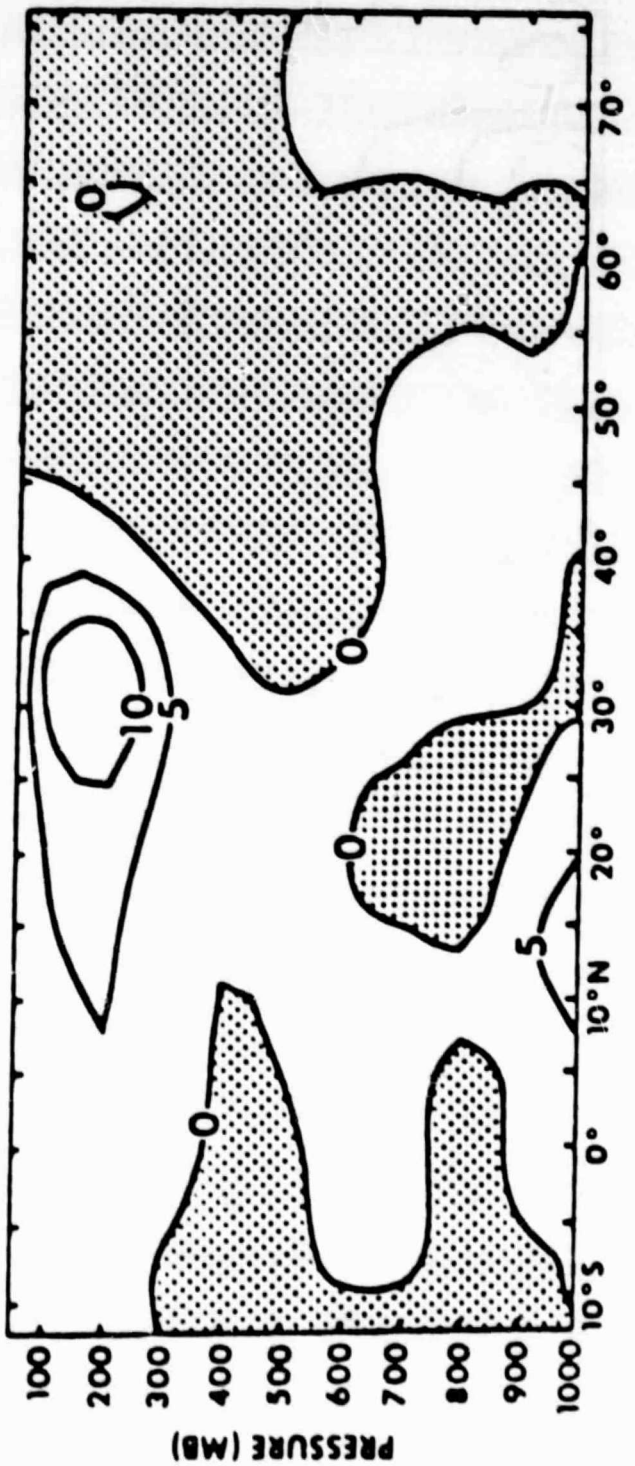

Figure 5.48a Observed July stationary eddy momentum flux, in units of $(m/sec)^2$.

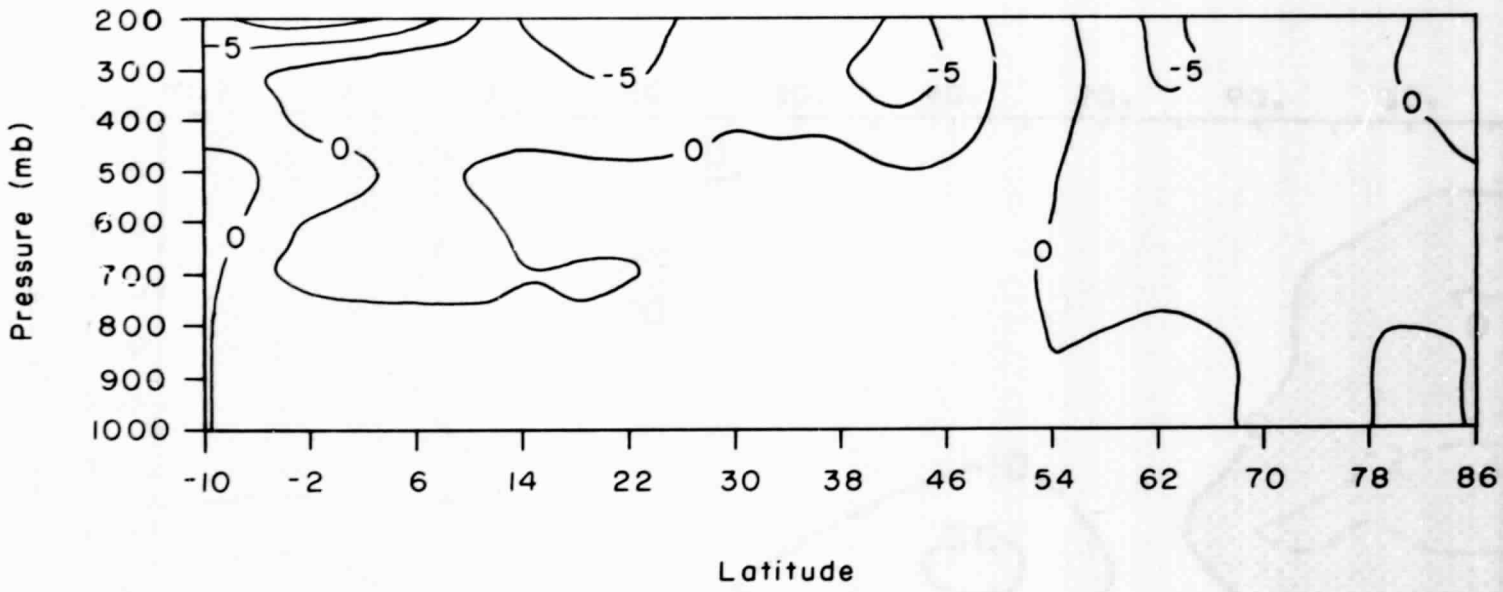

Figure 5.48b GCM July stationary eddy momentum flux, in units of $(m/sec)^2$.

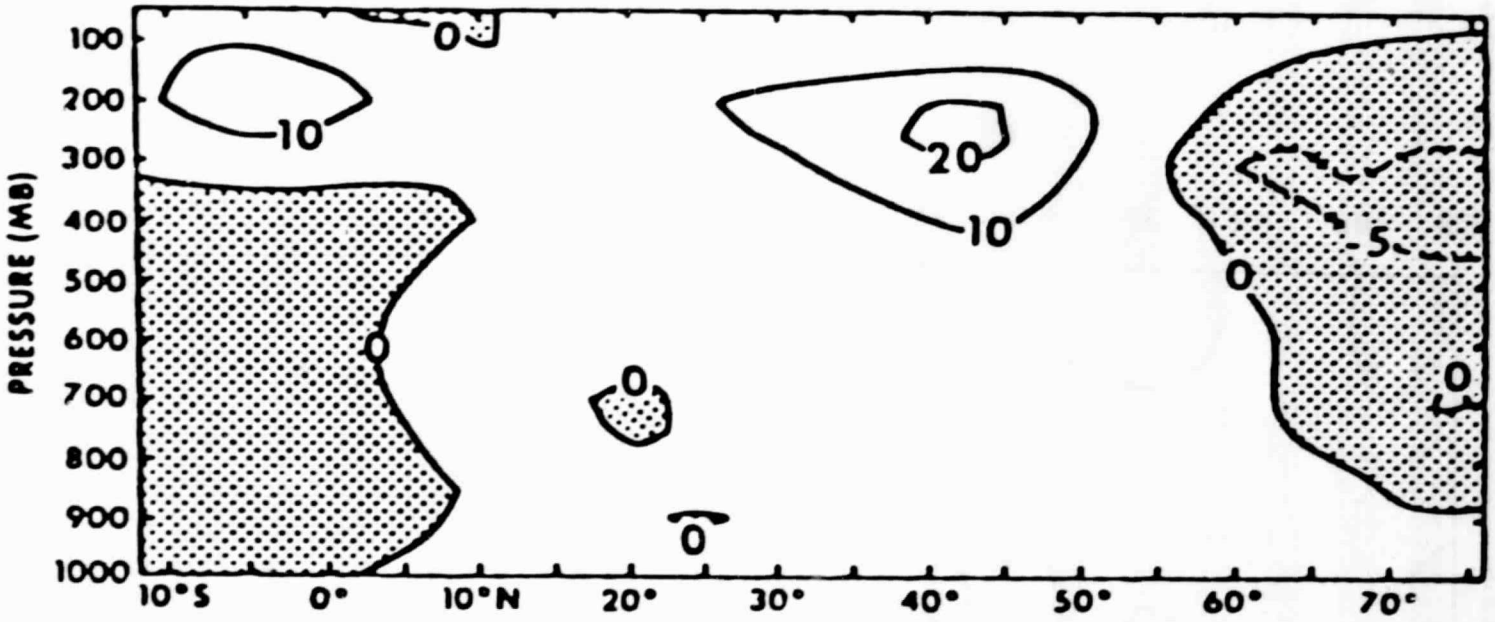

Figure 5.49a Observed July transient eddy momentum flux, in units of $(m/sec)^2$.

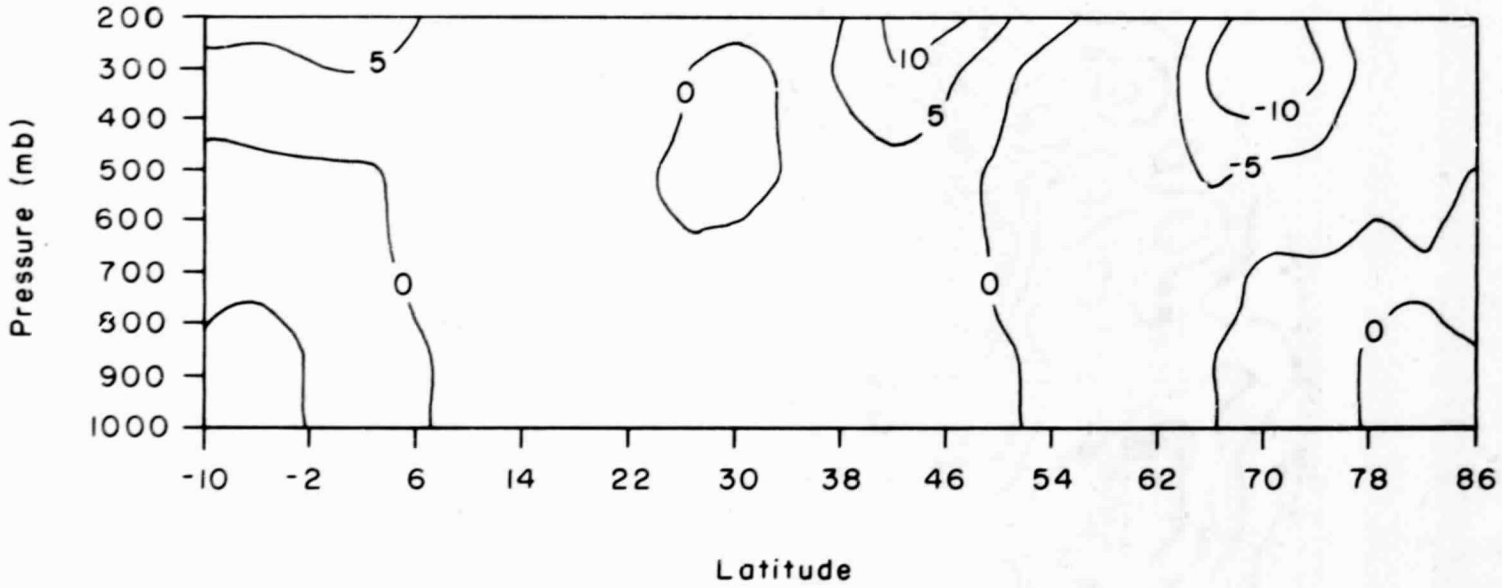

Figure 5.49b GCM July transient eddy momentum flux, in units of $(m/sec)^2$.

Figure 5.50a Observed winter local transient momentum flux at 250 mb in units of $(m/sec)^2$. Contour interval is 20 $(m/sec)^2$ (Northern Hemisphere).

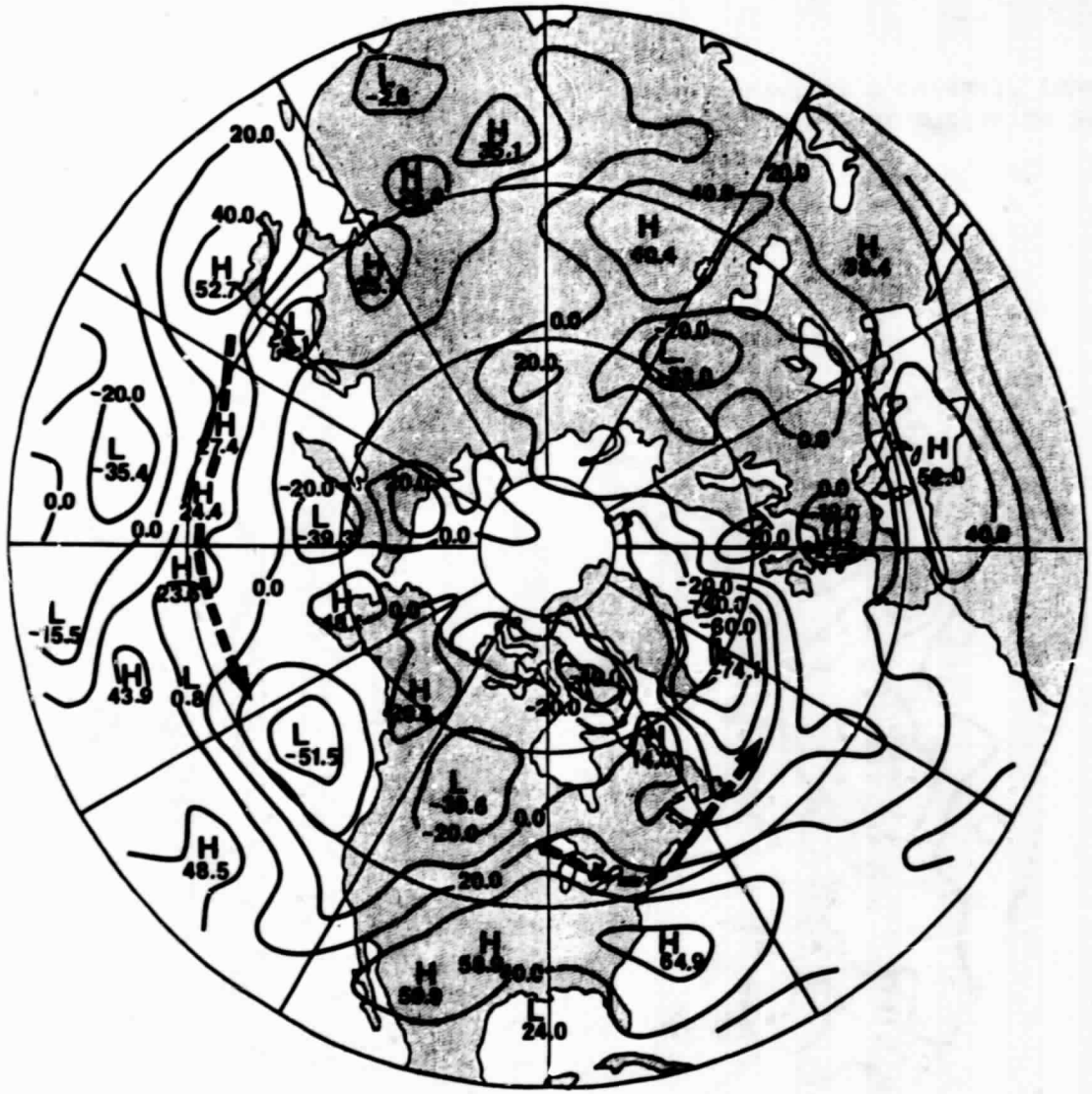

Figure 5.50b GCM winter local transient momentum flux at 200 mb in units of $(m/sec)^2$. Contour interval is 20 $(m/sec)^2$ (Northern Hemisphere).

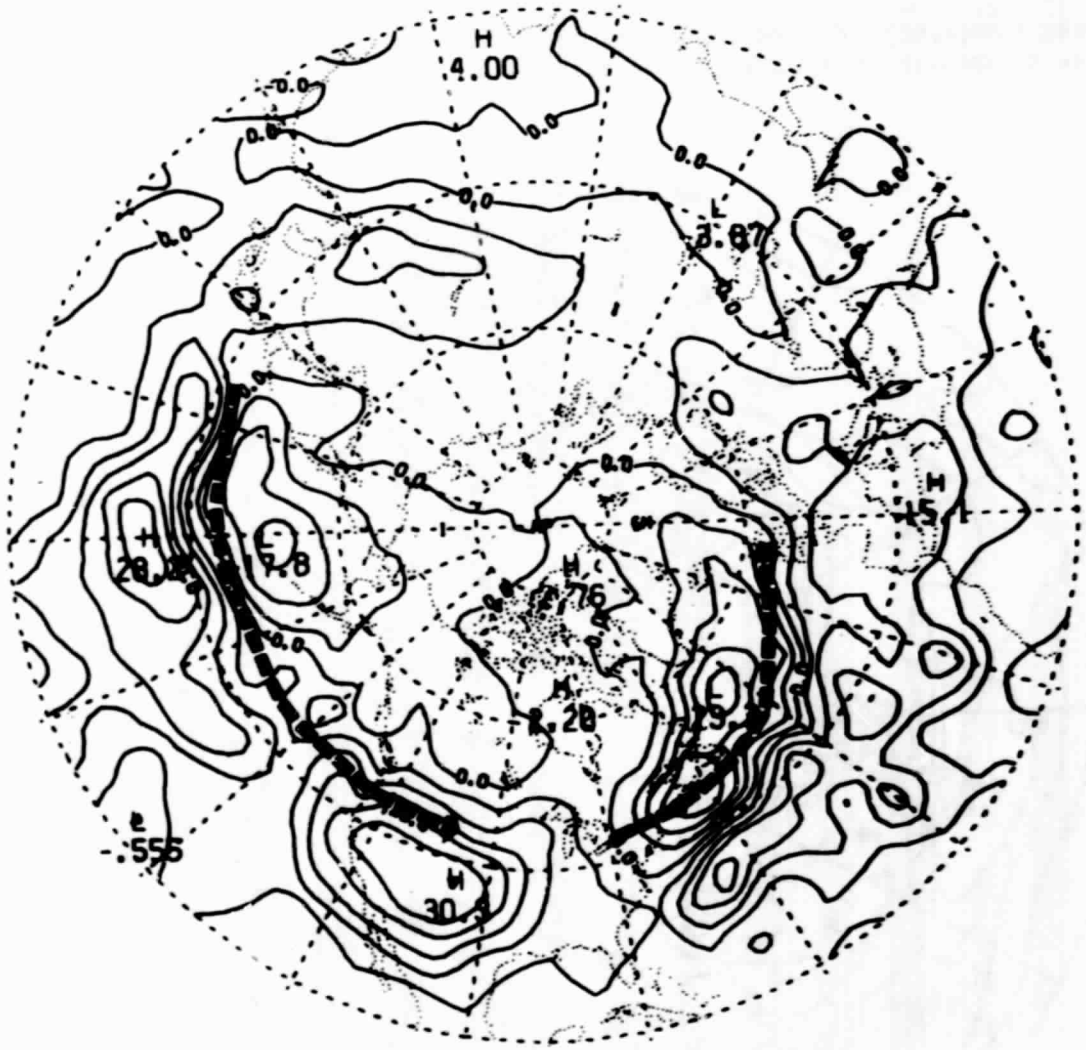

Figure 5.51a Observed winter local band-pass transient momentum flux at 250 mb in units of $(m/sec)^2$. Contour interval is 5 $(m/sec)^2$ (Northern Hemisphere).

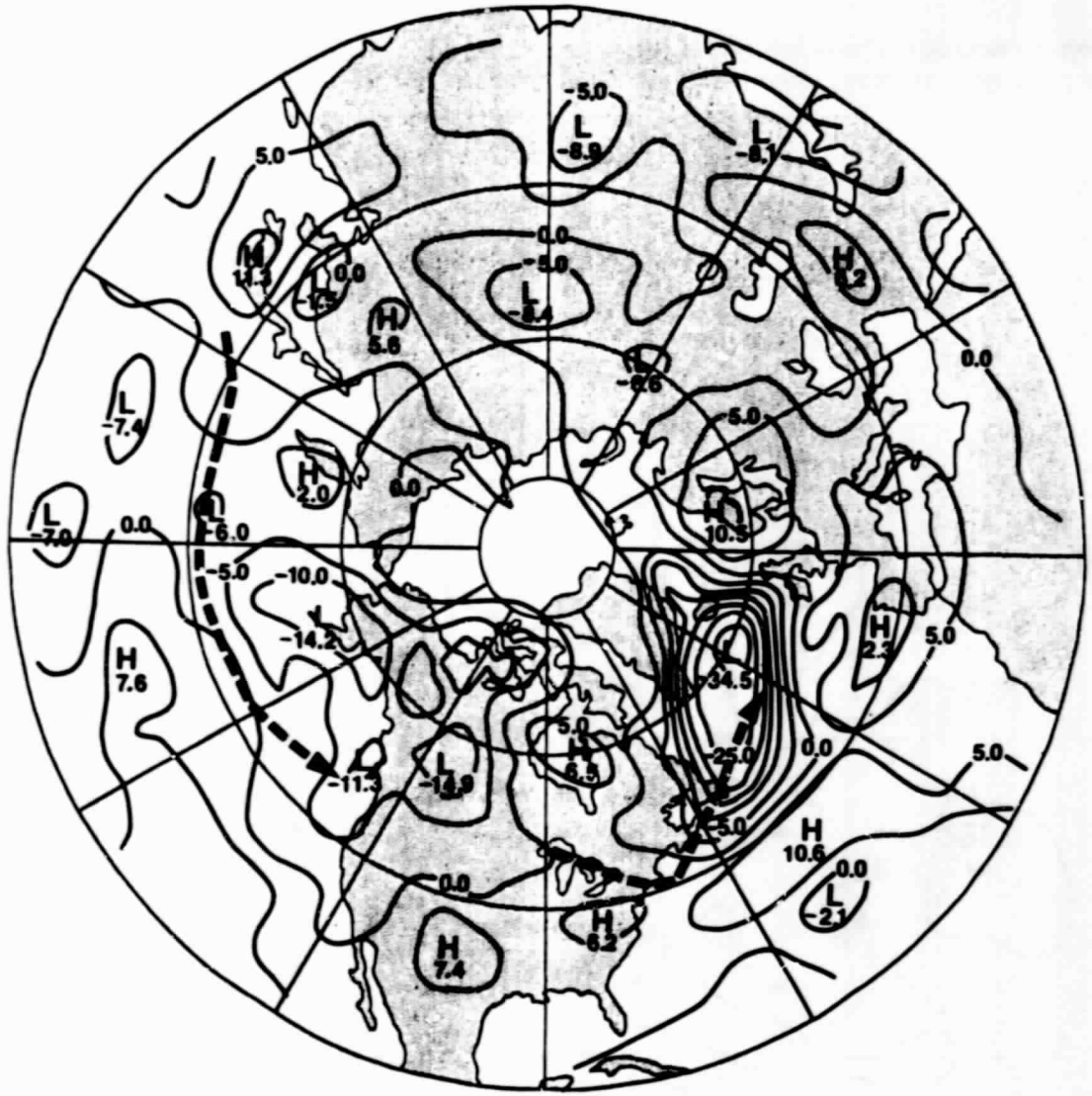

Figure 5.51b GCM winter local band-pass transient momentum flux at 200 mb in units of $(m/sec)^2$. Contour interval is 5 $(m/sec)^2$ (Northern Hemisphere).

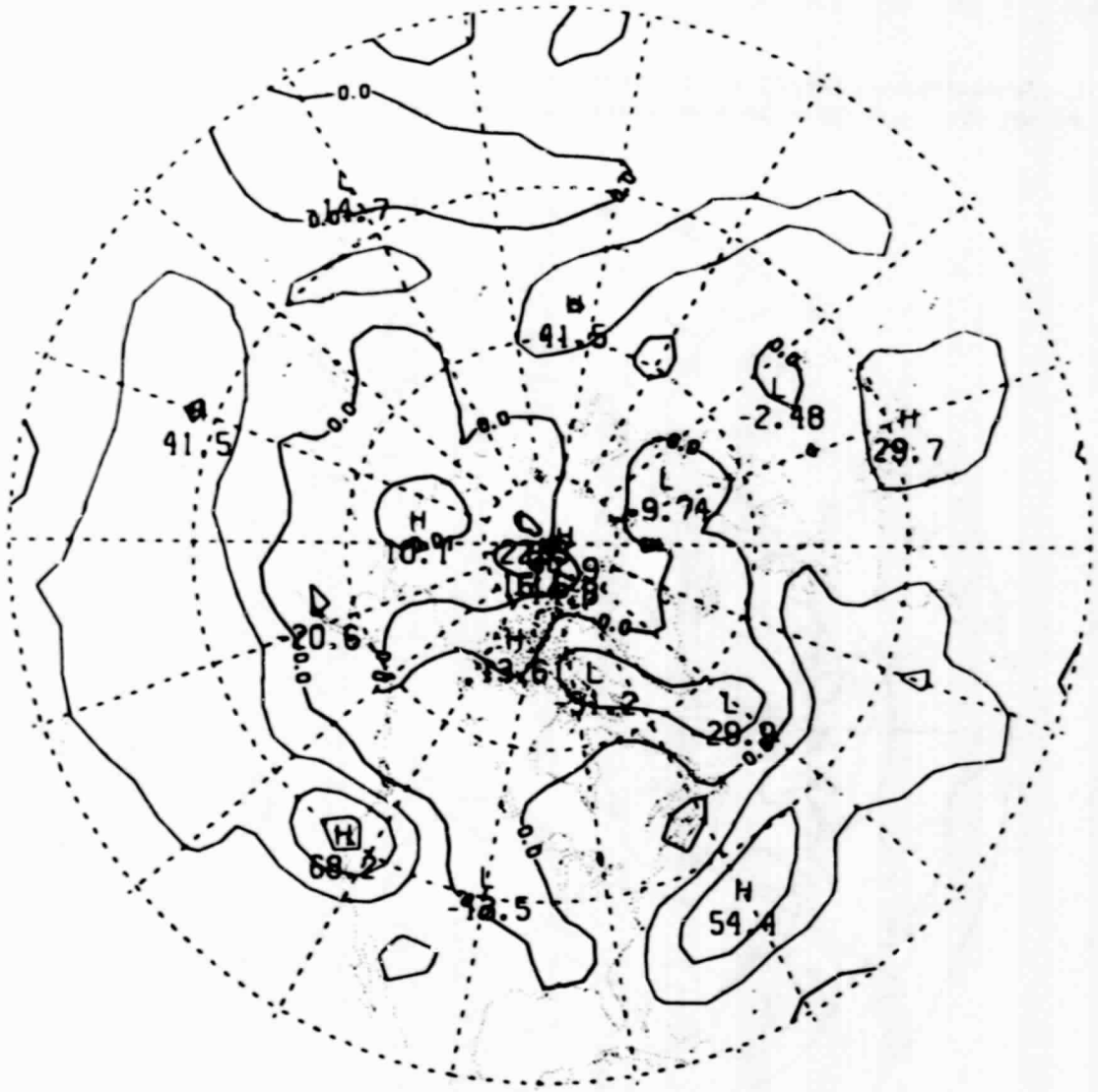

Figure 5.52a Observed winter local transient momentum flux at 500 mb in units of $(m/sec)^2$. Contour interval is 20 $(m/sec)^2$ (Northern Hemisphere).

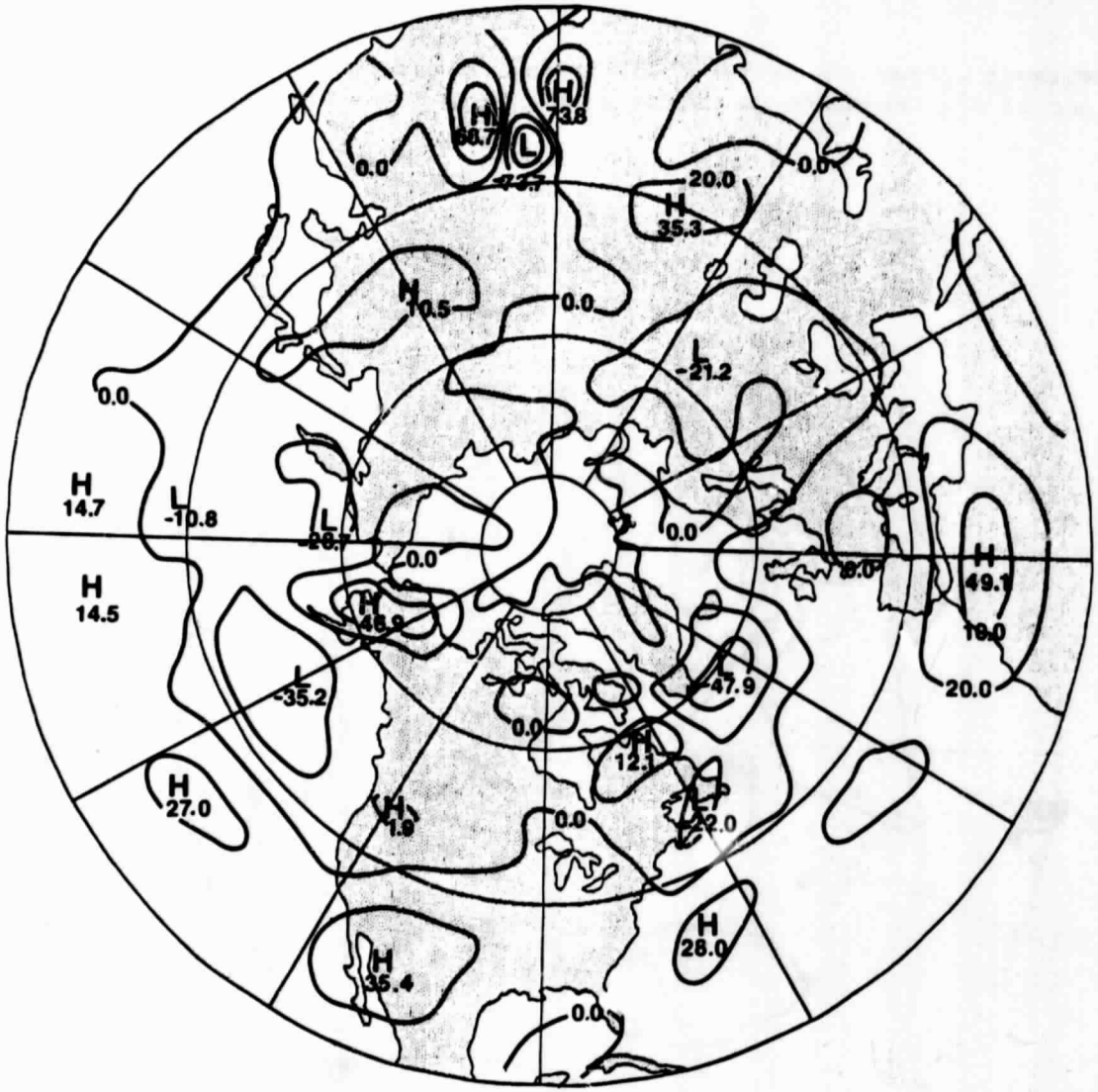

Figure 5.52b GCM winter local transient momentum flux at 500 mb in units of $(m/sec)^2$. Contour interval is 20 $(m/sec)^2$ (Northern Hemisphere). (Several contours have been omitted in the immediate vicinity of very sharp maxima or minima.)

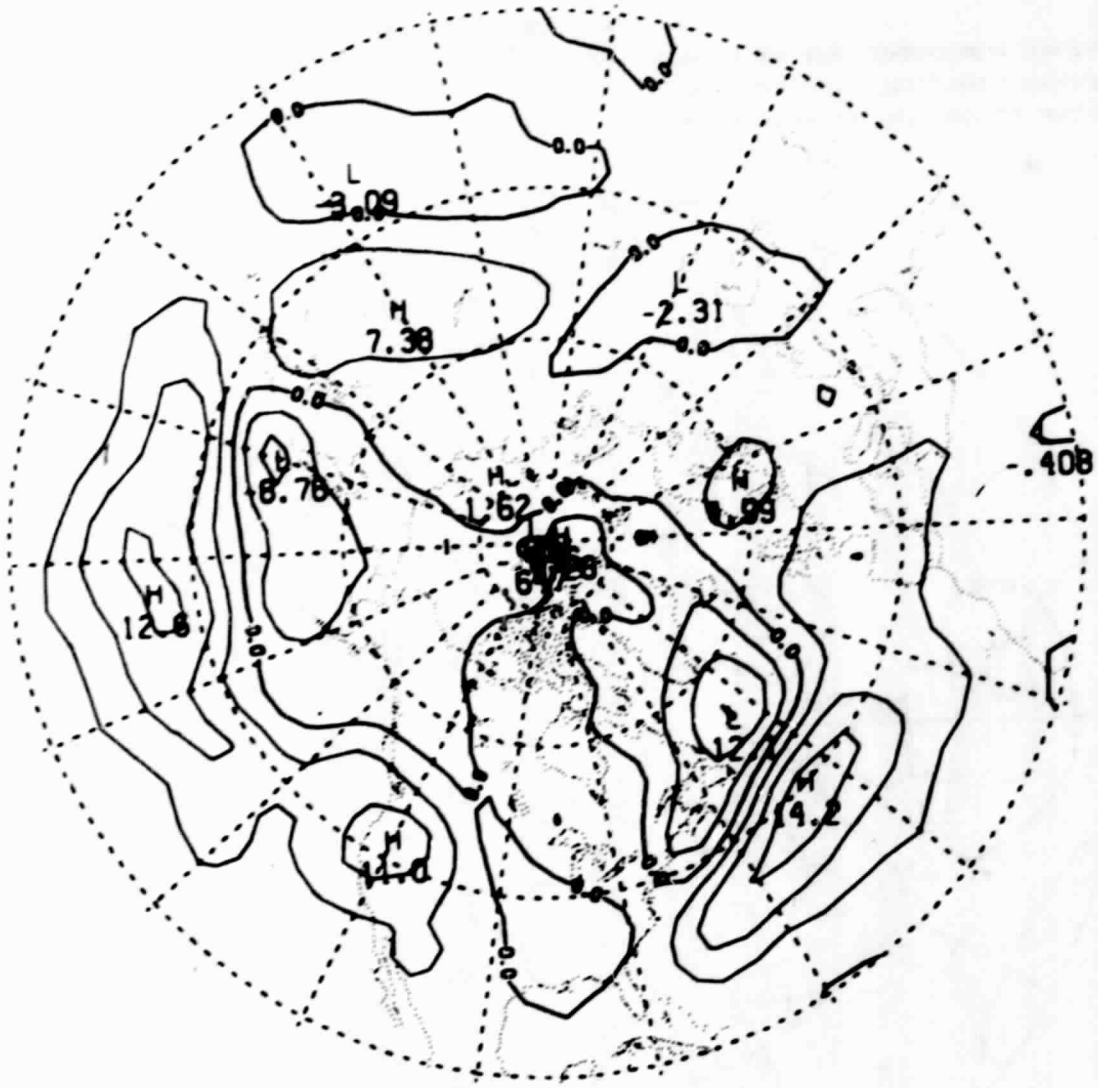

Figure 5.53a Oserved winter local band-pass transient momentum flux at 500 mb in units of $(m/sec)^2$. Contour interval is 4 $(m/sec)^2$ (Northern Hemisphere).

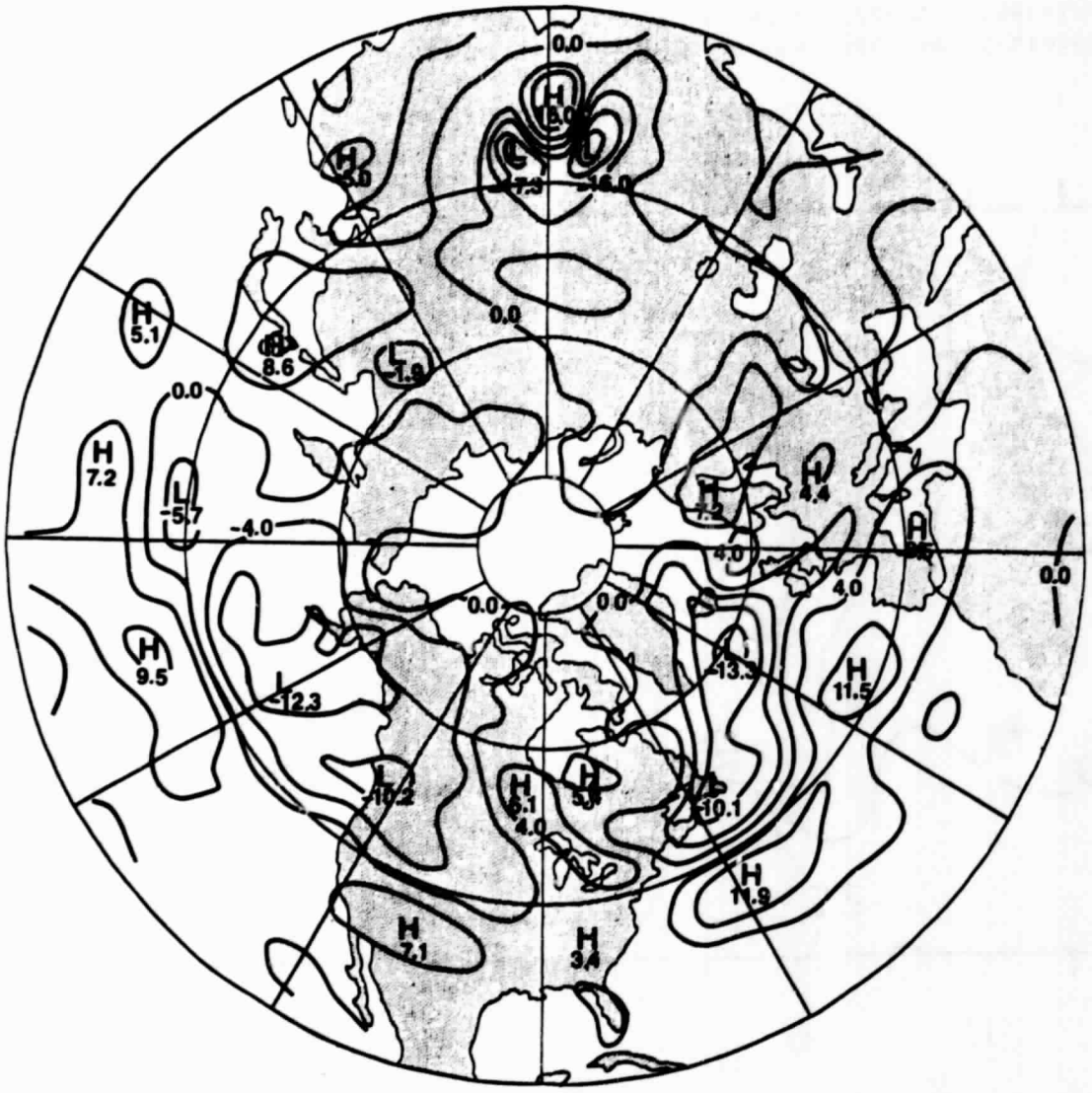

Figure 5.53b GCM winter local band-pass transient momentum flux at 500 mb in units of $(m/sec)^2$. Contour interval is 4 $(m/sec)^2$ (Northern Hemisphere). (Several contours have been omitted in the immediate vicinity of very sharp maxima or minima.)

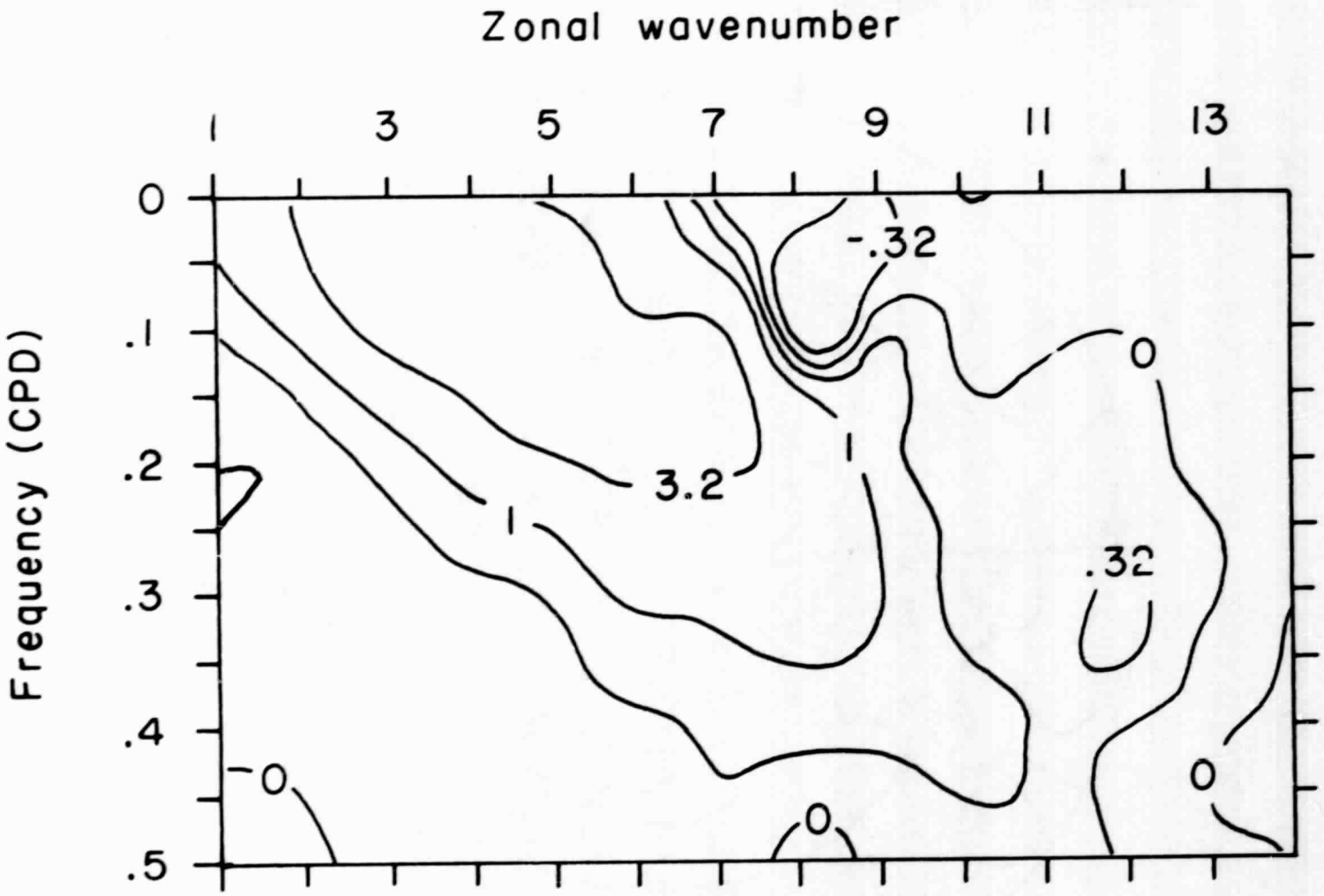

Figure 5.54a Observed wavenumber-frequency cospectral density of winter 300 mb momentum flux at 35N, in units of $(m/sec)^2/cpd$. Otherwise as in Figure 5.42a.

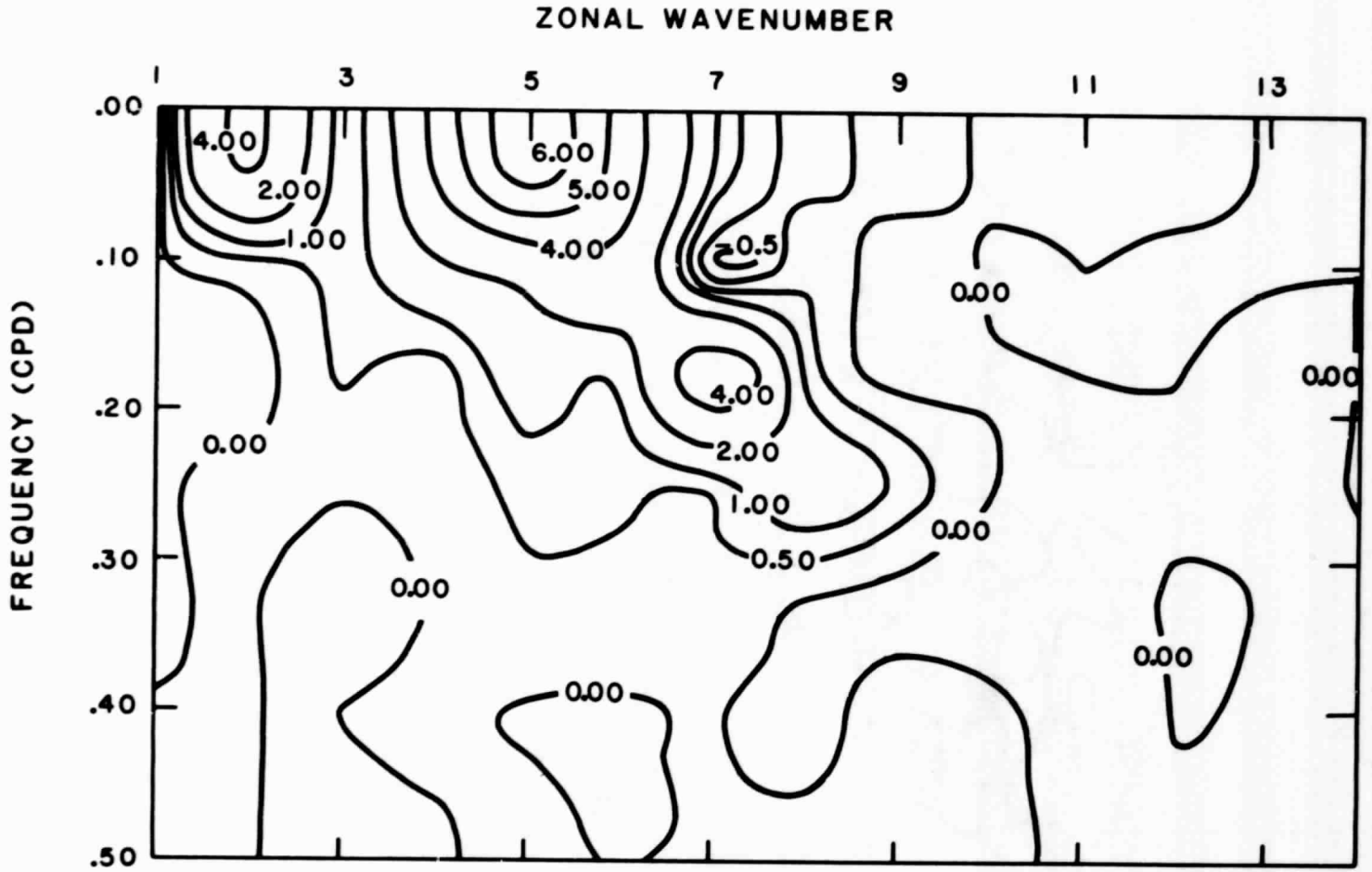

Figure 5.54b GCM wavenumber-frequency cospectral density of winter 300 mb momentum, flux at 34N, in units of $(m/sec)^2/cpd$. Otherwise as in Figure 5.42a.

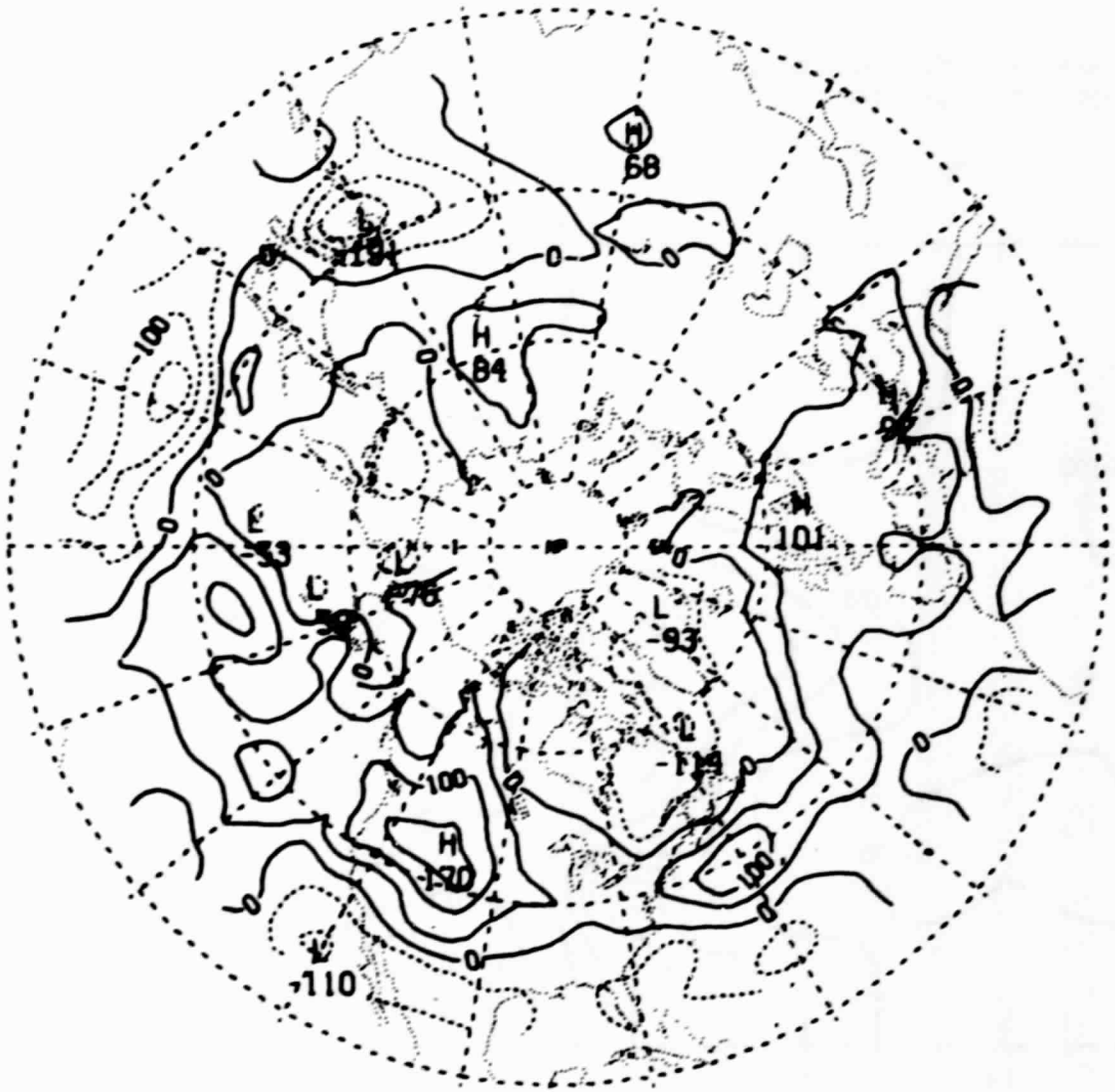

Figure 5.55a The observed local horizontal convergence of transient flux of westerly momentum for Northern Hemisphere winter at 250 mb. Plotted in units of 10^{-6} m/sec^2, with a contour interval of 50.

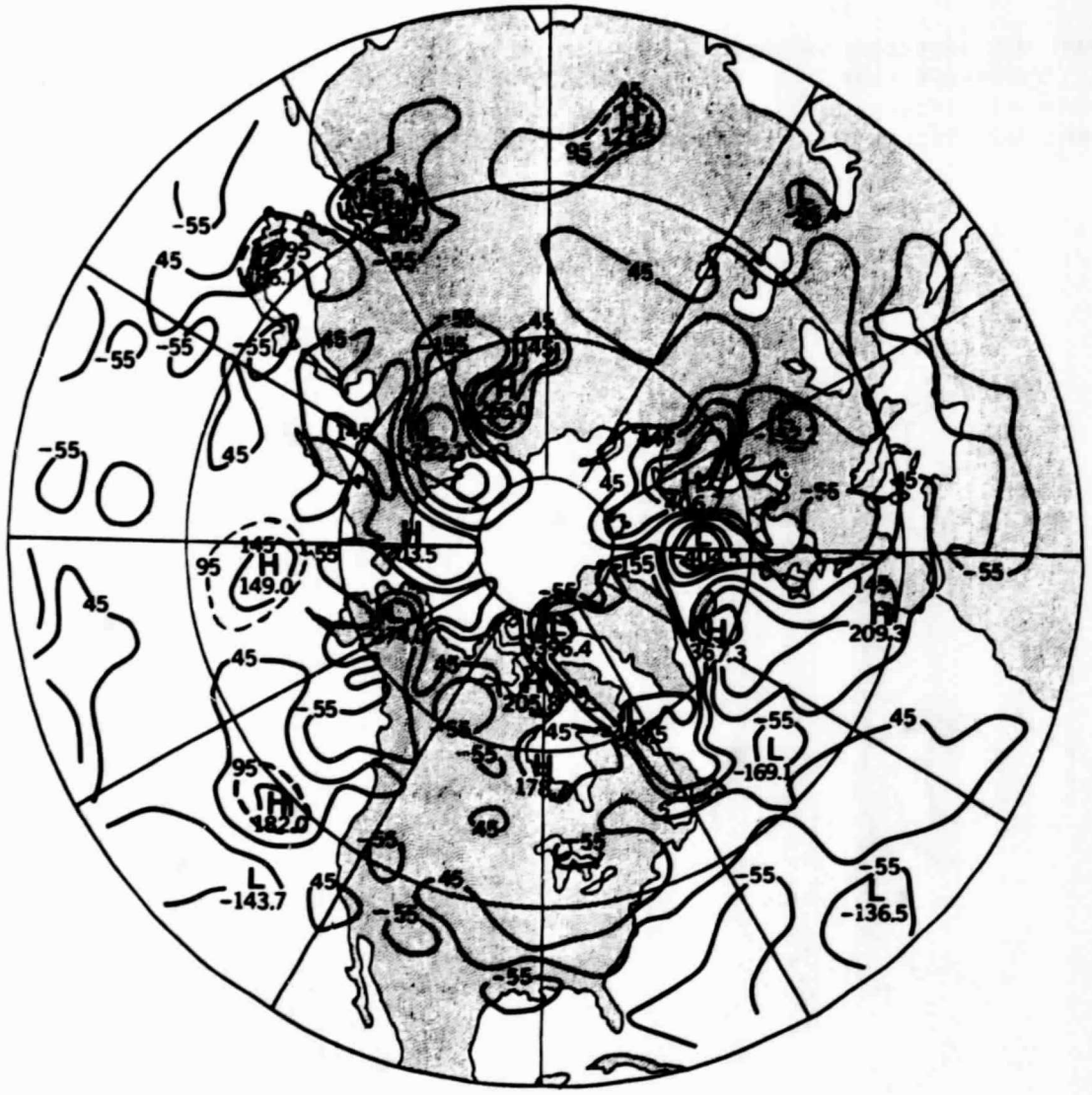

Figure 5.55b The GCM local horizontal convergence of transient flux of westerly momentum for the Northern Hemisphere during February at 285 mb. Plotted in units of 10^{-6} m/sec^2, with a contour interval of 100. (Several contours have been omitted in the immediate vicinity of very sharp maxima or minima.)

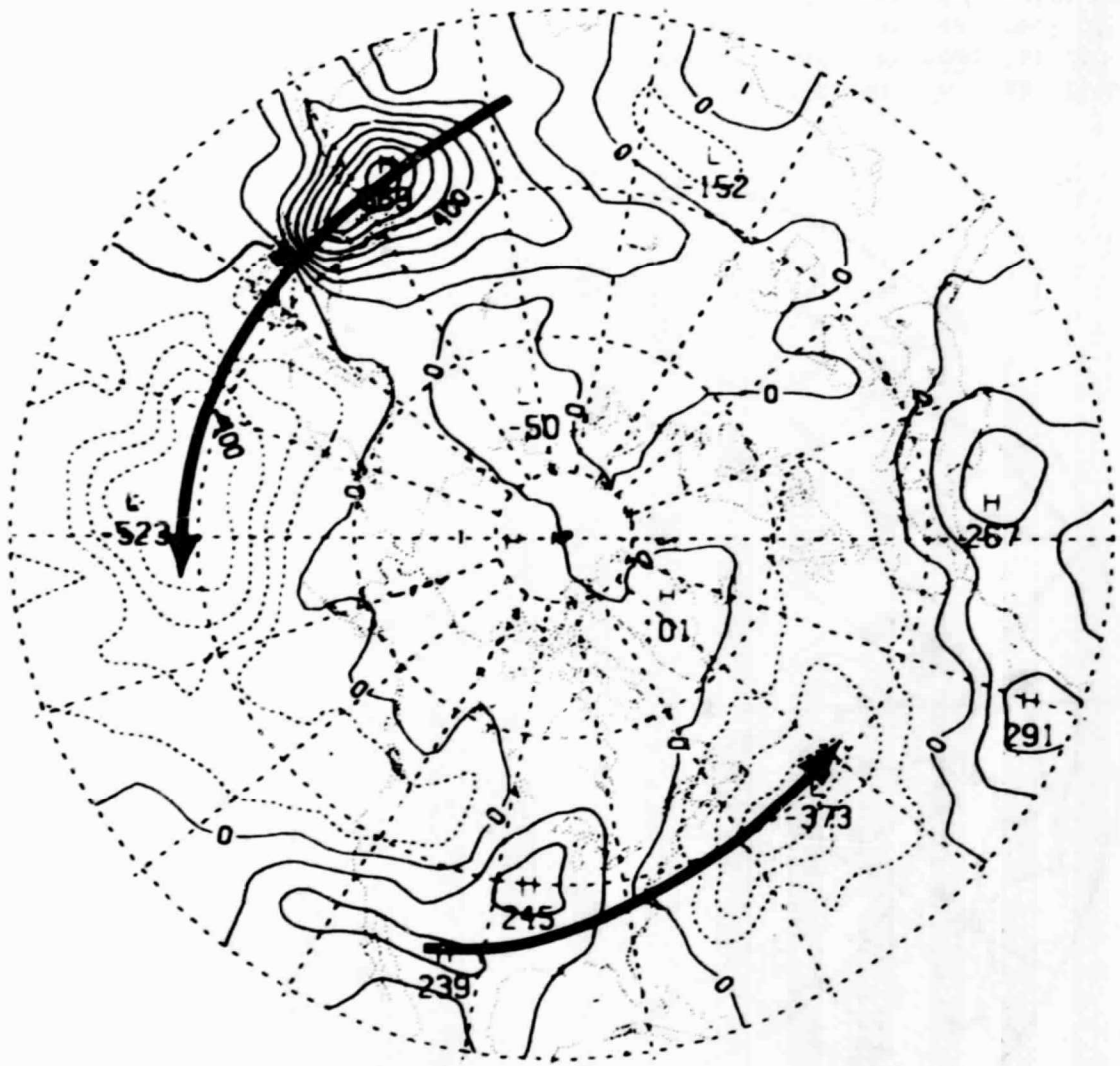

Figure 5.56a The observed local Coriolis acceleration accompanying the time-mean meridional ageostrophic flow for Northern Hemisphere winter at 250 mb. Plotted in units of 10^{-6} m/sec^2, with a contour interval of 100. Solid arrows denote the positions of the major jet streams.

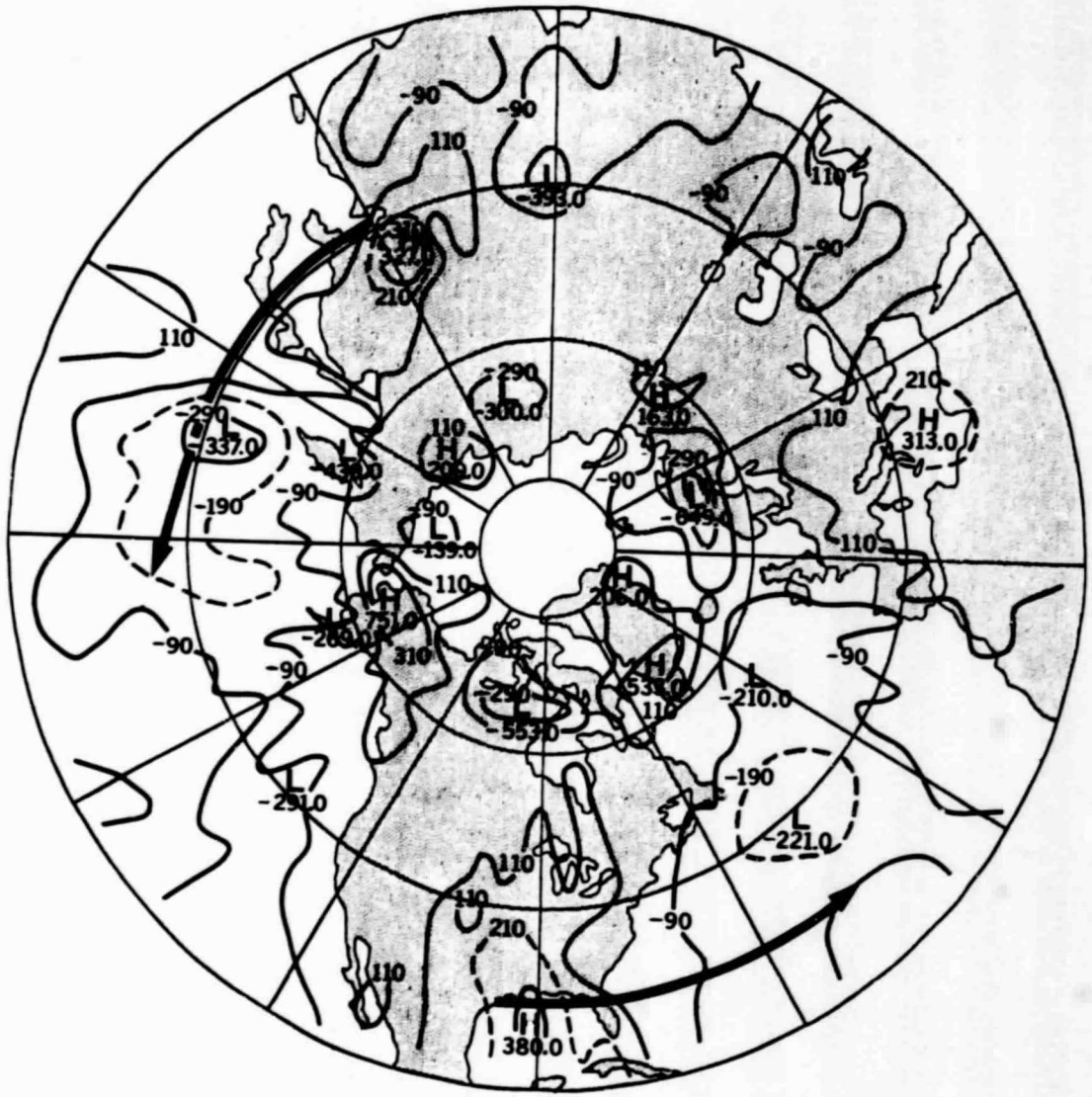

Figure 5.56b The GCM local Coriolis acceleration accompanying the time-mean meridional ageostrophic flow for the Northern Hemisphere during February at 285 mb. Plotted in units of 10^{-6} m/sec^2, with a contour interval of 200. Solid arrows denote the positions of the major jet streams. (Several contours have been omitted in the immediate vicinity of very sharp maxima or minima.)

6. Simulation of diabatic and frictional processes

a. Summary of the global sensible heat and moisture budgets. In both simulations all fluxes of heat and moisture across the top and bottom boundaries of the atmosphere were accumulated at every grid point. Global sums were carried out to obtain the average global values of each boundary flux. Figs. 6.1a-b and Tables 6.1 and 6.2 summarize the global sensible heat and moisture budgets for the February and July simulations, giving the globally averaged surface sensible heat flux, evaporation, their ratio (termed the global Bowen ratio), the precipitation rate, and the planetary albedo. The observed surface fluxes are these of Budyko (1963) as given by Schutz and Gates (1971, 1972), the observed precipitation rates are from Jaeger (1976), and the observed planetary albedoes are from Raschke, et al. (1973). The simulated global mean evaporation and precipitation rates agree well with observations, and are improved relative to earlier versions of the model. The simulated surface sensible heat flux is also significantly improved, but it continues to be excessive. Finally, the simulated planetary albedoes are too high in both February and July, and are inferior to those obtained with earlier versions of the model.

The following subsections explore these and other results in more detail.

b. Surface fluxes. The simulated and observed (Schutz and Gates, 1971, 1972) January/February and July geographical distributions and zonal means of the evaporation are shown in Figs. 6.2a-f. In the February simulation, the evaporation maxima off the east coasts of Asia and North America have their observed magnitudes, although their shapes are not well-simulated and the secondary maximum south of Greenland is missed. The observed equatorial minimum is simulated in the Eastern Pacific, but is missed in Melanesia and the Indian Ocean. The zonal mean does not show the observed sharp equatorial minimum. Observed maxima in the tropical South Atlantic, Indian, and South Eastern

Pacific oceans are either missing or weak and malformed.

Similarly, the simulated and observed (Schutz and Gates, 1971, 1972) heat flux distributions and zonal means for January/February and July are shown in Figs. 6.3a-f. The February simulated surface sensible heat flux has maxima of the observed intensities off the east coasts of Asia and North America, but the Atlantic maximum fails to extend to the west coast of Scandinavia; it hugs the coast of North America more closely than observed.

In the July simulation, the evaporation maxima off the coasts of Brazil and Madagascar are correctly simulated, as are the minima over Australia and North Africa. To some extent, the minima over such desert areas must be correctly simulated, since the ground moisture distribution was initialized from observations and has a memory of several weeks. The general pattern of oceanic evaporation is not very satisfactory. The simulated maximum in the tropical Western Pacific is too strong, and does not show the observed relative minimum at the equator. The equatorial minimum is also missed in the central Pacific.

The zonal mean of the simulated surface sensible heat flux is much stronger than observed. The simulated relative minimum at 10° north is about 20 W m^{-2}. The largest zonal mean values occur at 30° north, in both the simulation and the observations, but the simulated maximum is too strong.

Figs. 6.4b and d show the simulated global surface stress distribution for February and July, and Figs. 6.4a and c show the corresponding observed stresses, over the oceans only, as derived by Mintz (1979) from the data of Hellerman (1967). The simulation is reasonably successful in reproducing the observed stresses, except in the "roaring fifties" around Antarctica, where the simulated stresses are weak and disorganized, reflecting the model's failure to simulate the dynamics of that region.

c. Precipitation. The simulated and observed (Jaeger, 1976) February and July distributions of precipitation are shown in Fig. 6.5a-d. The simulated

precipitation field is in excellent agreement with observations. Almost all important features are well-simulated in both position and intensity. Perhaps the single major discrepancy is the somewhat excessive (2 mm/day too large) February precipitation over the Tibetan plateau. In the July simulation the major monsoons are captured. The observed maximum over eastern North America is somewhat overpredicted.

Figs. 6.5e and f show the partitioning of the simulated total precipitation between large-scale-saturation and convection, in the zonal mean, for February and July. In both seasons, cumulus precipitation dominates in the tropics, while large-scale precipitation dominates in higher latitudes.

d. Cloudiness and albedo. The simulated and observed February and July distributions of total cloudiness are shown in Fig. 6.6a-d. It is apparent that the simulated cloudiness is excessive. This is confirmed by the fact that the simulated planetary albedoes are too high (see again Tables 6.1-2): the simulated February and July planetary albedoes are 0.390 and 0.380, while the corresponding observed values (Raschke et al., 1973) are 0.283 and 0.281, respectively. Much of the excessive cloudiness is due to widespread "supersaturation" in the lowest model layer. Moeng and Randall (1982) show that even if cumulus cloudiness is completely neglected, the simulated albedo is practically unchanged. Apparently the boundary layer and cumulus parameterizations of the model do not allow realistic transport of moisture up out of the lowest model layer (Randall, 1982).

The model correctly simulates the seasonal increase in zonally-averaged cloudiness from summer to winter in the high latitudes of each hemisphere, except that the observed increase in Arctic cloudiness from February to July is missed. The cloudiness of the ITCZ is reasonably well-simulated, particularly for February, and the observed subtropical minima are also captured.

The simulated longitudinal distribution of cloudiness is much less satisfactory. The observed subtropical July maxima off the west coasts of North America, South America, and South Africa are not only missed; they are replaced by minima. The observed maxima are known to be associated with stratus and stratocumulus clouds within the planetary boundary layer. The fact that the model has not simulated these maxima indicates that an improved planetary boundary layer parameterization is needed (Randall, 1982).

e. Total diabatic heating. Fig. 6.7a shows the "observed" zonally averaged total diabatic heating reported by Newell et al. (1972), and Figs. 6.7b and c show the corresponding simulations for February and July. The simulations produce deep equatorial maxima associated with the convection of the ITCZ, and prominent low-level winter-hemisphere maxima due to boundary layer heating. The middle and upper troposphere are radiatively cooled. In each season, cooling predominates above 800 mb in the subtropics of the winter hemisphere. This radiative cooling is balanced by the adiabatic warming in the descending branch of the Hadley circulation (see Section 7). The low-level equatorial heating reported by Newell et al. is negative, but it is positive in the model.

Table 6.1

	Surface Sensible Heat Flux W m^{-2}	Surface Evaporation mm dy^{-1}	Global Bowen Ratio	Total Precipitation mm dy^{-1}	Planetary Albedo
Observed February	17.3	3.12	0.192	2.80	0.283
Simulated February	27.5	3.03	0.312	3.07	0.390
Observed July	20.7	3.28	0.218	2.84	0.281
Simulated July	32.5	3.22	0.347	3.24	0.380

Table 6.2a February energy balance (W m^{-2}).

Items	Analysis of heat budget fields		
	S. hemisphere	N. hemisphere	Global
	Mean	Mean	Mean
Top Boundary of Atmosphere			
Incoming short wave flux	440.18	273.14	356.83
Outgoing short wave flux	178.59	100.09	139.34
Outgoing long wave flux	196.12	194.24	195.18
Within the Atmosphere			
S.W. absorbed	65.18	40.80	52.99
L.H. release by precip.	99.67	78.70	89.19
S.H. increase	1.12	2.16	1.64
KE increase	0.05	-0.06	-0.005
LE increase	.70	.66	.68
Bottom Boundary of Atmosphere			
S.W. absorbed	196.40	132.60	164.50
L.W. outgoing	27.78	35.49	31.63
S.H. flux outgoing	23.53	31.55	27.54
L.H. flux outgoing	88.78	87.54	88.16
Net Energy Absorbed			
Land	- -	- -	-1.30
Ocean	- -	- -	25.08
Lower boundary	56.32	-21.98	17.17
Top boundary	65.47	-20.85	22.31
Planetary Albedo	0.41	0.37	0.39

Table 6.2b July energy balance (W m^{-2}).

Items	Analysis of heat budget fields		
	S. hemisphere	N. hemisphere	Global
	Mean	Mean	Mean
Top Boundary of Atmosphere			
Incoming short wave flux	214.99	458.18	336.58
Outgoing short wave flux	76.14	180.80	128.47
Outgoing long wave flux	199.78	210.02	204.90
Within the Atmosphere			
S.W. absorbed	33.30	69.30	51.30
L.H. release by precip.	84.30	103.76	94.03
S.H. increase	-1.24	6.15	2.45
KE increase	0.098	0.056	0.021
LE increase	0.044	2.729	1.387
Bottom Boundary of Atmosphere			
S.W. absorbed	105.54	208.09	156.81
L.W. outgoing	32.76	35.75	34.26
S.H. flux outgoing	31.54	33.42	32.48
L.H. flux outgoing	95.72	91.37	93.54
Net Energy Absorbed			
Land	- -	- -	3.60
Ocean	- -	- -	-6.48
Lower boundary	-54.48	47.54	-3.47
Top boundary	60.94	-67.38	-3.22
Planetary Albedo	0.35	0.39	0.38

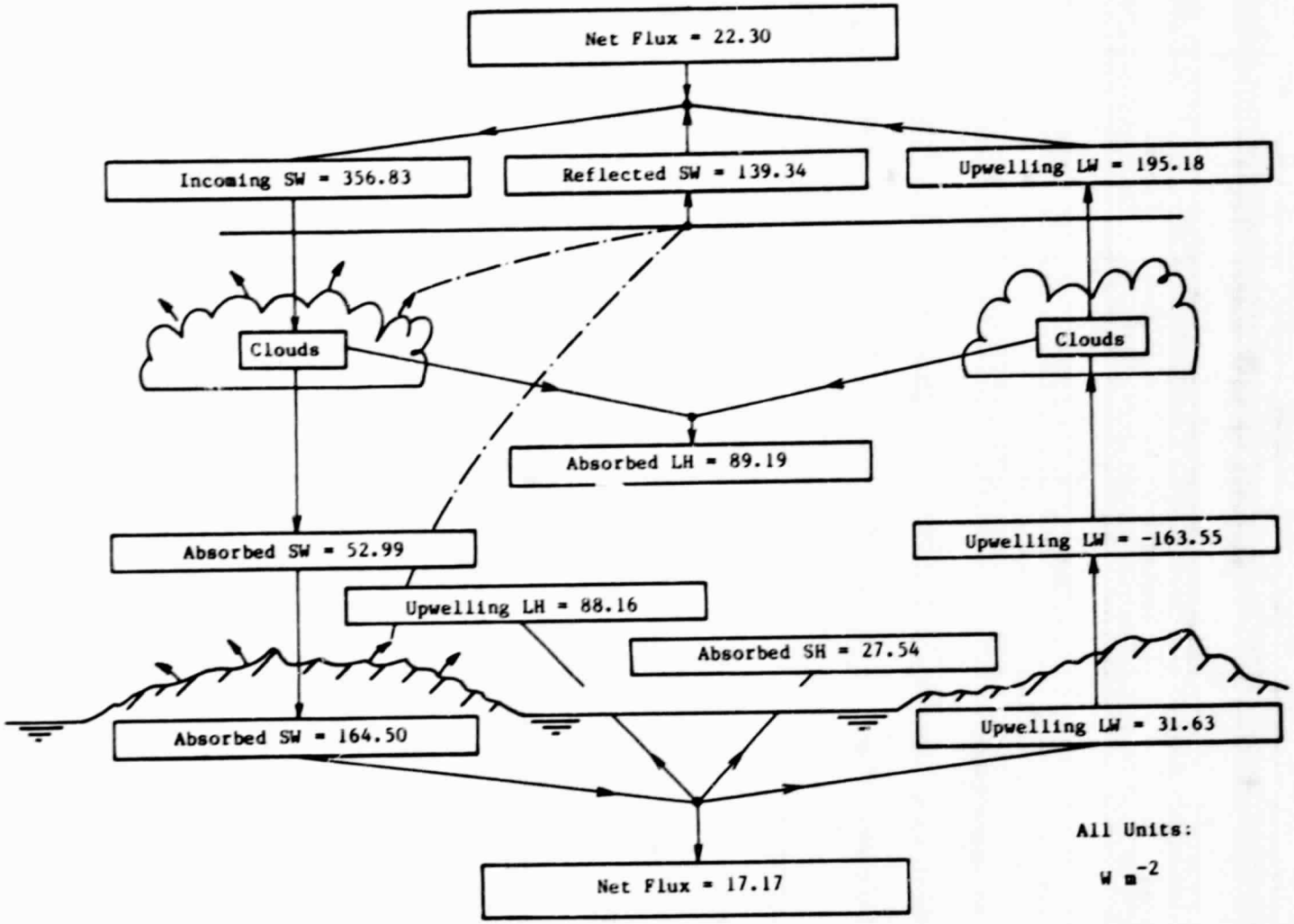

Figure 6.1a February summary of the globally integrated atmospheric budgets of thermodynamic energy and moisture, in W m^{-2}. The symbol meanings are: SW = short-wave (solar) radiation, LW = long-wave (thermal) radiation, SH = sensible heat, LH = latent heat.

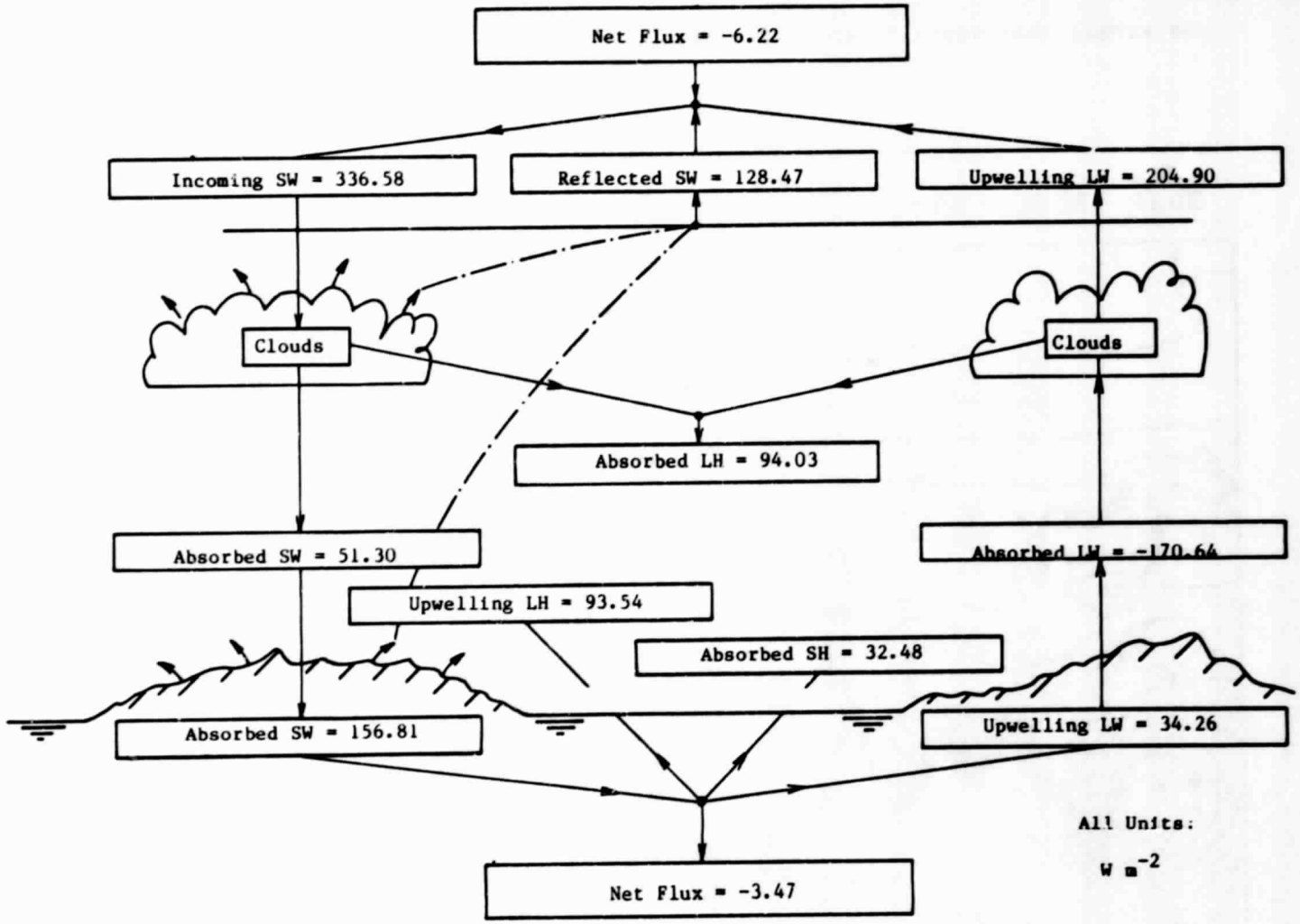

Figure 6.1b July summary of the globally integrated atmospheric budgets of thermodynamic energy and moisture, in W m^{-2}. The symbol meanings are: SW = short-wave (solar) radiation, LW = long-wave (thermal) radiation, SH = sensible heat, LH = latent heat.

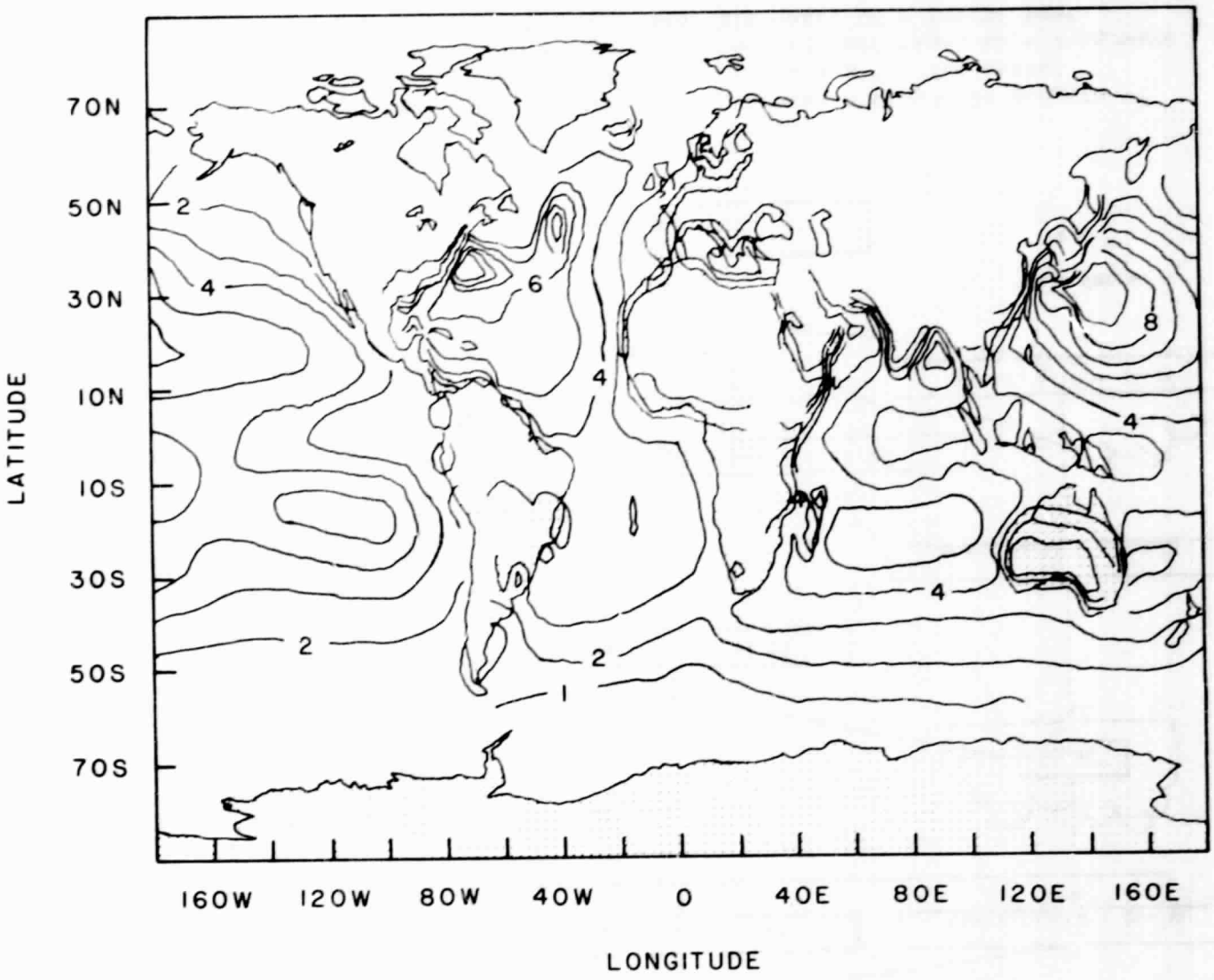

Figure 6.2a January observed evaporation, in mm dy^{-1}, taken from Schutz and Gates (1971).

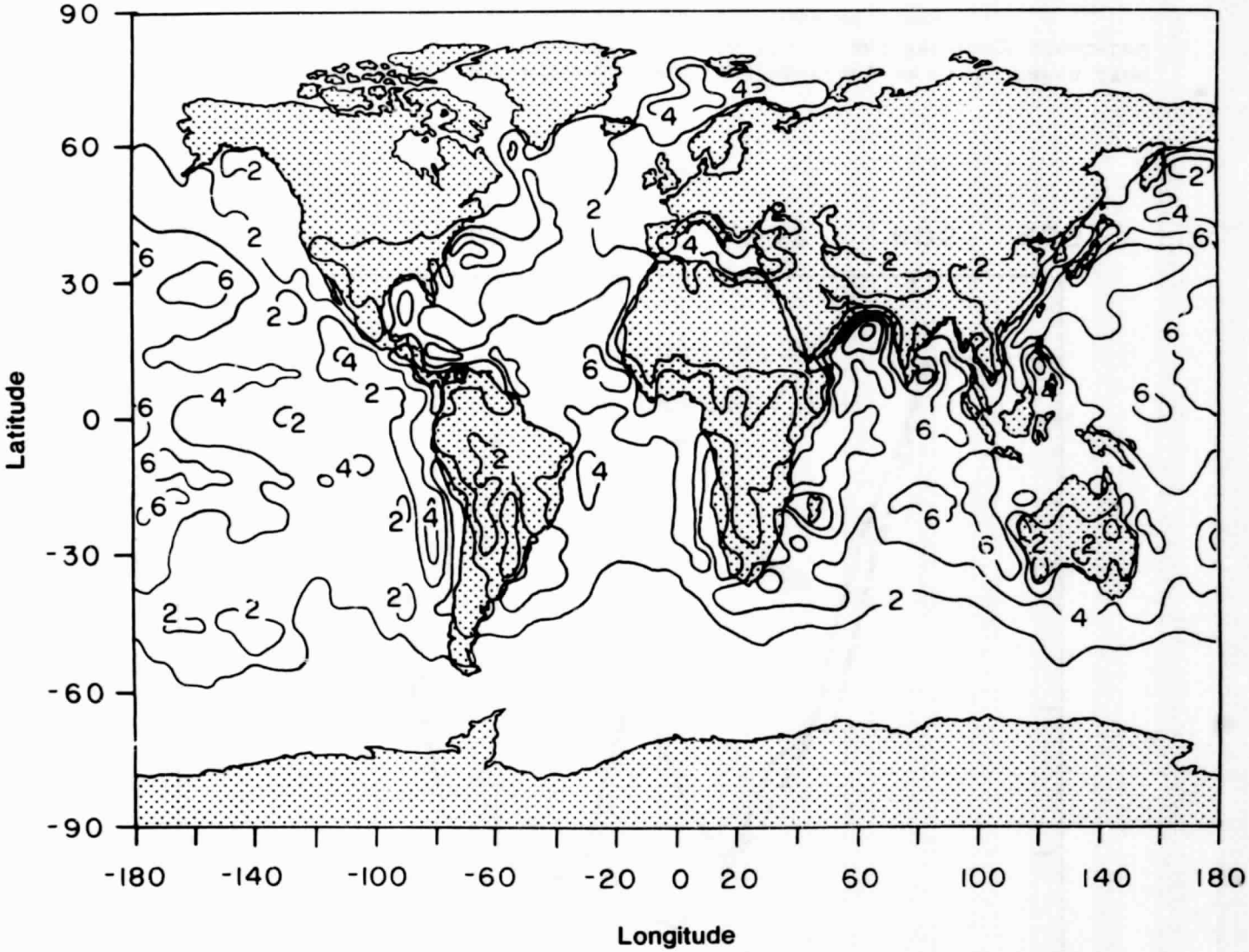

Figure 6.2b February simulated evaporation, in mm dy^{-1}.

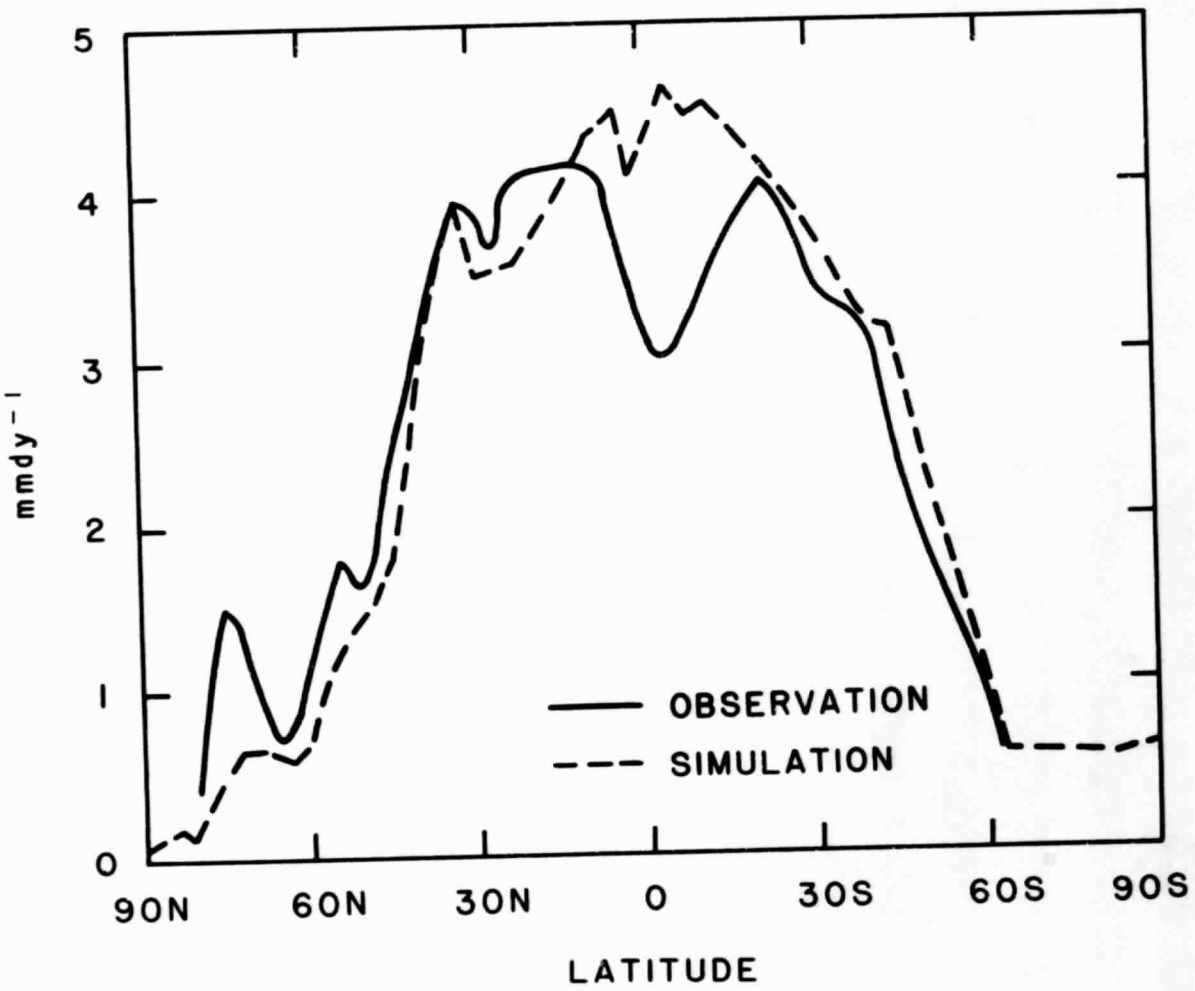

Figure 6.2c January observed zonal mean evaporation, mm dy^{-1}, taken from Schutz and Gates (1971) (solid line), and February simulated zonal mean evaporation, mm dy^{-1} (dashed line).

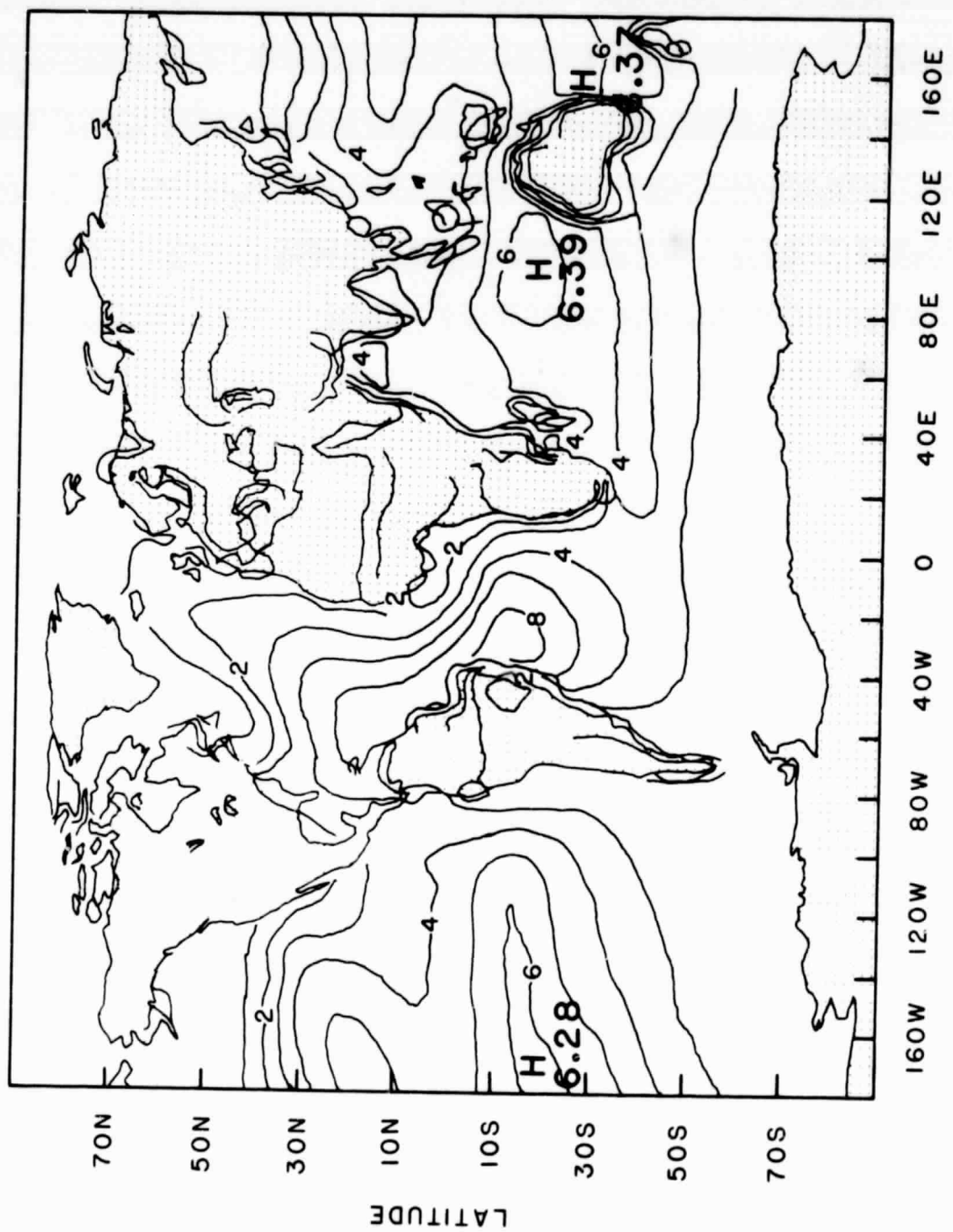

Figure 6.2d July observed evaporation, taken from Schutz and Gates (1972). The contour interval is 1 mm dy^{-1}.

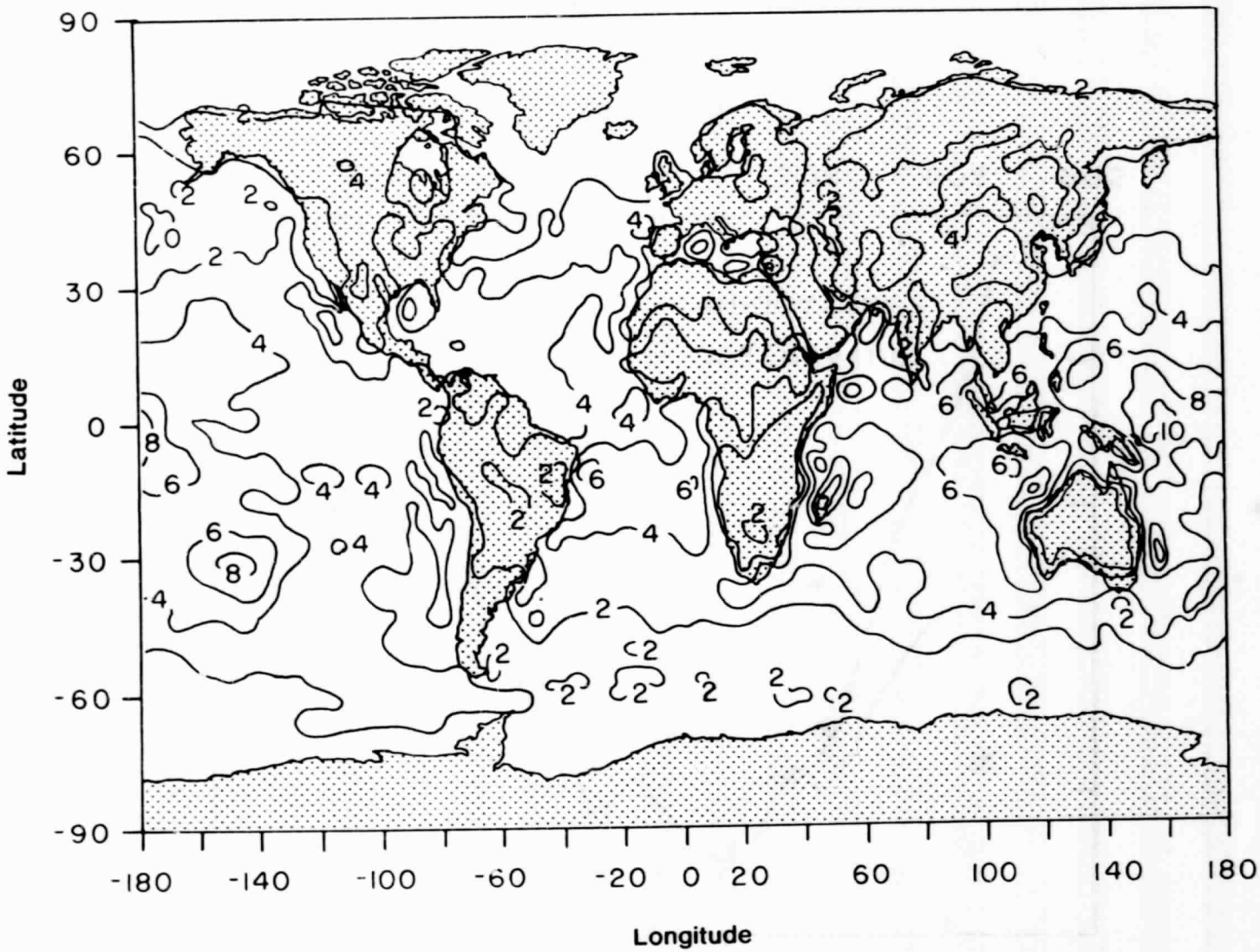

Figure 6.2e July simulated evaporation, mm dy^{-1}.

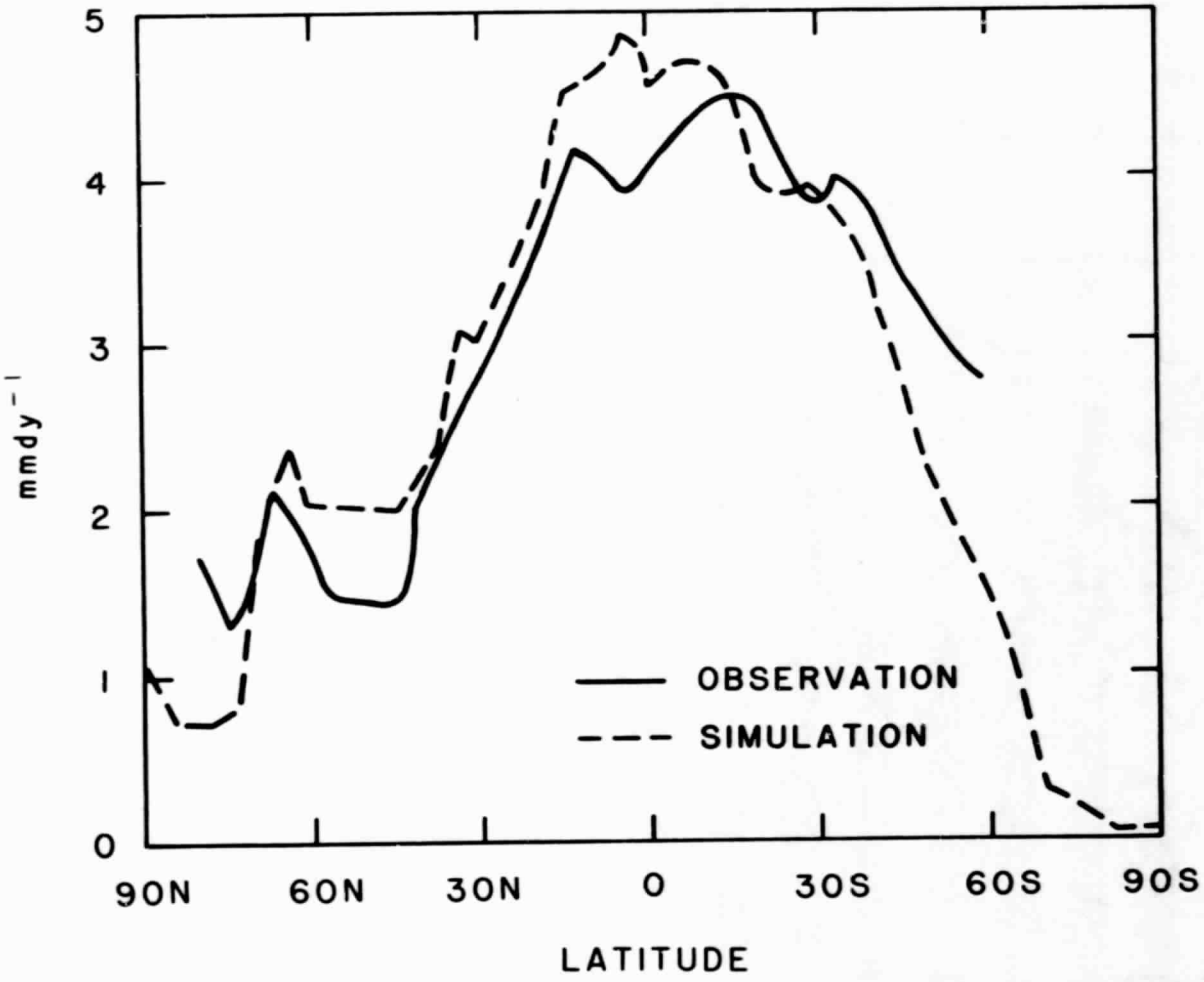

Figure 6.2f July observed zonal mean evaporation, mm dy^{-1}, taken from Schutz and Gates (1972) (solid line), and July simulated zonal mean evaporation, mm dy^{-1} (dashed line).

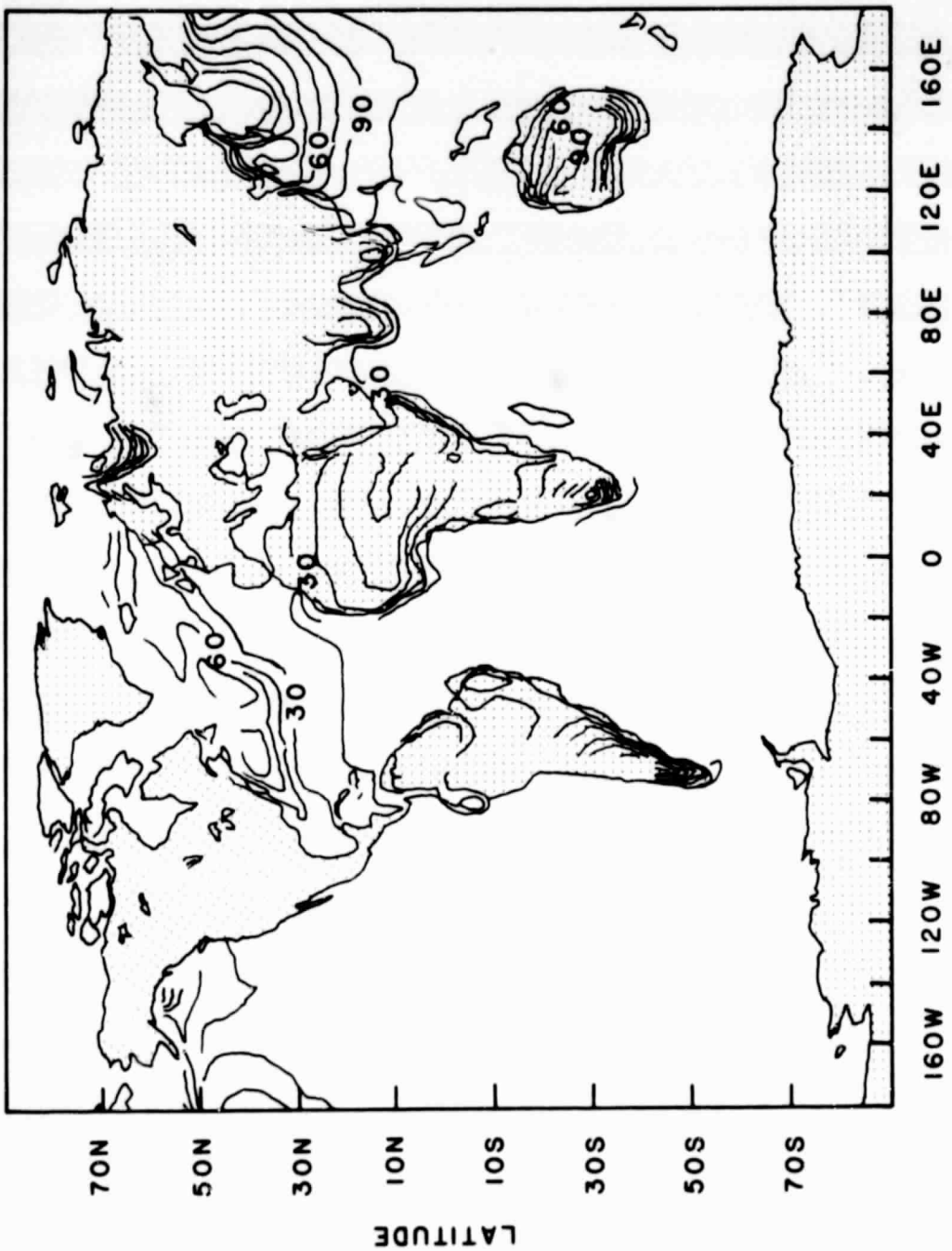

Figure 6.3a January observed surface sensible heat flux, in W m^{-2}, taken from Schutz and Gates (1971).

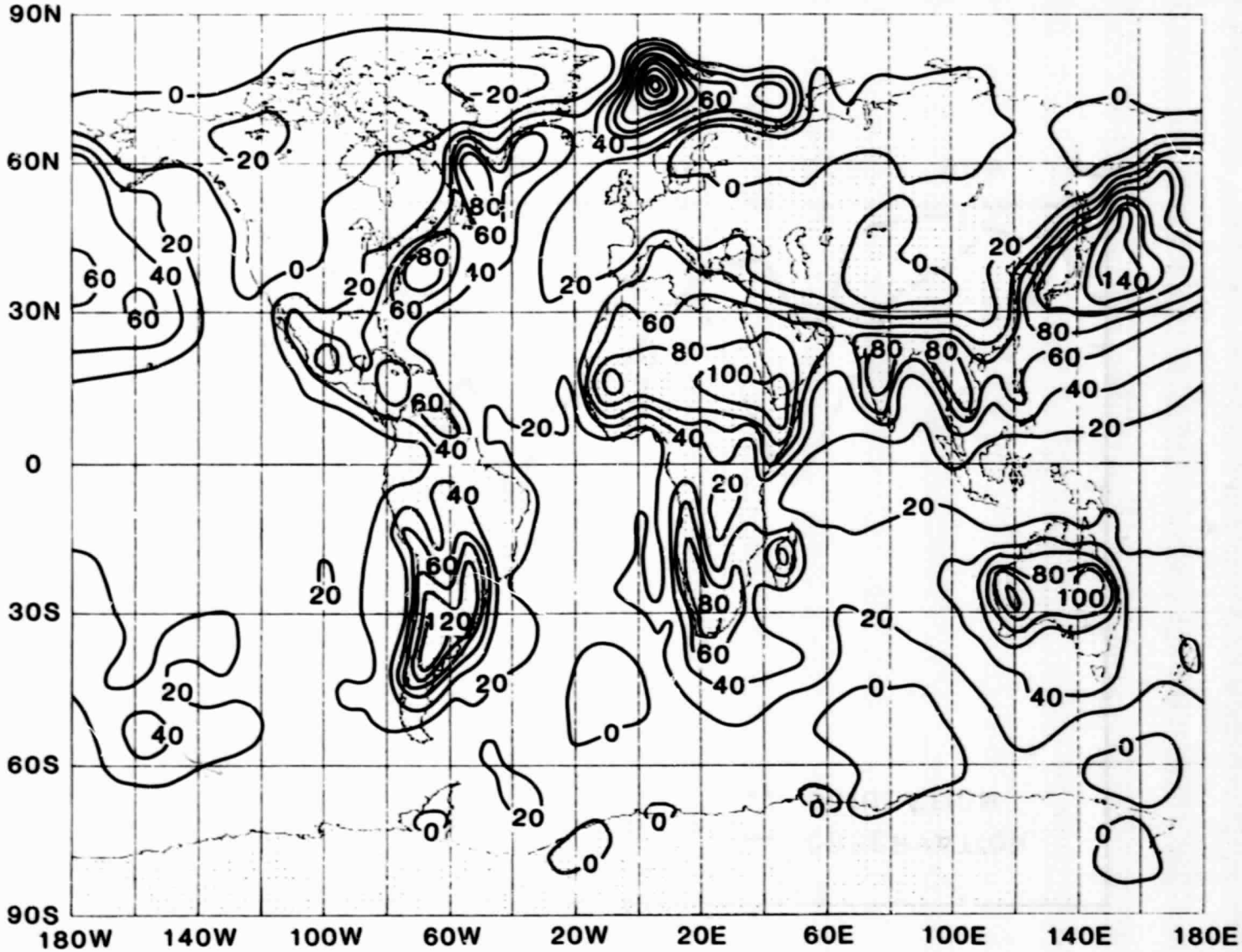

Figure 6.3b February simulated surface sensible heat flux, W m^{-2}.

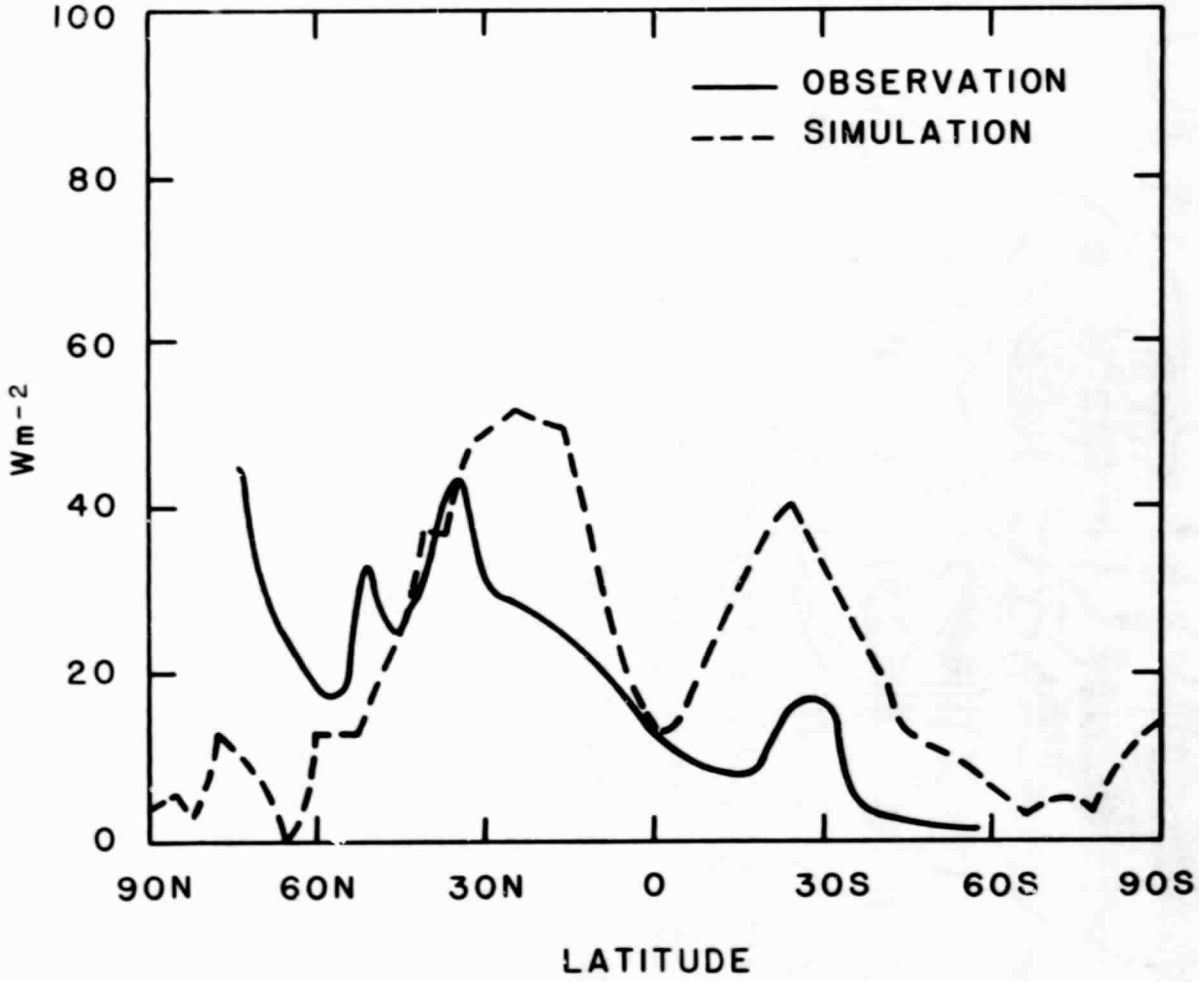

Figure 6.3c January observed zonal mean surface sensible heat flux taken from Schutz and Gates (1971) (solid line), and February simulated zonal mean surface sensible heat flux, Wm^{-2} (dashed line).

Figure 6.3d July observed surface sensible heat flux taken from Schutz and Gates (1972).

239

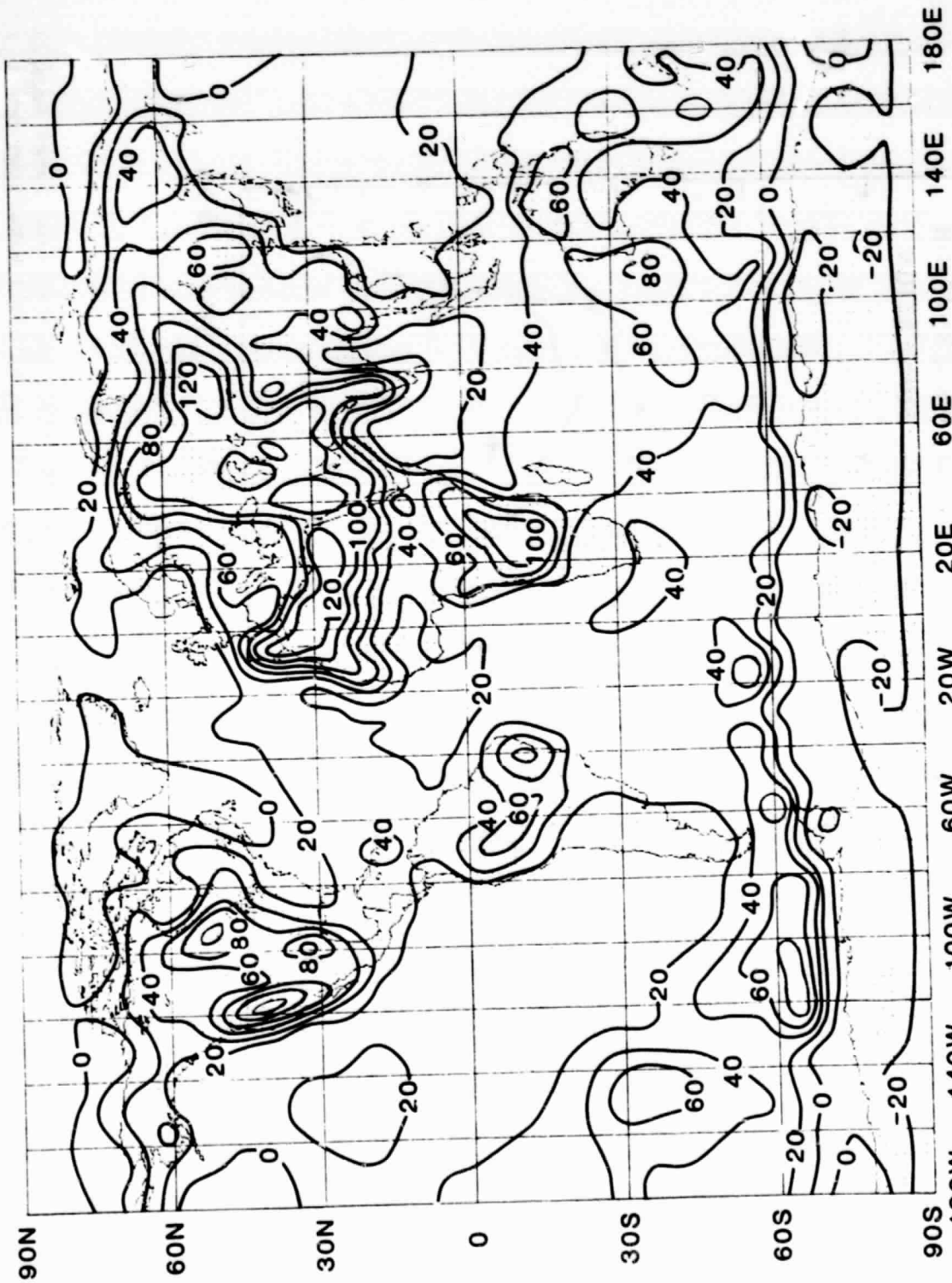

Figure 6.3e July simulated surface sensible heat flux, W m^{-2}.

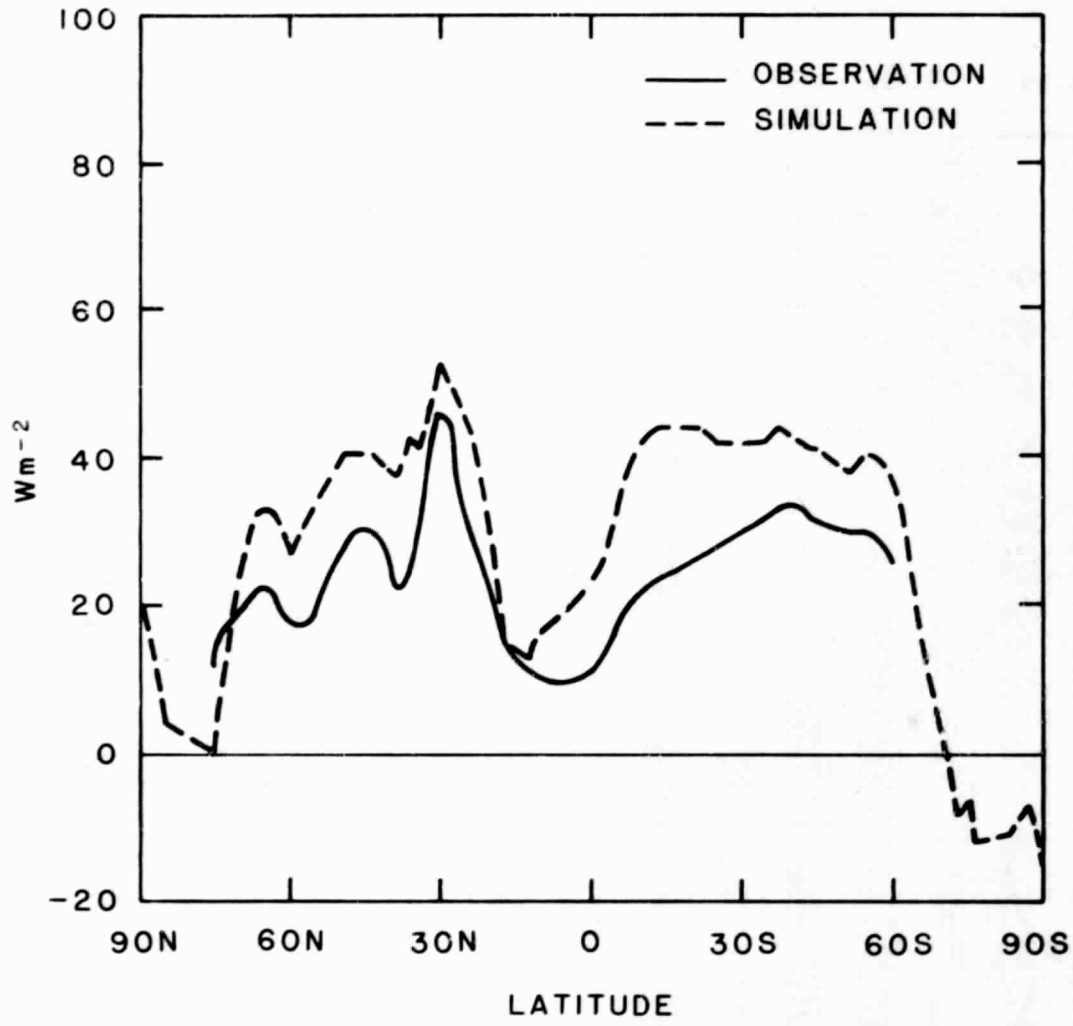

Figure 6.3f July observed zonal mean surface sensible heat flux taken from Schutz and Gates (1972) (solid line), and July simulated zonal mean surface sensible heat flux, W m^{-2}.

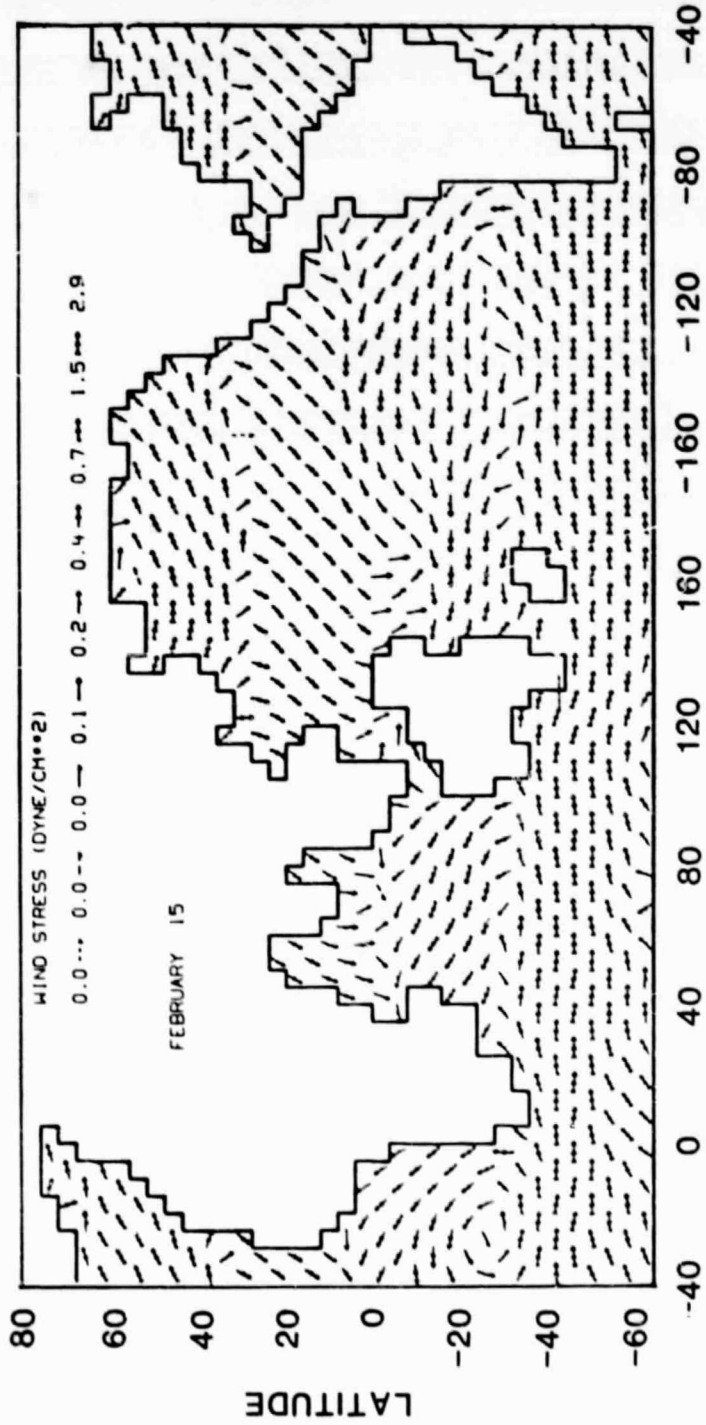

Figure 6.4a February observed surface stress, dynes cm^{-2}, taken from Mintz (1979) as derived from Hellerman (1967).

243

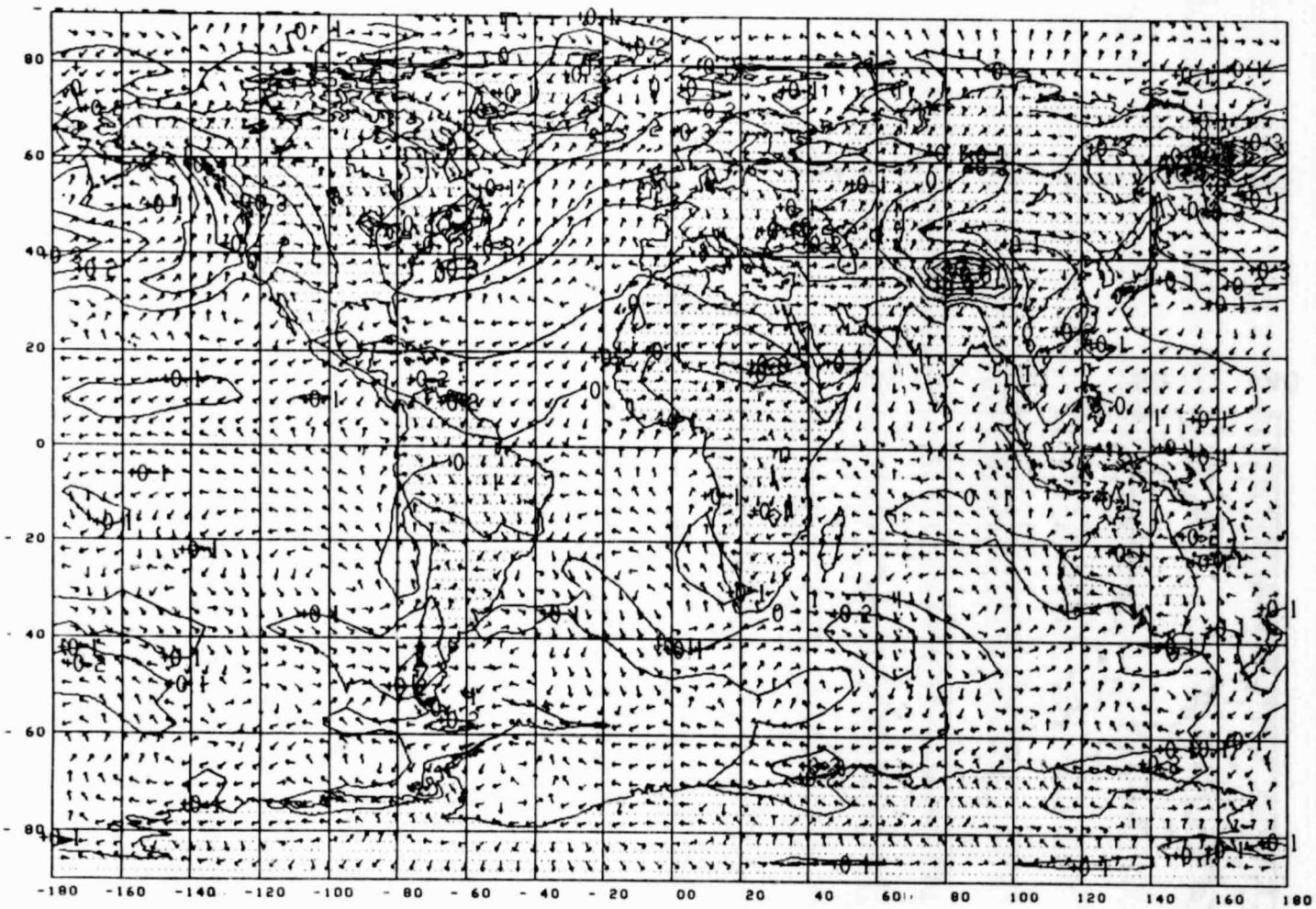

Figure 6.4b February simulated surface stress. The arrows indicate direction and the contour lines indicate magnitude. The contour interval is 0.1 pascal.

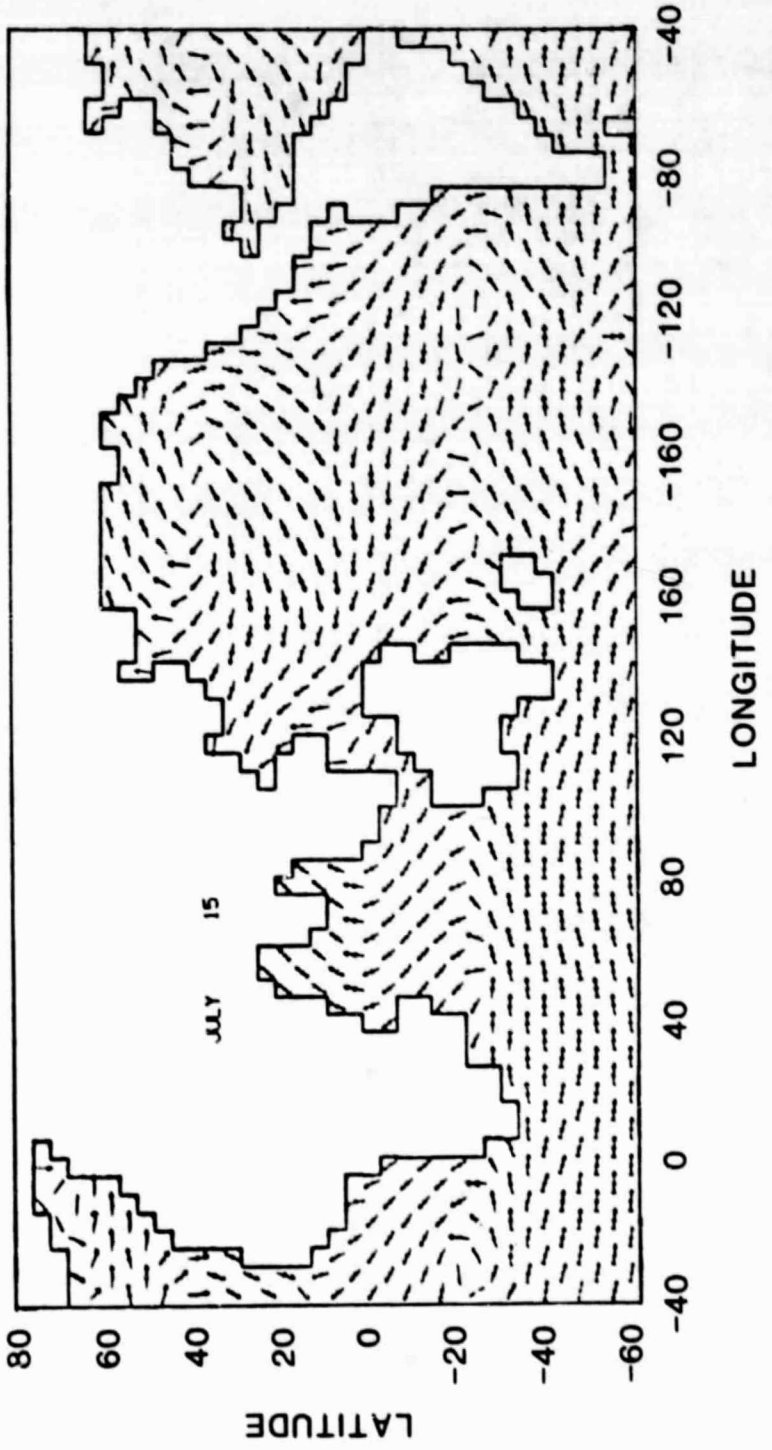

Figure 6.4c July observed surface stress, dynes cm^{-2}, taken from Mintz (1979) as derived from Hellerman (1967).

Figure 6.4d July simulated surface stress. The arrows indicate direction and the contour lines indicate magnitude. The contour interval is 0.1 pascal.

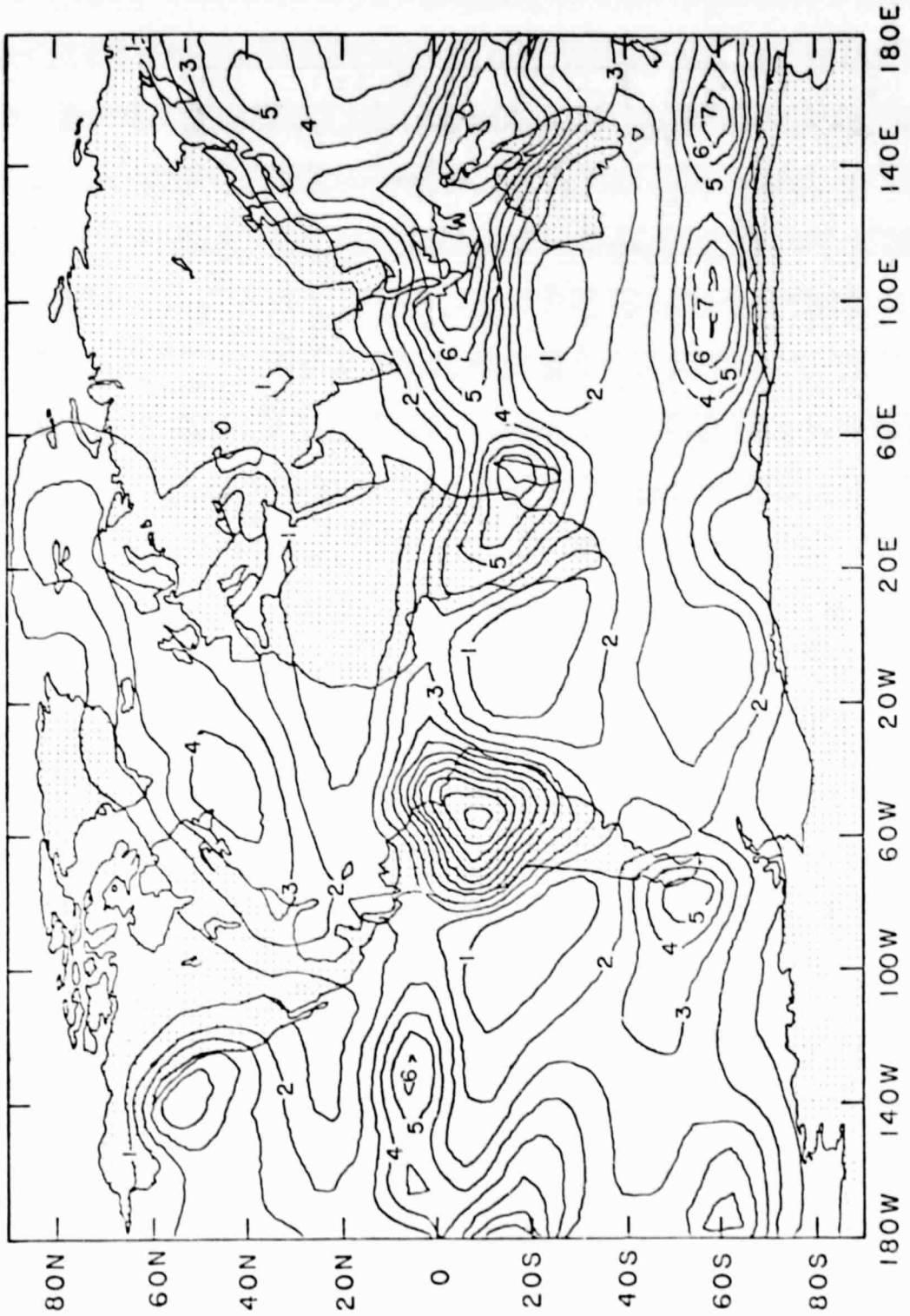

Figure 6.5a February observed precipitation, taken from Jaeger (1976). The contour interval is 1 mm dy^{-1}.

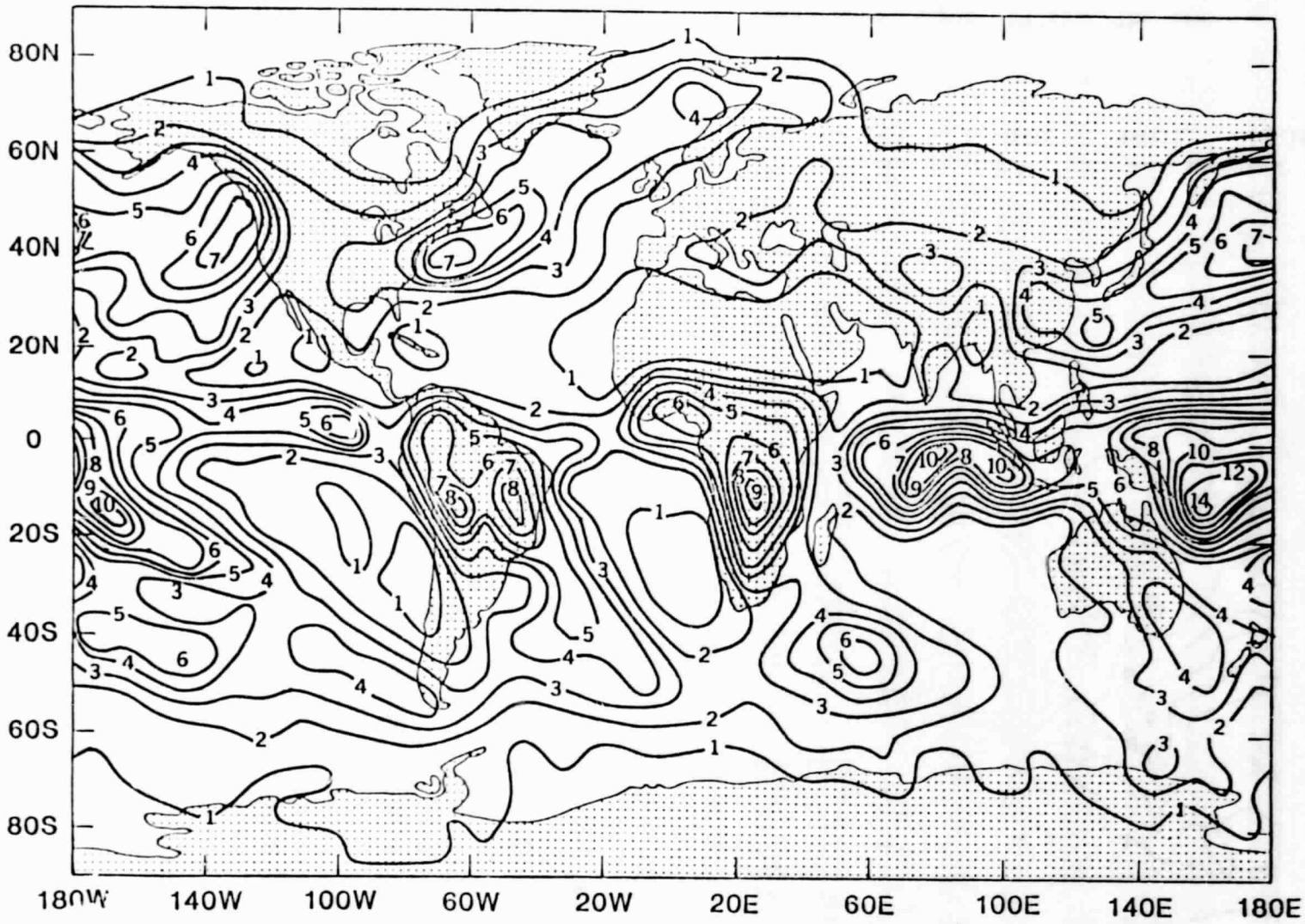

Figure 6.5b February simulated precipitation. The contour interval is 1 mm dy^{-1} except in congested regions.

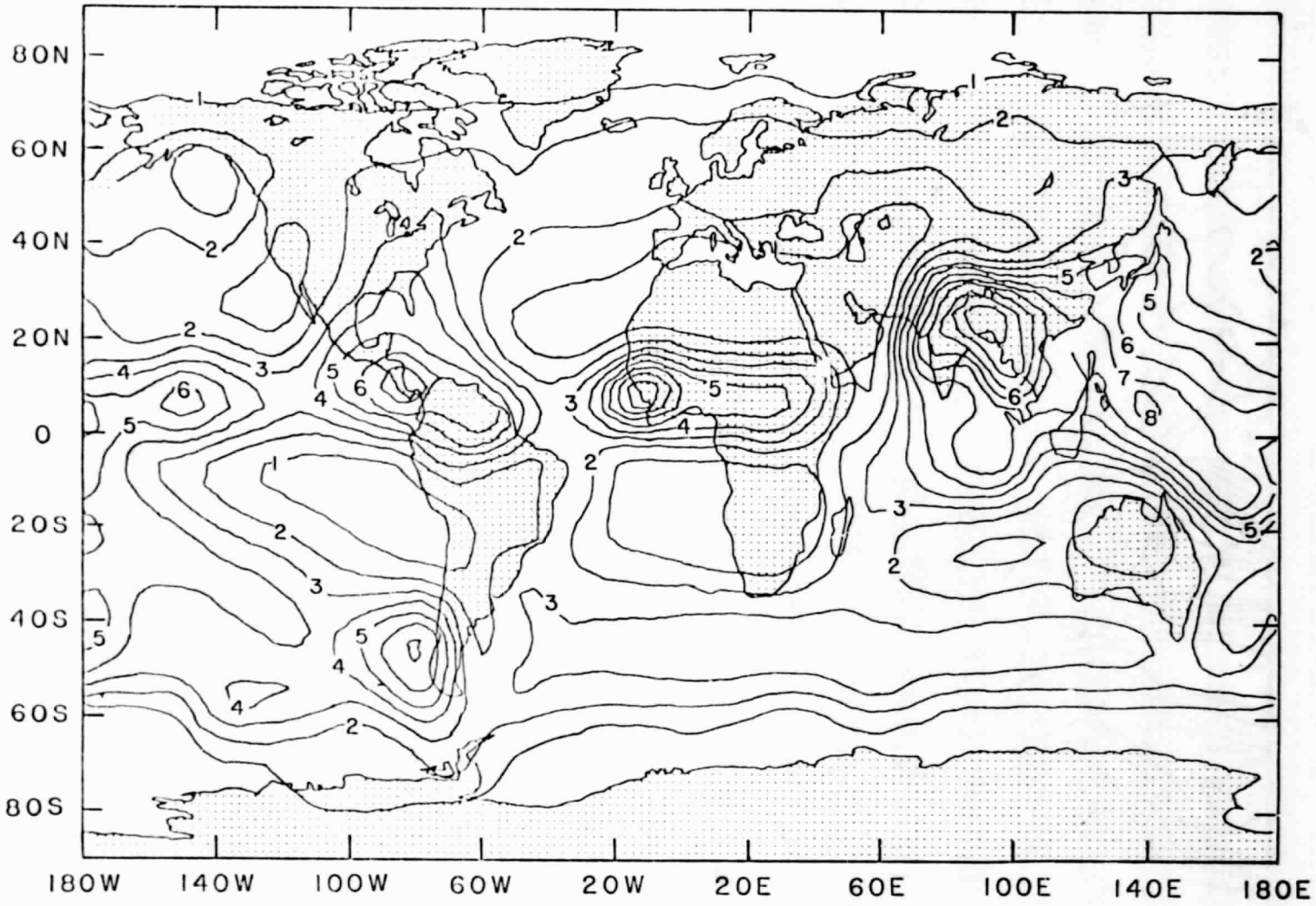

Figure 6.5c July observed precipitation, taken from Jaeger (1976). The contour interval is 1 mm dy^{-1}.

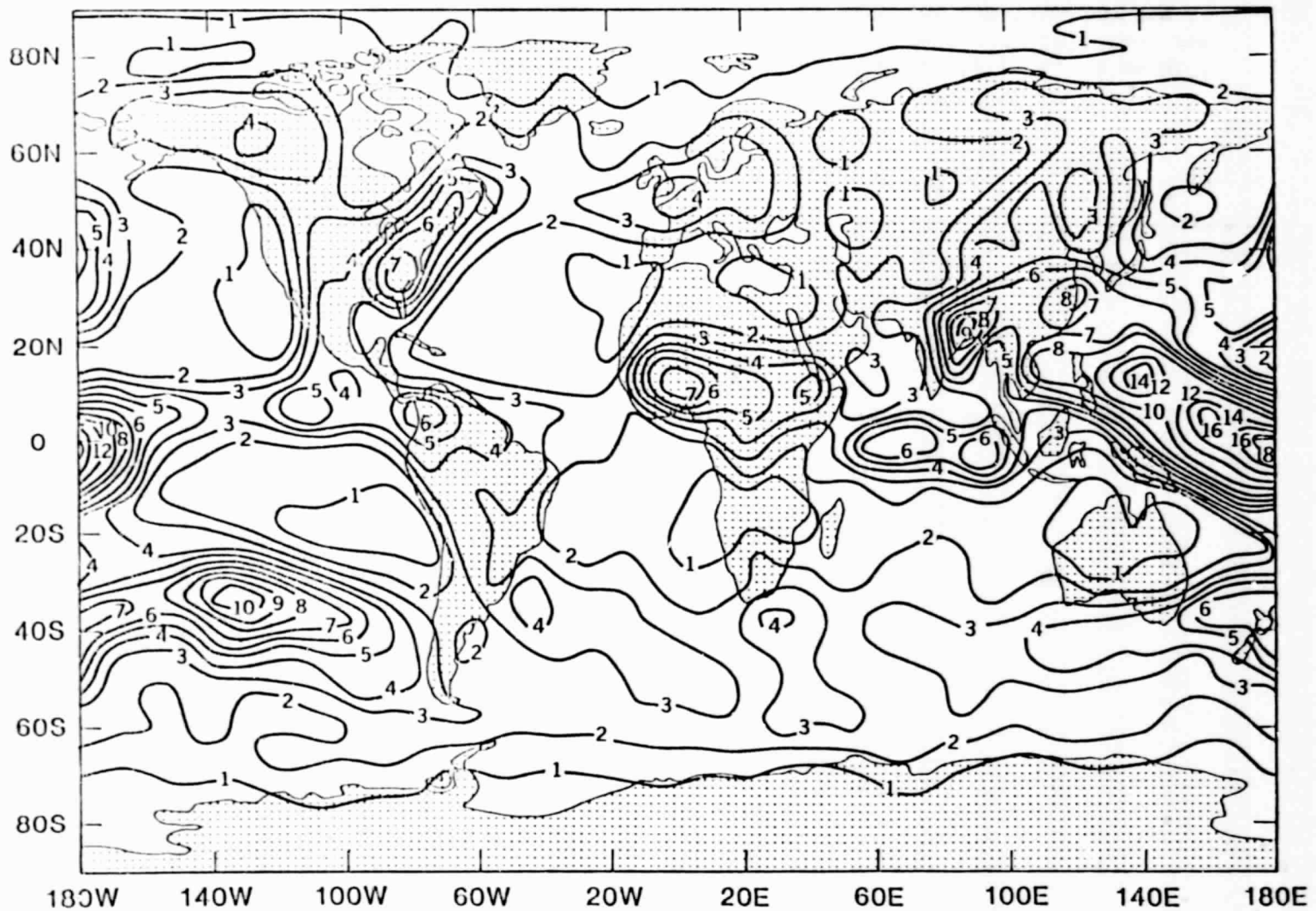

Figure 6.5d July simulated precipitation. The contour interval is 1 mm dy^{-1} except in congested regions.

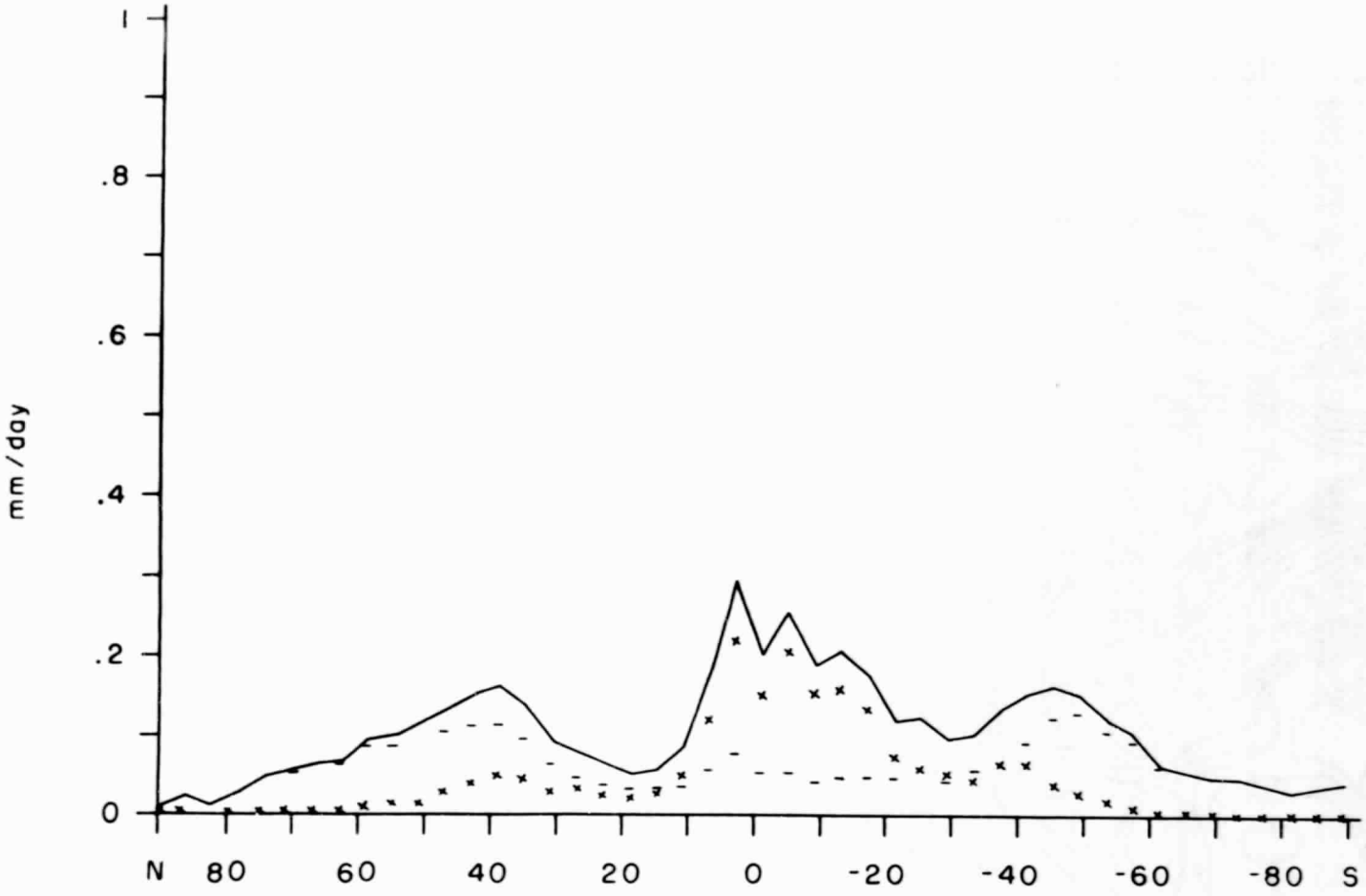

Figure 6.5e February simulated zonal mean precipitation by type, in mm hr^{-1}: The solid line is the total. The *'s give the contribution due to cumulus convection, and the -'s give the contribution due to large-scale saturation.

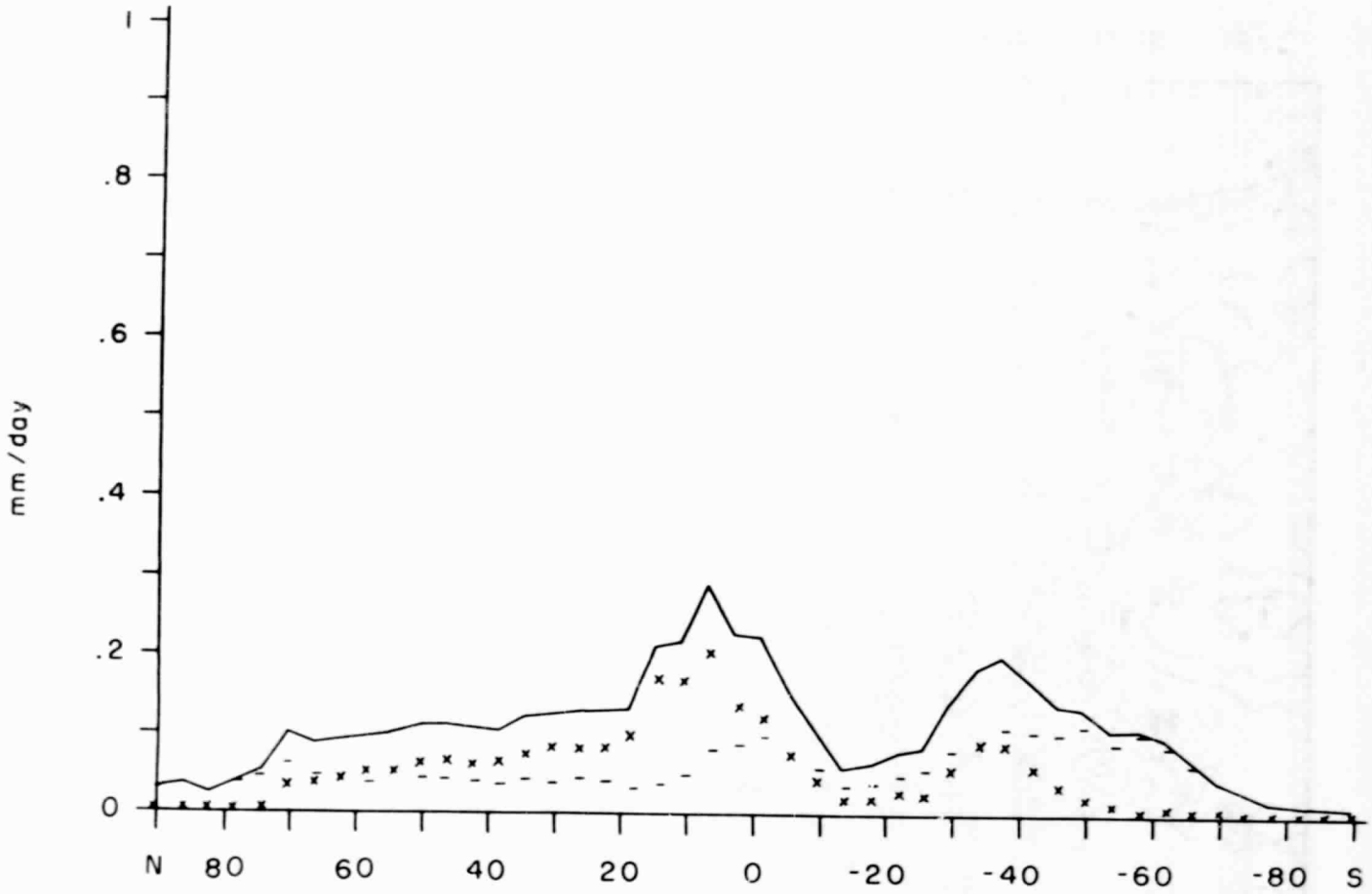

Figure 6.5f July simulated zonal mean precipitation by type, in mm hr^{-1}: The solid line is the total. The *'s give the contribution due to cumulus convection, and the -'s give the contribution due to large-scale saturation.

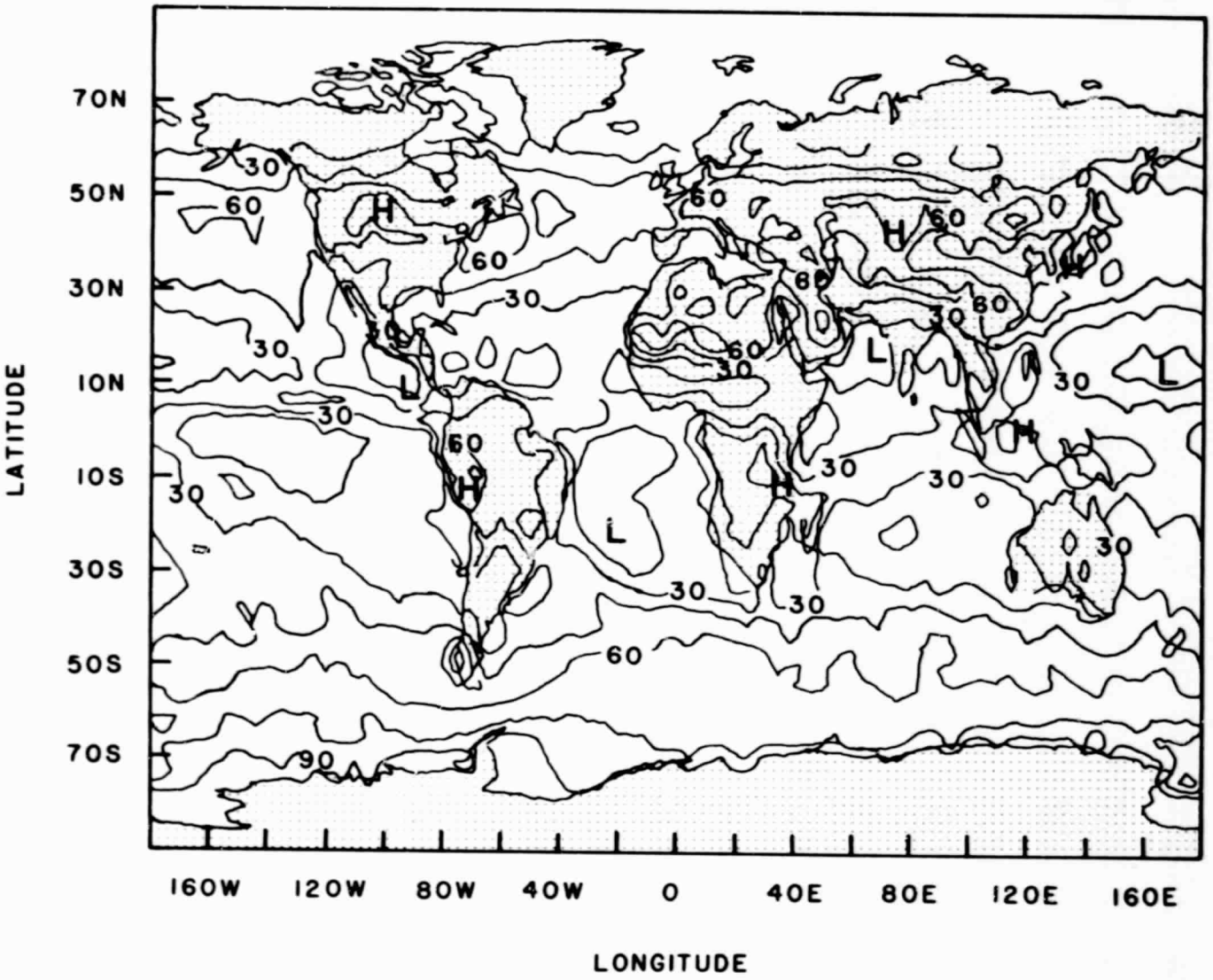

Figure 6.6a January observed total cloudiness, taken from Schutz and Gates (1971). The contour interval is 15 percent.

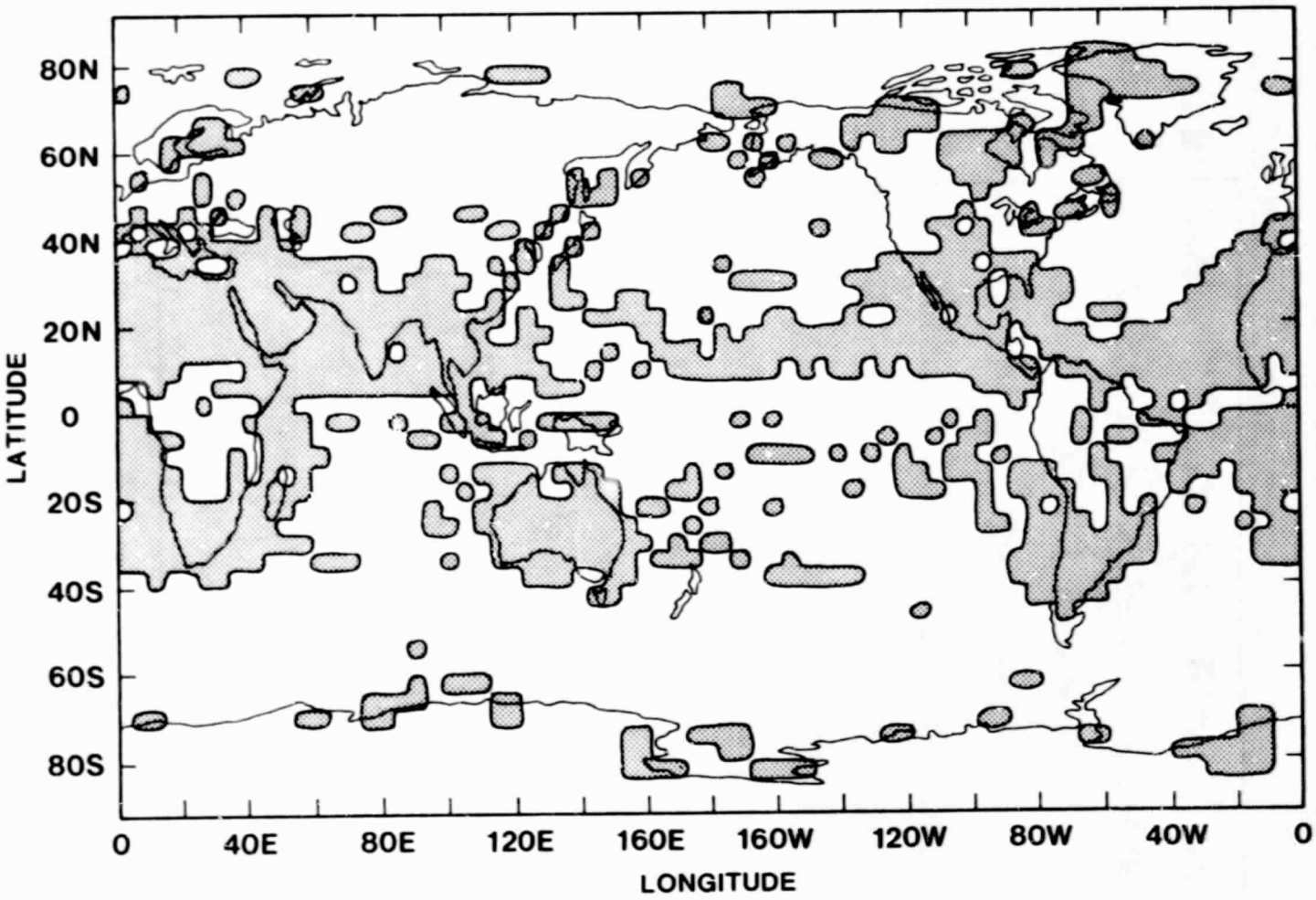

Figure 6.6b February simulated total cloudiness, in tenths. Regions with less than 7/10 cloudiness are shaded.

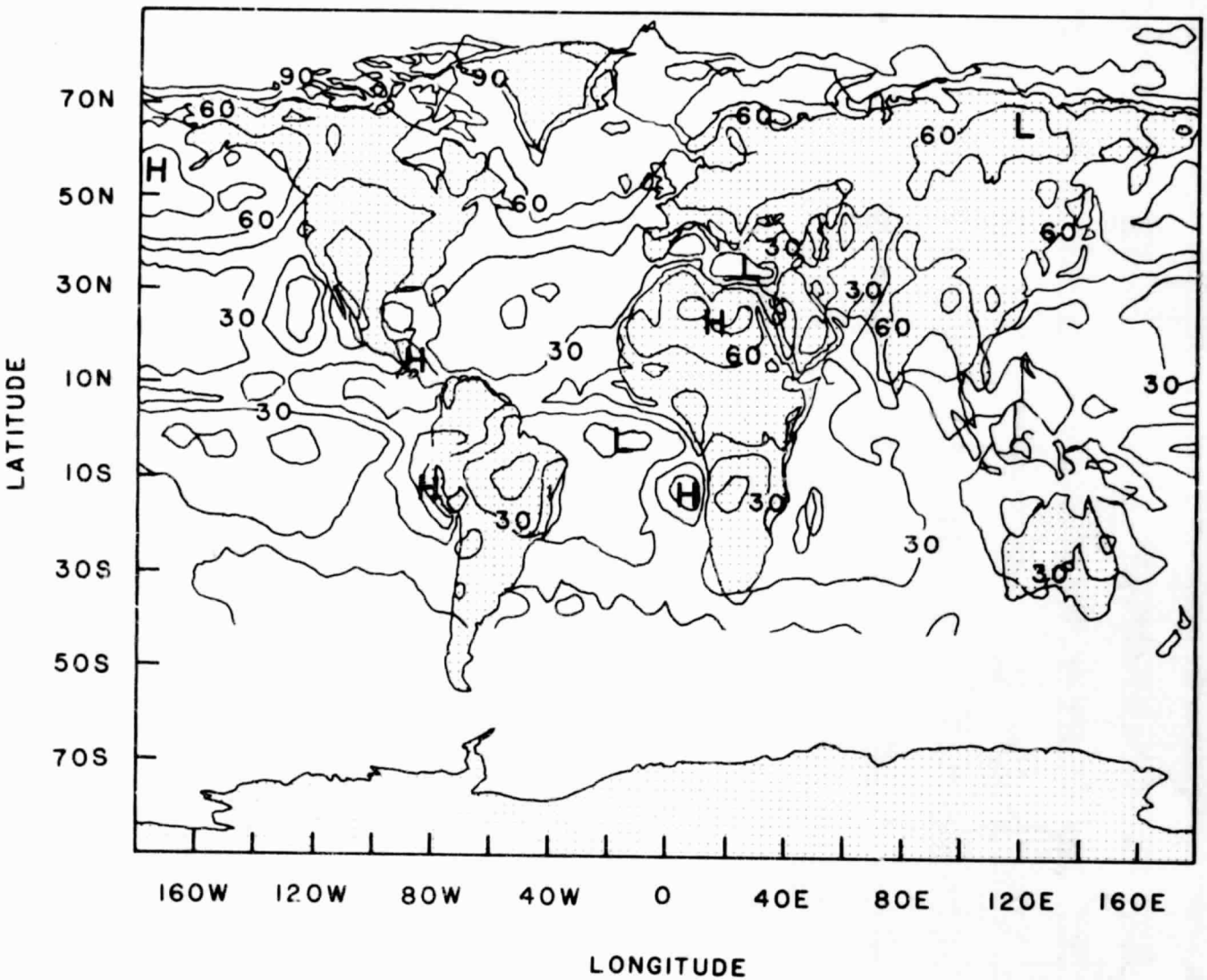

Figure 6.6c July observed total cloudiness, taken from Schutz and Gates (1971, 1972). The contour interval is 15 percent.

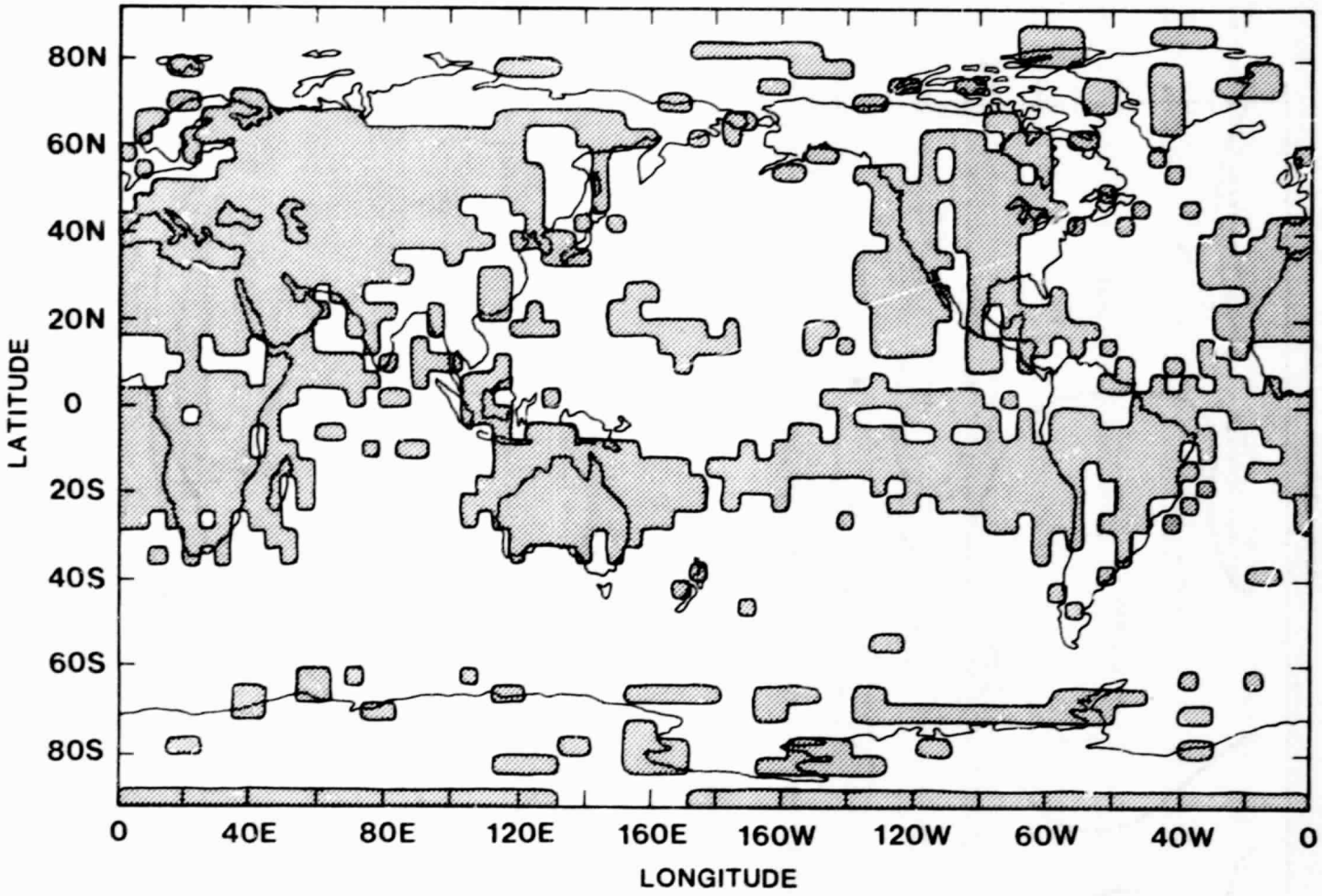

Figure 6.6d July simulated total cloudiness. Regions with less than 7/10 cloudiness are shaded.

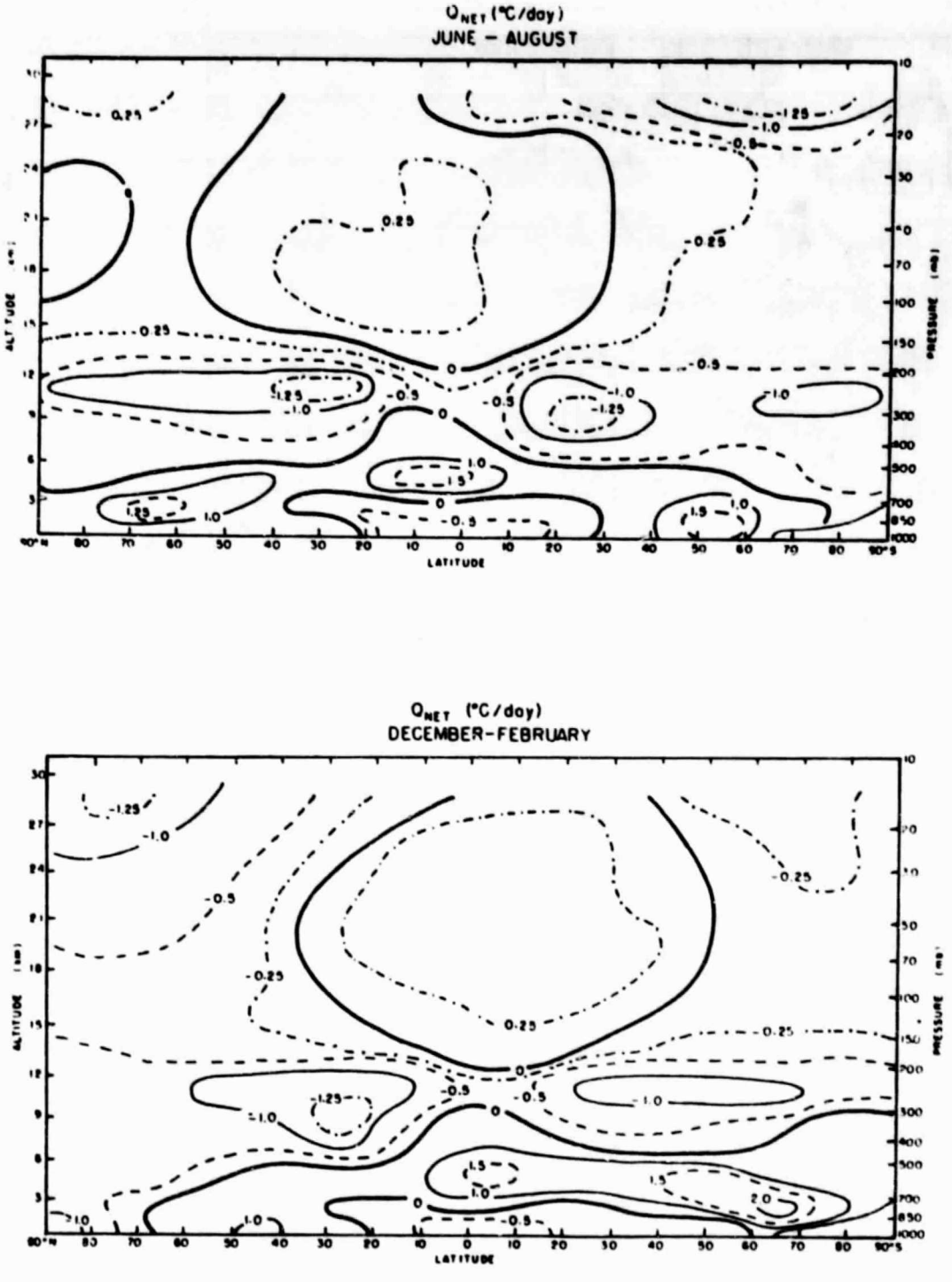

Figure 6.7a Zonally averaged total diabatic heating in K day^{-1} from observations, according to Newell et al. (1972).

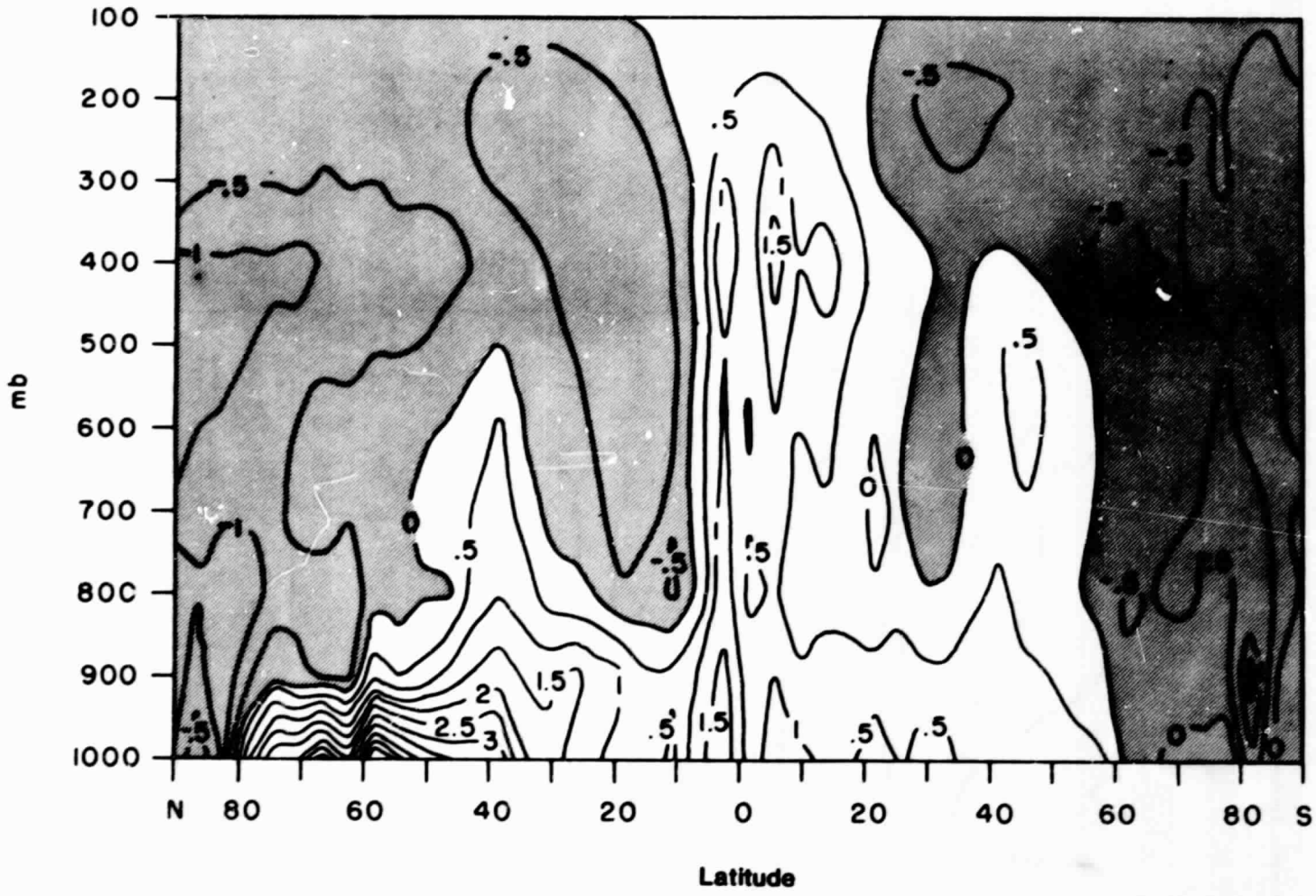

Figure 6.7b February simulated zonally averaged total diabatic heating, K day^{-1}.

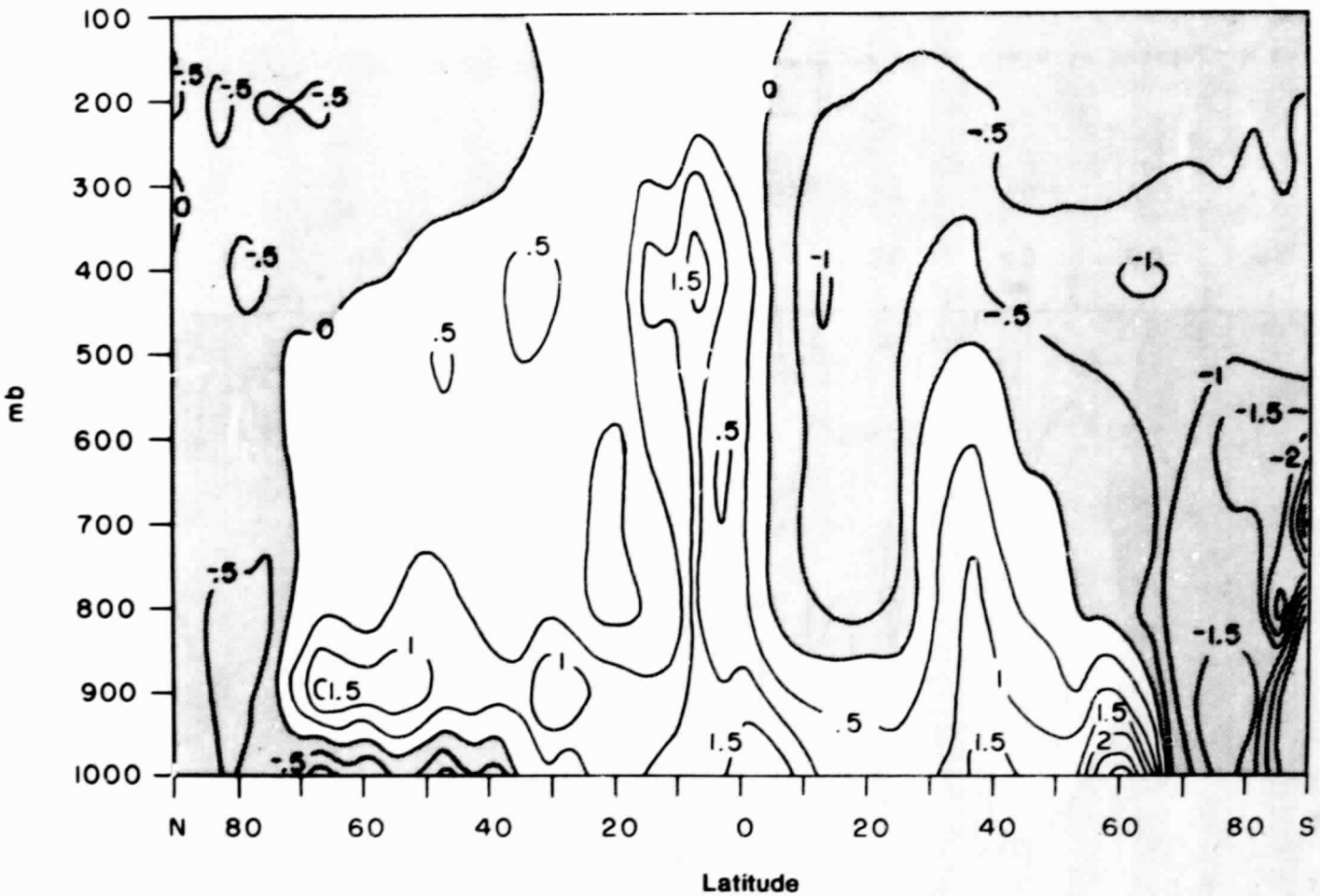

Figure 6.7c July simulated zonally averaged total diabatic heating, K day^{-1}.

7. Large-scale overturnings

a. Mean meridional circulations. The mass transport streamfunctions of the simulated February and July mean meridional circulations have been determined by interpolating the six-hourly simulated meridional winds to isobaric surfaces, time- and zonally-averaging the result, and subtracting away its vertical mean. The streamfunction for the time- and zonally-averaged meridional circulation is then given by

$$\Psi_H(\phi,p) = -(1/g)\int_p^{p_S} [\bar{v}]\, 2\pi a \cos\phi \, dp' , \tag{7.1}$$

where v is the meridional wind, the overbar denotes a time average, [ ] denotes a zonal average, a is the radius of the earth, ϕ is latitude, p is pressure, and subscript S denotes the earth's surface. The simulated latitude-height distributions of Ψ_H for February and July are given in Fig. 7.1b and c; the observed distributions obtained by Newell et al. (1972) are shown for comparison in Fig. 7.1a. In both seasons, but particularly in July, the simulated Hadley cells are somewhat weaker than observed. In view of the present model's lack of cumulus friction, and the widespread belief (e.g., Helfand, 1979) that cumulus friction acts to strengthen the Hadley circulation, this result is to be expected if not welcomed. The simulated mid-latitude Ferrel cells are also weaker than observed.

b. The Walker circulations. Bjerknes (1969) suggested the possible importance of large-scale equatorial east-west overturnings, which he called Walker circulations. It is believed (Cornejo-Garrido and Stone, 1977) that the Walker circulation is driven by a longitudinal variation of the latent heating. Newell et al. (1972) suggested that the term "Walker circulation" be generalized to include any longitudinal overturning, tropical or otherwise.

We have computed the simulated Walker mass transport streamfunctions by the following procedure: The zonal wind field is interpolated to isobaric surfaces, and subsequently time-averaged. At each level and latitude the zonal mean of the result is then subtracted away. Finally, the vertical mean of the result is subtracted away at each latitude and longitude to yield closed circulations. For convenience, let the residual zonal wind obtained by this procedure be denoted by $\tilde{\bar{u}}_*$, where the overbar again denotes a time mean, the * denotes a departure from the zonal mean, and the tilde denotes a departure from the vertical mean. The mass transport stream function is then given by

$$\Psi_W = (1/g) \int_p^{p_S} (\tilde{\bar{u}}_*)_{\phi_{1,2}} a \, dp' \qquad (7.2)$$

where $(\ )_{\phi_{1,2}}$ denotes an average over latitude from ϕ_1 to ϕ_2.

For both February and July, we have computed Ψ_W for the latitude strips 30°S-Equator and Equator-30°N; the results are shown in Fig. 7.2b-e. For comparison, Fig. 7.2a shows with the observations reported by Newell et al. (1972), for 5°S and 5°N. The most striking finding in the simulations is the very large, well-organized Northern Hemispheric circulation in February. The rising branch of this Walker cell is near 140° west longitude, over the eastern North Pacific. As shown in Fig. 6.5, there is an intense precipitation maximum at about 10°N at this longitude. The sinking branch of the Walker cell is near 90° east longitude, in the vicinity of the Siberian high. In July, the simulated Northern Hemisphere Walker circulation is much weaker and less well-organized.

In the Southern Hemisphere winter, there is a modest Walker cell whose rising branch is near the spectacular precipitation maximum on the date line, and whose sinking branch is near South Africa. The February simulation exhibits a weaker, less well-organized Southern Hemispheric Walker circulation.

Summarizing, the model has produced vigorous winter-hemisphere Walker circulations in both February and July. The cells have their rising branches over oceanic regions of strong latent heat release, and their sinking branches over land. The summer-hemisphere circulations are much weaker in both February and July.

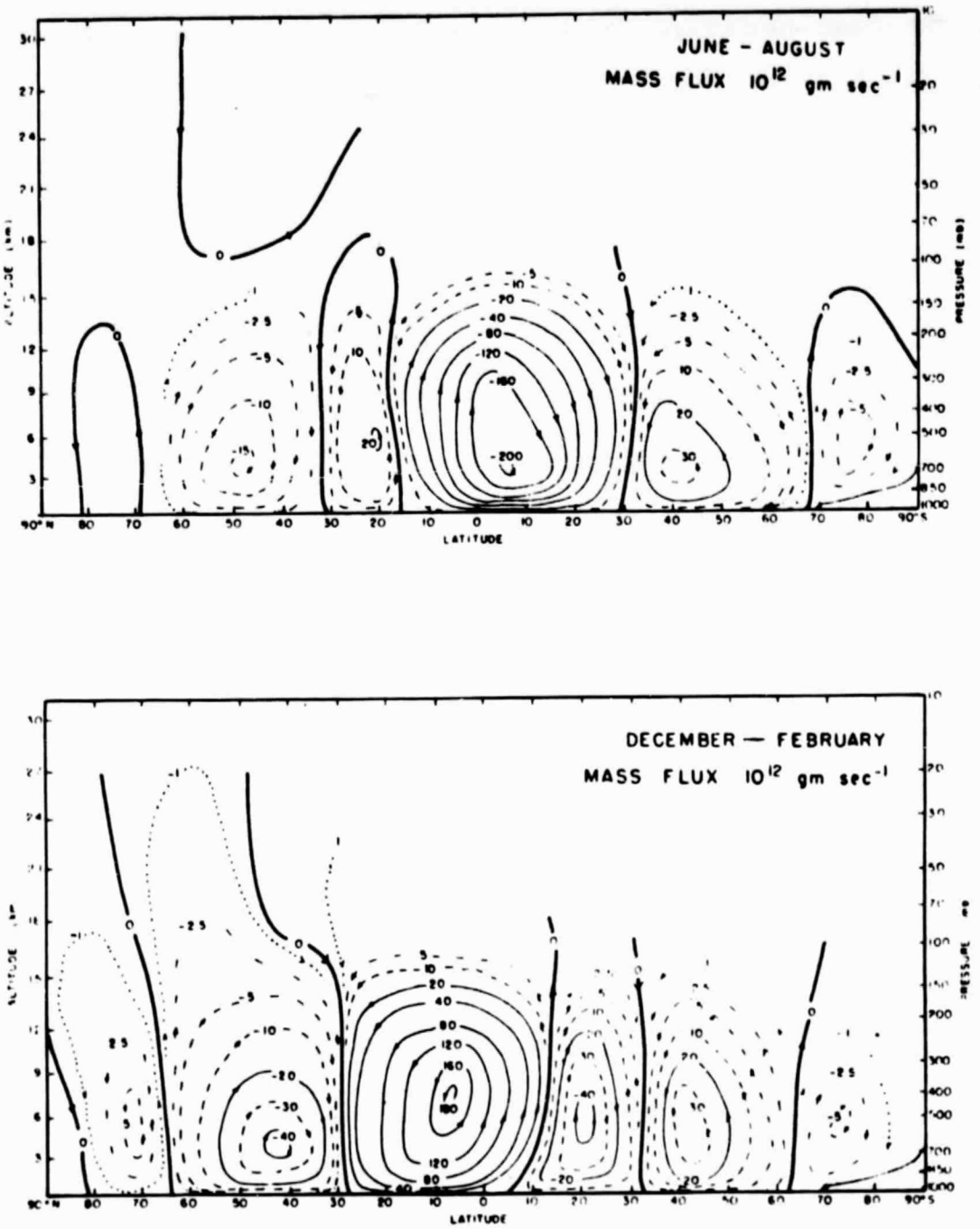

Figure 7.1a Stream function for the mean meridional circulations, according to Newell et al. (1972), in units of 10^9 kg s^{-1}.

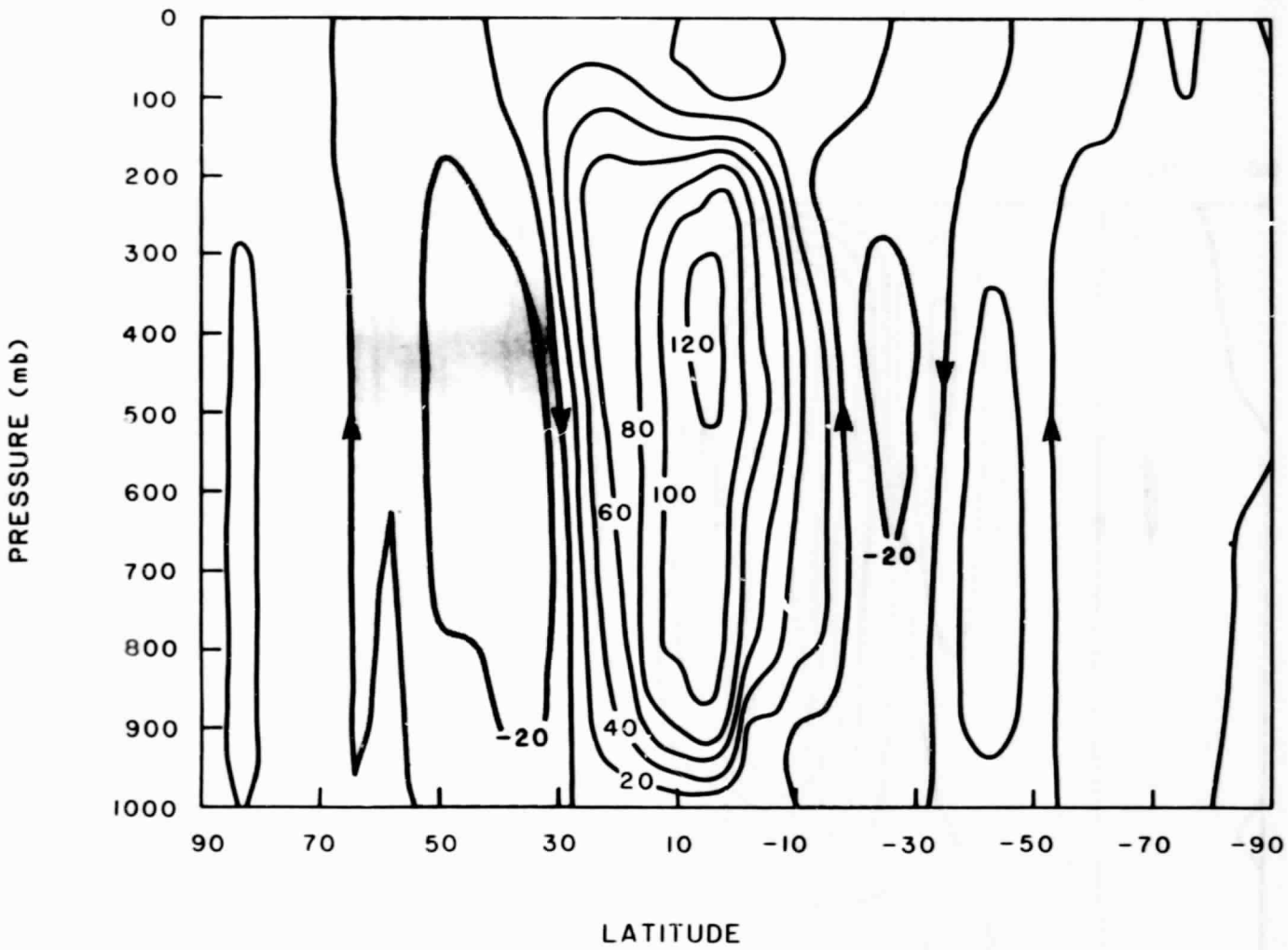

Figure 7.1b February simulated stream function for the mean meridional circulations, in units of 10^9 kg s^{-1}.

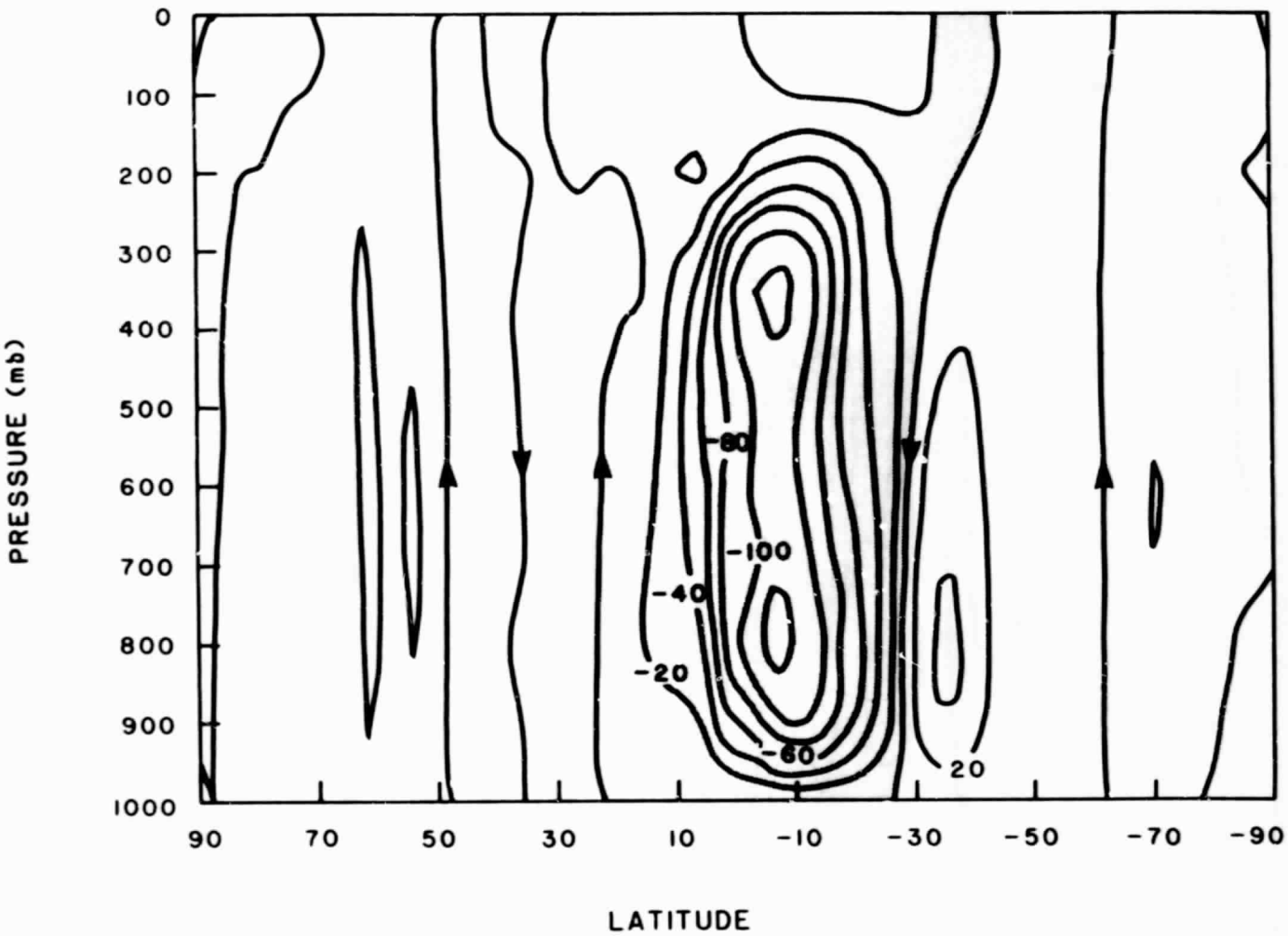

Figure 7.1c July simulated stream function for the mean meridional circulations, in units of 10^9 kg s^{-1}.

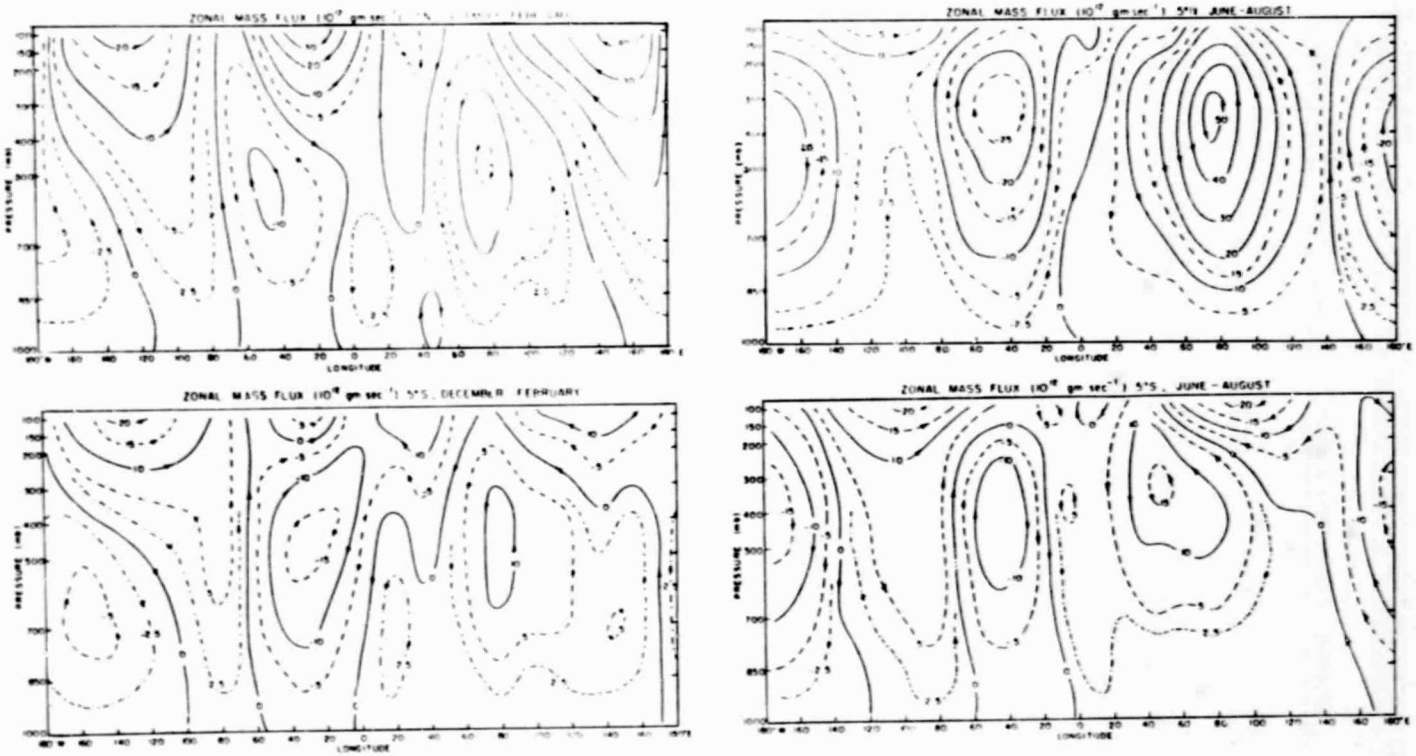

Figure 7.2a Observed stream function for the Walker circulations, according to Newell et al. (1972), for latitudes 5°S and 5°N, in units of 10^9 kg s^{-1}.

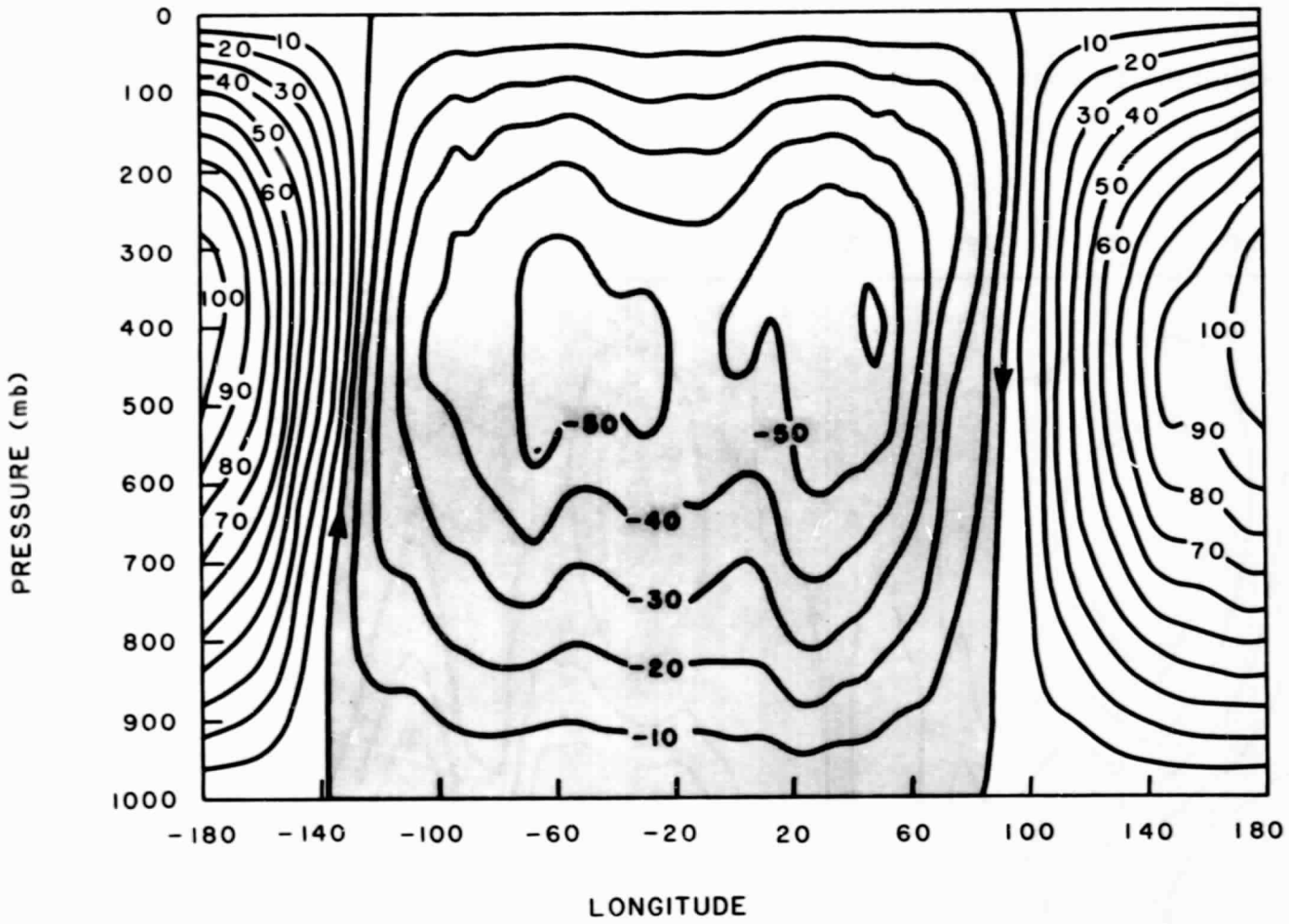

Figure 7.2b February simulated stream function for the Walker circulations, from the Equator to 30°N, in units of 10^9 kg s^{-1}.

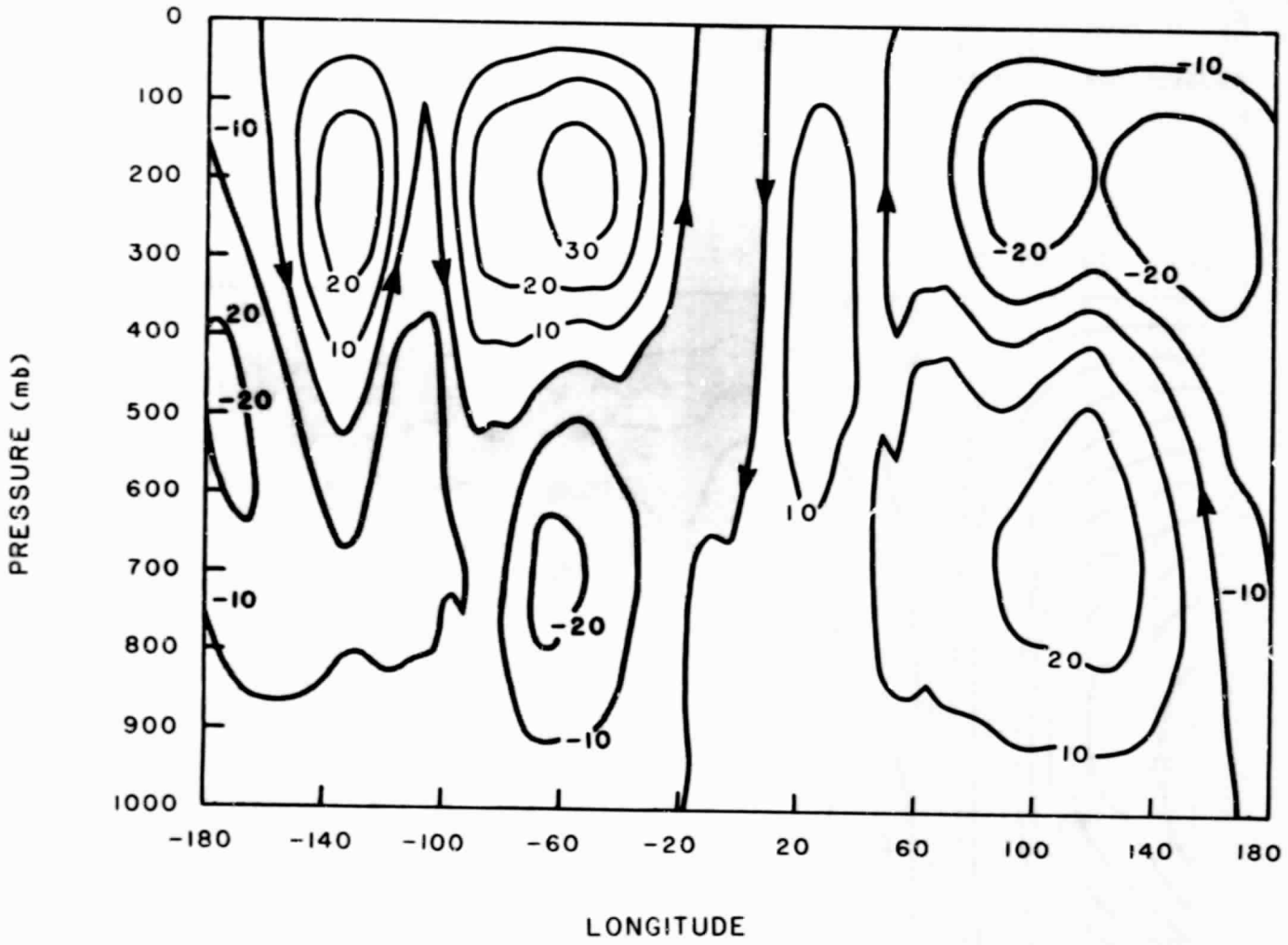

Figure 7.2c July simulated stream function for the Walker circulations, from the Equator to 30°N, in units of 10^9 kg s^{-1}.

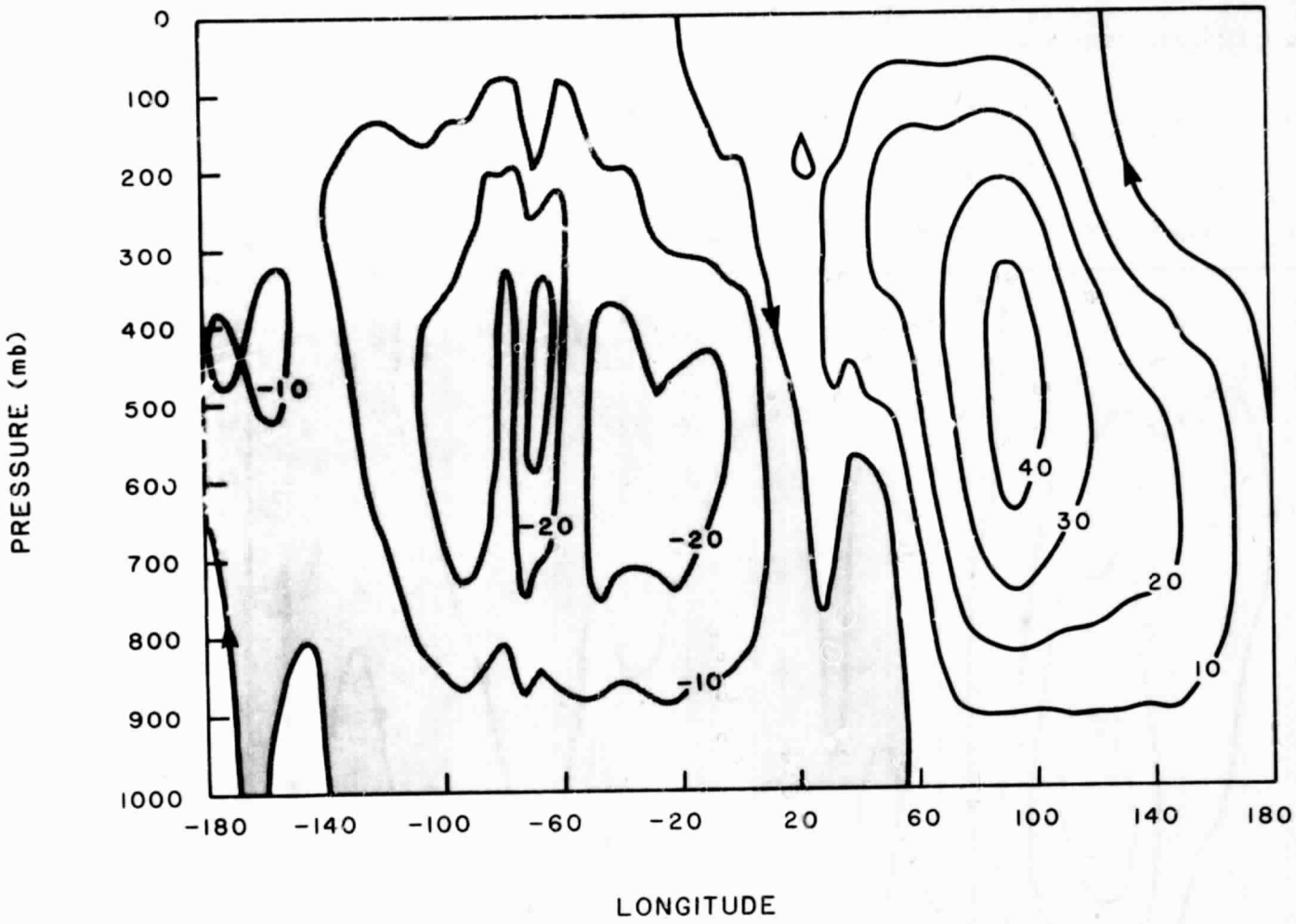

Figure 7.2d July simulated stream function for the Walker circulations, from 30°S to the Equator, in units of 10^9 kg s^{-1}.

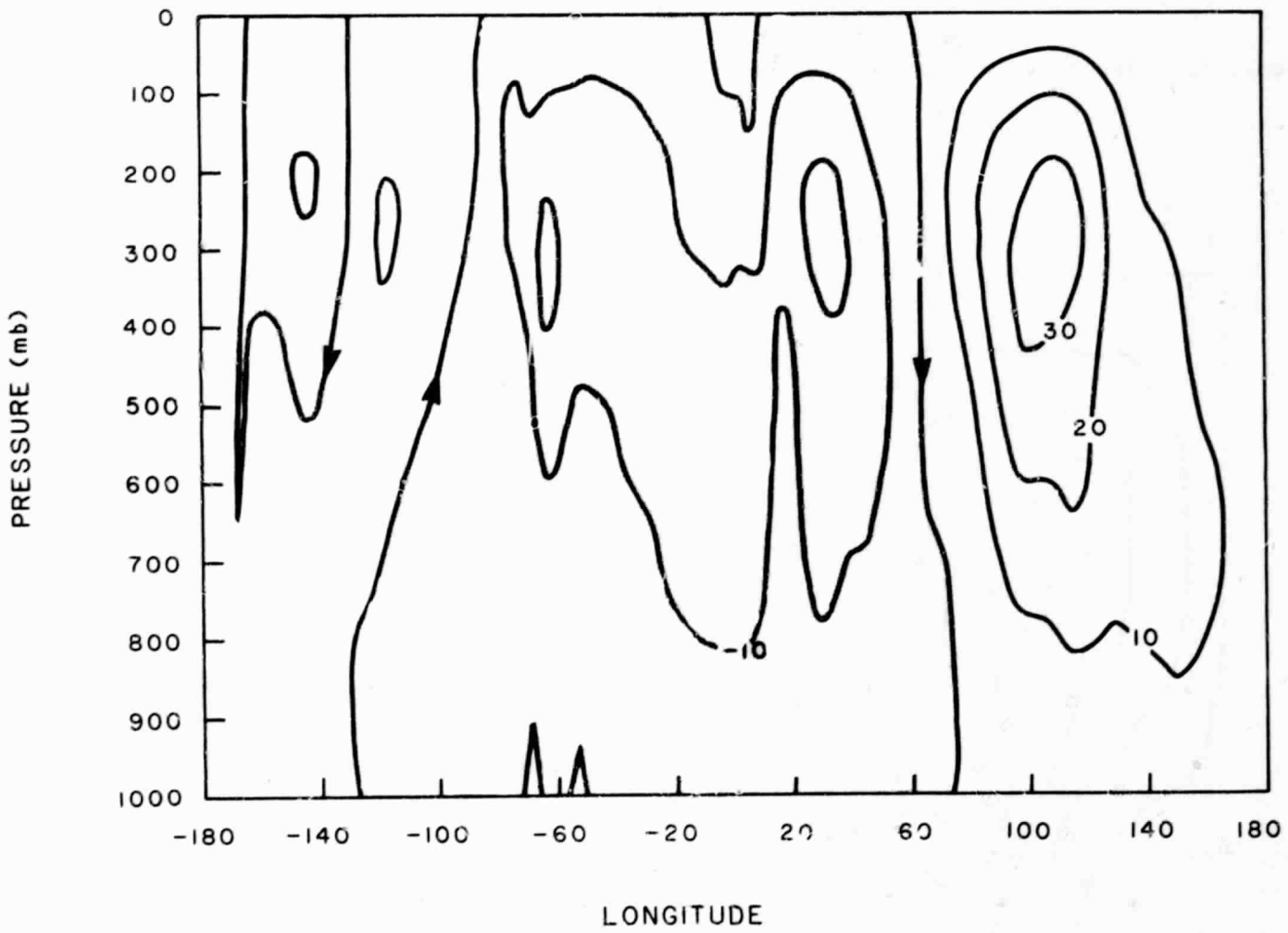

Figure 7.2e February simulated stream function for the Walker circulations, from 30°S to the Equator, in units of 10^9 kg s^{-1}.

8. Summary and Conclusions

The GLAS climate model simulation of the mean dynamical fields is quite reasonable for winter and summer circulations. In general, the lower tropospheric summer circulation features and the upper troposheric winter circulation features compare very well with the respective observed circulations. This is not the case for the upper tropospheric summer circulation and the lower tropospheric winter circulation features. One of the serious deficiencies of the model both in summer and winter simulations is the unrealistically cold polar upper troposphere and the excessive zonal velocity at the uppermost level.

The analysis of spatial and temporal fluctuations indicates that, while the GCM behaves realistically in many respects, some discrepancies between the model and the atmosphere are evident. With regard to the stationary wave field, the zonal variance in the model planetary waves shows a latitude-height structure very similar to that observed. However, the GCM's simulation of the amplitude and phase of individual planetary waves is not as realistic. Maps of local variability show that the model's band-pass variances generally are in accord with observations, with the exception of the upper level transient heat and momentum fluxes. The low-pass variances are not successfully simulated however. In the wavenumber-frequency domain, the model is very skillful in handling the medium frequency synoptic scale waves, but has much less success in the simulation of the low frequency planetary waves. With regard to the latitude-height structure of the total transient fluxes, the heat flux is much more realistically simulated than is the momentum flux.

The model's simulation of diabatic and frictional processes is generally satisfactory. The simulated evaporation, surface sensible heat flux, and surface stress are in good agreement with observations, although the sensible

heat flux is somewhat too high. The simulated precipitation distribution is realistic and shows the expected predominance of cumulus precipitation in the tropics. The most serious deficiency is the excessive frequency of supersaturation clouds in the lowest model layer. We believe that the problem is due to certain weaknesses in the boundary layer parameterization; appropriate revisions are in preparation.

The simulated Hadley circulations are weaker than observed, but their location and depths are satisfactory. The model produces a vigorous subtropical Walker circulation in the winter hemisphere. The rising branch of the Walker cell coincides with an oceanic precipitation maximum, while the sinking branch is over land.

REFERENCES

Arakawa, A., 1969: Parameterization of cumulus convection. Proc. WMO/IUGG Symposium on Numerical Prediction in Tokyo, IV8, 1-6.

Arakawa, A., 1972: Design of the UCLA General Circulation Model. Numerical Simulation of Weather and Climate, Technical Report No. 7, Dept. Meteorology, UCLA.

Arakawa, A., A. Katayama and Y. Mintz, 1969: Numerical simulation of the general circulation of the atmosphere. Proc. WMO/IUGG Symposium on Numerical Prediction, Tokyo, 1968, pp. IV-7 to IV-8-12.

Arakawa, A., and W. H. Schubert, 1974: Interaction of a cumulus cloud ensemble with the large-scale environment, Part I. J. Atmos. Sci., 31, 674-701.

Arakawa, A., and V. R. Lamb, 1977: Computational design of the basic dynamical processes of the UCLA general circulation model. Methods in Computational Physics, 17, Academic Press, New York, 173-265.

Berlyand, T. G., and L. A. Strokina, 1980: Global distribution of a cumulative number of clouds. Leningrad : Gidrometeoizdat.

Bjerknes, J., 1969: Atmospheric teleconnections from the equatorial Pacific. Mon. Wea. Rev., 97, 163-172.

Blackmon, M. L., 1976: A climatological spectral study of the 500 mb geopotential height of the Northern Hemisphere. J. Atmos. Sci., 33, 1607-1622.

Blackmon, M. L., J. M. Wallace, N. C. Lau and S. L. Mullen, 1977: An observational study of the Northern Hemisphere wintertime circulation. J. Atmos. Sci., 34, 1040-1053.

British Meteorological Office, 1977 "Monthly Ice Charts", Meteorological Office, London Road, Bracknell, Berkshire.

Budyko, M. I., 1963: Atlas of Heat Balance of the Earth. (In Russian) Academy of Sciences, Moscow, 69 pp. (Also, Guide to the Atlas of the Heat Balance of the Earth. Translated from Russian by I. A. Donehoo, U. S. Weather Bureau, WB/T-106, Washington, DC, 25 pp.)

Charney, J. G., W. J. Quirk, S. H. Chow, and J. Kornfield, 1977: A comparative study of the effects of albedo change on drought in semi-arid regions. J. Atmos. Sci., 34, 1366-1385.

Cornejo-Garrido, A. G., and P. H. Stone, 1977: On the heat balance of the Walker circulation. J. Atmos. Sci., 34, 1155-1162.

Crutcher, H. L., and O. M. Davis, 1969: U.S. Navy Marine Climatic Atlas of the World. NAVAIR 50-1C-54, Naval Weather Service Command, Washington, D.C.

PAGE INTENTIONALLY BLANK

Godbole, R. V., and J. Shukla, 1981: Global analysis of January and July Sea Level Pressure. NASA Tech. Memo. 82097.

Godson, W. L., 1955: The computation of infrared transmission by atmospheric water vapor. J. Meteorol., 12, 272-284.

Halem, M., and G. Russell, 1973: A split-grid differencing scheme for the GISS model. Research Review, 1973, (Part 2: Applications), Goddard Institute for Space Studies, NASA/GSFC.

Halem, M., J. Shukla, Y. Mintz, M. L. Wu, R. Godbole, G. Herman, and Y. Sud, 1979: Comparisons of observed seasonal climate features with a winter and summer numerical simulation produced by the GLAS general circulation model. GARP Pub. Series No. 22, 207-253, WMO, Geneva, Switzerland.

Haltiner, G. J., 1971: Numerical weather prediction. Wiley, 317 pp.

Helfand, H. M., 1979: The effect of cumulus friction on the simulation of the January Hadley circulation by the GLAS model of the general circulation. J. Atmos. Sci., 36, 1827-1843.

Hellerman, S., 1967: An Updated Estimate of the Wind Stress on the World Ocean, Mon. Wea. Rev., 95, 607-626 (correction, 1968: 96, 63-74.)

Herman, G. F., and W. T. Johnson, 1978: The sensitivity of the general circulation to Arctic sea-ice boundaries: A numerical experiment. Mon. Weather Rev., 106, 1649-1664.

Jaeger, L., 1976: Monatskarten des Niederschlags fur die ganze Erde. Berichte des Deutschen Wetterdienstes, 18, No. 139. Im Selbstverlag des Deutschen Welterdienstes, Offenbach, W. Germany.

Kurihara, Y., 1965: Numerical integration of the primitive equations on a spherical grid. Mon. Wea. Rev., 93, 399-415.

Lacis, A. A., and J. E. Hansen, 1974: A parameterization for the absorption of solar radiation in th earth's atmosphere. J. Atmos. Sci., 31, 118-133.

Lau, N. C., 1978: On the three-dimensional structure of the observed transient eddy statistics of the Northern Hemisphere wintertime circulation. J. Atmos. Sci., 35, 1900-1923.

Lau, N. C., H. Tennekes and J. M. Wallace, 1978: Maintenance of the momentum flux by transient eddies in the upper troposphere. J. Atmos. Sci., 35, 139-147.

Leith, C. E., 1964: Numerical simulation of the earth's atmosphere. Methods in computational physics, Vol. 4. New York, Academic Press, 1-28.

Lin, J. D., J. Alfano, and P. Bock, 1978: Documentation of a ground hydrology parameterization for use in the GISS General Circulation Model. NASA CR158766, 143 pp.

Lord, S. J., and A. Arakawa, 1981: Interaction of a cumulus cloud ensemble with the large-scale environment, Part II. J. Atmos. Sci., 37, 2677-2692.

Lorenz, E. N., 1955: Available potential energy and the maintenance of the general circulation. Tellus, 7, 157-167.

Lorenz, E. N., 1960: Energy and numerical weather prediction. Tellus, 12, 364-373.

Manabe, S., J. Smagorinsky and R. F. Strickler, 1965: Simulated climatology of a general circulation model with a hydrologic cycle. Mon. Wea. Rev., 93, 769-798.

Matson, M., 1978: Winter snow-cover maps of North America and Eurasia, 1966-1976. Unpublished manuscript.

Miller, D. B., and R. G. Feddes, 1971: Global atlas of relative cloud cover 1967-1970. Joint production by U.S. Dept. of Commerce and U.S. Air Force. Washington, DC, September, 1971.

Mintz, Y., 1964: Very long-term global integration of the primitive equations of atmospheric motion. WMO-IUGG Symposium on Research and Development Aspects of Long Range Forecasting. World Meteor. Org., Tech. Note No. 66, 141-155.

Mintz, Y., 1979: On the simulation of the oceanic general circulation. GARP Pub. Series No. 22, 607-687. WMO, Geneva, Switzerland.

Moeng, C.-H., and D. A. Randall, 1982: The radiative impact of cumulus cloudiness in a general circulation model. Submitted to the Mon. Wea. Rev.

Newell, R. E., J. M. Kidson, D. G. Vincent and G. J. Boer, 1972: The general circulation of the atmosphere and interactions with extratropical latitudes, Vols. 1 and 2, MIT Press, Cambridge, Massachusetts.

Oort, A. H., 1964: On estimates of the atmospheric energy cycle. Mon. Wea. Rev., 92, 483-493.

Oort, A. H. and J. P. Peixoto, 1974: The annual cycle of the energetics of the atmosphere on a planetary scale. J. Geophys. Res., 79, 2705-2719.

Oort, A. H. and E. M. Rasmusson, 1971: Atmospheric circulation statistics. NOAA Prof. Paper 5, 373 pp. U. S. Government Printing Office, Washington, DC.

Peixoto, J. P. and A. H. Oort, 1974: The annual distribution of atmospheric energy on a planetary scale. J. Geophys. Res., 79, 2149-2159.

Phillips, N. A., 1956: The general circulation of the atmosphere: a numerical experiment. Q. J. Roy. Meteor. Soc., 82, 123-164.

Phillips, N. A., 1957: A coordinate system having some special advantages for numerical forecasting. J. Meteor., 14, 184-185.

Posey, J. W., and P. F. Clapp, 1964: Global distribution of normal surface albedo. Geofisica International, 4, 33-43.

Pratt, R. W., 1975: Space-time spectral analysis of large-scale mid-latitude disturbances. Ph.D. dissertation, University of Washington.

Pratt, R. W., 1977: Space-time kinetic energy spectra in mid-latitudes. J. Atmos. Sci., 34, 1054-1057.

Pratt, R. W., 1979: A space-time spectral cmparison of the NCAR and GFDL general circultion models to the atmosphere. J. Atmos. Sci., 36, 1681-1691.

Pratt, R. W. and J. M. Wallace, 1976: Zonal propagation characteristics of large-scale fluctuations in the mid-latitude troposphere. J. Atmos. Sci., 33, 1184-1194.

Randall, D. A., 1982: Performance of the PBL parameterizations in the GLAS and UCLA models. Proceedings of the Workshop on the Planetary Boundary Layer of the European Centre for Medium Range Weather Forecasts, Reading, England (to appear).

Raschke, E., T. H. VonderHaar, M. Pasternak, and W. R. Bandeen, 1973: The radiation balance of the earth-atmosphere system from Nimbus-3 radiation measurements. NASA TND-7249, NASA, Washington, D.C.

Sadler, J. C., 1975: The upper tropospheric circulation over the global tropics. Department of Meteorology, University of Miami, Florida.

Schutz, C., and W. L. Gates, 1971: Global climatic data for surface, 800 mb, 400 mb: January. The Rand Corp., R915-ARPA.

Schutz, C., and W. L. Gates, 1972: Global climatic data for surface, 800 mb, 400 mb: July. The Rand Corp., R-1029-ARPA.

Shapiro, R., 1970: Smoothing, filtering and boundary effects. Rev. Geophys. and Space Phys., 8, 359-387.

Smagorinsky, J., 1963: General circulation experiments with the primitive equations. I. The basic experiment. Mon. Wea. Rev., 91, 99-164.

Somerville, R. C. J., P. H. Stone, M. Halem, J. E. Hansen, J. S. Hogan, L. M. Druyan, G. Russell, A. A. Lacia, W. J. Quirk, and J. Tennenbaum, 1974: The GISS model of the global atmosphere. J. Atmos. Sci., 31, 84-117.

Stone, P. H., S. Chow, and W. J. Quirk, 1977: The July climate and a comparison of the January and July climates simulated by the GISS general circulation model. Mon. Wea. Rev., 105, 170-194.

Straus, D. M., and J. Shukla, 1981: Space-time spectral structure of the geopotential height of a GLAS General Circulation Model and a comparison to the atmosphere. J. Atmos. Sci., 38, 902-917.

Sud, Y. C., and J. A. Abeles, 1981: Calculation of surface temperature and surface fluxes in the GLAS GCM. NASA Tech. Memo. 82167.

Sud, Y., V. Krishnamurthy, L. Marx and E. Sabatino, 1982: The GLAS climate model: A documentation and user's guide. In preparation as a NASA Tech. Memo.

Wu, M. L., 1976: Longwave radiation and its effect on the atmosphere. Ph.D. Thesis, The University of Chicago, 160 pp.

Wu, M. L., L. D. Kaplan, and R. Godbole, 1978: Influence of systematic radiadion differences on the dynamics of a model atmosphere. Third Conf. on Atmos. Rad. of the Amer. Meteor. Soc., June 28-30, 1978, Davis, CA.

Wu, M. L., 1980: The exchange of infrared radiative energy in the troposphere. J. Geophys. Res., 85, 4084-4090.

APPENDIX

The GLAS Climate Model

- A Bibliography -

Arakawa, A., 1969: Parameterization of cumulus convection. Proc. WMO/IUGG Symposium on Numerical Prediction in Tokyo, IV8, 1-6.

Arakawa, A., 1972: Design of the UCLA General Circulation Model. Numerical Simulation of Weather and Climate, Technical Report No. 7, Dept. Meteorology, UCLA.

Charney, J. G., W. J. Quirk, S. H. Chow, and J. Kornfield, 1977: A comparative study of the effects of albedo change on drought in semi-arid regions. J. Atmos. Sci., 34, 1366-1385.

Godbole, R. V., and J. Shukla, 1981: Global analysis of January and July Sea Level Pressure. NASA Tech. Memo. 82097.

Halem, M., J. Shukla, Y. Mintz, M. L. Wu, R. Godbole, G. Herman, and Y. Sud, 1979: Comparisons of observed seasonal climate features with a winter and summer numerical simulation produced with the GLAS general circulation model. GARP Publ. Series No. 22, 207-253, WMO, Geneva, Switzerland.

Haltiner, G. J., 1971: Numerical weather prediction. Wiley, 317 pp.

Helfand, H. M., 1979: The effect of cumulus friction on the simulation of the January Hadley circulation by the GLAS model of the general circulation. J. Atmos. Sci., 36, 1827-1843.

Helfand, H. M., 1981: Dependence of tropospheric temperature on the parameterization of cumulus convection in the GLAS model of the general circulation. Mon. Wea. Rev., 109, 65-76.

Herman, G. F., and W. T. Johnson, 1978: The sensitivity of the general circulation to Arctic sea-ice boundaries: A numerical experiment. Mon. Weather Rev., 106, 1649-1664.

Herman, G. F., M. L. Wu, and W. T. Johnson, 1980: The effect of clouds on the earth's solar and infrared radiation budgets. J. Atmos. Sci., 37, 1251-1261.

Herman, G. F., and W. T. Johnson, 1980: Arctic and Antarctic climatology of a GLAS general circulation model. Mon. Wea. Rev., 108, 1974-1991.

Herman, G. F., 1980: Cloud-radiation experiments conducted with GLAS general circulation models. Paper presented at the Workshop on Radiation and Cloud-Radiation Interaction, Eur. Cen. Med. Range Wea. Pred., 15-17 October.

Parkinson, C. L., and G. F. Herman, 1980: Sea-ice simulations based on fields generated by the GLAS GCM. Mon. Wea. Rev., 108, 2080-2091.

Shukla, J., and B. Bangaru, 1979: Effect of a Pacific SST anomaly. GARP Publ. Series No. 22, 501-518, WMO, Geneva, Switzerland.

Shukla, J., and Y. Sud, 1981: Effect of cloud-radiation feedback on the climate of a general circulation model. J. Atmos. Sci., 38.

Shukla, J., and A. D. Moura, 1981: On the dynamics of droughts in northeast Brazil: Observations, theory and numerical experiments with a general circulation model. J. Atmos. Sci., 38.

Shukla, J., and Y. Mintz, 1981: The influence of land-surface evapotranspiration on the earth's climate. Accepted for publication in Science.

Stone, P. H., S. Chow, and W. J. Quirk, 1977: The July climate and a comparison of the January and July climates simulated by the GISS general circulation model. Mon. Wea. Rev., 105, 170-194.

Straus, D. M. and J. Shukla, 1981: Space-time spectral structure of a GLAS general circulation model and a comparison with observations. J. Atmos. Sci., 38, 902-917.

Sud, Y. C., and J. A. Abeles, 1981: Calculatin of surface temperature and surface fluxes in the GLAS GCM. NASA Tech. Memo. 82167.

Sud, Y., and M. Fennessy, 1981: A numerical simulation study of the influence of surface albedo on July climatology in semi-arid regions. Accepted for publication in J. Climat.

Tenenbaum, J., 1976: Spectral and spatial energetics of the GISS model atmosphere. Mon. Wea. Rev., 104, 15-30.

Tenenbaum, J., 1980: Integrated and spectral energetics of the GLAS general circulation model. To be published in Mon. Wea. Rev.

Wu, M. L., 1967: Longwave radiation and its effect on the atmosphere. PhD Thesis, The University of Chicago, 160 pp.

Wu, M. L., L. D. Kaplan, and R. Godbole, 1978: Influence of systematic radiation differences on the dynamics of a model atmosphere. Third Conf. on Atmos. Rad. of the Amer. Meteor. Soc., June 28-30, 1978, Davis, CA.

Wu, M. L. 1980: The exchange of infrared radiative energy in the troposphere. J. Geophys. Res., 85, 4084-4090.